Impact of Wall Surface Characteristics on Deposit Formation of Evaporating Urea Water Solution

Einfluss von Wandoberflächeneigenschaften auf die Ablagerungsbildung von verdunstender Harnstoff-Wasser-Lösung

Zur Erlangung des akademischen Grades Doktor-Ingenieur (Dr.-Ing.)
Genehmigte Dissertation von Olaf Schumacher, M.Sc.
Tag der Einreichung: 30. September 2024, Tag der Prüfung: 11. Dezember 2024

1. Gutachten: Prof. Dr.-Ing. Peter Stephan
2. Gutachten: Prof. Dr. Olaf Deutschmann
Darmstadt, Technische Universität Darmstadt

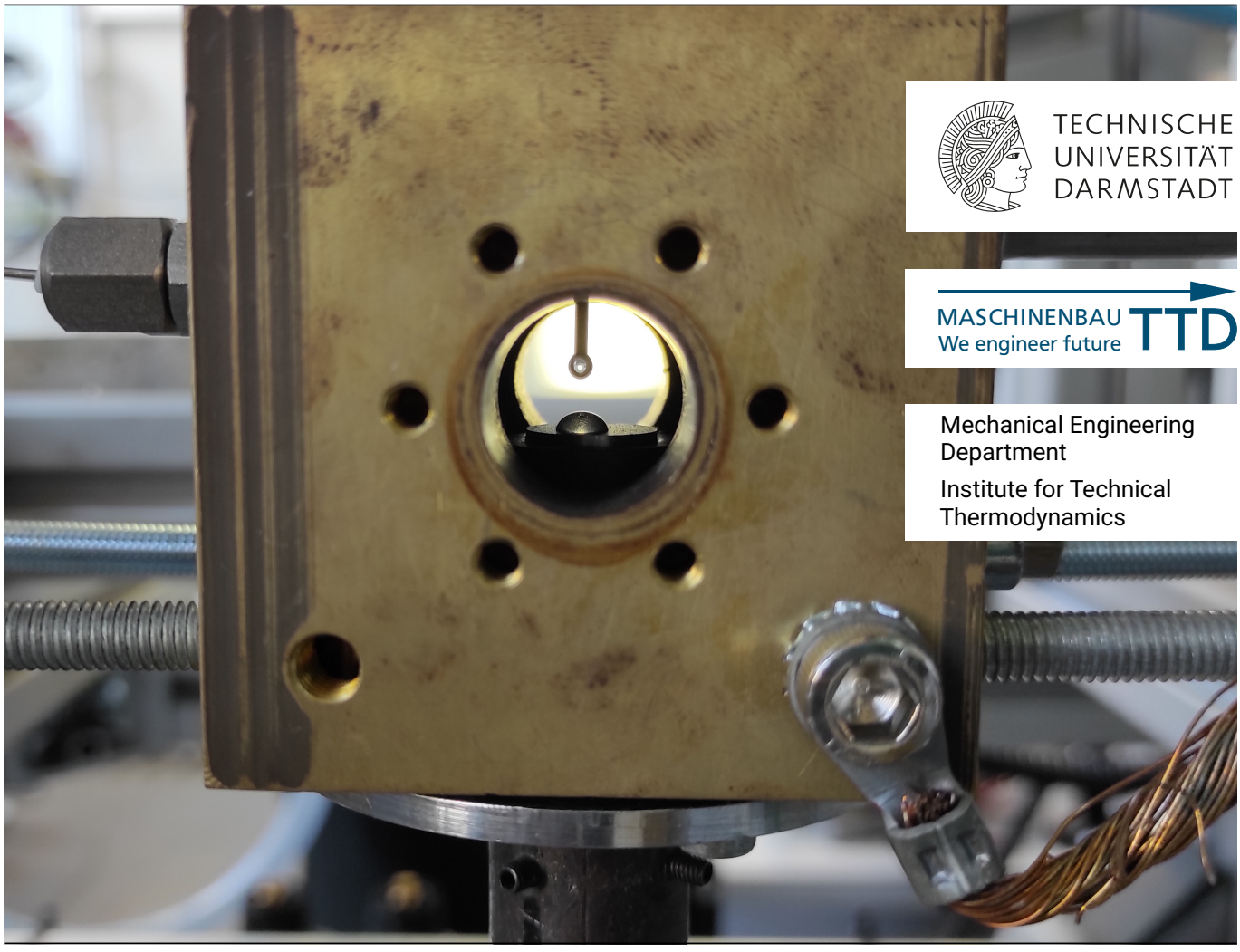

Impact of Wall Surface Characteristics on Deposit Formation of Evaporating Urea Water Solution
Einfluss von Wandoberflächeneigenschaften auf die Ablagerungsbildung von verdunstender Harnstoff-Wasser-Lösung

Accepted doctoral thesis by Olaf Schumacher, M.Sc.

Date of submission: September 30, 2024
Date of thesis defense: December 11, 2024

Darmstadt, Technische Universität Darmstadt

Bitte zitieren Sie dieses Dokument als:
URN: urn:nbn:de:tuda-tuprints-289314
URL: http://tuprints.ulb.tu-darmstadt.de/28931
DOI: https://doi.org/10.26083/tuprints-000028931
Jahr der Veröffentlichung auf TUprints: 2024

Dieses Dokument wird bereitgestellt von tuprints,
E-Publishing-Service der TU Darmstadt
http://tuprints.ulb.tu-darmstadt.de
tuprints@ulb.tu-darmstadt.de

Für Horst Schumacher

Danksagung

Die vorliegende Arbeit[1] entstand während meiner Anstellung als wissenschaftlicher Mitarbeiter am Institut für Technische Thermodynamik der Technischen Universität Darmstadt. Ich bedanke mich ganz herzlich bei meinem Doktorvater, Herrn Prof. Dr.-Ing. Peter Stephan, für die Möglichkeit, diese Arbeit zu verfassen. Die am Institut geschaffenen Rahmenbedingungen, der wissenschaftliche Austausch und das entgegengebrachte Vertrauen haben wesentlich zum Erfolg dieser Dissertation beigetragen und über die vergangenen Jahre stets zu einem angenehmen und produktiven Arbeitsumfeld geführt. Herrn Prof. Dr. Olaf Deutschmann danke ich ebenfalls sehr herzlich für die Übernahme des Korreferats. Nicht zuletzt möchte ich auch meinem Gruppenleiter, Herrn Dr. Axel Sielaff, für seine fachliche Expertise, die freundlichen Gespräche und die stets offene Tür herzlich danken.

Auch die Zusammenarbeit und der Austausch mit meinen Kolleginnen und Kollegen haben meine Promotionszeit in vielerlei Hinsicht bereichert. Ich durfte zahllose lehrreiche, spannende und humorvollen Begegnungen erleben und möchte mich besonders bei meinen Kollegen aus dem Kompetenzbüro – Henrik Sontheimer, Michael Heinz, Imdad Chowdhury und Ehsanul Alam – für die gegenseitige Unterstützung und die gute Arbeitsatmosphäre bedanken. Mein Dank gilt ebenso allen, die durch fachlichen Austausch und Korrekturlesen zum Gelingen dieser Arbeit beigetragen haben: Robin Behle, Till Pfeiffer, Johannes Kind, Julia Eicke und insbesondere Jannik Neumann.

Ein wesentlicher Teil meiner Arbeit wäre ohne den Einsatz der Werkstatt um Roland Berntheisel, Dirk Feldmann und Robert Schrod nicht möglich gewesen. Ob bei der Fertigung komplizierter Bauteile oder fachlicher Beratung, hier habe ich stets unkompliziert die benötigte Hilfe erhalten. Gleiches gilt für das IT-Team um Markus Keiner, Lidia Querling und Voker Bartsch. Ich danke auch Heike Kagerbauer und Gaby Gunkel für ihre Unterstützung bei organisatorischen und administrativen Tätigkeiten. Ihr offenes Ohr und ihre langjährige Erfahrung waren äußerst wertvoll und haben den Institutsalltag auch menschlich geprägt.

Den Initiatoren, Mitarbeiterinnen und Mitarbeitern des Sonderforschungsbereichs/Transregio 150 gebührt ebenfalls mein herzlicher Dank. Die Möglichkeit, in einem solchen Verbund mitarbeiten zu dürfen, hat mir viele wertvolle Erfahrungen und Einblicke über das eigene Fachgebiet hinaus verschafft. In diesem Zusammenhang bedanke ich mich auch bei der Deutschen Forschungsgemeinschaft für die finanzielle Unterstützung.

Da auch der Tag eines Doktoranden nur 24 Stunden hat, war ich auf die Hilfe vieler Studierender angewiesen. Ihnen allen gilt mein herzlicher Dank, denn ohne ihren engagierten, tatkräftigen und sorgfältigen Beitrag wäre meine Arbeit am Institut nicht möglich gewesen. Ein besonderer Dank gilt meinen HiWis Tamara Hintz,

[1] The author utilized ChatGPT, developed by OpenAI [102], for editorial review in this thesis. All research, analysis, and conclusions are the author's own.

Henning Schubert, Kim Jaich und Pavit Singh Sachdeva – für eure tolle, selbstständige Arbeitsweise und das gegenseitige Vertrauen. Ich wünsche euch alles Gute und viel Erfolg auf eurem weiteren Weg.

Von Herzen danke ich auch meinen Eltern, Andrea und Horst Schumacher, die mich während meiner gesamten Laufbahn gefördert und stets an mich geglaubt haben. Mein ganz besonderer Dank gilt abschließend meiner Frau, Wienke Schumacher. Dein Beitrag zu dieser Arbeit und deine bedingungslose Unterstützung lassen sich nicht in Worte fassen. Ich bin unendlich dankbar, dich an meiner Seite zu haben.

30.09.2024

Olaf Schumacher

Abstract

Health hazards and strict regulatory requirements make the reduction of NO_x emissions from indispensable combustion processes, such as those in construction vehicles, waste incineration plants, and industrial boilers, essential. A highly relevant technological solution is the Selective Catalytic Reduction (SCR), in which an aqueous urea solution is injected into the exhaust gas treatment system. The urea decomposes into ammonia, which reduces NO_x emissions to nitrogen and water in the presence of a catalyst.

A disadvantage of this method is the unavoidable formation of liquid films on the system walls. Upon evaporation, these films leave behind solid deposits of urea and, at higher temperatures, increasingly heat-resistant decomposition products such as biuret, cyanuric acid, and ammelide. These deposits significantly impair the overall process by disrupting spray formation or increasing back pressure.

To minimize such deposits, this work focuses on the surface characteristics of the involved system walls. By collecting data from generic experiments and modeling the influencing factors, the understanding of the deposit formation process and the effects of modifiable parameters will be improved.

In the experiments, several drops of an aqueous urea solution are evaporated on heated metal samples under precise control of the boundary conditions. The samples are prepared to test the influences of different wall surface characteristics. A statistical experimental design is conducted beforehand to allow for thoroughly analyzing the effects and their interactions. The studied influences include various roughness levels, submillimeter-scale structures, and chemical coatings that vary the wetting behavior. Additionally, the influence of sample temperature and heating duration is investigated. The final deposits are characterized in terms of their mass, volume, and the wall area they cover.

In addition to detailed phenomenological observations, the collected data is used for subsequent regression analysis. Models are developed to determine the dependency of the deposit metrics on the investigated influences. The results and analyses show that the preliminary processes of wetting and evaporation are significantly influenced by the surface characteristics. Depending on the structure geometry, capillary forces have a considerable effect on liquid spreading, while in other cases, wall films are noticeably hindered in their spread by the structures. Introduced surface roughness exhibits a clear dependence on the respective surface coating. At roughness values $\geq 1.6\,\mu m$, significantly enhanced wetting or non-wettability of the surfaces is observed depending on the chemical pretreatment. These phenomena also affect the subsequent deposit formation. By purposefully maximizing film spreading, deposit mass and volume can be minimized. Wall surface structuring, on the other hand, is particularly suitable for minimizing the deposit area due to its effect on initial film spreading. Overall, the analyses highlight both complex interactions between surface characteristics as well as fundamentally distinct effects of influencing factors at the two considered wall temperatures.

The developed models show very good agreement with the experimental data and expand the insights gained by quantifying the relevant effects, leading to a more detailed understanding of the deposit formation process. Additionally, the models form the foundation for an optimization strategy demonstrated in this work. This is necessary because the target variables, like deposit area and mass, respond oppositely with respect to the investigated influences. Thus, model-based optimization that considers individual objectives proves valuable for deriving insights for engineering applications from the findings. This approach is ultimately demonstrated through an application featuring a user-friendly interface.

Zusammenfassung

Gesundheitliche Gefahren und strenge gesetzliche Vorgaben machen die Reduktion von NO_x-Emissionen aus nach wie vor unverzichtbaren Verbrennungsprozessen, wie sie beispielsweise in Baufahrzeugen, Müllverbrennungsanlagen und industriellen Boilern auftreten, unabdingbar. Eine dazu hochrelevante technologische Lösung ist die Selektive Katalytische Reduktion (SCR), bei der eine wässrige Harnstofflösung in das Abgasreinigungssystem injiziert wird. Der Harnstoff zersetzt sich zu Ammoniak, welches in Gegenwart eines Katalysators NO_x zu Stickstoff und Wasser reduziert.

Ein Nachteil dieser Methode ist die unvermeidbare Filmbildung der eingesprühten Lösung an den Systemwänden. Die Filme hinterlassen beim Verdampfen feste Ablagerungen aus Harnstoff und bei höheren Temperaturen zunehmend hochtemperaturfeste Zersetzungsprodukte wie Biuret, Cyanursäure und Ammelide. Diese Ablagerungen beeinträchtigen den Gesamtprozess erheblich, etwa indem sie die Spraybildung beeinträchtigen oder den Gegendruck erhöhen.

Mit dem Ziel, solche Ablagerungen zu minimieren, liegt der Fokus dieser Arbeit auf den Auswirkungen der Oberflächeneigenschaften der beteiligten Systemwände. Durch in generischen Experimenten erhobene Daten und Modellierung der Einflussgrößen soll das Verständnis für den Ablagerungsbildungsprozess und die Effekte modifizierbarer Parameter verbessert werden.

In den Versuchen werden mehrere Tropfen einer Harnstoff-Wasser-Lösung unter präziser Kontrolle der Randbedingungen auf beheizten Metallproben verdampft. Die Proben sind so präpariert, dass die Einflüsse verschiedener Wandeigenschaften getestet werden. Um alle Effekte sowie deren Wechselwirkungen genau analysieren zu können, wird zuvor eine statistische Versuchsplanung durchgeführt. Die untersuchten Einflüsse umfassen verschiedene Rauheiten, Strukturen im Submillimeter-Bereich und chemische Beschichtungen, die das Benetzungsverhalten variieren. Zusätzlich werden die Einflüsse der Probentemperatur sowie der Beheizungsdauer untersucht. Die finalen Ablagerungen werden hinsichtlich ihrer Masse, ihres Volumens und der von ihnen bedeckten Wandfläche charakterisiert.

Neben genauen phänomenologischen Betrachtungen werden die erhobenen Daten einer Regressionsanalyse unterzogen. Dabei werden Modelle für die Abhängigkeit der Ablagerungsgrößen von den untersuchten Einflüssen entwickelt. Die Ergebnisse und Analysen zeigen, dass die vorgelagerten Teilprozesse Benetzung und Verdampfung erheblich von den Oberflächeneigenschaften beeinflusst werden. Je nach Strukturgeometrie zeigt sich ein deutlicher Einfluss von Kapillarkräften auf die Flüssigkeitsausbreitung, während die Wandfilme in anderen Fällen von den Strukturen merklich in ihrer Ausbreitung behindert werden. Eingebrachte Oberflächenrauheiten wirken dagegen in deutlicher Abhängigkeit von der jeweiligen Oberflächenbeschichtung. Bei Rauheitswerten $\geq 1.6\,\mu m$ werden je nach chemischer Vorbehandlung deutlich verstärkte Benetzung oder Nicht-Benetzbarkeit der Oberflächen beobachtet. Diese Phänomene wirken sich auch auf die nachgelagerte

Ablagerungsbildung aus, sodass durch zielgerichtete Maximierung der Filmausbreitung die Ablagerungsmasse und das Volumen minimiert werden können. Oberflächlich eingebrachte Strukturen hingegen sind aufgrund ihrer Wirkung auf die initiale Filmausbreitung besonders zur Minimierung der Ablagerungsfläche geeignet. Insgesamt zeigen sich teilweise komplexe Wechselwirkungen zwischen den Oberflächeneigenschaften, aber auch grundsätzlich unterschiedliche Effekte der Einflussgrößen bei unterschiedlichen Wandtemperaturen.

Die entwickelten Modelle zeigen eine sehr gute Übereinstimmung mit den experimentellen Daten und erweitern die daraus gewonnenen Erkenntnisse um eine Quantifizierung der relevanten Effekte sowie ein umfassenderes Prozessverständnis. Zusätzlich bilden die Modelle die Grundlage für eine im Rahmen der Arbeit demonstrierte Optimierungsstrategie. Eine solche ist notwendig, da die untersuchten Zielgrößen, wie Ablagerungsfläche und -masse, in Bezug auf die untersuchten Einflüsse gegensätzlich reagieren. Daher ist eine modellgestützte Optimierung unter Berücksichtigung individueller Zielvorgaben wertvoll, um aus den Versuchen hilfreiche Erkenntnisse für die ingenieurtechnische Anwendung abzuleiten. Ein solcher Ansatz wird abschließend durch eine Anwendung mit einer benutzerfreundlichen Schnittstelle demonstriert.

Contents

Nomenclature

Symbols

Symbol	Description	SI unit
A	Area	m^2
B	Channel distance of a surface structure	m
d	Diameter	m
H	Channel height of a surface structure	m
I	Interval	–
k	Number of independent variables	–
K	Number of folds used in K-fold cross validation	–
l	Number of settings of the independent variables, levels	–
m	Mass	kg
MSE	Mean squared error	–
MST	Mean of total squares	–
n	Sample size, more generally: number	–
p	p-value of a hypothesis test	–
P	Electrical power	W
r	Radius	m
Ra	Roughness (Arithmetic average of profile height deviations from the mean)	m
R_A	Ratio of true to projected surface area, surface area ratio	–
R^2	Coefficient of determination	–
R^2_{adj}	Adjusted coefficient of determination	–
RMSE	Root mean square error	–
s	Sample standard deviation	–
s^2	Sample variance	–
SE	Standard error	–
SSE	Sum of squared errors	–
SSM	Sum of squared model deviations	–
SST	Total sum of squares	–
t	t-value from Student's t-test	–
T	Temperature	°C
u	Experimental standard uncertainty	–
U	Expanded uncertainty	–
V	Volume	m^3
w	Weights of multi-objective optimization problem	–
W	Channel width of a surface structure, structure distance	m

x	Independent variable, factor, predictor	–
$\mathbf{X}$	Matrix of values for all independent variables x_i across all measurements	–
y	Dependent variable, target variable	–
z	z-Score	–
α	Significance level	–
$(1-\alpha)$	Confidence level	–
β	Model coefficient	–
γ	Surface energy	$\mathrm{J\,m^{-2}}$
δ	Measurement deviation	–
$\Delta\tau$	Duration	s
ΔT	Temperature difference	°C
ϵ	Model residual	–
θ	Contact angle	°
θ^*	Contact angle on non-ideal surfaces	°
λ	Thermal conductivity	$\mathrm{W\,m^{-1}\,K^{-1}}$
μ	Population mean, expected value	–
σ	Population standard deviation	–
τ	Time	s
ζ	Distance	m

Accents

Symbol	Description
$\bar{x}$	Mean
$\vec{x}$	Vector
$\hat{x}$	Estimation

Acronyms and abbreviations

Symbol	Description
BFGS	Broyden-Fletcher-Goldfarb-Shanno algorithm
CCA	Constant contact angle
CCD	Central composite design
CCR	Constant contact radius
CFD	Computational fluid dynamics
DOC	Diesel oxidation catalyst
e.g.	*exempli gratia*, for example
FCCCD	Face centered central composite design
i.e.	*id est*, that is
SCR	Selective catalytic reduction
UWS	Urea-water solution

Subscripts

Symbol	Description
0	Starting point
A	Area
adv	Advancing
adj	Adjusted
air	Air
c	Coating
comb	Combined
cr	critical
dep	Deposit
e	Equilibrium
exp	Experiment
h	Hysteresis
htr	Heater
lg	Liquid-gas
ls	Liquid-solid
m	Mass
max	Maximum
meas	Measurement
min	Minimum
proj	Projected
real	Real
rec	Receding
scl	Scaled
sg	Solid-gas
smooth	Smooth
sub	Substrate
surf	Surface
textured	Textured
T	Temperature
V	Volume
wall	Wall

Dimensionless quantity

Symbol	Description
We	Weber number

Chemical compound

Symbol	Description
CO_2	Carbon dioxide
H_2O	Water

N_2	Nitrogen
NH_3	Ammonia
NO_x	Nitrogen oxide

CHAPTER 1

Introduction

Technological advancements that shape our daily lives heavily depend on a reliable energy supply. Increasingly, this demand is met by renewable sources like solar, hydro, and wind power, which accounted for 30 % of total electric power generation in 2023 [42]. However, combustion processes remain a cornerstone of the world's energy system due to existing infrastructure, technical challenges, and political and social factors. Power plants fueled by coal, waste, or natural gas continue to play a significant role in meeting our energy needs, while boilers and gas turbines are essential for providing the energy required for industrial applications.

A similar situation applies to transportation, which is crucial for today's interconnected goods chains and global trade. While personal transport via cars is increasingly shifting towards electric drives, heavy machinery such as trucks, construction equipment, and marine applications still heavily depend on combustion, particularly diesel engines. These transport sectors are challenging to electrify due to high energy density requirements, long travel distances without refueling, especially for ships and airplanes, and the long refueling times associated with battery vehicles. Therefore, as the transition to sustainable energy sources progresses, optimizing combustion processes remains highly relevant.

One critical area for ongoing improvement is the control of harmful emissions produced by combustion processes. These emissions include carbon dioxide (CO_2), unburned hydrocarbons, particulates, and nitrogen oxides (often collectively referred to as NO_x). NO_x emissions are associated with several health risks, such as respiratory issues and cardiovascular effects [150, 156]. They also contribute to acid rain, affect water bodies and soil chemistry, and play a crucial role in forming ground-level ozone [91, 138].

Figure 1.1 provides an overview of the sources of NO_x emissions in Germany in 2022 [145]. The substantial contributions from traffic and the energy industry, although significantly reduced since 1990, still indicate considerable potential for further improvement. This need for improvement is underscored by strict legislative requirements such as the European emission standards, currently at the EURO 6d stage. Additionally, while the increasing utilization of lean combustion operation reduces CO_2 emissions and increases efficiency, it simultaneously increases NO_x emissions. This applies not only to diesel operation but also to other fuels, including hydrogen and natural gas [126, 157].

A very effective solution to reduce NO_x emissions from exhaust gases is the implementation of air pollution control equipment using selective catalytic reduction (SCR). This technology was first used in power plants and other stationary applications, such as industrial boilers [23]. Ammonia (NH_3) is utilized as a reducing

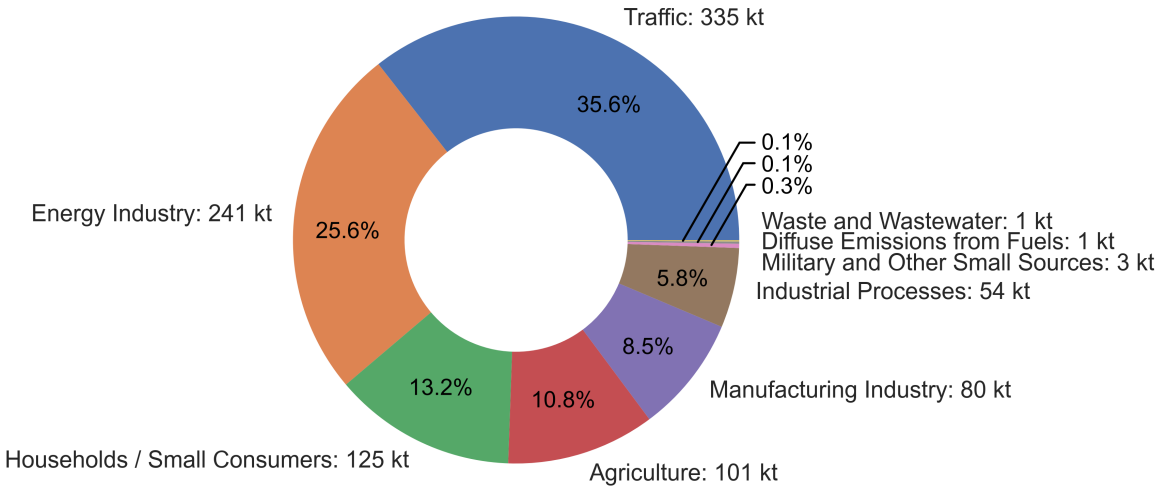

Figure 1.1.: NO_x emission sources in Germany in 2022 according to [145], all quantities are given in kilotons (kt) per year

agent, converting NO_x into nitrogen (N_2) and water (H_2O). This reaction takes place on a catalyst, which is often made of vanadium dioxide or zeolites. The standard SCR reaction is given by:

$$4\,NH_3 + 4\,NO + O_2 \longrightarrow 4\,N_2 + 6\,H_2O. \tag{1.1}$$

A more favorable reaction is the fast SCR reaction given in Equation (1.2), which is promoted by the presence of NO_2 in the exhaust gas. The NO_2:NO ratio can be increased by converting NO to NO_2 using an upstream diesel oxidation catalyst (DOC). However, if the proportion of NO_2 in the total nitrogen oxides exceeds 50 %, the undesired slow SCR reaction, as shown in Equation (1.3), occurs [66]:

$$2\,NH_3 + NO + NO_2 \longrightarrow 2\,N_2 + 3\,H_2O \tag{1.2}$$

$$4\,NH_3 + 3\,NO_2 \longrightarrow 3.5\,N_2 + 6\,H_2O. \tag{1.3}$$

In mobile applications, carrying ammonia is impractical due to safety concerns related to its toxicity. Instead, an aqueous solution containing 32.5 wt% urea, known by the brand name *AdBlue*, is used. This urea-water solution (UWS) is stored in a separate tank and injected into the SCR system as a spray. The spray is designed to evaporate in the exhaust gas flow, where the thermal decomposition of urea produces the ammonia needed for the reduction process. Figure 1.2 illustrates the design of such an SCR system.

As an undesired consequence of spray injection, wall films can form on the solid surfaces of the system due to liquid impingement. Despite significant efforts, preventing wall film formation in SCR systems is nearly impossible given the wide range of operating conditions. The risk increases further with high urea dosing rates aimed at maximizing NO_x reduction, lowered exhaust temperatures, and reduced system dimensions due to space constraints.

Upon evaporation, these wall films form solid deposits, negatively affecting the entire process. The deposits are composed of urea and heat-resistant decomposition products such as biuret, cyanuric acid, and ammeline [81].

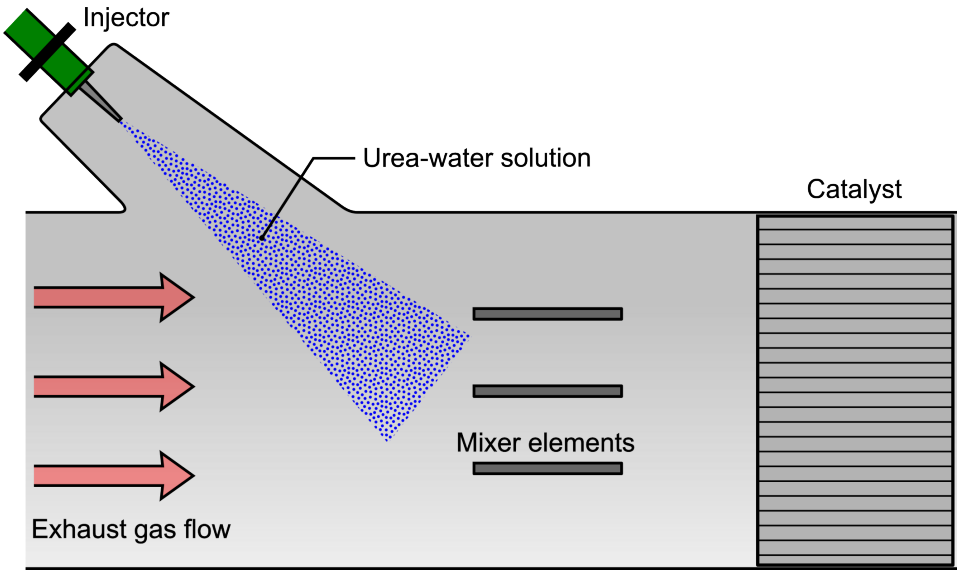

Figure 1.2.: Schematic representation of an SCR exhaust gas treatment system with integrated mixer elements for secondary atomization and turbulence generation

They impair the flow field in the system, especially at the mixer elements, potentially increasing backpressure or even causing blockages. When the deposits accumulate at or near the injector, they interfere with spray formation and the required homogeneous distribution of ammonia in the gas flow. Such deposits are therefore highly undesirable, making effective measures to reduce deposit formation essential. This work aims to contribute to this goal in two ways:

1. By thoroughly studying the formation of solid deposits from aqueous urea solution films under controlled conditions. This enhances the understanding of the deposit formation process and identifies key influencing factors. The gained knowledge provides a foundation for developing and improving technical solutions.

2. By investigating potential solutions with a specific focus on the impact of wall surface characteristics. This exploration operates under the assumption that film formation cannot be entirely prevented, such as on mixer elements. From this research, concrete design recommendations are derived.

To achieve this, Chapter 2 presents the current literature on deposit formation, including the relevant fundamentals of the included processes, and identifies the open scientific questions for this work. Chapter 3 outlines the experimental design for systematically studying the influencing factors on deposit formation in a generic experimental setup. This setup, along with the employed measurement methods and data processing steps, is detailed in Chapter 4. Chapter 5 then presents the basics of statistical description and evaluation, as well as a method to model the experimental data to maximize the knowledge gained from the experiments. The results from the experiments and the models are presented in Chapter 6. Chapter 7 summarizes the findings with regards to the scientific questions and provides an outlook.

CHAPTER 2

State of Research

Deposit formation represents the final stage in a series of interconnected physico-chemical processes. Each of these subprocesses is influenced by various factors that collectively determine the characteristics of the resulting deposit. This complex interplay of influencing factors affects not only the chronological sequence of sub-processes, but also a wide range of relevant time and length scales. This multiscale nature of the processes in deposit formation is depicted in Figure 2.1. Prerequisite for any solid deposit is the formation of a wall film (1), which is determined by droplet-wall interactions during droplet impact (2) and the fluid dynamics of surface wetting (3). The subsequent evaporation of the liquid (4) necessitates the consideration of heat and mass transfer phenomena, particularly for mixtures. Ultimately, deposits might form (5), and while influenced by the preceding processes, their formation is also strongly reliant on the chemistry of urea decomposition.

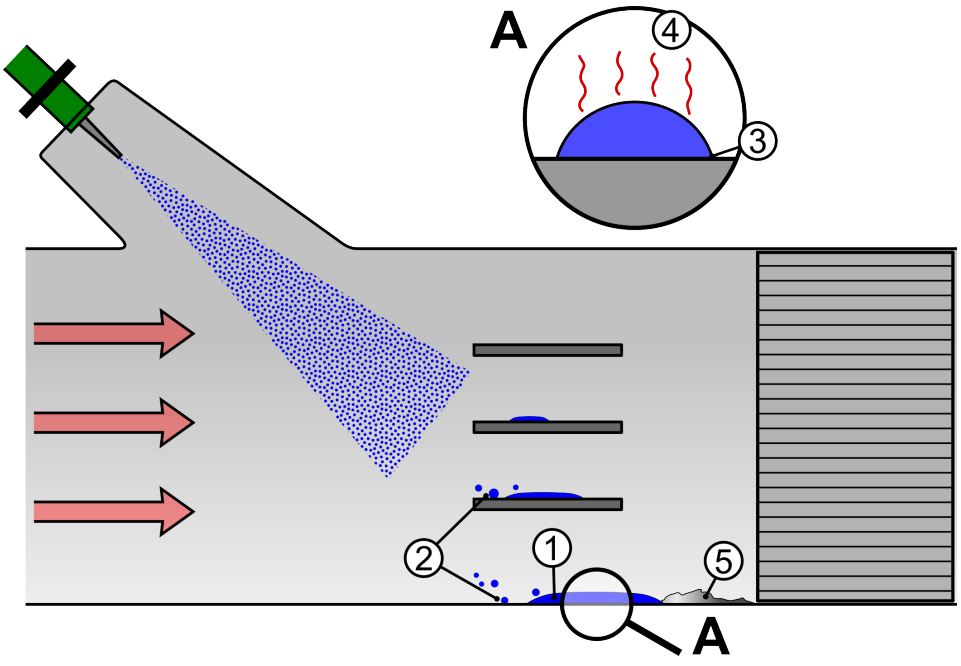

Figure 2.1.: Relevant processes and mechanisms involved in deposit formation from UWS in SCR systems

The combined influence of these processes, along with the effects of external conditions at each relevant time and length scale, adds complexity to the problem of deposit formation. To address this topic effectively, it is crucial to understand all the involved processes and the relevant thermodynamic and fluid dynamic

principles. Therefore, the following section 2.1 provides an overview of the fundamentals and the current state of research on liquid-wall interaction, evaporation, and deposit formation. Section 2.2 then reviews studies focused on the effects of external factors, such as wall characteristics, on urea deposit formation and the preceding processes of wetting and evaporation. The aim is to consolidate existing knowledge on the influencing parameters of deposit formation and identify open questions and potential approaches. The goals of the thesis are presented in the final section 2.3.

2.1. Fundamentals

Each part of the following section discusses general fundamentals first before exploring the specific findings related to UWS.

2.1.1. Liquid/Wall interactions

In SCR systems, the interaction between spray droplets and system walls is a determining factor for liquid-wall contact and subsequent film formation. Specific areas, summarized in Figure 2.2, are particularly prone to film and deposit formation [23].

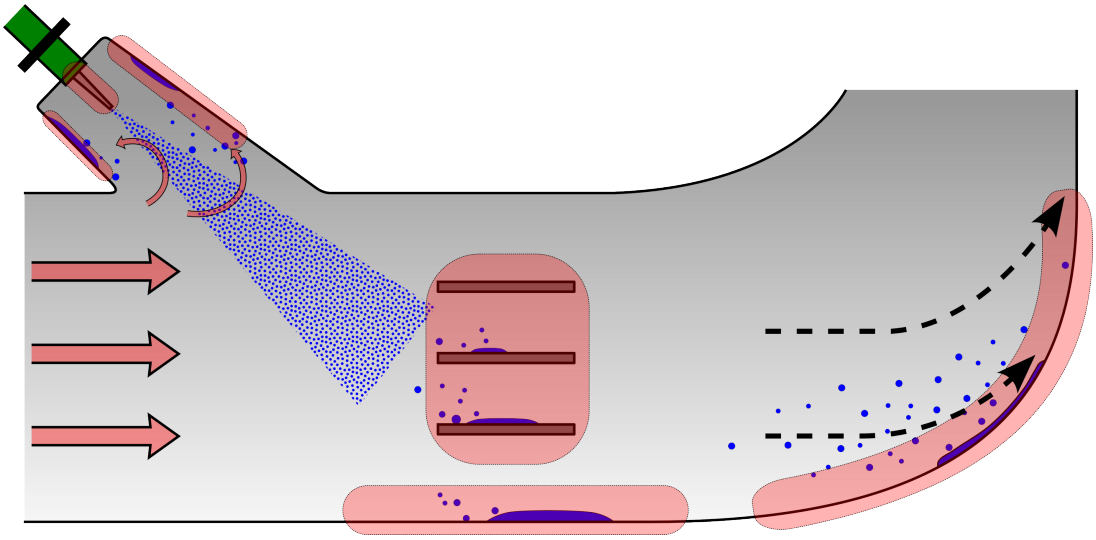

Figure 2.2.: SCR system with highlighted regions of high vulnerability to spray impact and wall film formation. The added 90° channel redirection before the catalyst is often necessary due to space constraints

The vulnerability of the injector region and the system wall opposite the injector results from conflicting spray parameter requirements. If the spray momentum is too low, the liquid fails to travel past the stagnant water region in the dosing flange, which is essential for protecting the injection valve from excessive thermal loads. Conversely, if the spray momentum is too high, the spray is unable to follow the gas flow and impacts the opposite system wall. This challenge is exacerbated by the push for more compact system configurations. Additionally, secondary droplets can contribute to film development within the flange. The mixer elements are also, by design, prone to film formation and accumulation. The task of these mixer elements is to generate

turbulence to ensure the even distribution of the solution in the exhaust gas. For this purpose, they also serve as a primary impingement target for larger droplets, which is intended to result in secondary atomization. Lastly, they increase the thermal decomposition by increasing the necessary heat transfer via direct solid-liquid interaction. [13, 24, 56]

In SCR systems, the UWL is typically injected as spray. However, the subsequent section will narrow its focus to individual droplet-wall interactions, treating them as a simplified representation of spray impact. This emphasis on single droplets is primarily because they are central to the following work, given their accessibility for measurements and the straightforward control and variation of specific boundary conditions. Numerically, many models addressing spray impact derive their foundation from the physics and data associated with single droplet impact events [17].

It must be mentioned that the primary objective of this work isn't centered on droplet impact or its modification. Yet, since this process is a foundational step leading to deposit formation, it warrants attention. This is essential not only for a holistic grasp of the topic but also to delineate the scope of this work and to guide later considerations in experimental design and execution. Additionally, this knowledge is required to weigh different goals when formulating specific recommendations for the practical application from the results of this work.

Droplet impact regimes

Droplet impact on non-heated, dry targets is typically classified into three distinct regimes: deposition, splash, and rebound [108]. In the deposition regime, the droplet mass adheres to the solid surface. The splash regime is characterized by the droplet's high kinetic energy, which results in the creation of secondary droplets. In the rebound regime, the droplet extensively spreads post-impact and then undergoes a rapid receding phase, leading to either a partial or complete rebound of the droplet. To determine these regimes, the Weber number We is used, which takes into account the droplet diameter, impact velocity, liquid density, and surface tension [108]. For the purpose of distinguishing between the regimes, a critical Weber number We_{cr} is defined [93].

In addition to fluid dynamics, heated targets introduce thermal interaction regimes, in particular boiling-induced breakup and the Leidenfrost effect [3, 110]. The breakup regime refers to the thermally driven disintegration of the droplet. The Leidenfrost effect, on the other hand, is characterized by the formation of an insulating vapor layer between the droplet and the wall, resulting in reduced heat transfer. The distinction between these regimes is determined by the ratio of the wall temperature to the respective liquid's boiling temperature [18].

The impact regimes are concisely visualized in regime maps using dimensionless parameters, addressing both the thermal and fluid dynamic effects of droplet impingement [134]. These maps display the relationships between thermal boundaries, Weber number, splash threshold, and temperature, and establish the wetting boundary that differentiates wetting from non-wetting regimes. Regime classification and boundary definition are complex tasks that rely on several parameters, including droplet temperature, surface tension, heat capacity, and impact angle, as well as wall attributes such as thermal conductivity, heat capacity, roughness, and wettability [78, 80, 79].

The behavior of solutions such as UWS is inherently more complex than that of pure liquids. Numerous studies have resulted in regime maps and models specifically for the impact of UWS droplets [13, 16, 78, 107]. Research conducted by Börnhorst [20] with varying urea concentrations indicates that dissolved urea significantly modifies droplet impact in comparison to pure water. The presence of the solute tends to facilitate droplet breakup at elevated temperatures. This is attributed to the increased nucleation of bubbles and the formation of gaseous decomposition products. However, it is noteworthy that regime boundaries remain largely unaffected by urea concentration increases up to 40 wt%.

The direct comparison of results across studies is hindered primarily due to variations in experimental conditions, especially in terms of droplet size and velocity [20]. For instance, documented Leidenfrost temperatures span a wide range, from 198 °C to 310 °C [17]. Additionally, most of these studies do not investigate the influence of the target material or surface characteristics. Yet, it was shown that surface roughness can significantly shift regime boundaries [8, 77].

The experimental setup used in this study is designed to ensure that the droplets are applied in the deposition regime. This is necessary to precisely characterize the resulting deposits, which forms the basis for further evaluation. However, as the following section shows, a behavior within the non-wetting regime would be desirable in practical applications.

UWS spray wall film formation

Understanding the conditions under which liquid films form from UWS spray impact on the SCR system walls is essential as it precedes deposit formation. The boundary between wetting and non-wetting regimes is defined by a critical wall temperature T_{cr} [13]. Wall temperatures below this boundary lead to liquid deposition, while temperatures above it result in localized cooling without wetting. If the system could be operated permanently in a non-wetting state, the absence of film formation would also prevent deposit formation. However, while non-wetting interactions exhibit limited heat transfer, repeated injections can cool the system walls to as low as 97 °C [24]. Together with the design requirements discussed in Section 2.1.1, this eventually leads to the inevitable wetting of the wall. Once this occurs, heat transfer increases significantly, and if the evaporation time exceeds the interval between impact events, a film accumulates [120].

Experiments typically examine film formation from spray injections under various conditions to validate computational fluid dynamics (CFD) models [24, 105, 129]. Birkhold [13] performed experiments in a hot gas test rig which showed that the wetting boundary depends not only on the Leidenfrost temperature but also on factors such as the gas flow rate. Grout et al. [56] studied liquid film dynamics under realistic conditions and found that film formation starts after a characteristic time interval influenced by gas temperature and mass flow. Liao et al. [85] identified spray impingement momentum as a key factor for liquid accumulation at the opposite wall. Additionally they observed, that deposits always form downstream of the impingement area.

Wetting and spreading

When liquid-solid contact occurs, the wetting behavior dictates the size of the wetted area, the dynamics of film flow, and significantly influences the subsequent evaporation process. These mechanisms are pivotal

in determining the size and quantity of the deposits that will form. Therefore, understanding fundamental wetting phenomena is essential when choosing experimental parameters and analyzing the results.

In the straightforward scenario of a liquid droplet resting on an ideally smooth, solid surface, the interaction between the surface tension γ at the liquid-gas interface (lg) and the surface energies at the liquid-solid (ls) and solid-gas (sg) interfaces governs the wetting of the solid by the liquid. As a system generally aims to reduce its surface free energy, a solid with a high surface energy is likely to be wetted by a liquid with a lower surface tension [52]. Due to these interactions, a characteristic angle forms at thermodynamic equilibrium between the ls and lg interfaces where the solid, liquid, and gas phases converge, as depicted in Figure 2.3. This intersection is called the three-phase contact line, or simply the contact line. The resulting angle is the equilibrium contact angle θ_e and can be determined using the Young equation [54]:

$$\cos\theta_\mathrm{e} = \frac{\gamma_\mathrm{sg} - \gamma_\mathrm{ls}}{\gamma_\mathrm{lg}}. \tag{2.1}$$

When the value of $\cos\theta_\mathrm{e}$ is less than $90°$, the behavior is categorized as (partial) wetting. Conversely, values greater than $90°$ indicate non-wetting behavior.

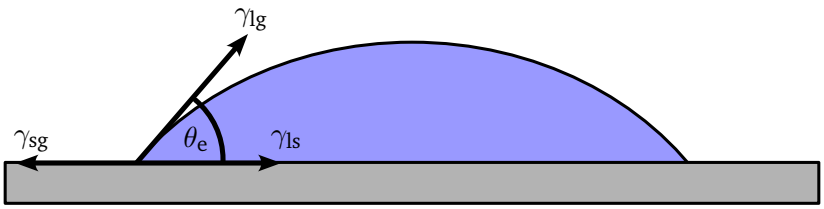

Figure 2.3.: Equilibrium of forces at the three-phase contact line of a sessile droplet in thermodynamic equilibrium

On technical, non-ideal surfaces, irregularities, often resulting from roughness, can cause the contact line to pin. Pinning occurs when the contact line's movement becomes stagnant during spreading or receding motions, such as during evaporation [50]. When the contact line pins on a surface defect, the contact angle can assume any value between the equilibrium contact angles of the involved surface slopes (see Figure 2.4) [101]. If the advancing contact line (a) of a spreading droplet pins at a surface defect, the observed contact angle can increase to the maximum possible angle, known as the advancing contact angle θ_adv. The contact line then detaches from the defect and continues to move. Similarly, a receding contact line (b), as observed during droplet evaporation, can remain pinned to a surface irregularity until the contact angle diminishes to its minimum threshold, the receding contact angle θ_rec, before moving on. Consequently, on real surfaces with dynamic contact lines, the macroscopically observed contact angle can fluctuate within the range defined by:

$$\theta_\mathrm{h} = \theta_\mathrm{adv} - \theta_\mathrm{rec}. \tag{2.2}$$

This variation is the contact angle hysteresis and can also occur on surfaces with varying wettability [68, 83].

In addition to contact angle hysteresis, the roughness or texture of a surface can lead to a contact angle, θ^*, that diverges from the equilibrium contact angle given by Young's equation. This phenomenon can be understood through an energetic consideration of the actually wetted surface area, which deviates from the projected, ideally smooth surface. In this context, a general distinction is made between two wetting states: the Wenzel state and the Cassie-Baxter state. Both are illustrated in Figure 2.5.

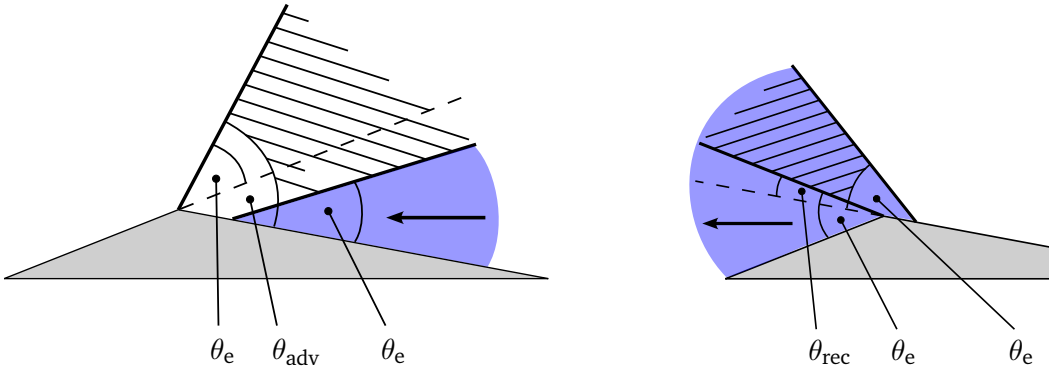

(a) Pinning of an advancing contact line until θ_{adv} is reached

(b) Pinning of a receding contact line until θ_{rec} is reached

Figure 2.4.: Advancing and receding contact angles of a contact line pinned at a surface irregularity, determined by the local surface slopes

In the Wenzel state (a), the liquid wets the entire surface morphology, filling all the grooves and cavities of the rough or textured solid. This results in an expanded contact area between the solid and the liquid. The resulting contact angle, θ^*, in this state is defined by the Wenzel equation [153]:

$$\cos\theta^* = \frac{A_{real}}{A_{proj}} \cos\theta_e. \tag{2.3}$$

Here, A_{real} represents the actual surface area, whileA_{proj} denotes the projected (or ideally smooth) area in contact with the liquid. Based on this equation, systems with $\theta_e < 90°$ exhibit enhanced wetting on rough surfaces. Conversely, for $\theta_e > 90°$, the wetting behavior is decreased further.

In contrast, the Cassie-Baxter state (b) sees the liquid making contact only with the elevated portions of the surface features, leaving air (or another gas) entrapped within the surface's grooves or cavities [106]. This state typically exhibits a hydrophobic behavior with a diminished contact area, occasionally resulting in superhydrophobic surfaces. The contact angle in the Cassie-Baxter state is given by the Cassie-Baxter equation [29]. In this equation, ϕ_{ls} and ϕ_{lg} represent the respective fractions of liquid-solid and liquid-gas interfaces at the bottom of the liquid:

$$\cos\theta^* = \phi_{ls} \cdot \cos\theta_e - \phi_{lg}. \tag{2.4}$$

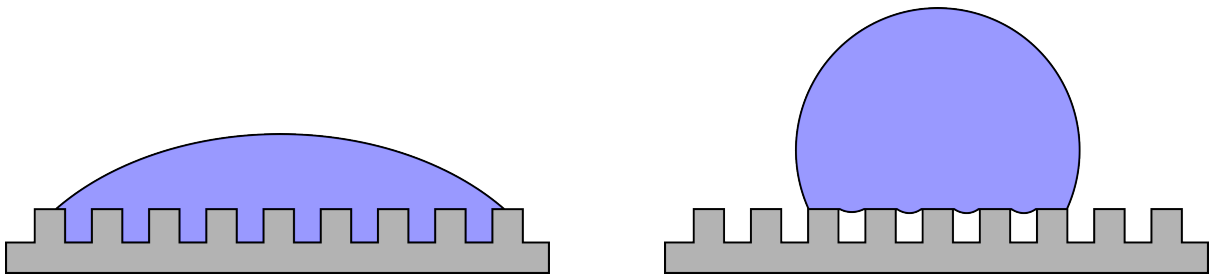

(a) Wenzel state

(b) Cassie-Baxter state

Figure 2.5.: Wetting states on structured surfaces

2.1.2. Evaporation

The formation of a wall film is necessarily followed by an evaporation phase before solid deposits can form. This leads to an increase of the urea concentration in the UWS and, depending on the temperature, the thermal decomposition of urea. As evaporation progresses, the volume of the droplet or film decreases. On real surfaces, this typically results in the pinning of the contact line as highlighted in Section 2.1.1. Picknett and Bexon [103] described that this phenomenon can cause sessile droplets to evaporate while maintaining a constant wetted area. The circular area wetted by a droplet is often quantified by its radius, the contact line radius or simply contact radius. Therefore, this evaporation mode is commonly termed constant contact radius (CCR) mode. Alternatively, on surfaces exhibiting minimal contact angle hysteresis, droplets can evaporate with a continuously decreasing contact radius while maintaining a constant contact angle, known as the constant contact angle (CCA) mode.

Several studies have investigated droplet evaporation on different surfaces [21, 33, 122, 125]. Typically, multiple evaporation modes are observed, with the exact sequence being influenced by the surface wettability. For instance, a notably rough surface increases the likelihood of prolonged CCR mode evaporation due to an increased chance of pinning. Upon reaching θ_{rec}, both contact angle and radius decrease simultaneously until the liquid is fully evaporated. Birdi and Vu [12] analyzed droplet evaporation rates on surfaces of different wettability. They conclude that the rate correlates with the contact line radius. For contact angles less than $90°$ in CCR evaporation, constant evaporation rates were observed, while CCA mode evaporation on hydrophobic surfaces showed decreasing evaporation rates.

Deegan et al. [37] and Hu and Larson [64], using both theoretical and experimental approaches, demonstrated that the evaporation mass flux is not uniformly distributed across the liquid-gas interface. Instead, it increases significantly at the contact line when the contact angle is below 90°. This occurs because molecules evaporating at the contact line have the lowest chance of being reabsorbed due to the lower density of neighboring evaporation sites in this region. Therefore, when the contact line is pinned (i.e., in CCR mode), an internal flow must exist to replenish the evaporating fluid at the contact line. This capillary-driven flow can transport solutes or particles from the liquid bulk to the contact line, potentially leading to deposition and further reinforced pinning [36]. Figure 2.6a illustrates this for an aqueous urea-water solution on a wetting substrate. This process results in the formation of a distinct deposit pattern, often called a “coffee ring” due to its resemblance to dried coffee stains. Deposits of this shape are reported in numerous studies concerning deposit formation from urea- and salt-water solutions [69, 95, 114, 142].

Beyond this capillary flow, other currents may occur in the liquid, such as convective flows or Marangoni flows. The latter are driven by gradients of the liquid-vapor surface tension along the interface, caused, for example, by concentration differences of a solute. These solutal Marangoni flows have been shown to transport accumulated salt away from the contact line and distribute it along the liquid-vapor interface [26, 132]. Together with the increasing homogeneity of the evaporation mass flux at larger contact angles, these flows can compensate for or even reverse the coffee ring effect [65, 136], as Figure 2.6b and Figure 2.6c show.

Musa et al. [94] demonstrated that the presence of urea in an aqueous solution results a three-stage evaporation process, each with distinct evaporation rates. For comparison, pure water evaporation is typically characterized by a linear decline of the squared droplet diameter over time, known as the d^2-law [43]. In the initial stage of UWS evaporation, water is the primarily evaporating component. Consequently, the behavior and evaporation

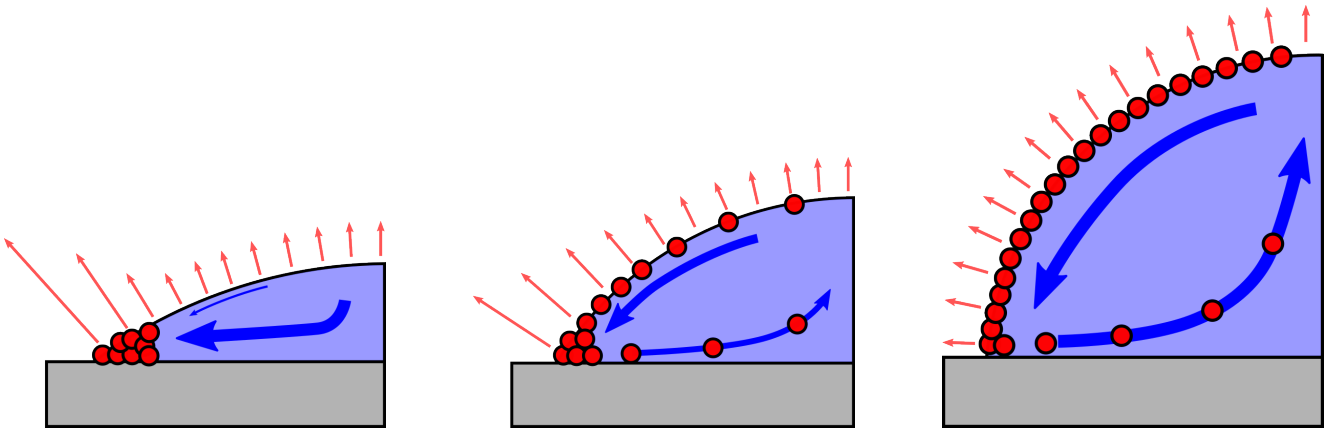

(a) At low contact angles, locally increased evaporation at the contact line and capillary flow lead to a local increase in urea concentration

(b) Increase in solutal Marangoni flow distributes urea more evenly along the liquid-gas interface

(c) Strong Marangoni flow at high contact angles dominates the flow field, leading to saturation of the liquid-gas interface

Figure 2.6.: Mass transport and urea distribution (indicated by red dots) in an evaporating droplet depending on contact angle, red arrows indicate the evaporation mass flux [115]

rate align with that of a pure water droplet. The subsequent stage exhibits a diminished evaporation rate due to the increase of urea concentration at the liquid-gas interface, decreasing the vapor pressure [14, 34]. If sufficient heat is transferred from the wall, the liquid temperature can then rise above 133 °C, where the urea melts and begins to evaporate and decompose into the gas phase. This acts as the primary cause for volume reduction in the second stage. Notably, during this phase, bubble formation and, at temperatures above 300 °C, micro-explosions have been observed within the droplet due to the entrapment and subsequent evaporation of volatile components [149]. Some UWS droplet evaporation models, such as that proposed by Stein et al. [135], are based on the premise that thermal decomposition does not begin until all the water has evaporated. However, experimental findings from Heyden [62] indicate the presence of urea in the gas phase even before the complete evaporation of water.

The final stage in UWS droplet evaporation is the crystallization of the urea. This occurs as long as temperatures lie below the melting point of urea at 133 °C and the concentration exceeds the solubility in water. Kontin et al. [74] highlighted that this phase transition can form a solid crust at the liquid-gas interface, further impeding evaporation of remaining liquid. Yet, at elevated temperatures, this oversaturation effect is negligible. Wei et al. [152] introduced the initial temperature rise of the solution as a fourth phase to UWS droplet evaporation. This phase continues until the boiling point of water is reached, with the concentration remaining largely unchanged.

For modeling UWS droplet evaporation, Birkhold [13] proposed a rapid mixing approach, balancing computational effort and precision. This method assumes infinitely fast diffusion, preventing the emergence of temperature and concentration gradients within the droplet. However, this approach cannot account for the significant spatial concentration gradients observed in the experimental findings of Kontin et al. and in other numerical studies [99, 111]. Bender et al. [7] formulated a model for UWS evaporation that delineates temperature and concentration fields within the evaporating droplet. With this, the temporal progression of local urea mass fractions can be determined. A parametric study was conducted, revealing that wall

temperature strongly influences droplet evaporation and deposition. Higher temperatures lead to higher evaporation rates and to an earlier onset of crystallization. Additionally, lower temperatures increase diffusive mass transport inside the droplet, resulting in different shapes of the final deposits. This emphasizes the diverse impact of environmental conditions on the various sub-processes involved in deposit formation.

2.1.3. Deposit formation

At lower temperatures, the formation of deposits from UWS is always accompanied by the crystallization of dissolved urea. Crystallization generally refers to the transition of a dissolved substance into a solid with a three-dimensional, periodic structure of molecules or atoms. This process typically occurs when the solution becomes supersaturated, either due to ongoing evaporation or changes in solubility, such as those caused by decreasing temperature.

In SCR systems, temperatures often exceed 133 °C, meaning that any crystallized urea will melt. At these temperatures, urea undergoes thermal decomposition. Consequently, deposits formed under such conditions are not solely composed of crystallized urea but also include its decomposition products. The following sections will review the literature on both of these processes.

Crystallization

If the droplet is pinned on a substrate with $\theta > 90°$, the increased evaporation at the contact line (see Section 2.1.2) can cause a localized increase in urea concentration, triggering crystallization once the solubility is exceeded. When this crystallization is limited to the contact line region, ring-like deposit patterns form [6, 95, 114, 115]. If the contact line contracts abruptly and repeatedly during evaporation, a behavior known as slip-stick, caused by reaching the receding contact angle, several concentric rings are formed [69]. However, internal mass transport mechanisms, such as diffusion or Marangoni flows, can equilibriate the concentration distribution and produce uniform deposits covering the entire previously wetted area [22, 26, 84, 112, 136, 142]. Uniform deposits are also observed when contact line evaporation is not predominant, as seen on hydrophobic surfaces [36].

Schmid et al. [114] conducted experiments on urea crystallization from droplets and found that small contact angles led to ring-shaped deposits with distinct crystal structures. On hydrophobic surfaces and at elevated temperatures, however, a layer of solid urea formed across the entire liquid-gas interface. Again, the crystallization started at the contact line but enclosed the remaining liquid within fractions of a second. These findings are consistent with results from our own work [115], which attributed the different deposition patterns to the dominant internal mass transport mechanisms. These mechanisms vary depending on the wettability of the surface, the associated contact angle, and the wall temperature. Additionally, the crystallization dynamics are influenced by the solid surface morphology. Rough surfaces, for instance, promote early crystallization due to an abundance of nucleation sites [55]. Conversely, high evaporation rates combined with smooth surfaces can result in high supersaturation, causing abrupt crystallization of the entire liquid-gas interface [49, 60, 109, 159]. The work of Ryddner and Trujillo [111] supports these observations, indicating that at higher temperatures, more urea is accumulated at the droplet's liquid-gas interface. They attribute this to slower

homogenization of the urea distribution at these temperatures, which in turn promotes the formation of a solid layer.

Urea decomposition

Schaber et al. [113] conducted a thermogravimetric analysis of urea, measuring the change in mass as a function of temperature under a controlled atmosphere. Their results reveal that the mass remains almost constant until the decomposition temperature is reached. Above this point, urea melts and begins to evaporate. Starting at around 150 °C, increasing thermal decomposition produces ammonia and isocyanic acid. This isocyanic acid can then interact with remaining urea to produce biuret, which itself begins to decompose at approximately 190 °C. Concurrently, other by-products such as cyanuric acid, ammelide, and ammeline are formed. By the time the temperature reaches 600 °C, most of the initial mass has disappeared.

The kinetics of urea decomposition are significantly influenced by experimental conditions, such as the heating rate and the sample's surface-to-volume ratio [113]. Specifically, larger ratios promote the release of gaseous by-products and affect the decomposition rate [23]. Nicolle et al. [97] developed a model detailing the decomposition kinetics of urea in an aqueous solution. Their findings indicate that the presence of water hinders the release of isocyanic acid into the gas phase.

Deposit formation under application-oriented operating conditions

In addition to the few generic experiments on dropwise evaporation of UWS, many studies address deposit formation resulting from injection under application-oriented operating conditions. These investigations are mostly carried out in hot gas or engine test benches [4, 19, 24, 27, 85, 105, 130, 129, 139]. The results indicate that operating parameters, such as the UWS dosing rate, gas temperature, flow rates, and spray impact locations, significantly influence deposit formation.

Liao et al. [85] detailed the sequence and timing of deposit formation in an SCR system. They identified that spray impingement cools the wall, leading to urea crystallization. As the wall temperature increases, the crystallized urea melts and starts evaporating. Concurrently, the molten urea is carried downstream by the hot exhaust gas flow, where it decomposes into solid deposits, primarily consisting of ammeline, isocyanic acid, and biuret. Smith et al. [129] distinguished between two distinct deposit growth mechanisms in an SCR system. The first, termed *damming growth*, is characterized by an upstream expansion of the deposit due to consecutive UWS injections. The second, *peripheral growth*, occurs at the deposit's outer edges, which are not in direct contact with the liquid UWS. This growth is attributed to the capillary-driven movement of the liquid through the porous deposit structure.

Findings such as those from Smith et al. [129] suggest that the structure of the initial deposits affects their subsequent growth. However, characterization of deposit structure, specifically deposit topology and morphology, is rarely found in the related literature since most works focus primarily on chemical analysis of the deposits. Börnhorst et al. [19] offered topological insights on a global structural scale, based on experiments from hot gas test rigs under varied conditions. Ates et al. [2] presented a comprehensive assessment of SCR deposits, including 2D and 3D height profiles, surface roughness, and analyses using power spectral density

and fractal methods. Their findings revealed varying morphologies based on operating temperatures and identified self-affine surfaces with consistent fractal dimensions in the deposits they analyzed. Further research in our own work [115] identified trends in the morphological scaling tendencies of deposits under different wall conditions that agree well with proposed crystallization mechanisms. Such detailed analyses of deposit structures can significantly contribute to the quantitative description of deposits and reveal relationships between wetting, heat and mass transfer, and the kinetics of deposit formation. However, further research is required on this topic.

2.2. Relevant impact factors

The following review of the literature aims to summarize how the wall surface characteristics influence the deposit formation of urea-water solutions. The focus lies on observations in the period following the droplet impact or the formation of a wall film. Ideally, in order to prevent deposits, one would aim to entirely avoid liquid-wall contact, ensuring a consistent non-wetting impact regime, for example through the Leidenfrost effect. However, due to conflicting injection requirements [24] and the inevitable interaction between the spray and the wall on mixer elements, this is not feasible in practice. Therefore, the emphasis will be on understanding wall-related impact factors, including their influence on the extent of wetting and heat transfer.

Wall temperature and residence time

Wall temperature plays a decisive role in determining not only the extent of evaporation but also the interaction between the liquid and solid. Bernardin et al. [9] showed that for water droplets in a pressure vessel exceeding 120 °C, the contact angle decreases with rising temperature, indicating improved wetting behavior. On the other hand, Gholijani et al. [51] reported decreasing values for the wetted area of a sessile perfluorohexane droplet with increasing wall superheat, i.e., temperatures above the liquid's saturation temperature. They attribute this to increased evaporation rates near the contact line at higher superheats.

With urea, the temperature and the supplied heat also dictate the chemical reactions taking place in the liquid phase, with high temperatures promoting the formation of water-insoluble and highly heat-resistant decomposition products. Brack et al. [24] outlined the relationship between deposit quantity and wall temperature. They found that temperatures below 150 °C primarily result in crystalline urea deposits with minor amounts of biuret. The range between 150 °C and 250 °C is considered critical, as it often leads to extensive deposit formation and possible pipe blockage. However, only minimal amounts of deposits were observed at temperatures exceeding 250 °C. These observations are consistent with those of Bai et al. [4], who found no deposits in the SCR system at exhaust gas temperatures above 272 °C. In contrast, Eakle et al. [40] identified deposits even with exhaust gas temperatures surpassing 300 °C. Their findings on deposit composition at specific operating temperatures deviated from expectations based on thermogravimetric analysis, which they attributed to insufficient removal of decomposition products in the SCR system.

Börnhorst et al. [19] highlighted that even at standard operating temperatures, up to 10 % of the deposits are composed of high-temperature decomposition products, able to withstand temperatures as high as 700 °C. They argued that high-temperature operation does not necessarily mitigate the risks of deposit formation, as is

commonly believed. Smith et al. [130] discussed the potential for deposit formation on mixer elements based on the time scales of urea decomposition and subsequent solidification. They found that the decomposition of urea at temperatures below 160 °C lasts longer than 600 s, minimizing the risk of deposit formation, apart from urea crystallization. However, temperatures above 290 °C result in rapid reactions and solidification, leading to the significant accumulation of critical deposits. Weeks et al. [151] also investigated the interaction of temperature and exposure time and observed strong variations in the composition of deposits formed at exhaust gas temperatures between 200 °C and 250 °C. Their results include deposits consisting of pure biuret, biuret-cyanuric acid mixtures and even pure urea, which should have decomposed at the given temperatures. They concluded that the duration of the experiment likely influenced these results, but that additional factors besides temperature and time must have also played a role in decomposition and deposit formation.

Surface material

The solid surface material is expected to have an effect on deposit formation, as its thermal properties affect both heat transfer coefficients [92] and evaporation rates [35]. Misyura and Morozov [88] conducted experiments in the film boiling region and observed varying evaporation times for droplets on different wall materials. This observation aligns with other studies indicating that Leidenfrost temperature is also affected by the wall material [8]. Despite the evident impact of the wall material on heat transfer, which influences the evaporation of water and urea as well as decomposition, there is a noticeable lack of research specifically addressing its influence on deposit formation. Schweigert et al. [118] incorporated the influence of wall material on heat transfer in SCR systems in their studies, considering various metals such as steel, iron, and nickel, as well as ceramics. Their results indicated only a minor influence of the material's thermal effusivity on the evaporated mass fraction of UWS wall films. Interestingly, they pointed out that this material effect is even less significant than the influence of oxide layers present on the same surface. This indicates that the wetting characteristics can affect the evaporation as they change with the degree of oxidation.

Roughness, surface structures, and wettability

Surface irregularities such as roughness and structures are also expected to have a strong effect on deposit formation. As highlighted in Section 2.1.1, these inhomogeneities can lead to phenomena such as pinning and contact angle hysteresis, which can result in characteristic deposition patterns such as coffee rings. However, most existing studies focus on the influence of surfaces on wetting and heat transfer, with limited research specifically addressing UWS or deposit formation. One example for the potential of surface characteristics to influence the formation and composition of urea deposits via the intermediate step of wetting follows from the work of Brack [23]. He emphasized that larger film surface areas promote the evaporation of urea films. Despite faster reactions at higher temperatures, the short residence time of the film could prevent the formation of solid urea byproducts. Schweigert [117] observed a small influence of surface roughness on the evaporation of a UWL on metallic surfaces. However, he noted that this effect may be due to changes in surface chemistry resulting from surface treatment processes, such as sandblasting, rather than roughness itself. Studies by Schmid et al. [114] and Schumacher et al. [115] have shown that hydrophobizing a surface can effectively reduce the area covered by both the liquid and subsequent deposits. This effect persists even during rewetting and partial dissolution of the deposits, which is common in SCR systems. However, these studies focused on temperatures below 133 °C, so no effects on the mass and composition of the deposits were observed.

As known from the lotus effect [96], adding roughness to hydrophobic surfaces can increase their hydrophobicity, even allowing the transition to the Cassie-Baxter state [98, 148]. The trapped air under the droplet minimizes the contact area and consequently the heat flux between the solid and the liquid. There are however, to the knowledge of the author, no findings on how this affects the trade-off between evaporation and reaction kinetics with regard to the severity of deposits.

Conversely, increasing roughness can also enhance the hydrophilic behavior of already wetting surfaces, as shown by the Wenzel equation and confirmed by experiments [28, 124]. However, additional effects such as strong pinning due to surface defects can lead to deviations from the energy-based formula derivations and potentially even reverse the hydrophilic character of a surface [133]. Wolansky and Marmur [155] found that the Wenzel equation only serves as a valid description when the roughness scale is much smaller than the droplet size because else it might induce additional capillary forces.

In summary, the existing literature does not provide definitive insights into how roughness, in combination with surface chemistry, affects the wetting behavior of a given liquid-solid pairing. Specific studies on UWS evaporating on metal surfaces are not available, making it difficult to predict the effects on deposit formation.

Purposefully structured surfaces can instead utilize capillary action to significantly improve wetting. This effect, which depends on the contact angle [106], can manifest, for example, as a film spreading between an array of columns or as a droplet being drawn into the surface structure. This behavior, known as wicking, has been observed by researchers such as Tekidou et al. [143] and Semprebon et al. [119]. Semprebon found that a higher density of pillar-shaped surface structures enhances the capillary effect. In contrast, a lower structure density can cause pinning of the contact lines, hindering liquid propagation. Sivakumar et al. [128] also demonstrated that if the structure does not induce capillary-driven spreading, the propagation of an impinging droplet is instead hindered.

Yan and Li [158] studied heat transfer on column-textured surfaces and reported that the heat transfer rate increases with decreasing column spacing, provided the liquid is in the Wenzel state. On hydrophobic surfaces, however, smaller column spacing can induce the Cassie-Baxter state, resulting in lower heat transfer. This condition occurs when the impact of a droplet does not reach a critical velocity, which depends on the contact angle, as described by Vaikuntanathan and Sivakumar [146]. Additionally, Tsai et al. [144] found that the wetting state of a sessile droplet can change from the Cassie-Baxter to the Wenzel state as a result of evaporation.

The observations from Yan and Li [158] are consistent with other findings that heat transfer improves with better wetting [31, 53, 71] and a larger effectively wetted surface area [89]. Surface structuring provides a suitable method to increase this effective surface area and thus enhance heat transfer [90, 158].

Two other effects of surface structures on heat transfer should be mentioned. First, the aforementioned pinning and resulting contact angle hysteresis can cause evaporating droplets to remain in CCR mode for an extended period. This means that they maintain a larger liquid-gas interface compared to droplets on smooth surfaces, which promotes heat transfer. Second, high structures can cause liquid films to rupture, creating additional contact lines and increasing heat flux, as demonstrated by Sodtke and Stephan [131].

The results of the literature study about the influences of material parameters, wall temperature and liquid residence time as well as surface roughness, structure and wettability on the relevant sub-processes for deposit formation are summarized in Table 2.1. It should be noted that the classification of the influence of wall

temperature on deposit severity varies because some works used the raw mass and others the composition of deposits as the decisive criterion.

Table 2.1.: Summary of the literature study concerning influences on relevant sub-processes of deposit formation (increasing ↑, decreasing ↓, ambiguous ↔)

Influencing Factors	Spreading extent	Heat Transfer/Evaporation	Deposit severity
Wall temperature ↑	Bernardin et al. [9]↑ Gholijani et al. [51]↓	Moriyama et al. [92]↓[1]	Brack et al. [24]↔ Bai et al. [4]↓ Eakle et al. [40]↔ Börnhorst et al. [19]↓ Smith et al. [130]↑ Weeks et al. [151]↔
Residence time ↑	-	-	Smith et al. [130]↑ Weeks et al. [151]↔
Thermal effusivity of the wall material ↑	-	Schweigert et al. [118]↓	-
Thermal diffusivity of the wall material ↑	-	Moriyama et al. [92]↓[1] David et al. [35]↑ Misyura and Morozov [88]↓[1]	-
Surface wettability ↑	Birdi and Vu [12]↑ Good [54]↑	Birdi and Vu [12]↑ Brack [23]↑ Chandra et al. [31]↑ Gleason et al. [53]↑ Kim et al. [71]↑ Misyura et al. [89]↑ Yan and Li [158]↑	Brack [23]↓ Schmid et al. [114]↑[2] Schumacher et al. [115]↑[2]
Surface roughness ↑	Schumacher et al. [116]↑ Neinhuis [96]↓[3] Nilsson et al. [98]↓[3] Wang et al. [148]↓[3] Busscher et al. [28]↑[4] Shibuichi et al. [124]↑[4] Spori et al. [133]↔	Schweigert [117]↓	Schmid et al. [114]↑[2] Schumacher et al. [115]↑[2]
Surface structure ↑	Tekidou et al. [143]↑ Semprebon et al. [119]↔ Sivakumar et al. [128]↔ Yan and Li [158]↔	Yan and Li [158]↔ Moon et al. [90]↑ Yan and Li [158]↑ Sodtke and Stephan [131]↑	-

[1] Film boiling
[2] No urea decomposition
[3] Hydrophobic surface
[4] Hydrophilic surface

2.3. Open questions and goals of the thesis

The previous section illustrates that the literature on urea deposit formation has mainly focused on the influence of operating conditions, such as spray settings. There is a lack of work addressing the effects of system parameters that can be influenced at the design engineering level, including material selection and surface characteristics. At the same time, such adjustments are becoming increasingly important due to the growing relevance of mixer elements. Few works, such as [23] or [117], provide some recommendations based on their findings. Nevertheless, to the author's knowledge, there has not yet been a comprehensive investigation aiming to quantify relevant influences and derive practical recommendations.

The previous section also highlights that deposit formation depends strongly on the exhaust gas or wall temperatures. High temperatures can ideally prevent film formation by inducing droplet impact phenomena such as rebound, thermal dissolution, and the Leidenfrost effect. Additionally, high temperatures accelerate the evaporation and decomposition of any films that do form. Consequently, it is standard practice to activate exhaust gas purification only when a minimum temperature, often 180 °C [20], is reached. However, repeated spray impacts were found to cool the walls below 100 °C, leading to inevitable film and deposit formation. Even small deposits can then accumulate to a critical mass over time. Therefore, this work does not focus on optimizing wall temperature.

Despite extensive literature on fundamental effects such as wall wetting, deposit formation remains a complex interplay of successive sub-processes, making it difficult to provide meaningful recommendations. Achieving this goal requires precise control and measurement of the relevant influencing factors throughout the entire sequence that ultimately leads to deposit formation. By doing so, relevant phenomena can be identified, and the numerous interactions between sub-processes and their influences can be accounted for.

Therefore, the aim of this work is to conduct a systematic, experimental investigation covering a defined parameter space. It is assumed that film formation has already occurred on a solid wall. The focus is on the influence of wall surface characteristics. Pre-existing deposits are not considered, as it is not possible to produce sufficiently comparable samples. A statistical approach will be used to identify and quantify the dominant effects from the collected data, including interactions between effects. For instance, surface structure and equilibrium wettability may strongly affect each other, as shown previously. Characteristic and application-relevant properties of the deposits are chosen as target variables. The final step is to model the behavior of the overall process, enabling the determination of optimal variable configurations for desired deposit formation behavior. In that regard, only the formation of deposits is to be minimized as the objective function. Economic and production-related aspects are not considered.

The two main research questions pursued in this work are therefore:

1. *How can deposit formation of UWS on hot walls be prevented or minimized using suitable wall surface characteristics?*
2. *How can the effects of surface and process properties and their interactions on deposit characteristics be quantified and modeled?*

Related topics arising from these questions, addressed in this work, include: Which variables are most effective in reducing deposit formation and why? Is there an optimal setting for each characteristic? What would an optimal combination of different influencing variables look like?

CHAPTER 3

Experimental Design

Answering the scientific questions posed in Section 2.3 using experimental results and associated models requires the development of an appropriate experimental design. The necessary considerations and the definition of the final design are described in this chapter. The wall surface characteristics to be studied constitute the independent variables of the mathematical model to be built. In statistical design of experiments, these variables are referred to as factors, and their respective settings as levels. These terms will also be used here.

3.1. Design of experiments

One way to carry out the experiments is to vary each factor individually from a predefined reference point while keeping all other factors constant. This approach, known as the one-factor-at-a-time method, allows the isolated effects of the factors on one or more dependent variables (also called target variables) to be determined. However, this method carries the risk of misinterpretation, as it remains unclear how the system would react if a different reference point were used. It assumes that the effect of each factor is independent of the settings of the others. As in many real-world systems, this is not a realistic assumption to make here. Instead, interactions between the factors are quite likely.

3.1.1. Interactions

An interaction occurs when the effect of one factor x_1 on the target variable y depends on the level of another factor x_2. A simple model for this scenario can be written as [127]:

$$y = \beta_0 + \beta_1 x_1 + \beta_2 x_1^2 + \beta_3 x_2 + \beta_4 x_2^2 + \beta_5 x_1 x_2. \tag{3.1}$$

Here, β_i are the model coefficients to be determined. The interaction term $\beta_5 x_1 x_2$ allows the model to capture how the effect of x_1 varies with different values of x_2. Figure 3.1 demonstrates this in (b), where the model responses for x_1 are not parallel for different values of x_2. When this occurs, the two main effects are not purely additive, and including the interaction term allows for a more accurate representation of the system's behavior. Figure 3.1a demonstrates the case where the two effects are purely additive.

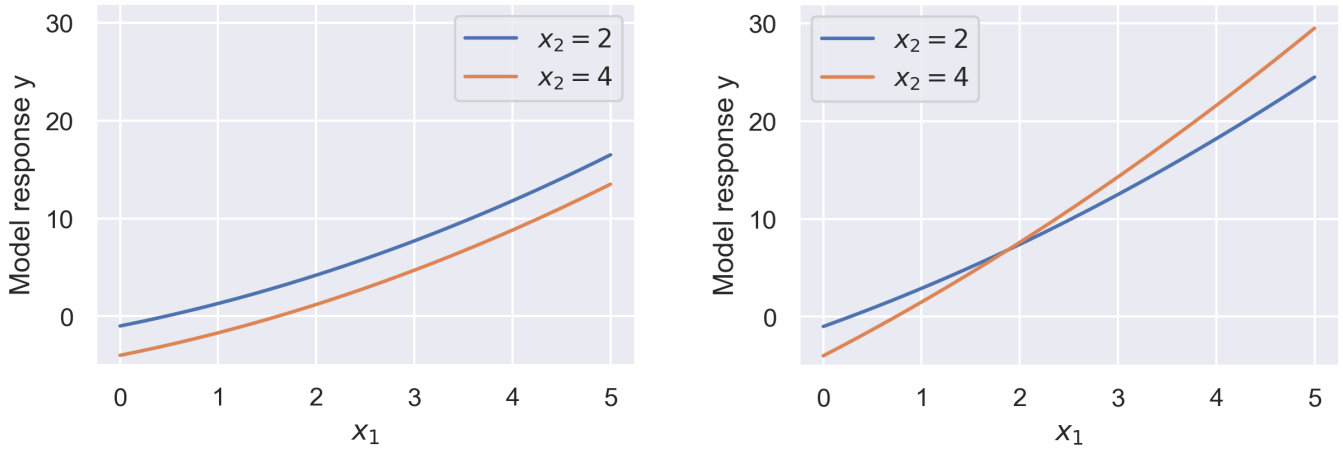

(a) The interaction coefficient in Equation (3.1) is $\beta_5 = 0$. Therefore, different values of x_2 do not affect the course of the model response for x_1, and the superposition of the respective effects is purely additive.

(b) Different values of x_2 influence the response curve for x_1 due to an interaction given by $\beta_5 = 0.8$ in Equation (3.1).

Figure 3.1.: Difference in model responses for Equation (3.1) with and without interaction of two independent variables, the remaining coefficients are: $\beta_0 = 2$, $\beta_1 = 2$, $\beta_2 = 0.3$, $\beta_3 = -1.5$, $\beta_4 = 0$

An example of a likely interaction in this study is the interaction between surface roughness and a coating that changes the wetting behavior. According to the Wenzel equation (2.3), the effect of roughness on surface wettability is significantly influenced by the initial wettability, which can be chemically modified by a coating.

To capture such interactions, a full factorial design can be employed, testing all possible combinations of factor settings. However, the number of experiments required increases exponentially with the number of factors k. For instance, varying five factors at three levels l (the minimum needed to model nonlinear effects) would require 243 experiments:

$$n_{\text{exp}} = l^k = 3^5 = 243. \tag{3.2}$$

Conducting such a high number of experiments is generally neither feasible nor practical, as it would be very time-consuming and costly, even before considering the need for replications. The field of statistical design of experiments addresses this issue by providing methods to define what is known as partial factorial designs. These designs allow for the determination of the individual effects with a reduced number of experiments.

3.1.2. Partial factorial design

Partial factorial designs take advantage of the fact that full factorial designs can be represented by a system of linear equations, such as Equation (3.1), where each experiment j corresponds to an equation with the respective factor settings $x_{j,i}$ and the measured result y_j as the dependent variable. To determine all unknown coefficients β_i of the equation system, all experiments must be performed. However, with a sufficient number of factors, the unknowns include not only the main effects and two-way interactions but also interactions between three, four, or even more factors. In practice, it is commonly demonstrated that these higher-order interactions do not significantly contribute to explaining the system behavior and can be neglected.

Consider, for instance, the speed of a car as the target variable y depending on the engine power x_1, aerodynamics x_2, and tire type x_3. The relationship between the factors and the car speed can be expressed as:

$$y = \beta_0 + \beta_1 x_1 + \beta_2 x_2 + \beta_3 x_3 + \beta_4 x_1 x_2 + \beta_5 x_1 x_3 + \beta_6 x_2 x_3 + \beta_7 x_1 x_2 x_3. \tag{3.3}$$

Here, the squared terms are neglected for simplicity. Including the intercept β_0, eight experiments would be required to determine all coefficients, assuming the factors are varied at two levels. The three-way interaction $x_1 x_2 x_3$ would describe how the combined effect of engine power, aerodynamics, and tire type influences the car's speed. This interaction is complex because it examines whether the effect of aerodynamics on speed depends on both engine power and tire type. Neglecting this interaction and focusing on the main effects x_1, x_2, and x_3 as well as the two-way interactions $x_1 x_2$, $x_1 x_3$, and $x_2 x_3$ is often sufficient for understanding the primary influences on car speed.

Neglecting these higher-order interactions results in an overdetermined system of equations, where there are more equations (experiments) than unknown coefficients. The experiments freed up by this simplification, with their respective settings for the remaining factors, can then be used to determine the effect of additional factors not previously included. In the above example, this would mean conducting all eight experiments, but replacing the settings of $x_1 x_2 x_3$ with the different levels of a new factor, fuel type x_4. This allows for estimating a fourth effect without increasing the necessary number of experiments. Mathematically, this procedure confounds the effect of the neglected interaction $x_1 x_2 x_3$ with the main effect of the newly added factor x_4. The effects are represented in the system of equations by the same coefficient β_7 and cannot be separated. However, assuming the overly complex multifactorial interactions are insignificant, this confounding is acceptable.

With well-designed experimental designs, the main effects and relevant interactions can be identified with significantly less experimental effort than by using a full factorial design. One disadvantage of partial factorial designs is the reduced number of available data points for estimating effects and interactions. This can lead to wider confidence intervals and lower statistical confidence (see Section 5.1). For more detailed explanations and examples of statistical design of experiments, please refer to the literature [72, 127].

3.1.3. Selected experimental design

The experimental design employed here is based on a central composite design (CCD). Its foundation is a full factorial, two-level (per factor) design, which can, in the case of three factors, be visually represented as a cube. This is shown by the gray corner points in Figure 3.2. This structure is then extended by a third factor level in the center and the star points (red and yellow points in the figure). Each factor is therefore tested at three different settings, allowing the main effects and two-way interactions to be accurately identified. Note that the yellow star points in a CCD typically extend beyond the cube, resulting in five levels per factor. This would not be possible in this work due to the complex manufacturing and preparation of the samples. Instead, the star points are positioned on the planes defined by the cube. This modification is called face centered central composite design (FCCCD). In both cases, the number of necessary measurements increases only moderately with the number of factors, so that the aforementioned example with five factors and three levels each is sufficiently covered with only 27 experiments.

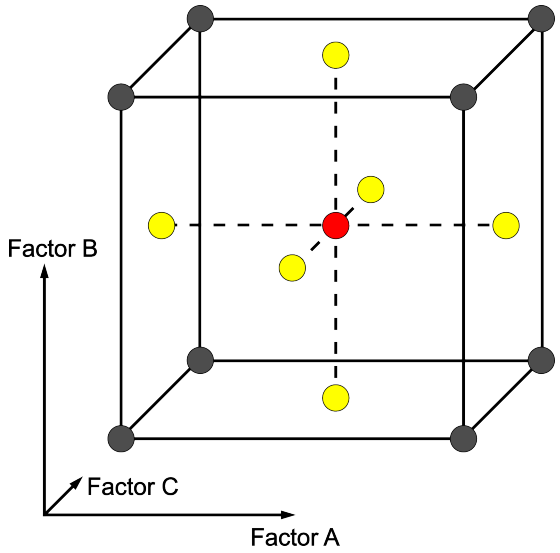

Figure 3.2.: Face centered central composite design as basis for the experiments, each point represents an experiment with the respective settings of the individual factors

3.2. Discussion of possible target variables and factors

In the following, several possible target variables for the experiments are discussed. The key criteria here are whether the respective variable is suitable for characterizing deposits (i.e. whether it is relevant in practical applications) and whether it can be determined with high accuracy and reasonable effort. Possible influencing factors and their levels are then discussed, primarily taking into account the findings from Chapter 2. The last section summarizes the final experimental design.

3.2.1. Target variables

Deposit mass

The mass of the formed deposits represents the most obvious target variable. It is easy to determine with an accurate analytical balance and is very suitable for comparison, as it provides an indication of how many deposits have formed under the given conditions.

Chemical composition

The chemical composition of the formed deposits would also be of interest as a target variable, as this would allow for comparisons with findings from other studies (e.g. [19]). However, unlike the deposit mass, it is not clear which composition would be desirable in practical application, making it challenging to compare or evaluate the results. Additionally, chemical analysis is not feasible with the available equipment.

Covered surface area

The area of the sample surface covered by the deposit can be determined using confocal images. This lateral spreading is highly relevant in practice, as it influences the wetting behavior of subsequent droplets. When the primary wall is covered with deposits, wetting is no longer governed solely by the initial wall surface characteristics. Previous work [115] has shown that deposits are re-wetted more readily due to their porous structure, which favors new film formation and creates a self-enhancing process. In a catalyst, the chemically active surface is diminished by being covered with deposits, thereby reducing the overall system effectiveness.

Deposit volume

This is a very important factor as it could predict a potential increase in flow resistance due to deposits or even the risk of clogging of the system. It can also be determined from the results of the confocal measurements, but requires additional post-processing of the data.

Porosity

The porosity can be useful for characterizing deposits under different boundary conditions and is expected to have a decisive influence on subsequent wetting. However, it is not possible to measure this factor in a meaningful way, as the interior of the structure cannot be recorded. This would only be achievable by destroying the deposit, for which often only a single sample is available per factor combination. The risk of losing individual data points (and thus the potential model accuracy as a whole) is therefore very high.

Density

Without knowledge of the porosity of the deposit, the density of the structure cannot be determined either. As some of the deposits are water-soluble, it is also not possible to determine them by means of displacement. However, it is unlikely that this factor would have any relevant implications for a practical application.

Time until the formation of solid deposits

The time span between wetting and the formation of solid deposits could be used as an indicator of whether a wall film can be removed by the exhaust gas flow without forming deposits. However, this would require a clear identification of the onset of deposit formation, which, as preliminary tests have shown, is not possible with the used equipment.

3.2.2. Influencing factors

In principle, an improved heat supply to the wall film not only accelerates the evaporation but also the thermal decomposition of the urea. This means that less urea remains to form solid deposits. In order to accomplish this, it is desirable to maximize the film surface area and minimize the film thickness. Generally, the selected surface characteristics should result in the best possible wetting given that film formation has already occurred. In contrast, poor wetting is generally desirable in order to completely avoid initial film formation [117]. However, this is not the focus of the present work, as it is assumed here that wetting cannot be prevented completely. Nevertheless, such conflicting objectives require a final discussion and consideration.

Wall temperature

The overview in Chapter 2 already emphasizes the importance of temperature for the formation of deposits. However, due to wall cooling by evaporation, temperature cannot be considered an independent factor that can be freely adjusted in practice. Despite this, the deposit formation process is expected to vary significantly with temperature due to thermal decomposition, warranting investigations at various temperature levels. This approach aims to cover a wide range of practical conditions and enhance the informative value of the model. Nevertheless, in this study, temperature is not considered as an adaptable influencing factor.

Wall material

As discussed in Chapter 2, different materials possess individual properties that can influence wetting and evaporation. Besides surface energy, these properties primarily include thermal parameters such as thermal conductivity, thermal diffusivity, heat penetration coefficient, and heat capacity. Additional material properties to consider include porosity, density, and corrosion tendency. Naturally, these properties are inherently combined in a material and cannot be varied independently. The observed effect of a material cannot be isolated and attributed to a specific property, making a clear assignment to a material property impossible. Therefore, only a qualitative statement about the “optimal material” could be made, which contradicts this study’s goal of quantifying influencing variables. Despite the practical relevance of using different materials and considering their various properties, this study is therefore limited to one material only (see Section 4.2).

Roughness

The roughness of the metal surface is an important factor as it has a significant effect on the wetting behavior. This will most likely influence the evaporation rate and, at the very least, impact the area covered by the final deposits. Surface roughness can be adjusted relatively easily and on a continuous scale. It is essential to ensure that the same material is used for processing each surface (i.e. the blast medium for sandblasting). This follows from the argumentation of Schweigert [117], who attributed the observed influence of roughness to differences in surface chemistry as a result of different processing methods. This confounding influence must be avoided in order to quantify the effect of roughness in a meaningful way.

Surface texture

Compared to roughness, the introduction of a surface structure is much more complex in terms of manufacturing technology. In order to be able to compare the effects and possibly provide motivation for the use of structured surfaces, the influence of an introduced surface pattern should nevertheless be investigated. Possible options include parallel or intersecting channels and variation of the structure heights as well as the channel width and distance. While a parallel structure perpendicular to the flow direction would significantly influence film spreading, a cross structure could even enhance wetting due to capillary forces. Combined with its more versatile applicability, this is why a cross structure was ultimately chosen.

Several geometric variables can be used to define the factor levels of a structure. These include the channel width W between the pillars, the channel distance B (i.e. the width of the rectangular pillars), and the channel height H (see Figure 3.3). Different scenarios are compared in a separate analysis, such as the variation of the ratio B/H or the variation of single variables like B. This also includes examining how additional ratios calculated from the basic variables vary. A particularly informative variable is the surface area ratio R_A, which relates the actual surface area in the structured case to the equivalent surface area of a smooth sample:

$$\begin{aligned} R_A &= \frac{A_{\text{textured}}}{A_{\text{smooth}}} = \frac{(B+W)^2 + 4BH}{(B+W)^2} \\ &= 1 + \frac{4BH}{(B+W)^2}. \end{aligned} \tag{3.4}$$

Since this variable determines the interface between the liquid and the solid, it is particularly relevant for heat transfer. In the interest of ease of fabrication and assigning effects to as few geometry variables as possible, only the spacing between the pillars W is varied. The height and width of the structures are kept constant at $B = 0.5\,\text{mm}$ and $H = 1\,\text{mm}$. It is assumed that W, also referred to as structure distance, has the greatest effect on wetting, since the influence of the capillary force is high at small distances. Large values, on the other hand, could restrict film spreading, because the droplet front gets pinned to the pillars and cannot overcome the distance to the next row. The individual values for the structure distance W are chosen so that the ratio R_A covers as wide a range as possible from 1.5 to 5.1.

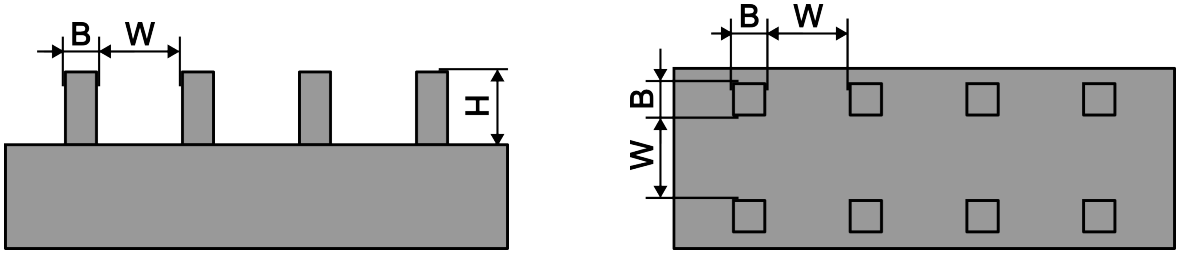

(a) Side view of the structured surface **(b)** Top view of the structured surface

Figure 3.3.: Geometric dimensions of the structured surfaces

Chemical coating

The aim of a coating should be to vary the wettability of the surfaces without changing the surface geometry or the wall material. It is therefore desirable to use at least one hydrophilic and one hydrophobic surface coating

and to compare them with the uncoated case. In contrast to all other influencing variables, the question arises here as to how the levels can be quantified. A categorical classification is possible, but not desirable, as this would reduce the informative value for practical application. Chemical coatings must therefore be quantified by their effect, i.e. the resulting wettability (measured by the contact angle θ). However, since other variables, such as roughness, also influence the contact angle, care must be taken. Classification of chemical surface treatment by contact angle is appropriate only if the following conditions are met:

1. Interactions between the variables are taken into account in the model, as the setting of one wetting-relevant factor can influence the effect of another.

2. All factors can be set independently of each other, so that no factors are correlated with each other.

In this sense, the term contact angle (and the associated symbol θ_c) will be used in the following to refer to the quantifiable influence of the chemical coating. This explicitly does not refer to the actual contact angle being present in the experiment, which ultimately results from the combination of all surface characteristics. Measuring the corresponding contact angle θ_c for a coating has to be done on a reference object. Since only one material is used, the reference surface is defined as the one with the low roughness setting. The same assignment of coating to contact angle is then used for the structured case as well. This means that there is no separate determination of the coating dependent contact angle on structured surfaces.

Oxidation

Depending on the material used and its tendency to oxidize, the influence of an oxidation layer on deposit formation could be considered. As reported by Schweigert et al. [118], the pure oxide layer already results in a reduced surface energy and wettability. Although it would be possible to influence the oxidation of the surface by thermal pretreatment or surface cleaning, the effect would only be temporary due to the high oxidation tendency of aluminum and ultimately not feasible in practice. In addition, the oxide layer formed can only be quantified using complex methods such as X-ray photoelectron spectroscopy. However, such a classification would be essential for use as a factor in the model. It would also be unclear if and how an independent variation of the oxide layer and the chemical coating could be implemented. Since deliberately varying the coating seems to be more realistic in practice, the influence of oxidation is not investigated.

To ensure that the oxide layer does not act as a confounding influence on the experiments, all samples are stored at ambient conditions for at least 24 h after cleaning. This allows a uniform oxide layer to form on all surfaces before weighing and subsequent experiments.

Residence time

In the range up to 150 °C, solid deposits are expected to form only after the film has cooled, due to the absence of solid decomposition products. The residence time of the liquid on the heated surface, together with the respective evaporation rate, should therefore have a significant influence on the amount of deposits. At higher temperatures, increasing amounts of urea decompose into by-products, leading to the expectation that the residence time will determine the resulting degree of decomposition. To capture these phenomena, residence

times of up to 60 min must be considered. For simplicity, this factor will be referred to as duration in the following.

3.3. Final design

Following the above considerations, deposit mass m_{dep}, covered surface area (referred to simply as deposit area A_{dep}), and deposit volume V_{dep} are specified as appropriate target values or dependent variables. The factors, or independent variables, will be given by the wall temperature T_{wall}, the contact angle θ_{c} due to chemical surface treatment, the duration $\Delta\tau$, the surface roughness Ra, and the surface area ratio R_A, corresponding to the structure distance W of structured surfaces. For the reasons given, temperature is treated as not adaptable in practice. Instead, separate experimental designs for the remaining factors are carried out in full for two different wall temperatures: 150 °C and 200 °C. Both values are well-suited for investigation with the experimental setup. At the lower temperature, a high urea content and incipient decomposition to biuret can be assumed, while at the higher temperature one can expect an increasing fraction of biuret and cyanuric acid and very low amounts of urea in the deposits. This allows a wide range of temperature-related phenomena to be represented.

The factors of roughness and surface structuring are similar in consequence. Both variables cannot be freely varied on one and the same surface due to the necessary manufacturing process. They are therefore considered separately and also result in two separate experimental designs. In total, four complete designs (two temperatures for each of the two surface types, rough and textured) must therefore be run for the remaining factors. These factors are the contact angle, the duration and the level of the respective surface feature: roughness or structure distance. Each individual design is structured as an FCCCD and comprises the three factors in three settings to investigate non-linear effects. The central point is repeated twice in order to estimate the measurement uncertainty. This results in 17 experiments per design, for a total of 68 individual experiments. This is significantly more manageable than the 243 experiments of a full factorial design as calculated above. Even with the subdivision into four designs, each with three parameters at three settings, 108 experiments would have to be carried out and processed in the full factorial case.

Beyond the replications of the central point, no repetitions are performed, as the calculation of the individual effects is based on the entirety of the results. In other words, each factor is already measured at least five times at each level (with different settings for each of the other factors). This significantly reduces the influence of uncertainty on an individual measurement. Each test plan is randomized, i.e. processed in random order, to avoid systematic errors.

Table 3.1 briefly summarizes the levels of the individual factors. The contact angles result from three coatings that are considered appropriate to investigate one hydrophobic, one hydrophilic and one untreated surface (see Section 4.2). The structure distances and the resulting surface area ratios are the result of the aforementioned preliminary calculation, with the aim of covering as wide a possible linear range of ratios as possible. The roughness values are based on the roughness classes defined in DIN EN ISO 1302 [39] resulting from a variety of machining processes. These carefully chosen levels ensure a comprehensive investigation of the effects of each factor and its interactions on deposit formation and behavior.

No.	Factor		Level	
1.	Wall Temperature T_{wall} [°C]	150	-	200
2.	Duration $\Delta\tau$ [min]	10	30	60
3.	Contact angle θ_{c} [°]	37.8	77.7	116.6
4.	Roughness Ra [µm]	0.7	1.6	3.2
5.	Structure distance W [mm]	0.2	0.5	1.5
or 5.	Surface area ratio R_A [-]	5.1	3	1.5

Table 3.1.: Overview of the selected influencing factors and their respective levels for the experimental study. Surface area ratio R_A is the result of the structure distance W as given in Equation (3.4). The remaining texture dimensions B and H are constant at $0.5\,\text{mm}$ and $1\,\text{mm}$.

CHAPTER 4

Experimental Setup and Methods

The investigation of the wetting, evaporation and deposit formation behavior of UWS is conducted on flat, heated test samples, referred to as substrates. These substrates are intended to simulate the behavior of a section of the inner wall in an SCR system. They are part of a larger experimental setup designed to ensure constant and controllable boundary conditions, as well as the integration of measurement devices.

This chapter begins with the description of the experimental setup, followed by a detailed explanation of the individual samples. Next, the measurement technology is discussed, including both the equipment incorporated into the setup and the tools used for subsequent analysis outside the experiment. The experimental procedure is then outlined, leading into the methods for processing the collected data. The chapter concludes with an analysis of possible errors.

4.1. Experimental setup

The custom-designed experimental setup used for the experiments is shown in Figure 4.1. The heart of the setup is the test cell, made of brass and cubic in shape, with several openings for inserting an injector needle and thermocouples. These openings also facilitate gas exchange with the environment, preventing an increase in humidity inside the cell during the experiments. A central optical path runs through the cell, with a light source (*Schott KL 1600 LED*) and diffuser on one side. A color camera mounted on the opposite side records the wetting and evaporation of droplets on the substrate.

The substrates are heated via a copper element, referred to as the heater, attached to the bottom of the cell, as shown in the CAD model in Figure 4.2 (1). The substrates (2) are mounted at the top of the heater. Four heating cartridges (3), each with a maximum power of 90 W, are arranged circumferentially in the lower part of the heater. This configuration allows efficient conduction of heat through the copper, bringing the substrates to the target temperature. Figure 4.3 shows a photograph of the assembled cell and a closer look on the heater with the substrate.

The substrate temperature is measured by a thermocouple (Figure 4.2 (4)) that runs through the heater from below and fits precisely into a hole at the bottom of the substrates. The tip of the thermocouple is located 0.5 mm below the substrate surface. This positioning, combined with the high thermal conductivity of the

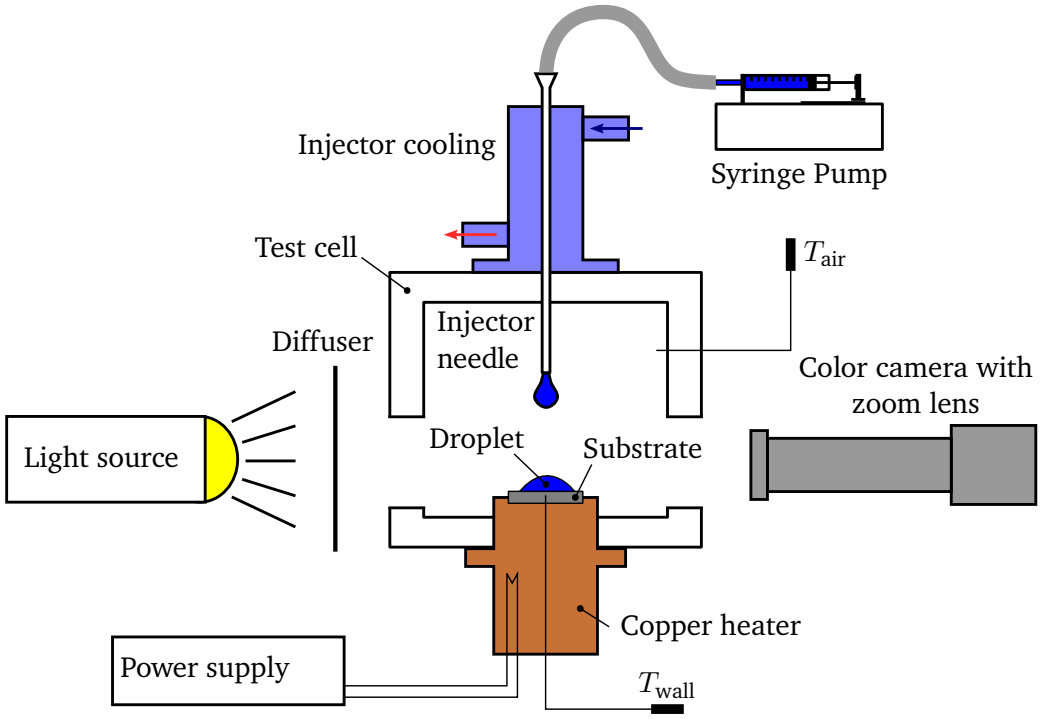

Figure 4.1.: Diagram of the experimental setup

substrate material (see Section 4.2), ensures accurate measurement of the surface temperature (referred to as the wall temperature, T_{wall}). Additional thermocouples (not shown in Figure 4.2) are placed above the substrate to monitor the gas temperature. The heater can be easily dismounted from the cell to remove the substrate for further analysis, such as microscopy, after the experiment.

The droplets are generated by a syringe pump (*LA100* from *Landgraf Laborsysteme HLL GmbH*) operated manually to supply a continuous volume flow. When the droplets at the tip of the needle become large enough for gravity to overcome the surface tension, they detach and fall onto the substrate. The distance between the needle and the substrate surface ranges from 7.5 mm to 8.5 mm, depending on the type of substrate. This distance ensures that the droplets do not touch the needle and the surface simultaneously, while also preventing the droplets from impacting at high speeds. The latter could cause impact in the splash regime, which is unwanted in this study. The injector is made of stainless steel and has an outer diameter of 0.9 mm.

Due to the high temperatures expected in the test cell during operation, cooling the needle is essential for two main reasons:

1. If the needle heats up, the material properties of the equally heated fluid will change. This affects the surface tension and, consequently, the volume of the detaching droplets, making it difficult to maintain consistency across experiments. This issue is particularly significant for tests conducted at different substrate temperatures or at varying times of the day, as the test cell may heat up over several hours.

2. Droplets forming on a needle at temperatures near 100 °C would begin to evaporate immediately. This complicates pump operation and causes fluctuations in the concentration of the applied fluid.

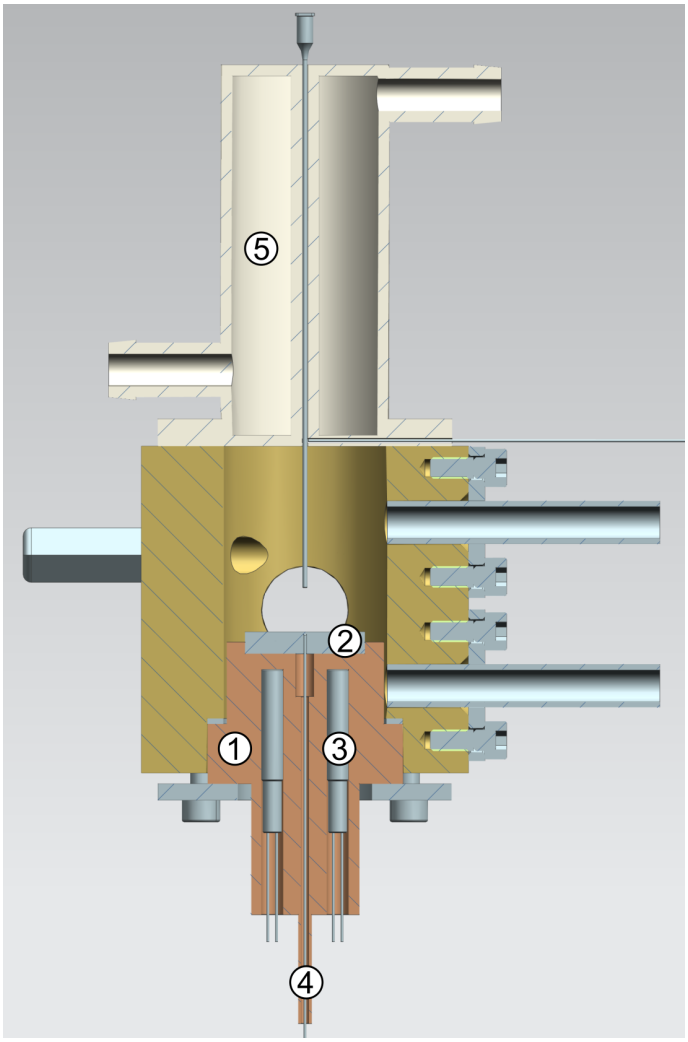

Figure 4.2.: Section view through the CAD design of the test cell. The design shows the bronze-colored heater with heating cartridges at the bottom and the white cooling system at the top of the cell.

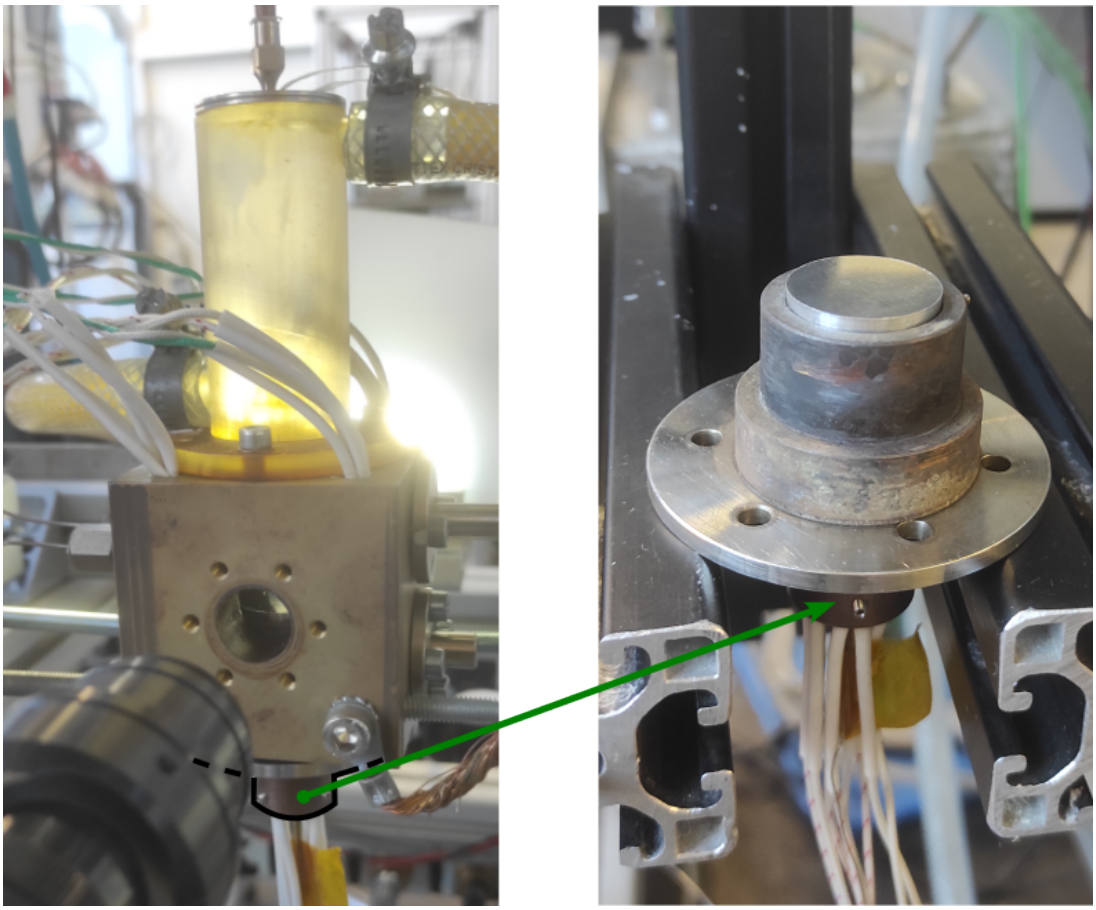

Figure 4.3.: Photographs of the assembled test cell (left) and the separate heating unit with a mounted substrate at the top (right)

Additionally, it results in significant crystallization of urea at the needle tip, which can further impact the droplet break-off volume.

In summary, it is crucial to ensure that the liquid does not heat up too early, as this would result in significant issues with the repeatability and comparability of the experiments. To achieve this, a cooling system was implemented on the test cell, as shown in Figure 4.2 (5). The part is manufactured from high-temperature resin using the 3D printing process of stereolithography, capable of withstanding temperatures up to 230 °C. This manufacturing choice allows the component to be built with a cavity and two tube connections as a single part.

A thermostat (*Huber Unichiller 020Tw-H*) pumps a −10 °C cooling mixture of water and glycol through the component. The needle, guided through the center of the cooling system, can thus be kept consistently below 30 °C, even during several hours of operation with gas temperatures exceeding 160 °C within the test cell. A thermocouple is inserted from the side up to the needle for temperature monitoring, as shown in Figure 4.2.

4.2. Sample surfaces

The substrates have a cylindrical shape with a diameter of 22 mm. Depending on the surface structure, the height is either 4 mm or 5 mm. All substrates are made of the same material, *AlMg4.5Mn0.7*, also known as *AW-5083*. This material was chosen for several reasons: Firstly, it meets the basic requirement of being corrosion-resistant due to the rapid formation of a protective oxide layer. Additionally, the material is comparatively easy to machine, allowing for the realization of the necessary and sometimes complex processing steps in the required quantity, both in terms of time and cost. Compared to materials closer to the application, such as steel or iron, the aluminum alloy substrates have a higher thermal conductivity. This is crucial for the experiments, as it not only enables reliable and rapid heating and control of the surface temperature, but also ensures homogeneous temperature distribution.

The surface structures are milled using a milling bit with a diameter of 0.1 mm. Figure 4.4 shows a direct comparison of the three structure geometries used. In contrast, the roughened surfaces are produced by ablation with an ultra-short pulse laser. This method is chosen because it ensures a uniform surface without directional dependence in the surface irregularities. Such directional dependencies would have occurred during grinding due to the grinding direction and could have influenced the spreading of the droplets, thereby affecting the comparability of results. Methods such as sandblasting are also considered unsuitable because, depending on the blasting medium, a change in the surface chemistry could result in an unintended influence on the measurements, as described by Schweigert [117].

In addition to the surface characteristics, some substrates are coated to investigate the influence of chemical treatment on deposit formation. A hydrophobic and a hydrophilic coating are selected, while the remaining substrates remain uncoated. All coatings are produced using the plasma polymerization process, a specialized form of plasma-enhanced chemical vapor deposition. In conventional chemical vapor deposition, gaseous precursor materials react on the target surface to produce the coating material. The necessary activation energy for these chemical reactions can be supplied thermally, but this can require very high temperatures of up to 4000 °C.

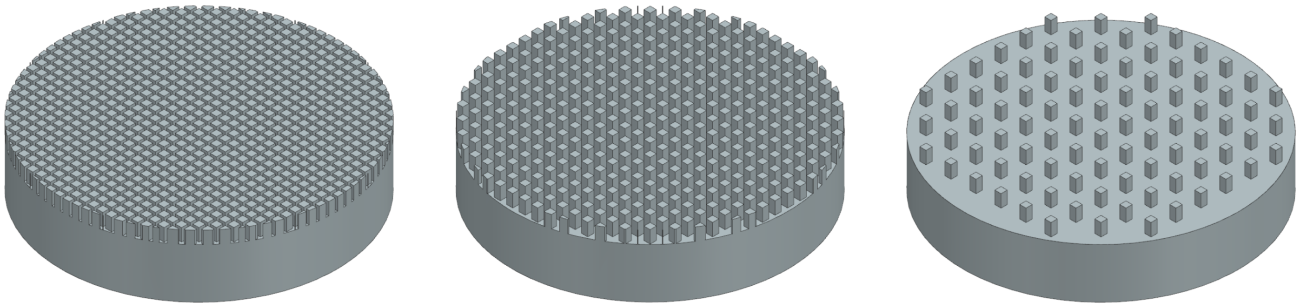

(a) $W = 0.2\,\text{mm}$, $R_A = 5.1$ **(b)** $W = 0.5\,\text{mm}$, $R_A = 3$ **(c)** $W = 1.5\,\text{mm}$, $R_A = 1.5$

Figure 4.4.: Substrates with structured surfaces and the respective structure distance W and surface area ratio R_A

Instead of high temperatures, plasma-enhanced vapor deposition uses a plasma to ionize the gas of the starting materials. This ionization occurs through collisions with free electrons and ultraviolet radiation, producing highly reactive radicals. This increased reactivity facilitates chemical reactions and the deposition of the coating material, enabling the coating of less temperature-resistant materials. The plasma is generated by an electric field coupled into the reactor, for example, between an electrode and the grounded substrate carrier.

In plasma polymerization, a specialized application of the aforementioned method, liquid or gaseous monomers are fed into the reactor. The plasma causes the precursors to break down into fragments, which then chain together to form special plasma polymers during condensation on the substrate. This process offers several advantages, including the ability to precisely influence the chemical and physical properties of the polymers, increased temperature resistance, a high degree of cross-linking resulting in a high-density layer, and simple adjustment of the layer thickness. [15, 147]

The monomers used for coating the substrates are acrylic acid for hydrophilic behavior and fluoroacrylate for hydrophobic behavior. To characterize the effect of the coatings and use it as a parameter for statistical evaluation, the wettability is measured on smooth substrates with $Ra = 0.7\,\mu\text{m}$. For each surface chemistry (hydrophobic, hydrophilic, and uncoated), eight substrates are tested. A 3 µL drop of deionized water is placed at two different points on each substrate surface, and the contact angles are then determined. The tests are conducted at room temperature in an open environment with relative humidity ranging between 43 – 48 %.

Figure 4.5 shows the measured contact angles as a box plot. For each measurement, the mean of the left and right side contact angles was considered. The difference between the various surface chemistries is clearly recognizable. Both the hydrophilic and hydrophobic surfaces exhibit only a small scattering of results. In contrast, the uncoated surfaces display a larger range of results, indicating that the influence of manufacturing-related surface irregularities is more pronounced. Nevertheless, the three groups can be clearly distinguished from each other based on their wettability.

The mean values of the results across all substrates in a group are used as factor settings for further analysis. The results, along with their respective standard deviations, are summarized in Table 4.1.

To affect the formation of deposits, the coatings must withstand the investigated temperatures. Therefore, the thermal resistance was tested on two hydrophobically coated samples with a roughness of 0.7 µm. First, the

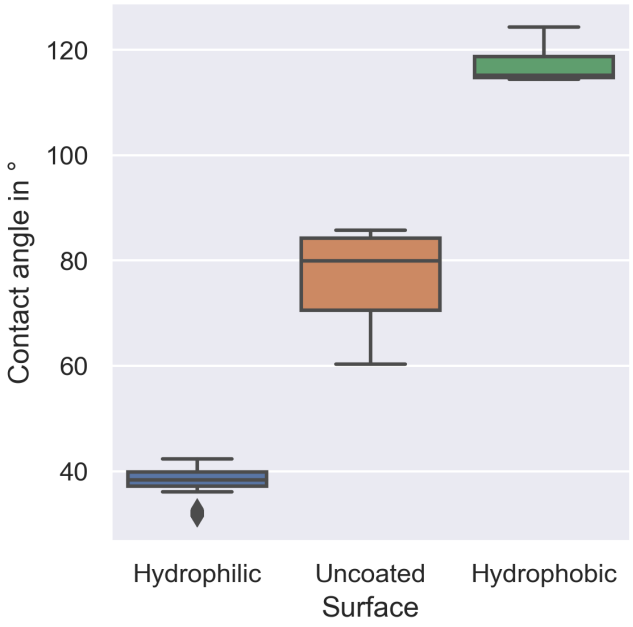

Figure 4.5.: Box plot of the contact angles on coated and uncoated smooth substrates with $Ra = 0.7\,\mu\text{m}$

Table 4.1.: Mean contact angle and standard deviation for each group with respect to surface chemistry

Surface	Mean contact angle [°]	Standard deviation [°]
Hydrophilic	37.8	2.7
Uncoated	77.7	8.9
Hydrophobic	116.6	3.4

contact angle with deionized water was measured. One sample was then heated to 150 °C and the other to 200 °C in the experimental setup. These temperatures were maintained for 60 min in each case. The contact angle was then measured again. At the lower temperature, the contact angle increased by 5.6° after heating, while at 200 °C it decreased by 2.7°. Both values are within the same order of magnitude as the standard deviation of the initial contact angle measurements. As there is no clear trend direction, it is assumed that the coatings are thermally stable.

4.3. Measurement technology

The camera used to record the experiments is a *Basler ace acA2040-90uc*, capable of recording at up to 90 Hz with a resolution of 2048 px × 2048 px. Additionally, a *Navitar Zoom 6000* zoom lens is used, which allows up to 6.5× magnification. In the experiment, this results in a pixel length of 8 µm. The formed deposits are then captured with a *Dino-Lite Edge* microscope camera. This camera has a resolution of 1280 px × 1024 px and allows up to 120× magnification. The images presented here are taken at 20× magnification.

All temperature measurements during the experiments are performed using type K thermocouples. The elements are of tolerance class 1 and thus have a maximum measurement deviation of 1.5 °C according to *DIN EN 60584-1:2014-07* [38]. Both the thermocouple that monitors the substrate temperature T_{wall} and the one used on the needle have a diameter of 0.5 mm. The thermocouples that measure the atmospheric temperature T_{air} in the cell (see Figure 4.1) have a diameter of 1 mm.

The signals from all temperature sensors are recorded using a measuring system from *National Instruments* (NI). Data acquisition is carried out using various measurement modules housed in an *NI SCXI 1000* chassis. On the computer side, data acquisition is done with an *NI 6289* measurement card. The custom test bench software, written in *NI Labview 2019*, handles the visual display, logging of the measured values, and control of the power supply units for heating. All measured values are saved at a frequency of 10 Hz.

Since manually adjusting the heating power would make it impossible to maintain a constant substrate temperature under the influence of the environment and evaporation, suitable temperature control is essential for the experiments. To achieve this, a control system with a PID controller was implemented in the test bench software. This part of the software continuously monitors and adjusts the substrate temperature based on the data for T_{wall} from the thermocouple. The target temperature of the substrate is specified as the reference variable, and the controller then determines the voltage of the power supply unit for the heating cartridges. This system ensures not only a rapid heating process but also maintains a constant substrate temperature despite the influences of the impinging liquid, evaporation, or the crystallization and decomposition of urea.

All deposits are weighed by taking the difference between the mass of the substrate before and after the experiment. The balance used for this purpose is a *Mettler Toledo AT20*, with a readability of 2 µg and a reproducibility of 3 µg. Before measuring the mass of the empty substrates, the uncoated samples are cleaned with acetone in an ultrasonic bath for 5 min and then dried for 24 h. The coated samples, on the other hand, were cleaned before the coating process and are therefore only lightly air-blasted to avoid damaging the coating. All substrates are weighed at least twice to ensure accuracy, with a maximum allowable difference of 30 µg between the measurements.

Finally, the deposits are examined under a confocal microscope. The device used is a *μsurf expert* from *NanoFocus AG*. In confocal microscopy, only a small part of the substrate is illuminated at a time, enabling more precise focusing. The reflected light must then pass through a pinhole aperture before reaching the detector. This pinhole is positioned so that only reflected light from the exact focal plane can pass through. By moving the lens and thus the focal plane vertically, the sample section is scanned layer by layer. This method allows for the recording of height information on the surface.

After scanning an area of the substrate, the device moves on to the next section. The individual scanned areas are combined to form a three-dimensional overall image of the sample. This high-resolution three-dimensional image is particularly valuable for detailed analyses of the deposit structure and geometry. A special feature of the microscope used is the multi-pinhole disk, which contains several pinholes on one disk. This configuration allows the illumination and scanning of several focal points simultaneously, resulting in significantly faster data acquisition.

In the work presented here, sections of 1.63 mm × 1.62 mm are scanned with a vertical step size of 0.937 µm and then used to compose the overall image. The lens used allows a 10× magnification, resulting in a lateral resolution of 1.36 µm × 1.35 µm per pixel.

The device used for contact angle measurement is an *OCA 25* from *dataphysics*. The measuring accuracy is specified as ±0.1°. A built-in syringe pump provides the liquid volume with high precision, after which the drop is manually detached from the needle onto the substrate. The software then defines the liquid-solid interface, and a polynomial fit algorithm detects the contour of the sessile drop. Based on this, the contact angle is determined on both sides of the drop and recorded at a frequency of 8 Hz. During evaluation, the first 100 measured values are averaged.

4.4. Experimental procedure

Before each test run, the substrate is cleaned with pressurized air to remove any dust residue or other contamination. The substrate is then fixed in the heater, as shown in Figure 4.3, before both parts are mounted in the cell from below using the flange on the heater. The tip of the needle is cleaned before each experiment or replaced entirely to prevent urea deposits from forming over time. Such deposits can cause the droplets to not detach cleanly from the tip but instead pull up the sides of the needle, as seen in Figure 4.6. This behavior leads to undesirable variations in the individual drop volumes. Additionally, deposits on the tip of the needle could dissolve in the new drop, changing its initial composition.

The substrates are heated in two phases. First, all substrates are heated to 90 °C, regardless of the final target temperature. Once this temperature is stable, five droplets are placed on the substrate with a continuous volume flow of 20 µL min^{-1}. Only then does the heating to the respective target temperature begin. This second heating phase lasts between 3 – 4 min, depending on the intended temperature. After the target temperature has been reached, the specified duration is counted down.

This two-stage heating approach is based on preliminary tests indicating that the Leidenfrost point is exceeded for some droplets at the targeted substrate temperatures. Figure 4.7 illustrates how a falling droplet at a substrate temperature of 200 °C does not wet the surface but instead rebounds and falls off the side of the substrate. With smooth, hydrophobically coated samples, this behavior occurred even below the lower target

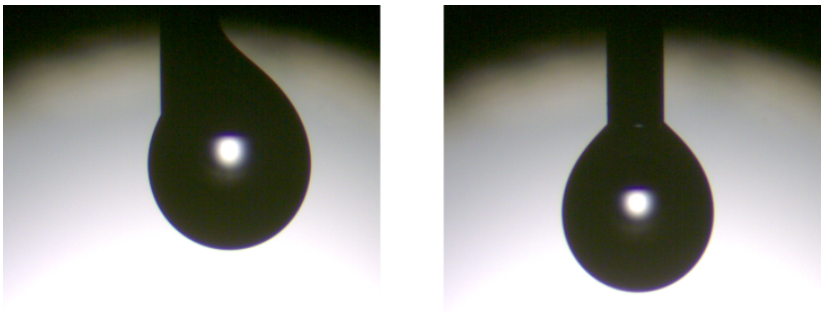

Figure 4.6.: Left: Droplet pulling up the side of the needle due to contamination or deposit formation, Right: desired generation of a droplet

temperature of 150 °C, preventing the intended wetting. This phenomenon occurs even below the Leidenfrost temperatures mentioned in the literature (see Section 2.1.1). These results demonstrate how the regime limits for droplet-wall interactions are strongly influenced by surface characteristics and wettability. As Schweigert [117] and Kim et al. [71] showed, hydrophobic wetting behavior can significantly reduce the Leidenfrost temperature.

In preliminary tests where T_{wall} remained below the Leidenfrost temperature, such as on uncoated samples at $T_{\text{wall}} = 150\,°\text{C}$, the droplets exhibited splash behavior and immediate boiling upon impact. As a result, a significant fraction of the liquid was deposited on the side walls of the cell, no longer contributing to deposit formation. This inconsistency in the deposited liquid volume contradicts the necessary model assumptions for evaluation, necessitating the previously explained procedure.

In fact, this approach increases comparability with conditions in real SCR systems. As described in Section 2.1.1, Brack et al. [24] demonstrated that repeated spray impingement can cool the system wall to temperatures below 100 °C due to the enthalpy of vaporization, making wall film formation likely. The film then moves downstream into areas with higher wall temperatures, where evaporation and decomposition of the urea begin and deposits accumulate. This successive process is well-represented by the employed two-phase heating.

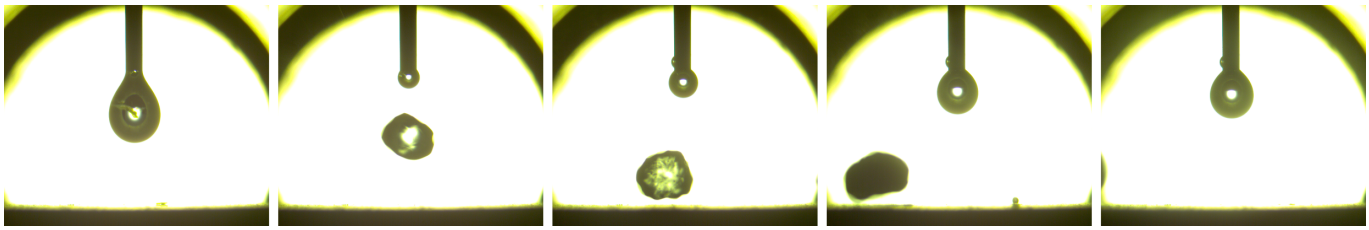

Figure 4.7.: Single droplet which rebounds and falls off the substrate at $T_{\text{wall}} = 200\,°\text{C}$

After the specified exposure time, the heater is switched off and dismounted from the cell. The substrate is then removed from the heating element and cooled under ambient conditions, specifically room temperatures between 18 °C and 21 °C and humidity levels between 35 % and 42 %. During this disassembly process, the substrate is no longer actively heated but remains in contact with the hot copper heater. This process lasts

about 2 min and is consistent for all substrates. Therefore, it is assumed that this duration does not interfere with determining the effect of the exposure time.

Despite the precautions described above, hydrophobically coated substrates with roughnesses of $Ra = 1.6\,\mu m$ and 3.2 µm exhibit non-wetting behavior even at room temperature. It was impossible to consistently deposit an initial droplet on the substrate without it rolling off the surface immediately, as shown in Figure 4.8a. This occurred in three different experiments for each of the wall temperatures.

To still perform these experiments, the process of depositing and heating the droplets was modified. Instead of at $T_{wall} = 90\,°C$, all droplets are applied to these substrates at room temperature. No effect on the composition of the deposits is expected, as the initial temperature in both cases is below the boiling point of water and the temperature at which thermal decomposition of urea begins. The heating phase to the target temperature is slightly longer in these cases, taking up to 5.5 min.

To prevent the droplets from rolling off, the first falling droplet is fixed with a small needle held by hand below the injection needle. As shown in Figure 4.8b, the droplet remains attached to the needle and is held in place until the remaining four droplets are applied. After carefully removing the needle from the liquid, the droplet stays in place due to its own weight.

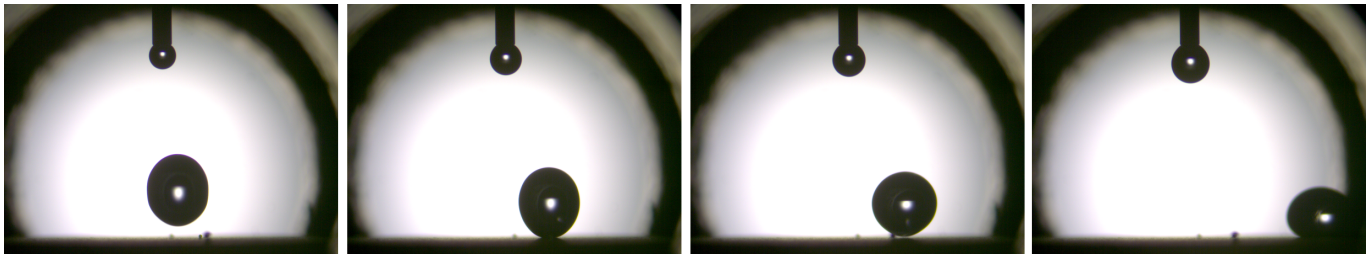

(a) Sequence of a droplet bouncing and rolling off the non-wetting substrate at $T_{wall} = 90\,°C$

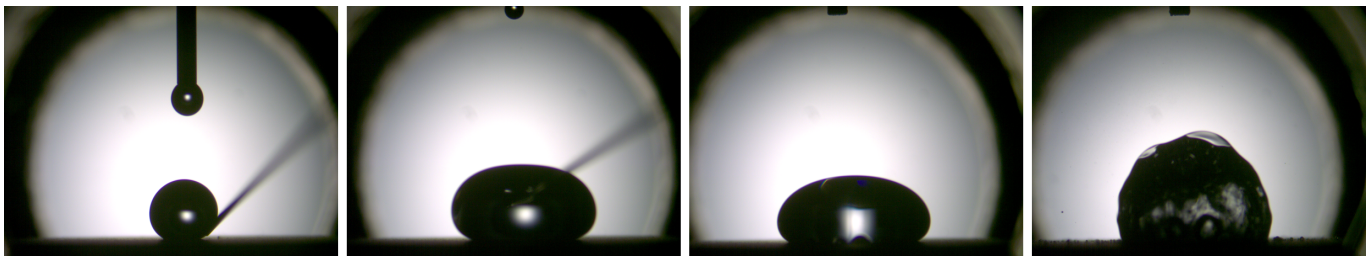

(b) The leftmost image shows the initial droplet being suspended by a needle at $T_{wall} = 25\,°C$, the two middle images show the final accumulated droplet staying in place due to its weight, the rightmost image shows the final droplet boiling upon reaching $T_{wall} = 100\,°C$

Figure 4.8.: Application of droplets on hydrophobic substrates with $Ra \geq 1.6\,\mu m$, exhibiting non-wetting behavior

The mean volume of the individual droplets is 15.5 mm^3, corresponding to an equivalent spherical diameter of 3.1 mm. The scatter of the volumes is very small, with a standard deviation of 0.27 mm^3. To determine the volume, 54 single images of droplets in free fall were selected from all experiments, and the droplet volume was determined for each as described in Section 4.5. This sample represents all possible parameter combinations to a similar degree. Maintaining low variation in the individual volumes between the experiments is crucial, as the volume of liquid applied directly affects the mass and geometry of the deposit.

4.5. Data processing

After the deposits have formed, the substrates are reweighed and scanned under the confocal microscope. While no further steps are required for the mass data, apart from subtracting the mass of the substrate, the confocal data needs further processing. The first step is to perform the pre-processing described in the following section for each measurement using the *NanoFocus Analysis* software. This is followed by additional data processing to determine the deposit volume and area from the pre-processed measurement data. These final steps are carried out using a custom-written program using the Python programming language, which is described in Section 4.5.2.

4.5.1. Pre-processing of confocal data

All of the processing steps described below are summarized in Figure 4.9. First, the 3D image of the deposit obtained with the confocal microscope is subjected to a filtering process to reduce measurement noise. In the first pass, the image is scanned pixel by pixel with a 3×3 filter kernel. If the Z-value (height) of a pixel falls within the first or last quartile of the surrounding pixels in the filter kernel, the Z-value is replaced by the median of the surrounding Z-values. This means that the height of the pixel is not changed if it is close to that of its neighbors. This procedure effectively removes isolated and unphysical spikes without a significant smoothing effect.

Next, missing values, i.e., pixels without height information, are filled to create a linear transition between the surrounding pixels. A second filter pass with a 9×9 filter kernel subsequently removes the so-called micro-roughness of the measured surface. In contrast to the first filter, the Z-value is always replaced by the median of the surrounding 9×9 pixels, so that the filter acts as a low-pass filter and smoothes the surface. The micro-roughness is usually a result of the measurement noise and does not reflect the actual surface.

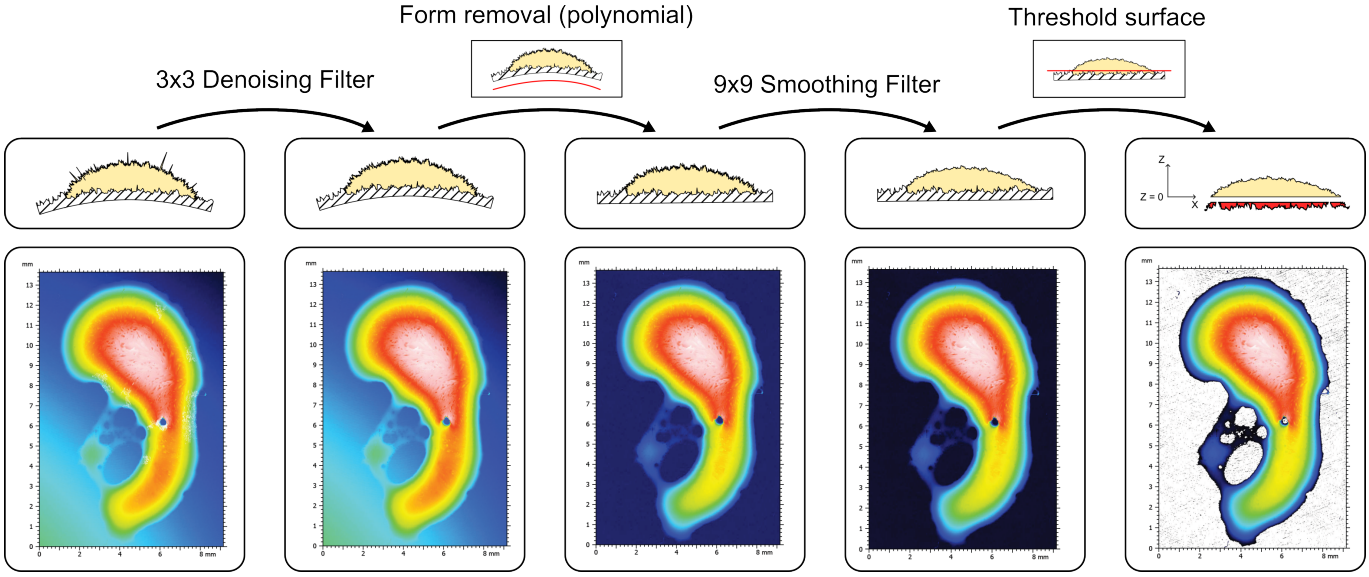

Figure 4.9.: Diagram showing the procedure for pre-processing the raw confocal measurements

Another important step for subsequent correct evaluation is form removal. This involves removing any long-wave deformation of the measured surface, caused, for instance, by imperfect milling, so that the measured substrate surface corresponds to a horizontal plane. This step is critical for isolating the deposit by removing the substrate surface from the measurement. During form removal, the free substrate surface is approximated by a polynomial, usually of the second degree, using a least-squares fit. For the surface $Z = f(X, Y)$, the second degree polynomial can be written as follows:

$$Z(X,Y) = \sum_{i=0}^{2} \sum_{j=0}^{2} a_{i,j} X^i Y^i \qquad \text{with } i + j \leq 2$$

To ensure that this approximation of the substrate surface is not distorted by the deposits or the structure blocks, these elements must first be manually excluded from the surface. The resulting correction surface is then subtracted from the corresponding measurement, eliminating the underlying deformation.

The final pre-processing step is the removal of the substrate surface from the measurement. This step is necessary to accurately calculate the volume and area of the deposit without the need to distinguish between the deposit and the uncovered substrate surface. Furthermore, the height of the uncovered surface is thereby defined as a reference level, allowing the height information of the deposit to be analyzed relative to this reference. This approach enables the determination of the actual deposit height relative to the substrate surface.

To remove the surface, a limit value is defined. Values below this threshold are set to “not measured” or NaN (not a number). This limit value remains constant across the entire measurement. Figuratively, the surface is cut off by a horizontal plane, leaving only the deposit. It is crucial to remove any deformations of the substrate surface beforehand, as these could prevent the constant limit value from effectively removing higher regions of the substrate. Increasing the limit value could risk cutting off parts of the deposit.

To determine the optimal limit value, the average height of all pixels, excluding the deposit, is calculated for each measurement without structured surfaces. On particularly rough substrates, this method fails to remove the peaks of the roughness, as they lie above the average height. At the same time, roughness valleys that are filled with deposits may lead to a loss of deposit volume when these valleys are cut off. In some cases, very thin deposit layers at the deposit edge could distort area calculations if the calculated limit value exceeds the height of these layers. Therefore, in each of theses cases, the limit value is manually adjusted to retain as much of the deposit area as possible. Any remaining bare substrate data is removed manually. The difference between the determined substrate height and the manually specified limit value is recorded and used later to correct any excessively removed deposit volume (see Section 4.5.2). In Figure 4.9, the rightmost image shows the final extracted deposit volume. The red-marked section in the upper pictogram indicates the “lost” volume within the roughness valleys that needs correction.

On structured surfaces, a different challenge arises. Similar to rough substrates, the limit value should correspond to the base of the deposit and the structure blocks, or pillars. However, calculating the mean surface height of the uncovered surface would result in an excessively high limit value due to the height of the included pillars. To address this, the average height of a line profile is determined, which is positioned between the pillars in a bare part of the measured section.

Finally, the remaining surface of the deposit is exported as a csv file for further processing. In this file, each pixel is represented by a tuple of its respective X, Y, and Z coordinates, with the Z-values of the substrate surface appearing as NaN. These NaN values can later be removed from the data set.

4.5.2. Determination of target variables from confocal data

Further data processing is performed by a self-written Python program, which implements a pipeline for raw data reading, processing, storage, and visualization. Figure 4.10 summarizes the entire sequence. The process begins by reading all the values and normalizing them so that the lowest measured Z-value (i.e., the smallest height) is exactly zero. Subsequently, all NaN values (particularly the height of the surrounding substrate surface) are set to zero to simplify subsequent calculations. The data set is then converted into a 2D array of Z-values, which retains the same shape as the original confocal image and serves as the starting point for all further steps.

The calculation of the deposit volume is based on the fact that each element of the array now represents a pixel whose value is the actual height of the deposit at that point in relation to the substrate surface. Since the lateral resolution of each pixel is known (see Section 4.3), the deposit volume can be calculated by simply multiplying the height by the lengths of the two pixel sides. The sum of these partial volumes over the entire area then gives the total volume of the measured region.

Depending on the substrate surface, this value must be corrected in one of two ways. For structured substrates, the structure blocks remain included in the data with their Z-values, as the substrate has been cut off at the base of the structure (i.e., in the structure valley). To determine the volume of the structures, several sections of the substrate with clean pillars (i.e., without deposits) are evaluated in the same manner as described above. A total of 10 to 30 clean blocks are evaluated for each surface. From these measurements, the average volume of a block is calculated. This value is then multiplied by the number of blocks that incorrectly contribute to the deposit volume calculation, and the resulting value is subtracted from the total volume. This process is illustrated on the left side of Figure 4.10.

On rough surfaces, the necessarily higher threshold for removing the substrate surface, as explained above, results in a loss of deposit volume in the roughness valleys. To correct for this error, the distance between the mean height of the uncovered surface and the limit value is multiplied by the calculated deposit area (see the following paragraphs) and added back to the calculated volume. In a few cases, this correction is also applied to structured surfaces, for example, if it is expected that part of the deposit volume has been cut off due to imperfect form removal.

To determine the area covered by the deposit, the 2D array of heights is first converted to grayscale and then binarized, producing a black and white image as shown on the right side of Figure 4.10. Contour detection is then performed using the algorithm described in [141]. From all the contours found, only the outer contours are selected, i.e., those not enclosed by another contour. This result, corresponding to the outer edges of all coherent deposits in the image, is also shown on the right side of Figure 4.10. In some cases, uncovered areas where no deposits have formed are included if they are surrounded by deposits on all sides. This inclusion aligns with the definition of the deposit area used here.

As a characteristic value of deposit severity, the area quantifies, among other things, the influence of the deposit on subsequent wetting events. As shown in [115], due to the porosity of the deposit, a subsequent droplet or formed film will spread over the entire deposit area, even if it is larger than the area that would otherwise be wetted by the droplet. This amplifying effect on wetting is determined by the outer edges of the deposit cluster and not affected by the (possibly clean) surface enclosed by it.

Finally, the area of all pixels within the contours is summed up to give the total deposit area. It should be noted that the result is not the surface area of the deposit, but the previously clean, flat substrate surface now covered by deposits.

4.5.3. Droplet volume determination

Data processing is also required to determine the droplet volumes described in Section 4.4. The images taken by the side-view camera during the experiment form the basis for this analysis. As the camera stores each frame as a separate image, there is no need to extract the frames for processing. All processing is done using a Matlab program developed at the Institute of Technical Thermodynamics, as detailed in Heinz et al. [61].

The first step is to select all images where the droplets are in free fall. Further processing benefits from the high contrast between the dark droplets and the bright background due to the backlighting (see Section 4.1). A second image, taken with the same settings but without the droplet, is subtracted from the image to be processed. This results in an inverted image cleaned of static background elements, as shown in Figure 4.11b. The droplet contour is then determined using the Gradient Change Point method [70, 82]. For each row and column of the image, the points with the sharpest gradient change are identified, defining the droplet contour at these points. The resulting contour is shown in Figure 4.11c.

To determine the droplet volume, the detected region is divided into a number of horizontal slices, each with the height of one pixel. Assuming that each slice is radially symmetric when viewed from above, the horizontal distance corresponds to the diameter of the respective droplet slice. With the known dimensions of the pixels, the individual volumes of the slices are calculated and then summed up to obtain the total volume of the droplet.

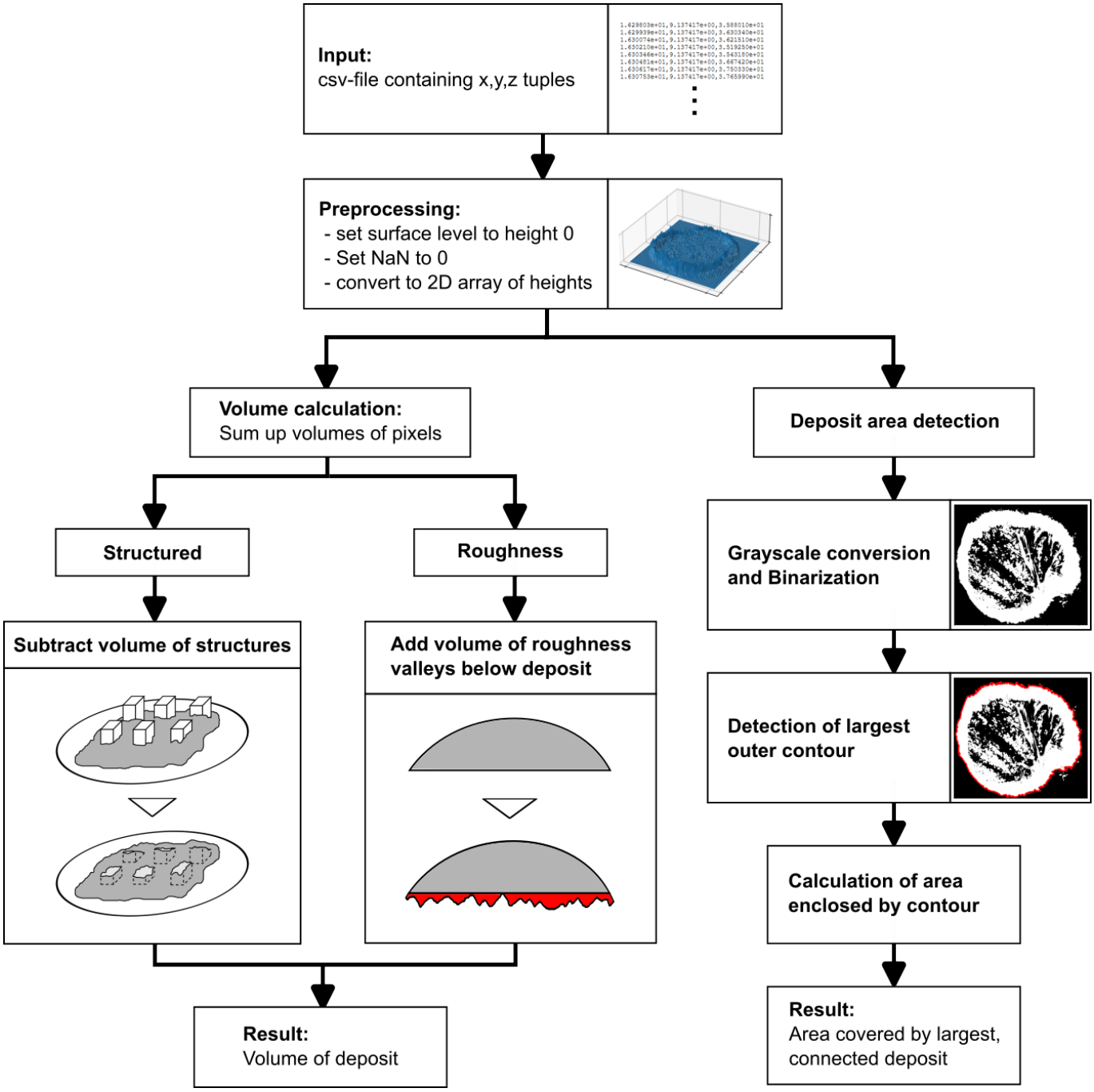

Figure 4.10.: Diagram showing the procedure for processing the confocal data to determine the deposit volume and covered surface area

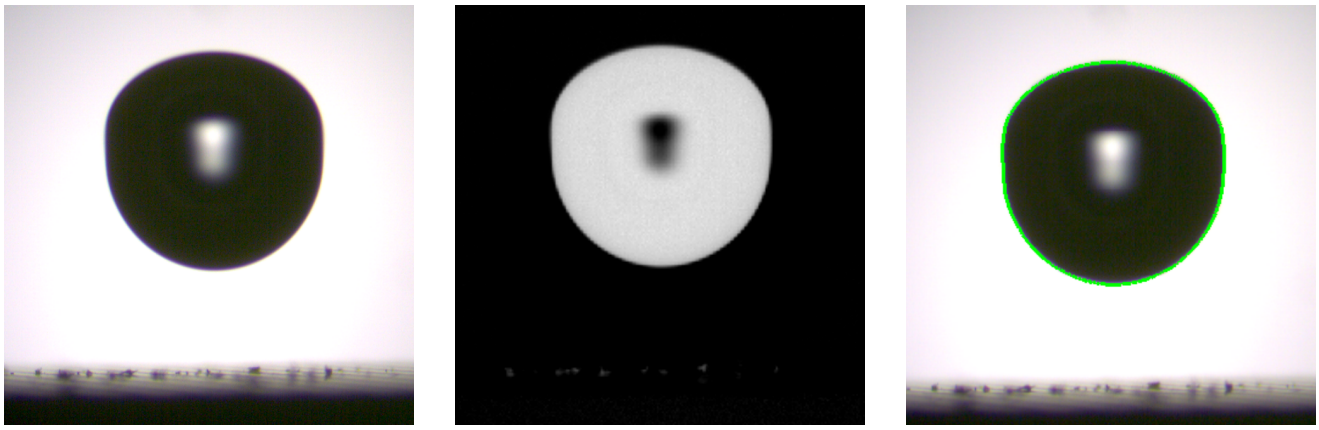

(a) Raw image of falling droplet **(b)** Difference to background image **(c)** Detected droplet contour

Figure 4.11.: Processing of camera images to determine the droplet volume

4.6. Measurement uncertainties

Where applicable, measurement uncertainty is calculated according to the *Guide to the Expression of Uncertainty in Measurement (GUM)* [11]. The standard uncertainty u for a mean value of n measurements is given by:

$$u = \sqrt{\frac{s^2}{n}} \tag{4.1}$$

where s^2 is the variance of the observations, calculated using Equation (5.2). To obtain the combined standard uncertainty u_{comb}, the individual standard uncertainty of each measurement u_{meas} must also be considered. This is typically obtained from manufacturer specifications, such as a calibration certificate. The combined uncertainty is then the square root of the sum of the squared uncertainties:

$$u_{\text{comb}} = \sqrt{u^2 + u_{\text{meas}}^2}. \tag{4.2}$$

Finally, the combined uncertainty is multiplied by a coverage factor of 2 to obtain the expanded uncertainty:

$$U = 2 \cdot u_{\text{comb}}. \tag{4.3}$$

This defines an interval $I = y \pm U$ around the measured value y within which the true value is expected to lie 95 % of the time. The coverage factor of 2 is derived from the properties of the normal distribution, where approximately 95 % of the data lies within 1.96 standard deviations of the mean. For simplicity and practicality, this value is often rounded up to 2, providing a slightly more conservative estimate for the expanded uncertainty. Additional information on this is provided in Section 5.1.

Deposit mass

For deposit mass, u is calculated from the variance of the repeated measurements for each substrate. Since the deposit mass is determined as the difference between the substrate mass before and after the experiment,

two separate uncertainties need to be considered: u_1 for the empty substrate and u_2 for the deposit-covered substrate. To conservatively estimate the maximum error, the maximum uncertainties from all measurements $u_{\text{max},1}$ and $u_{\text{max},2}$ are used.

Since no individual measurement accuracy is provided, u_{meas} is calculated from the readability of the scale, according to [11]:

$$u_{\text{meas}} = \frac{\text{Scale readability}}{\sqrt{12}} \tag{4.4}$$

The combined uncertainty is then calculated as follows:

$$u_{\text{max},1} = 1.6 \cdot 10^{-5}\,\text{g} \tag{4.5}$$
$$u_{\text{max},2} = 1.2 \cdot 10^{-5}\,\text{g} \tag{4.6}$$
$$u_{\text{meas}} = 8.6 \cdot 10^{-6}\,\text{g} \tag{4.7}$$
$$u_{\text{comb,max}} = \sqrt{u_{\text{max},1}^2 + u_{\text{max},2}^2 + u_{\text{meas}}^2} \tag{4.8}$$

Multiplying by the coverage factor 2 results in an expanded uncertainty for deposit mass of $U_{\text{m,max}} = 4.09 \cdot 10^{-5}\,\text{g} = 0.04\,\text{mg}$.

Contact angle

The measurement uncertainty of contact angles is predominantly affected by the evaporation of the droplets, which results in decreasing angles over the measurement period. Figure 4.12 shows a typical progression of the measured mean between the left and right side contact angle $\bar{\theta}$. During the first 100 measurements, corresponding to 12.5 s, the angle decreases by around 0.5°. The base diameter d remains constant, indicating that the contact line is pinned. Since the final contact angle value is defined as the mean over these first 100 measurements, the variance and the standard uncertainty u are also determined using this entire sequence.

The individual standard uncertainty of each measurement u_{meas} is calculated from the maximum deviation δ_{max}, provided in the calibration certificate as ±0.09°. According to [11], this corresponds to a rectangular distribution, where any measurement value within the range $[y - 0.09°, y + 0.09°]$ is equally likely to occur. The corresponding standard uncertainty is calculated as:

$$u_{\text{meas}} = \frac{\delta_{\text{max}}}{\sqrt{3}} \tag{4.9}$$

Using the equations introduced above, the maximum expanded uncertainty is $U_{\theta,\text{max}} = 0.13°$. Note that this is only the uncertainty in determining the individual contact angle of each substrate and should not be confused with the standard deviation given in Table 4.1, which corresponds to the mean of all measurements of a particular surface coating.

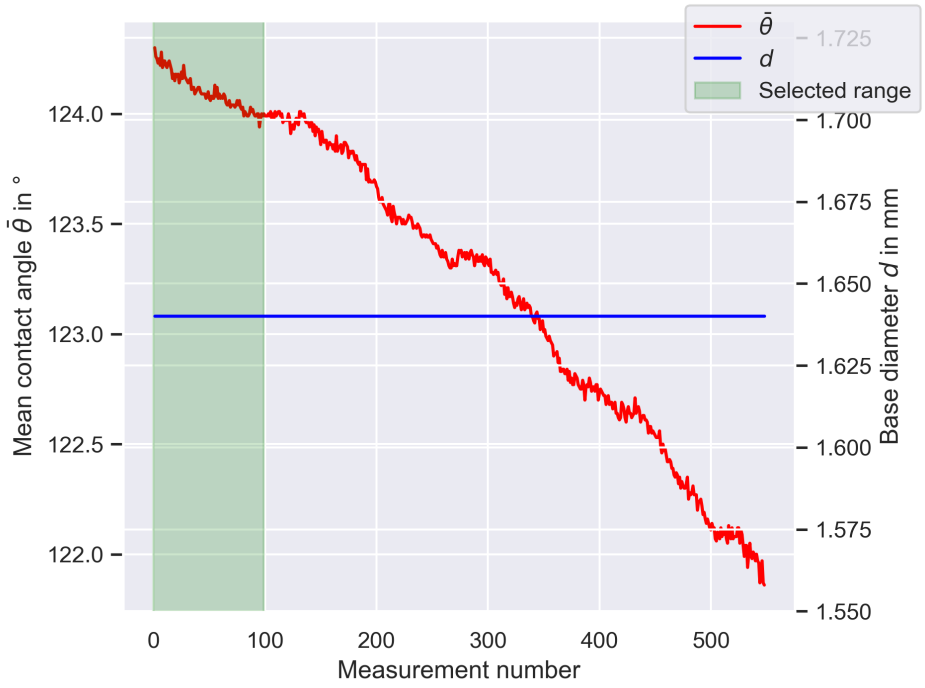

Figure 4.12.: Progression of the mean between left and right contact angle $\bar{\theta}$ over the duration of measurement due to evaporation. The sequence highlighted in green is used to determine the final value and the measurement uncertainty.

Surface temperature T_{wall}

Since the surface temperature is used as a single value and not as a mean over multiple measurements, the standard uncertainty u can not be determined. However, another error must be considered: the temperature deviation ΔT_{surf} between the measuring tip of the thermocouple and the substrate surface, where T_{wall} is defined. This deviation can be calculated by assuming one-dimensional heat conduction. The thermal conductivity of the substrate material AW-5083 is $\lambda_{\text{sub}} = 100\,\text{W}\,\text{m}^{-1}\,\text{K}^{-1}$. The average power supplied via the combined heating cartridges in the stationary case is $P_{\text{htr}} = 70\,\text{W}$. Given the distance between the sensor tip and the surface $\zeta_{\text{surf}} = 0.5\,\text{mm}$ and the substrate radius $r_{\text{sub}} = 11\,\text{mm}$, the temperature deviation is calculated using the following formula:

$$\Delta T_{\text{surf}} = \frac{P_{\text{htr}} \cdot \zeta_{\text{surf}}}{\lambda_{\text{sub}} \cdot \pi \cdot r_{\text{sub}}^2} \tag{4.10}$$

This results in a calculated temperature deviation of 0.92 °C in the stationary case. Relative to the target temperature, the error is less than 1 %. Consequently, the temperature of the substrate surface T_{wall} is determined with a very good approximation. However, under the influence of the evaporating droplet or during the heating phase, this deviation can temporarily increase.

ΔT_{surf} is combined with the individual standard uncertainty u_{meas}, derived from the maximum deviation of the tolerance class 1 (1.5 °C) and Equation (4.9), to calculate u_{comb} analogous to Equation (4.2). The final expanded uncertainty for measuring the wall temperature is $U_{\text{T}} = 1.26\,°\text{C}$.

CHAPTER 5

Modeling of Experimental Data

The first part of this chapter introduces the foundations of the employed statistical methods. This is followed by a detailed presentation on the modeling of the measured deposit results, including the selection, refinement, and evaluation of the models.

5.1. Statistical foundations

The fundamental statistical measures for describing a distribution, as well as the general principles of hypothesis testing, are presented below. These are necessary to test the significance of the effects estimated by the modeling procedure, ensuring that they are not products of measurement noise.

5.1.1. Key measures and confidence interval

As with any other experimental measurements, results from measuring the deposit formation process are subject to scatter caused by measurement noise (see Section 4.6) and other external influences. In many cases, this variability in measurement values can be well-described by a normal distribution with the expected value μ and the standard deviation σ. This distribution describes the probability of a certain measured value occurring for the respective process. A set of measurements y_j of the process can be viewed as a sample drawn from this underlying distribution. With the sample size n, one can calculate the sample mean $\bar{y}$, the variance s^2, and the standard deviation s of the sample as follows:

$$\bar{y} = \frac{1}{n} \sum_{j=1}^{n} y_j \tag{5.1}$$

$$s^2 = \frac{1}{n-1} \sum_{j=1}^{n} (y_j - \bar{y})^2 \tag{5.2}$$

$$s = \sqrt{s^2} = \sqrt{\frac{1}{n-1} \sum_{j=1}^{n} (y_j - \bar{y})^2}. \tag{5.3}$$

The mean value of the sample $\bar{y}$ serves as an estimate for the unknown expected value μ of the true distribution of measured values. However, because the sample consists of random values drawn from the underlying normal distribution, the sample mean is not guaranteed to equal the true expected value. Consequently, μ can only be determined with some degree of uncertainty from a single, finite sample. This uncertainty is quantified by an interval around the sample mean $\bar{y}$, which contains the expected value μ of the true distribution in $(1-\alpha)$ of all hypothetical samples. This interval is known as the confidence interval, and a common choice for the confidence level $(1-\alpha)$ is 0.95.

The confidence interval is determined using the standard error *SE*, which represents the variation of all sample means around the true mean μ of the population (the set of all possible measurements). As the standard error is unknown for the population, it is estimated using the standard deviation of the sample:

$$SE = \frac{s}{\sqrt{n}}. \tag{5.4}$$

The confidence interval for an experimentally collected sample mean can then be expressed as

$$\left[\bar{y} - z \cdot SE,\ \bar{y} + z \cdot SE\right]. \tag{5.5}$$

The z-Score z is determined from a standard normal distribution table based on the desired confidence level $(1-\alpha)$. For example, if the desired confidence level (the fraction of samples and their respective confidence intervals that include the true mean μ) is $(1-\alpha) = 0.95$, the corresponding z-Score is $z = 1.96$.

As an example, determining the mass m_{dep} of deposits in several measurements n under constant conditions allows the calculation of the sample mean value $\bar{m}_{\text{dep}}$ and the corresponding standard deviation $s_{\text{dep},m}$. With the confidence level set at $(1-\alpha) = 0.95$, the true mean value of the deposit mass will lie within the interval $\left[\bar{m}_{\text{dep}} - 1.96 \cdot s_{\text{dep},m}/\sqrt{n},\ \bar{m}_{\text{dep}} + 1.96 \cdot s_{\text{dep},m}/\sqrt{n}\right]$ for 95 % of all measurement samples collected in this manner. [25, 44]

5.1.2. Hypothesis testing

The scatter in measurement results and the inherent uncertainty in determining mean values are critical when assessing whether the mean deposit mass varies for different factor settings. If there is significant scatter in the measured values or if the sample size is small, observed differences between mean values might be coincidental and not caused by the independent variables. A related problem is determining whether a coefficient β_i in a regression model (see Section 5.2) is significantly different from zero, which would suggest that the associated independent variable x_i affects the target variable y. A small coefficient might only be different from zero due to measurement noise, rather than indicating an actual effect.

To address these problems, confidence intervals can be calculated alongside the coefficients, similar to the example presented earlier. The calculation of confidence intervals for model parameters relies on the variance of the residuals, which are the deviations of measured values from the values predicted by the model. Calculating a confidence interval for a model parameter provides the range of values that is likely to contain the true, unknown coefficient value. If zero is not included in this confidence interval, it can be concluded with sufficient certainty that the coefficient is different from zero, indicating that the independent variable has an impact on y.

Another widely used and fundamentally related approach is hypothesis testing. This approach begins by defining the null hypothesis, which states that a (mean) value (or the difference between two values) is exactly zero. The goal of hypothesis testing is to refute this null hypothesis with sufficient certainty. In regression analysis, the Student's t-test is commonly used for this purpose. First, the t-value t_i is calculated from the estimated coefficient value $\hat{\beta}_i$ and the corresponding standard error:

$$t_i = \frac{\hat{\beta}_i}{SE_{\beta,i}}. \tag{5.6}$$

The standard error $SE_{\beta,i}$ measures how much the coefficient is expected to vary due to random sampling error. Assuming the null hypothesis is true, t-values calculated in this way follow the Student's t-distribution, a probability distribution with an expected value of zero and a variance that depends on the sample size. Using this distribution, the probability that a t-value at least as extreme (i.e., as far away from zero) as the calculated one occurs can be determined. This probability is referred to as the p-value p and indicates the likelihood that the observed regression coefficient $\hat{\beta}_i$ would occur if the null hypothesis were true. If this probability is less than or equal to a predefined significance level α, the null hypothesis can be rejected with sufficient certainty. The coefficient is then said to be significantly different from zero, indicating that the corresponding independent variable x_i has a significant impact on the dependent variable y. Typical values for α are 0.05, 0.1, or 0.01.

At this point, it is important to note that, in addition to the t-test for individual coefficients, one can also perform an Overall-F-test. This test evaluates whether at least one of the independent variables in the model provides a significant explanatory contribution to the dependent variable. It calculates a different test statistic, the F-value, which follows its own distribution, but the underlying principle remains the same. For further information on statistical testing and other test procedures, please refer to the literature [44, 76].

In summary, a regression coefficient β_i with $p_{\beta,i} \leq \alpha$ indicates a significant relationship between the associated independent variable x_i and the dependent variable y, suggesting that the independent variable helps explain the variance of the dependent variable. However, it should be emphasized that a significant result does not necessarily mean that the effect of the independent variable is practically relevant. The practical relevance of the effect is determined by the value of the coefficient itself and its associated confidence interval. Conversely, a non-significant p-value does not mean that the independent variable has no influence. It is possible that the sample size was insufficient to detect the actual relationship due to experimental noise. Therefore, all coefficients and independent variables that potentially influence the deposit formation must be discussed and critically assessed. Statistical significance is only one step in this process.

5.2. Linear regression modeling

The data collection of deposit variables is used to build statistical models. These models not only identify and quantify the relevant effects and interactions but also enhance the understanding of the fundamental properties of the deposit formation process. Additionally, the models allow predictions about deposit formation for unmeasured settings of the independent variables (in this context also called predictors), provided these settings are within the parameter space covered by the measured data.

5.2.1. Model choice

Selecting the basic model to describe and analyze the data is primarily determined by the study's aim and the scaling of the collected data. The model should:

1. Identify relevant predictors for the target variable.
2. Quantify the effect of these predictors.
3. Provide good interpretability to gain fundamental insight into the deposit formation process.
4. Predict target responses for unknown data points within the covered parameter space.
5. Be well suited for independent and target variables on a continuous numerical scale.

While several models could satisfy at least the first three requirements, the latter criteria suggest that linear regression is the most appropriate choice. This is mainly due to the nature of the data, as all variables lie on a continuous scale and can theoretically take on any positive value within physical limits. In contrast, methods such as Analysis of Variance (ANOVA) are ideal for assessing continuous responses based on categorical predictors, while logistic regression is used when the target variable is categorical. [57, 87]

An alternative to these statistical approaches are deep learning algorithms, such as neural networks. These models are very versatile and can represent complex and non-linear relationships. However, given the small size of the database, such a model would be prone to overfitting to the data and the measurement errors it contains. Another option would be to use non-linear approaches, such as polynomial regression or machine learning algorithms like decision trees. However, since the correlations can be well represented linearly (see Section 5.3.4), these alternative methods are not explored further here. [67]

5.2.2. Fundamentals of linear regression

A linear regression model mathematically describes how the target variable y changes in response to the independent variables, or predictors, x_i. When only one independent variable is considered, it is referred to as simple linear regression. In contrast, when several independent variables are included, the regression is multivariate. In its basic form, this model corresponds to a linear function that fits a straight line through the measured data points:

$$\begin{aligned} y = f(x) &= \sum_{i=1}^{k} \beta_i x_i + \beta_0 \\ &= \sum_{i=0}^{k} \beta_i x_i = \vec{x}^{\mathrm{T}} \vec{\beta}, \text{ mit } x_0 = 1. \end{aligned} \tag{5.7}$$

Here, β_i are the model parameters (or coefficients) to be estimated, which describe the influence of the respective i-th independent variable x_i. Together, they specify the intercept and the slope of the function. To

determine $\vec{\beta}$, the deviations of the model predictions $\hat{y}_j$ from the observed data points y_j must be minimized globally. These deviations are characterized by the squared differences between the observed values and the model responses, known as squared residuals. The function to be minimized with respect to the parameters $\vec{\beta}$ is referred to as the sum of squared errors *SSE* and is derived from Equation (5.7) as follows:

$$\begin{aligned} SSE\left(\vec{\beta}\right) &= \sum_{j=0}^{n}\left(y_j - \vec{x}_j^{\mathrm{T}}\vec{\beta}\right)^2 \\ &= \left(\vec{y} - \mathbf{X}\vec{\beta}\right)^{\mathrm{T}}\left(\vec{y} - \mathbf{X}\vec{\beta}\right). \end{aligned} \tag{5.8}$$

Here, n corresponds to the number of observations or measurements of the target variable y with the corresponding settings of $\vec{x}$. To determine the vector of optimal model coefficients $\widehat{\vec{\beta}}$, the sum of squared errors is differentiated with respect to $\vec{\beta}$ and set to zero:

$$\frac{\partial SSE\left(\vec{\beta}\right)}{\partial\vec{\beta}} = -2\mathbf{X}^{\mathrm{T}}\left(\vec{y} - \mathbf{X}\vec{\beta}\right) = 0. \tag{5.9}$$

This ultimately results in the analytically solvable problem:

$$\widehat{\vec{\beta}} = \left(\mathbf{X}^{\mathrm{T}}\mathbf{X}\right)^{-1}\mathbf{X}^{\mathrm{T}}\vec{y}. \tag{5.10}$$

By providing the required vector of coefficients $\widehat{\vec{\beta}}$, the solution of Equation (5.10) yields the missing part for formulating the regression model, which can predict the model response $\hat{y}$ for any set of input data $\vec{x}^{\mathrm{T}}$:

$$\hat{y} = \vec{x}^{\mathrm{T}}\widehat{\vec{\beta}}. \tag{5.11}$$

Typically, the model response $\hat{y}$ will not exactly match the measured value y associated with the respective settings of $\vec{x}$. These remaining deviations between observed and predicted value, $\epsilon_j = y_j - \hat{y}_j$, are referred to as residuals. To compare how well a model describes a given data set, a measure based on these residuals is required, known as the *goodness of fit*.

5.2.3. Model evaluation

Coefficient of determination

In linear regression, the goodness of fit is measured by the coefficient of determination R^2. This coefficient is calculated using scatter decomposition, which quantifies how much of the variance in the target variable can be explained by the model. The total variance, referred to as the total sum of squares *SST*, is the sum of the squared deviations of the individual data points y_j from the corresponding mean of the data $\bar{y}$. The variance

explained by the model *SSM* is given by the sum of the squared deviations of the model predictions from the mean value of the data:

$$SST = \sum_{j=1}^{n} (y_j - \bar{y})^2 \tag{5.12}$$

$$SSM = \sum_{j=1}^{n} \left(\hat{y}_j - \bar{y}\right)^2. \tag{5.13}$$

Dividing the explained variance *SSM* by the total variance *SST* gives the proportion of the scatter in the data that is accounted for by the model, resulting in the value of R^2. This value will be 1 if the model explains the scatter perfectly, and 0 if the model offers no improvement over the pure mean of the data:

$$R^2 = \frac{SSM}{SST} = \frac{\sum_{j=1}^{n} \left(\hat{y}_j - \bar{y}\right)^2}{\sum_{j=1}^{n} (y_j - \bar{y})^2} \tag{5.14}$$

$$= 1 - \frac{SSE}{SST}. \tag{5.15}$$

Equation (5.15) follows from the fact that *SST* is the sum of *SSM*, the explained deviations, and the sum of squared errors *SSE*, introduced in Section 5.2:

$$SST = SSM + SSE. \tag{5.16}$$

In the case of multivariate regression, R^2 is only of limited use for comparing different models, especially when the number of independent variables changes. The reason is that the calculation of the coefficient of determination tends to produce higher R^2 values as the number of variables increases. Therefore, the adjusted coefficient of determination R^2_{adj} is often used, which penalizes the addition of independent variables to the model. Instead of using the sums of squares, this metric is calculated using the mean squares of the errors (*MSE*) and the total deviations (*MST*). These can be derived from the sums of squares by dividing by the respective degrees of freedom:

$$\begin{aligned} R^2_{\text{adj}} &= 1 - \frac{MSE}{MST} = 1 - \frac{SSE}{SST}\frac{n-1}{n-k} \\ &= 1 - \frac{n-1}{n-p}\left(1 - R^2\right). \end{aligned} \tag{5.17}$$

Cross validation

In addition to the coefficient of determination, which primarily describes the fit of the model to the available data, it is crucial to evaluate how well a model can predict unknown data points. An overly simplistic model may fail to capture the underlying relationship between independent and dependent variables, such as using a linear model for a non-linear relationship. Conversely, unnecessarily complex models tend to replicate the random scatter and measurement errors of the input data. This can lead to incorrect predictions for previously unknown data points (i.e., data not used for training), a phenomenon known as overfitting. The complexity of a model depends on both the model approach (e.g., linear vs. polynomial) and the number of independent variables.

To obtain a model that closely replicates the training data while generalizing well enough to predict unknown data, potential models need to be compared regarding their predictive performance on unseen data. If a sufficiently large data set is available, the data can be split into a training set and a test set. First, the model is trained with the training set and the known target variables. The model is then used to create predictions for the observations in the test set, which are compared with the true target values. The prediction accuracy for unknown data can then be assessed by calculating metrics such as the root mean square error *RMSE* (see Equation (5.18)).

With small data sets, as in this study, splitting the data can result in the loss of relevant information, leading to poorer overall models. Instead, cross-validation is employed to imitate the data split. This is achieved by dividing the data set into K parts of approximately equal size and training the model on $K-1$ of these parts. The remaining part serves as an unknown validation sample. This process is repeated K times, each time using a different subset exclusively for validation. The average *RMSE* from these K iterations is then used to compare the predictive quality of different models. Estimation of the coefficients for the final selected model is ultimately performed using all available data, i.e., all K sets. [45, 59, 73]

Root mean square error

This measure, also abbreviated as *RMSE*, is calculated by taking the square root of the previously introduced sum of squared errors *SSE*:

$$RMSE = \sqrt{\frac{1}{n}\sum_{j=1}^{n}\left(y_j - \hat{y}_j\right)^2}. \tag{5.18}$$

By taking the square root, the error is expressed in the same unit as the target value, simplifying the assessment. Note that, in contrast to the calculation of *MSE* for R^2_{adj} in Section 5.2.3, the sum of squared errors is not divided by the degrees of freedom but by the number of data points n to determine the average error per observation.

5.2.4. Model assumptions of linear regression

To examine and describe the relationship between the dependent variable y and the independent variables x_i using linear regression, several assumptions about the nature of this relationship must be met. These assumptions are briefly outlined below.

The first assumption is the *linearity of the influence of the independent variables*. This states that the relationship between the independent and dependent variables must be linear. However, this assumption does not mean that non-linear relationships cannot be modeled. For instance, quadratic, logarithmic, or other parameter effects can be included in a linear model by transforming the independent variable accordingly:

$$y = \beta_0 + \beta_1 \log x_1. \tag{5.19}$$

The assumption of *homoscedasticity*, or constant variance of the disturbance variables, implies that the variances of all errors in the model data are constant. The errors in the measurements must not systematically increase

or decrease with increasing values of y or any x_i. If this assumption is violated, the standard errors of the regression coefficients $SE_{\beta,i}$ in Equation (5.6) would be incorrectly estimated, leading to distorted confidence intervals and unreliable hypothesis tests. Since the true errors in the data are not known, they can only be estimated from the residuals ϵ. For this reason, residual plots, which plot the residuals of the model against the predicted values $\hat{y}$, are commonly used to check for homoscedasticity. The assumption is satisfied when no patterns, such as increasing or decreasing residuals, are observed. Additionally, the assumption of homoscedasticity can be tested by a statistical test, namely the White test [154]. Here, the null hypothesis states that the variance of the residuals is constant. Consequently, obtaining p-values larger than 0.05 (for $\alpha = 0.95$) indicates, that this null hypothesis can not be refuted, which is desired in this case.

Another assumption is that the *residuals must not be correlated* with each other. This means that all residuals occur independently and result from the natural variability of the data. This assumption is often violated in time series data when successive observations are not independent. To check this assumption, one can plot all residuals in the order of data collection, i.e., the respective order of experiments. If the values are regularly scattered around zero with no discernible pattern, it can be assumed that the residuals are independent.

The last assumption is that of the *normal distribution of the residuals*. This is important for performing significance tests and estimating the confidence intervals of the regression coefficients. This assumption is tested with Q-Q plots, also known as quantile-quantile plots, in which the quantiles of the frequency distribution of the data are visually compared with the quantiles of a normal distribution. Like homoscedasticity, normality can also be tested statistically. The corresponding test is the Shapiro-Wilk test [123], which assumes normality of the residuals as null hypothesis. [45, 44, 47]

5.3. Modeling of measured data

5.3.1. Model scope

The experimental design described in Chapter 3 aims to obtain four partial models for each target variable: two for structured surfaces and two for rough surfaces, with each model representing one of the two temperature levels. This design ensures an even distribution of the independent variable settings and allows for precise descriptions of the specific behavior associated with each combination of surface type and temperature.

However, by aggregating the measurements for all temperature levels and surface types, the available data for training the models can be greatly increased. This approach allows for creating a single overall model per target variable, resulting in three models (one for each target variable) instead of twelve (three target variables $\times$ two temperatures $\times$ two surface types). With a larger dataset, these comprehensive models can provide more reliable predictions. Additionally, they are more suitable for model-based optimization of surface parameters and can be more easily extended with future measurements, such as those involving different surface types or temperatures.

For these reasons, the partial datasets are merged. Combining results for different temperatures is straightforward, as the temperature variable clearly defines the respective temperature level of the experiment. However, merging data from different surface types (rough and structured) is more complex, as it would require a generalized measure to characterize the morphological influence of any surface as a model input. It is unlikely

that a single parameter could accurately represent the surface-specific behavior, as the linear model would then only have one cross-surface parameter. Additionally, the interactions with other factors, such as the coating, could not be accurately resolved.

This is why both surface-specific variables, i.e., the roughness Ra and the surface area ratio R_A, are included in the model for every sample. For tests on structured surfaces, the roughness is set to 0, and conversely, the surface area ratio is set to 0 for rough surfaces. This approach resembles the use of *dummy variables*, which convert categorical variables into numerical input variables during modeling [45].

This method allows for separate coefficients to be determined for each independent variable, effectively ensuring that non-relevant variables, such as the respective other surface morphology, do not contribute to the model response when they are not applicable. This approach enables the model to explicitly reflect the different effects between surface types and more accurately represent individual interactions between each surface and other variables, such as temperature. Moreover, it enhances the interpretability of surface-specific and universal effects.

This procedure is complemented by including an additional dummy variable, “Surface type”, which takes the value 0 for rough surfaces and 1 for textured surfaces. Including this variable allows the model to better handle the increased data complexity resulting from the additional variables in the aggregated data set. With the additional coefficient, different baseline levels of deposit formation behavior can be determined for the two surface types. Figure 5.1 illustrates data snippets being merged with the two surface variables and their respective interactions.

5.3.2. Preprocessing

Polynomial features

In addition to the individual influence of the main variables – wall temperature, wettability/contact angle, duration, and the surface-specific morphology parameters roughness and surface area ratio – it is also necessary to investigate the non-linear behavior and possible interactions of the individual variables. As described above, this is possible using a linear model, as each of these polynomial variables is connected to the model via a constant coefficient, i.e., included linearly. Higher-order terms are not considered, as it can be assumed they do not provide additional value in explaining the target variable. The same applies to interactions, where only the two-way interactions are considered.

For the models created here, all two-way interactions were included as separate variables by multiplying the variable values of two main effects in each possible case. This excludes interactions between the two morphology features, as they would always equal to zero when multiplied, and between the surface type and the respective morphology feature. The quadratic influences of the main effects were accounted for by including the squared values as independent separate variable. During the model training process, a separate coefficient is determined for each of these additional variables.

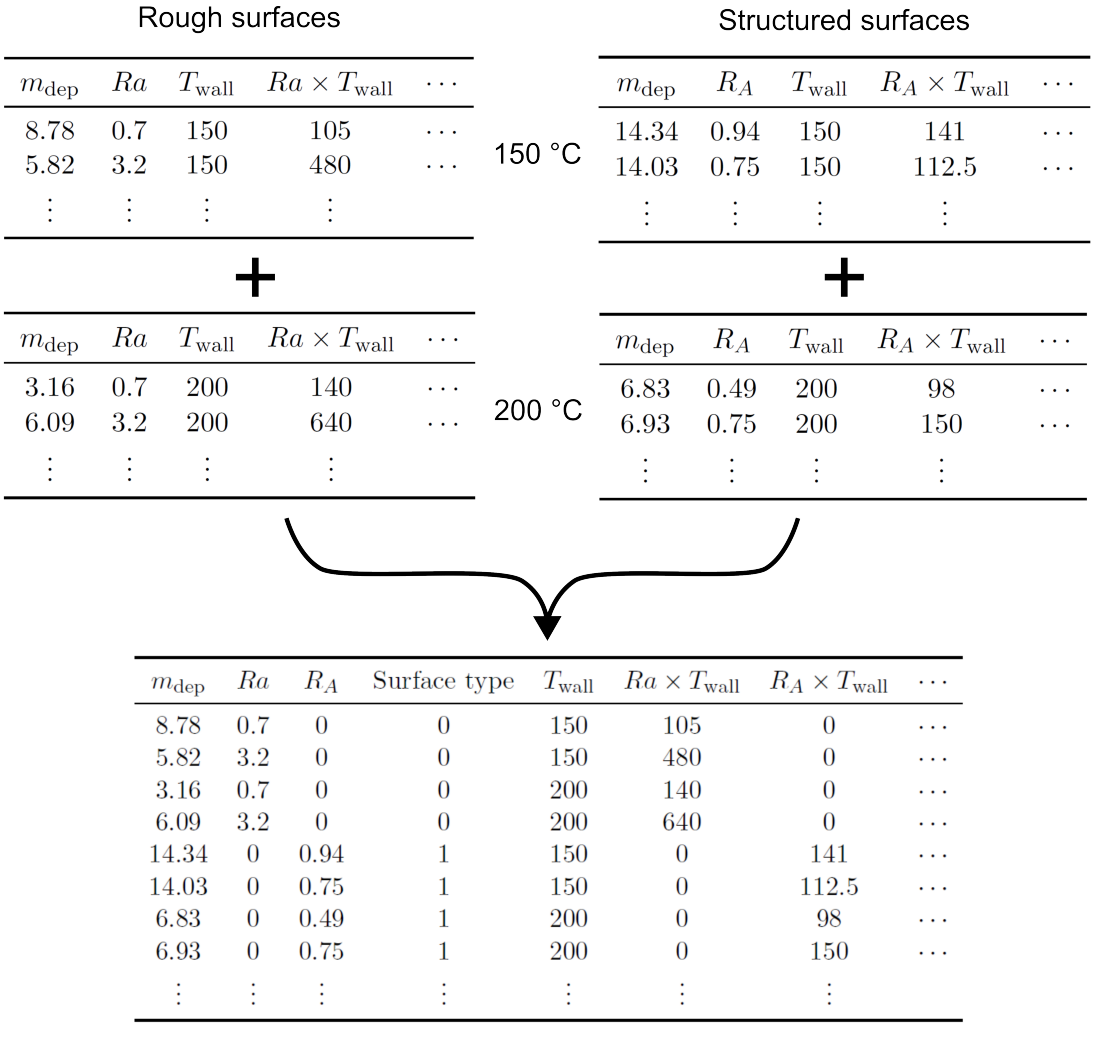

m_{dep}	Ra	T_{wall}	$Ra \times T_{\text{wall}}$	$\cdots$
8.78	0.7	150	105	$\cdots$
5.82	3.2	150	480	$\cdots$
$\vdots$	$\vdots$	$\vdots$	$\vdots$	

m_{dep}	R_A	T_{wall}	$R_A \times T_{\text{wall}}$	$\cdots$
14.34	0.94	150	141	$\cdots$
14.03	0.75	150	112.5	$\cdots$
$\vdots$	$\vdots$	$\vdots$	$\vdots$	

m_{dep}	Ra	T_{wall}	$Ra \times T_{\text{wall}}$	$\cdots$
3.16	0.7	200	140	$\cdots$
6.09	3.2	200	640	$\cdots$
$\vdots$	$\vdots$	$\vdots$	$\vdots$	

m_{dep}	R_A	T_{wall}	$R_A \times T_{\text{wall}}$	$\cdots$
6.83	0.49	200	98	$\cdots$
6.93	0.75	200	150	$\cdots$
$\vdots$	$\vdots$	$\vdots$	$\vdots$	

m_{dep}	Ra	R_A	Surface type	T_{wall}	$Ra \times T_{\text{wall}}$	$R_A \times T_{\text{wall}}$	$\cdots$
8.78	0.7	0	0	150	105	0	$\cdots$
5.82	3.2	0	0	150	480	0	$\cdots$
3.16	0.7	0	0	200	140	0	$\cdots$
6.09	3.2	0	0	200	640	0	$\cdots$
14.34	0	0.94	1	150	0	141	$\cdots$
14.03	0	0.75	1	150	0	112.5	$\cdots$
6.83	0	0.49	1	200	0	98	$\cdots$
6.93	0	0.75	1	200	0	150	$\cdots$
$\vdots$	$\vdots$	$\vdots$	$\vdots$	$\vdots$	$\vdots$	$\vdots$	

Figure 5.1.: Schematic example of the integration of the data sets at different temperatures and surface types into an overall data set to increase the available data for model training

Transformation of the target variable

As mentioned in Section 5.2.4, the independent variables of the model do not necessarily have to be linear. For example, an exponential model approach can be implemented by logarithmically transforming the dependent variable before training the model. This way, the logarithmized target variable is represented as a linear combination of the independent parameters, as shown in Equation (5.20). The subsequent equation demonstrates the resulting, back-transformed prediction $\hat{y}$ as the solution of an exponential approach.

$$\log y = \sum_{i=1}^{k} \beta_i x_i + \beta_0 \tag{5.20}$$

$$\hat{y} = e^{\sum_{i=1}^{k} \beta_i x_i + \beta_0} \tag{5.21}$$

Transformations of this kind are useful, for example, if the distribution of the input data suggests that a logarithmic representation could improve the model fit and ensure that the assumptions discussed in Section 5.2.4 are met. The former has been found in this study, as demonstrated by the distribution of the deposit area in Figure 5.2. The coefficient of determination R^2 of the final model is slightly higher with the logarithmic transformation.

However, such transformations inevitably complicate the interpretability of a model. A logarithmic transformation causes the quadratic and interaction variables to carry different meanings than in the linear case. This hinders a knowledge-based approach to selecting relevant influencing parameters during the model refinement process described in Section 5.3.3. Since one of the main objectives of this study is to gain a deeper understanding of the deposit formation process and its influences, maintaining the interpretability of the model is a high priority. Therefore, all final models are trained without transforming the target variable y.

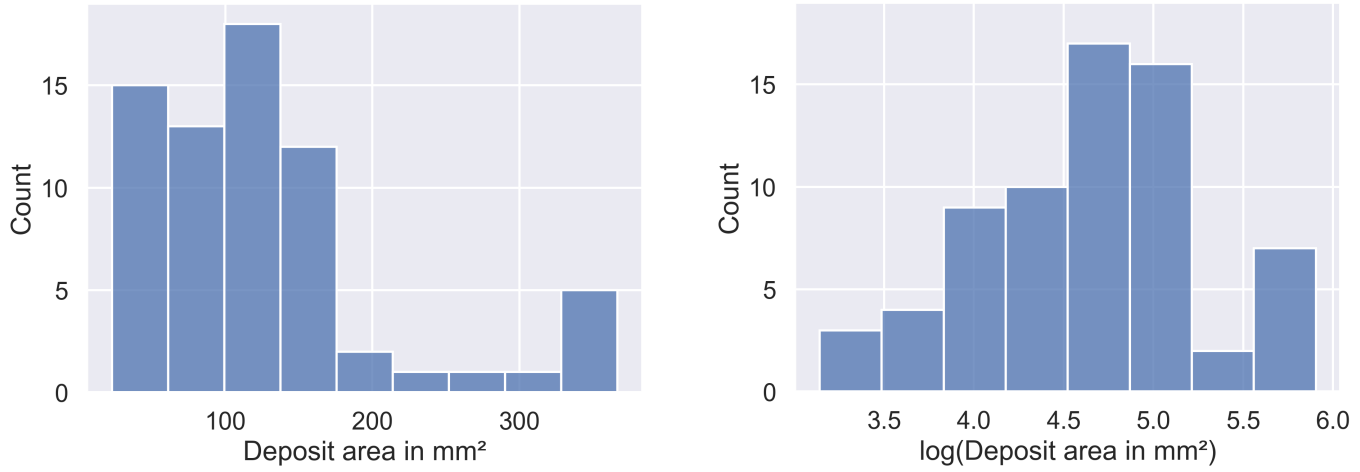

(a) Originally measured deposit area

(b) Logarithmic transformation of deposit area

Figure 5.2.: The logarithmic transformation of the dependent variable in (b) corresponds more closely to the normal distribution.

Scaling of independent variables

Before training the model, all variables are scaled in a pre-processing step to account for significantly different value ranges and to improve the model fit. Each input value $x_{i,j}$ is standardized according to the following formula:

$$x_{i,j,\text{scl}} = \frac{(x_{i,j} - \bar{x}_i)}{s_i}. \tag{5.22}$$

Here $\bar{x}_i$ denotes the mean value and s_i the standard deviation of all j values of the independent variable x_i. $x_{i,j,\text{scl}}$ is the resulting input value that is passed to the model.

5.3.3. Feature selection

This section describes the incremental refinement of the models by successively reducing individual features. Here, a feature refers to any input variable for the model, including the independent variables and their squared and interaction terms. The primary goal of this reduction is to identify the relevant factors for deposit formation and to accurately quantify the strength of their influence (represented by the respective model coefficient). Secondly, it serves to prevent possible overfitting (see Section 5.2.3).

As an alternative to the subset selection procedure described here, shrinkage methods such as ridge regression or lasso regression can also be employed. Instead of completely removing individual features from the model, these methods reduce the contributions of features by applying a penalty term, thus improving model performance and reducing overfitting. However, since manually removing irrelevant variables also enhances the interpretability of the model, such shrinkage methods are not used here. For further details on these methods, the reader is referred to the relevant literature [59, 67].

A total of four models must be individually refined: one for each target variable, with two models being created for the deposit volume (details on this are provided below). The starting point in each case is the full model, which includes all reasonably possible interactions and squared terms of the independent variables. This means that for each model, including the intercept coefficient β_0 and the surface type dummy variable, a total of 20 coefficients are initially determined.

The procedure used here is inspired by stepwise regression, particularly backward elimination. This method is often automated, with each step removing the feature from the full model that either has the greatest p-value or leads to the greatest reduction in model error when removed [45, 59]. However, this approach is subject to criticism [32, 46, 58], including risks of p-hacking, overfitting on the measurement data, and instability of the final models. P-hacking refers to the misuse of repeatedly calculating a large number of p-values, increasing the probability of randomly obtaining significant test results, although the coefficient doesn't actually reflect the underlying relationship.

To address this critique, model selection is carried out manually and guided by prior expertise on the process of deposit formation, as discussed in the final remarks in Section 5.1.2. During this feature selection, models are continuously validated through cross-validation to ensure that changes improve the predictive performance on unseen data. Feature removal ends when cross-validation indicates declining model performance or when the assumption of homoscedasticity is violated, as indicated by White's test and residual plots. Whenever

possible, normality of residuals, indicated by the Shapiro-Wilk test and Q-Q-plots, is maintained throughout the process.

Deposit area

Feature reduction is described below using the example of the model for predicting the deposit area. Appendix A.1 contains the results of all final models with the respective coefficient estimates, p-values and confidence intervals.

Figure 5.3 and Figure 5.4 show the partial regression plots for all features in the full deposit area model. Each of these plots illustrates the isolated relationship between one feature x_i and the remaining variance in the target variable A_{dep} after accounting for the effects of all other included features $\vec{x}_{-i}$. The vertical axis indicates the residuals ϵ of the target variable after it has been regressed on all features except the one under investigation. The horizontal axis indicates the residuals of the feature x_i after being regressed on all other features in the model $\vec{x}_{-i}$. This ensures that any contribution of the remaining features in explaining the variance of x_i is also eliminated, isolating the effect of x_i on A_{dep}. This effect is indicated by the slope in each plot. A positive slope suggests a positive relationship, while a negative slope suggests a negative relationship. A horizontal line indicates that the effect is close to zero and that the feature does not contribute to explaining the target variable variance.

The partial regression plots and the estimated coefficient values indicate that there is no significant interaction between the duration and several other features, such as contact angle (Figure 5.3h) or wall temperature (Figure 5.3k), for describing the deposit area. This is also apparent in Figure 5.5, where the model responses for the deposit area depending on the duration are separated by the wall temperature (a) and the contact angle (b). For each surface type, the curves progress approximately parallel. As explained in 3.1.1, this also indicates no interaction between the features. Consequently, the respective interactions of duration with wall temperature and contact angle are removed from the model first.

Next, the squared term for the duration is removed from the model. Figure 5.6 displays a slightly non-linear curve, but the maximum in the intermediate value range does not seem plausible and is likely the result of measurement error. Without additional data to confirm this trend with certainty, a linear decrease with increasing residence time is modeled by removing $\Delta\tau^2$.

Of the two remaining duration interactions with roughness and surface area ratio, the latter is considered highly insignificant based on its p-value and the nearly horizontal line in the partial regression plot in Figure 5.3j. However, the interaction between duration and roughness does contributes to explaining the variance of the deposit area, as Figure 5.3i illustrates. Since removing only one of the duration interactions with surface morphology features is considered illogical and increases the test statistic for heteroscedasticity, both interactions are kept in the model.

Likewise, the quadratic roughness and surface area ratio features have high p-values. In this case, however, the squared behavior appears plausible in the corresponding plots in Figure 5.7. The response for surface area ratio in (a) shows almost constant deposit areas for the highest structure distances (i.e., lowest surface area ratios $R_A = 1.5$ and $R_A = 3$) and an increase for the smallest distance ($R_A = 5.1$), consistent with

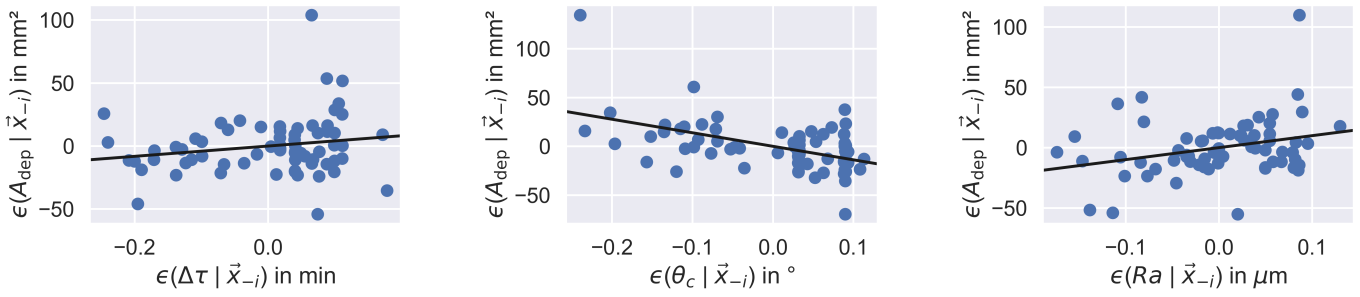

(a) Duration **(b)** Contact angle **(c)** Roughness

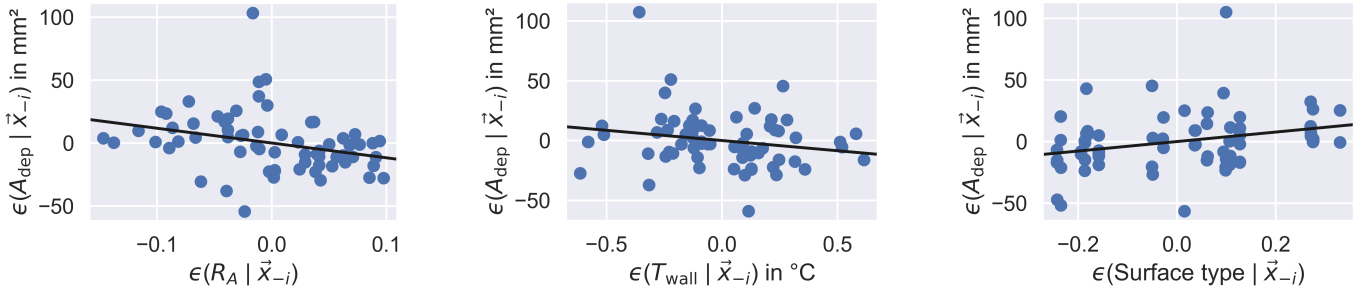

(d) Surface area ratio **(e)** Wall temperature **(f)** Surface type

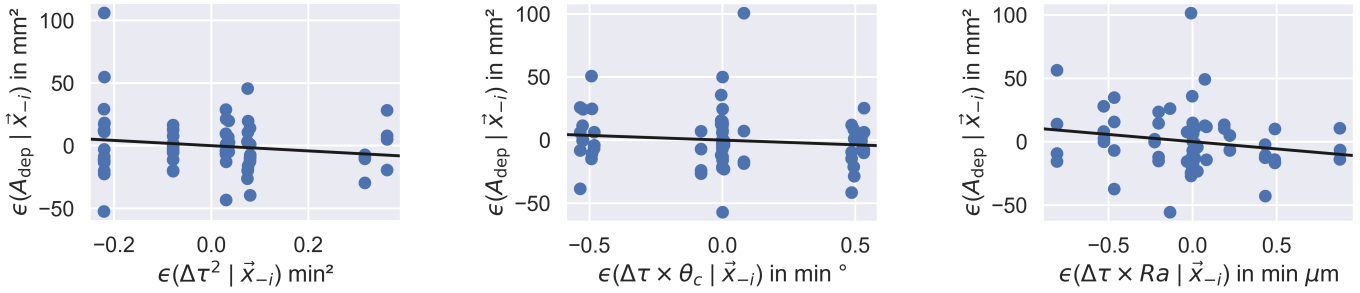

(g) Duration^2 **(h)** Duration $\times$ Contact angle **(i)** Duration $\times$ Roughness

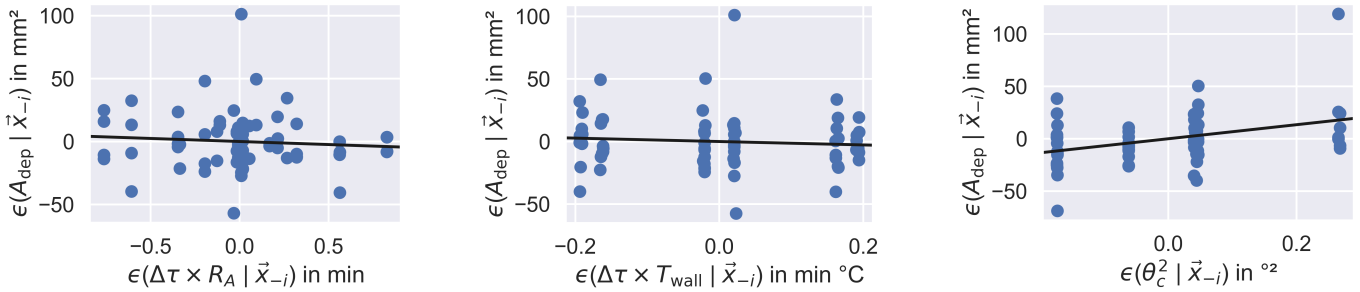

(j) Duration $\times$ Surface area ratio **(k)** Duration $\times$ Wall temperature **(l)** Contact angle^2

Figure 5.3.: Partial regression plots (1) for the features in the deposit area model. Each plot shows the isolated effect of the i-th feature on the deposit area A_{dep} after removing the impact of all other included features $\vec{x}_{-i}$.

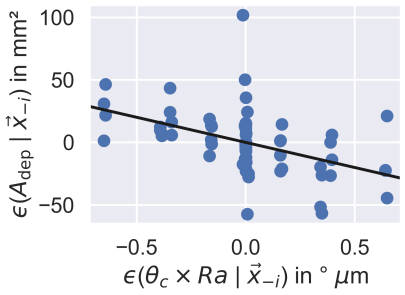

(a) Contact angle × Roughness

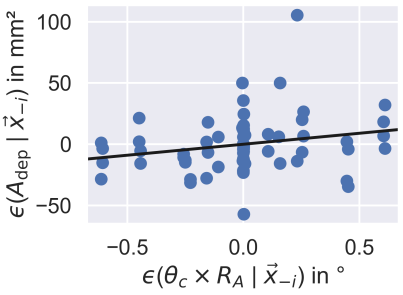

(b) Contact angle × Surface area ratio

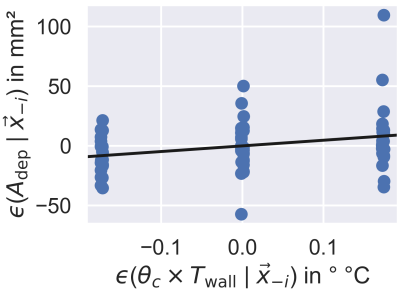

(c) Contact angle × Wall temperature

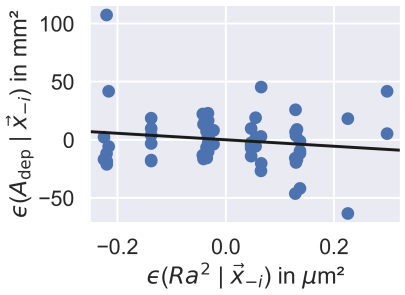

(d) Roughness^2

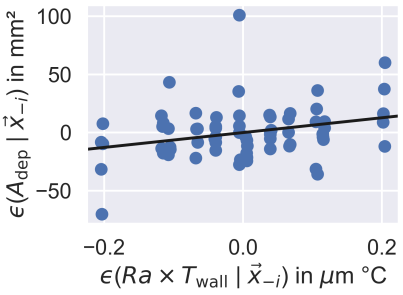

(e) Roughness × Wall temperature

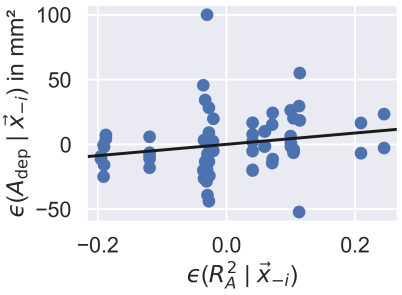

(f) $\text{Surface area ratio}^2$

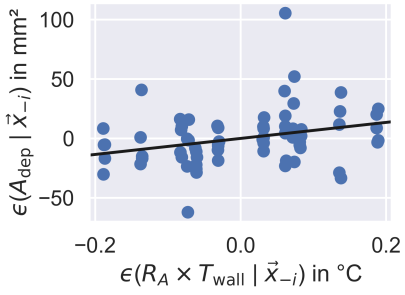

(g) Surface area ratio × Wall temperature

Figure 5.4.: Partial regression plots (2) for the features in the deposit area model. Each plot shows the isolated effect of the i-th feature on the deposit area A_{dep} after removing the impact of all other included features $\vec{x}_{-i}$.

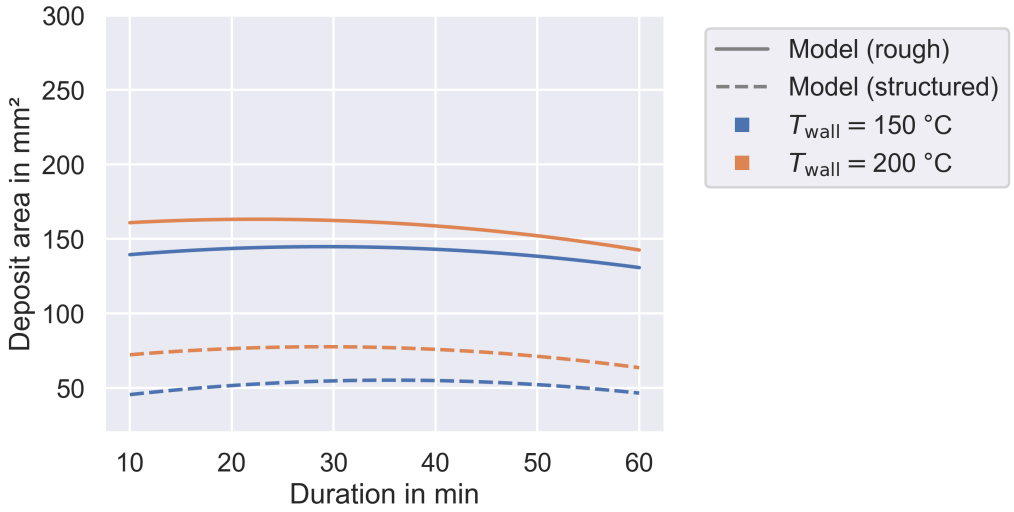

(a) Model responses separated by wall temperature

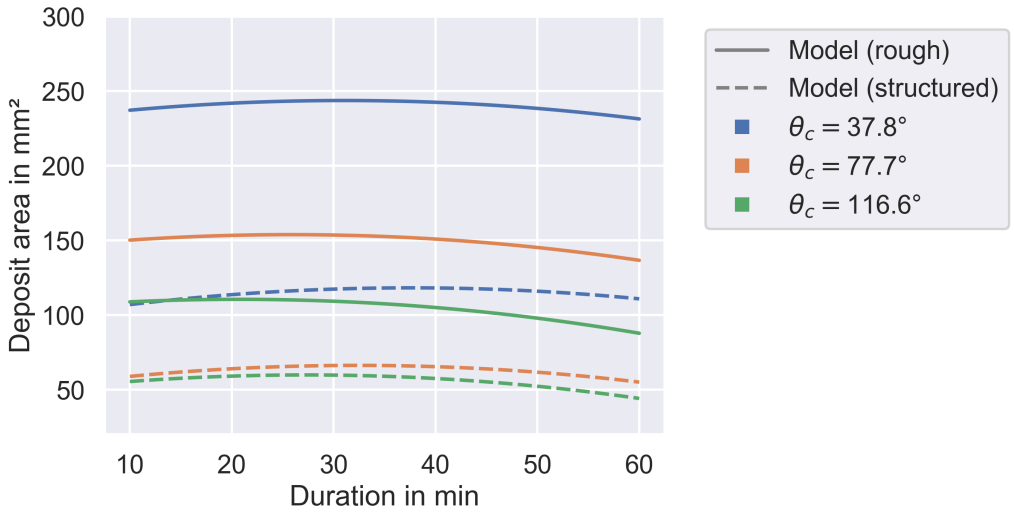

(b) Model responses separated by contact angle

Figure 5.5.: Model responses for deposit area depending on duration, indicating no significant interaction of duration with wall temperature or contact angle for each of the two surface type models

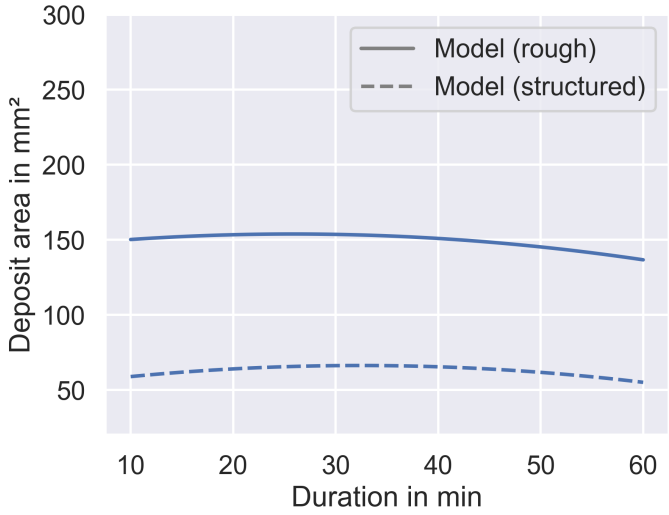

Figure 5.6.: Model response for deposit area depending on duration, exhibiting a non-plausible maximum for intermediate durations

observations in Section 6.1.1. The roughness curve (b) indicates equally plausible diminishing returns for higher roughness values. Therefore, both quadratic terms remain in the model.

Finally, the interaction between surface area ratio and contact angle is statistically insignificant, and the plots (not shown here) show minimal interaction. However, removing this interaction reduces R^2_{adj} and increases the cross-validation error, which is why this feature is not excluded either.

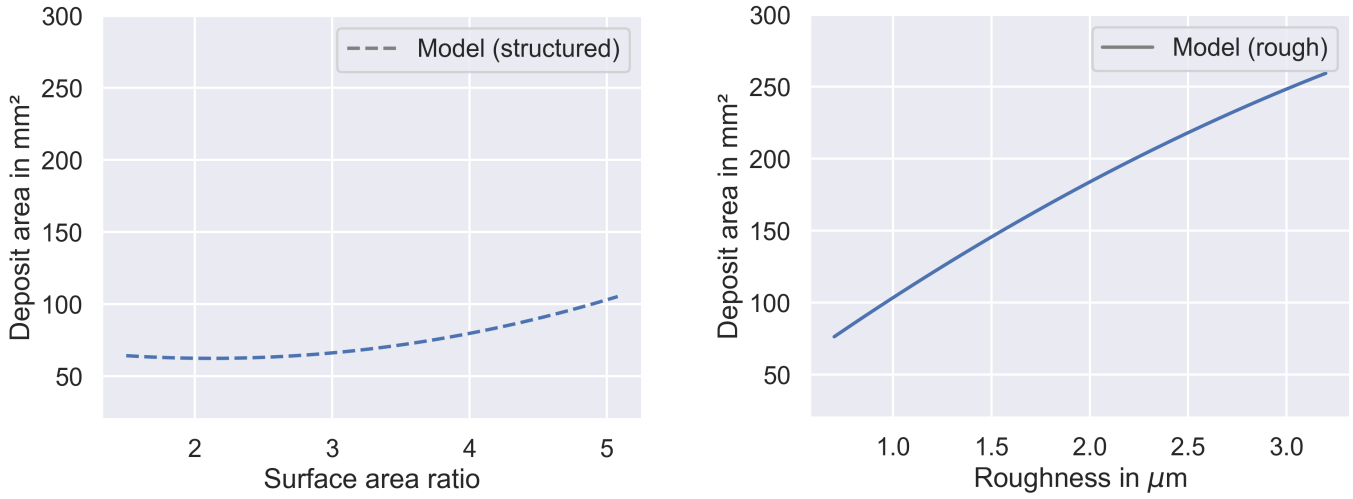

(a) Surface area ratio as independent variable

(b) Roughness as independent variable

Figure 5.7.: Model response curves for deposit area depending on surface area ratio and surface roughness, indicating plausible non-linear relationships despite high p-values

At this point, the model refinement for the deposit area is complete. This procedure is similarly repeated for each of the other target variables. Table 5.1 summarizes the feature selection for all target variables by

comparing the respective indicators before and after the reduction. After following the above procedure, the following features were removed from the individual models:

Mass: $\Delta\tau \times \theta_c$, $\Delta\tau \times R_A$, $\Delta\tau \times Ra$
Area: $\Delta\tau \times \theta_c$, $\Delta\tau \times T_{\text{wall}}$, $\Delta\tau^2$
Volume: $\theta_c \times T_{\text{wall}}$, $\theta_c \times Ra$, $\Delta\tau \times Ra$, $\Delta\tau^2$, Ra^2
Volume subset: $\Delta\tau \times \theta_c$, $\Delta\tau \times R_A$, $\Delta\tau \times Ra$, $Ra \times T_{\text{wall}}$, $\theta_c \times T_{\text{wall}}$, $\Delta\tau^2$, Ra^2

Note that the main independent variables are never removed, even if their partial regression plots or p-values indicate no effect. This is because each of these variables was deemed relevant in prior considerations, and because interpretations of the remaining interactions or squared terms would not be meaningful without the inclusion of the respective main variable.

	Mass		**Area**		**Volume**		**Volume subset**	
	full	reduced	full	reduced	full	reduced	full	reduced
R^2	0.946	0.945	0.93	0.927	0.941	0.941	0.842	0.839
R^2_{adj}	0.924	0.928	0.903	0.904	0.918	0.925	0.769	0.801
RMSE% from cv	16.32	15.68	22.50	22.15	28.10	25.25	27.84	21.29
White's test p	0.23	0.21	0.24	0.19	0.17	0.16	0.23	0.39
Shapiro-Wilks test p	0.20	0.26	0.00	0.00	0.03	0.04	0.54	0.19

Table 5.1.: Comparison of all metrics used to support feature selection for the full model and the final reduced model, "*RMSE*% from cv" refers to the *RMSE* calculated during cross validation in percent of the mean of all measured target variable values. For the deposit volume, a second model "subset" is created and refined, as explained in the following section.

The full regression formulas for predicting deposit mass $\hat{m}_{\text{dep}}$, deposit area $\hat{A}_{\text{dep}}$, and deposit volume $\hat{V}_{\text{dep}}$ are as follows:

$$\begin{aligned}\hat{m}_{\text{dep}} = {} & 0.0099 - 0.0149 \cdot \Delta\tau + 0.0078 \cdot \theta_c - 0.0059 \cdot Ra - 0.0006 \cdot R_A - 0.0045 \cdot T_{\text{wall}} \\ & - 0.0006 \cdot \text{surface type} + 0.0025 \cdot \Delta\tau^2 + 0.0110 \cdot \Delta\tau \cdot T_{\text{wall}} - 0.0007 \cdot \theta_c^2 + 0.0006 \cdot \theta_c \cdot Ra \\ & - 0.0016 \cdot \theta_c \cdot R_A - 0.0061 \cdot \theta_c \cdot T_{\text{wall}} + 0.0008 \cdot Ra^2 + 0.0028 \cdot Ra \cdot T_{\text{wall}} + 0.0001 \cdot R_A^2 \\ & + 0.0013 \cdot R_A \cdot T_{\text{wall}} \end{aligned} \tag{5.23}$$

$$\begin{aligned}\hat{A}_{\text{dep}} = {} & 127.1206 + 1.6646 \cdot \Delta\tau - 133.7038 \cdot \theta_c + 108.4374 \cdot Ra - 105.5286 \cdot R_A - 20.2283 \cdot T_{\text{wall}} \\ & + 37.1932 \cdot \text{surface type} - 11.3243 \cdot \Delta\tau \cdot Ra - 4.7603 \cdot \Delta\tau \cdot R_A + 57.9239 \cdot \theta_c^2 - 40.2426 \cdot \theta_c \cdot Ra \\ & + 17.8625 \cdot \theta_c \cdot R_A + 47.2806 \cdot \theta_c \cdot T_{\text{wall}} - 35.0966 \cdot Ra^2 + 63.5324 \cdot Ra \cdot T_{\text{wall}} + 35.1599 \cdot R_A^2 \\ & + 67.2596 \cdot R_A \cdot T_{\text{wall}} \end{aligned} \tag{5.24}$$

$$\begin{aligned}\hat{V}_{\text{dep}} = {} & 12.9368 - 6.0724 \cdot \Delta\tau - 1.9152 \cdot \theta_c - 7.0696 \cdot Ra - 20.5794 \cdot R_A - 4.8237 \cdot T_{\text{wall}} \\ & + 4.1150 \cdot \text{surface type} - 1.5365 \cdot \Delta\tau \cdot \theta_c - 1.3990 \cdot \Delta\tau \cdot R_A + 6.4147 \cdot \Delta\tau \cdot T_{\text{wall}} \\ & + 4.4508 \cdot \theta_c^2 - 4.5331 \cdot \theta_c \cdot R_A + 5.6322 \cdot Ra \cdot T_{\text{wall}} + 21.4214 \cdot R_A^2 + 8.2689 \cdot R_A \cdot T_{\text{wall}} \end{aligned} \tag{5.25}$$

$$\hat{V}_{\text{dep,subset}} = 9.4565 - 9.6699 \cdot \Delta\tau - 1.9558 \cdot \theta_c - 0.9751 \cdot Ra + 3.2454 \cdot R_A - 3.8834 \cdot T_{\text{wall}} + 1.2289 \cdot \text{surface type} + 8.8048 \cdot \Delta\tau \cdot T_{\text{wall}} + 4.0392 \cdot \theta_c^2 - 0.6667 \cdot \theta_c \cdot Ra - 4.0516 \cdot \theta_c \cdot R_A + 4.2205 \cdot R_A^2 - 4.1971 \cdot R_A \cdot T_{\text{wall}}. \quad (5.26)$$

Subset model for deposit volume

The measurement results for deposit volumes indicate an implausibly large increase in volume for the smallest structure distance/the highest surface area ratio (see Figure 5.8a). This anomaly is likely due to measurement errors caused by insufficient lighting inside the smallest structure channels. Additionally, the surface areas with deposits show distorted upper edges of the structure pillars (see Figure 5.9), which artificially inflate the detected volume. These artifacts are presumably caused by the deflection and absorption of incoming light by deposits at the base of the pillars.

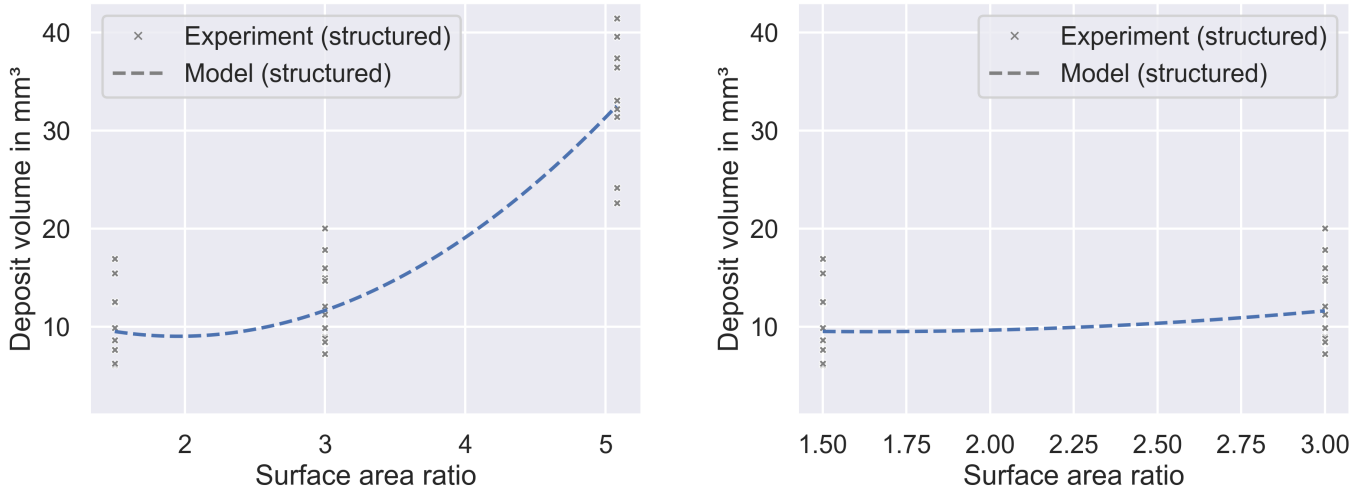

(a) Complete model for deposit volume including data with highest surface area ratio

(b) Model for deposit volume built on a subset of the data

Figure 5.8.: Comparison of responses from the complete and the subset model for deposit volume, (a) shows the large difference between the volumes for the last two values of the surface area ratio

In an overall comparison with all other results, the increase in volume with the surface area ratio remains plausible. However, the extent of this increase cannot be validated. Therefore, to accurately determine the influencing effects, a model is created using a subset of the measured data, excluding the results for the smallest structure distance. The model used for the optimization in Section 6.3, however, is based on the entire measurement data to maintain consistency in the range of variables covered by the other models.

5.3.4. Model validation

As described in Section 5.2.3, the model results must be evaluated with regard to the assumptions on which the linear regression is based. The previous section already included the results of statistical tests for the

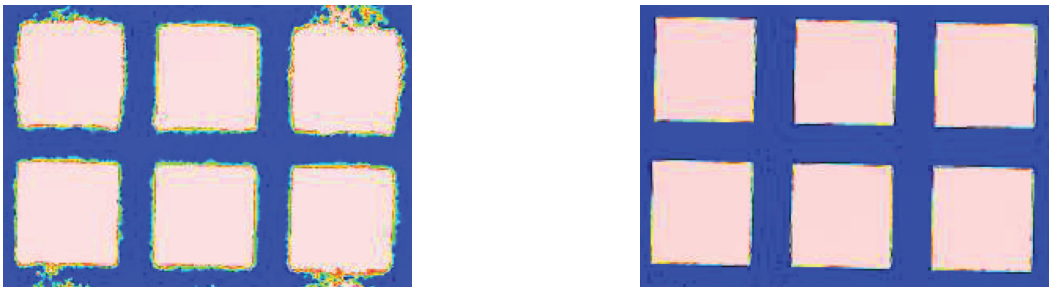

(a) Distorted pillar volume on substrate section with a flat layer of deposit between the structure

(b) Clean pillars from an uncovered section of the substrate

Figure 5.9.: Comparison of detected structure geometry from sections with and without deposits on a sample with $W = 0.2\,\mathrm{mm}$ / $R_A = 5.1\,\mathrm{mm}$

assumptions of normal distribution and homoscedasticity of the residuals. Since such tests always carry a small possibility of error, the results are supplemented here by graphical evaluations. Figure 5.10 shows all the necessary plots, using one model as an example – in this case, the deposit mass.

In Figure 5.10a, the actually measured masses are plotted against the masses predicted by the model. The alignment along the straight line shows good agreement and suggests that no additional influence is missing. Figure 5.10b is a residual plot showing the distribution of the residuals over the predicted values. Individual outliers are recognizable, but there is no noticeable trend pattern. Together with the aforementioned test results, this indicates homoscedastic variances. The third plot, Figure 5.10c, shows the residuals in the order of the corresponding experiments. This plot demonstrates that the model errors are independent of each other, as it shows no recognizable trend. Such a trend would imply that results could be estimated from knowledge of previous values. Here, too, individual outliers are apparent.

Finally, the Q-Q-plot in Figure 5.10d displays how the distribution of the residuals compares to a normal distribution by plotting the quantiles of the residuals against the quantiles of a normal distribution. As the individual residuals are positioned along the line, with the exception of a few outliers, the assumption of a normal distribution is also justified. Equivalent overviews to Figure 5.10 for the three remaining models are provided in Appendix A.2.

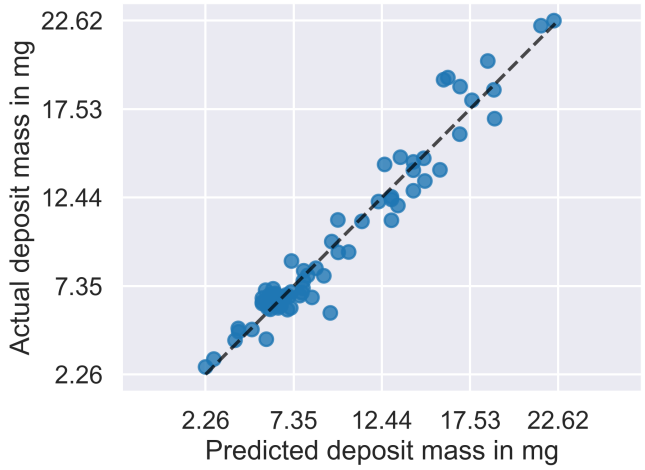

(a) Actual vs predicted values

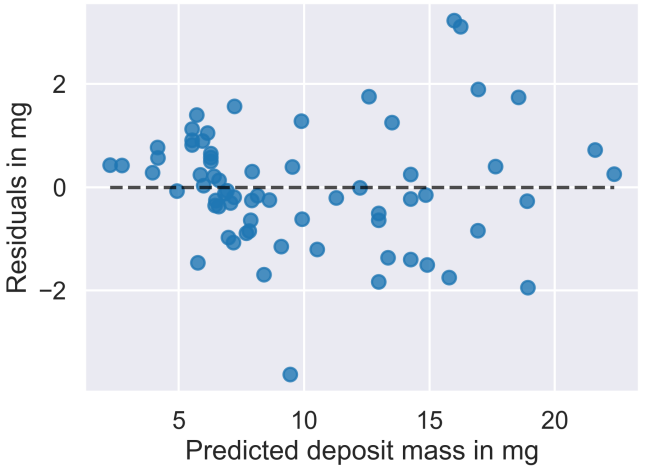

(b) Residuals vs predicted values

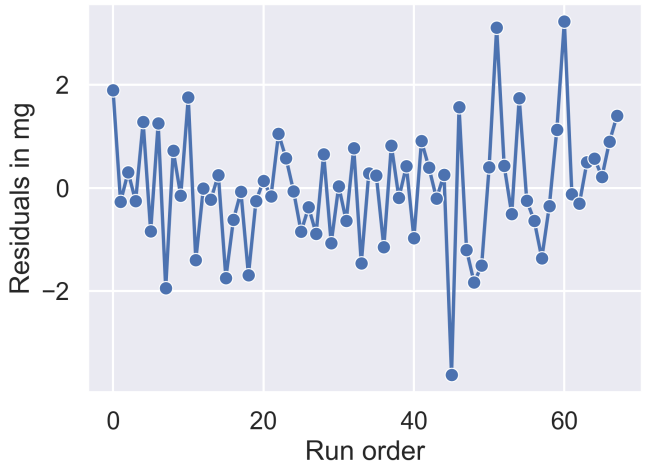

(c) Residuals vs run order of the respective experiments

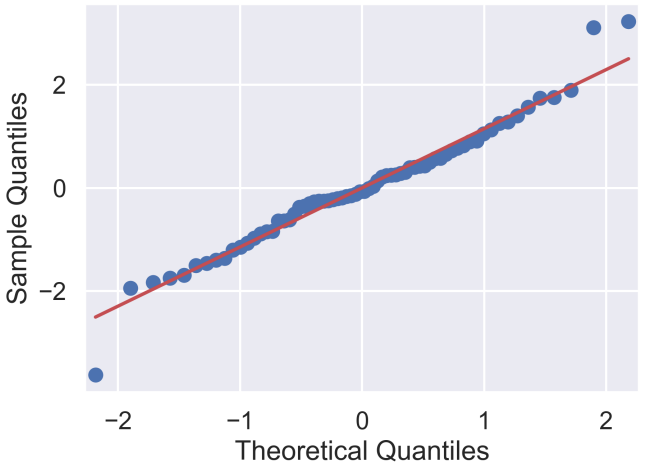

(d) Q-Q-plot illustrating how the distribution of measured values compares to a normal distribution

Figure 5.10.: Model evaluation plots of the regression model for deposit mass

CHAPTER 6

Results and Discussion

The first part of this chapter presents the observations and results of the experimental tests. This includes droplet impact and spreading on the heated substrate, the subsequent evaporation phase, and the final formation of solid deposits. The second part of the chapter discusses the measured deposit quantities and the model results.

6.1. Wetting and evaporation

The phenomena observed during wetting and evaporation are presented separately for structured and rough surfaces. It is important to note that all observations during the wetting phase are made at a constant wall temperature of 90 °C. As described in Section 4.4, the second heating phase to the target temperature begins only after five UWS droplets have been applied to the surface.

6.1.1. Structured surfaces

Wetting and spreading on structured surfaces

When considering the initial wetting of the structured surfaces by UWS, the substrates can be categorized into three groups. First, substrates where the liquid is drawn into the structure, referred to as wicking [106]. Second, substrates where the liquid accumulates on top of the structure pillars. Third, all surfaces with a structure distance of 1.5 mm, regardless of the coating. In this third group, the liquid also wets the channel grooves of the structure but not due to capillary force. Instead this is caused by the large distances between pillars, which prevent the solution from settling on them (see Figure 6.3). The surface tension is insufficient to prevent the liquid from being penetrated by the sparsely distributed pillars.

The first group, where wicking is observed, consists exclusively of hydrophilically coated surfaces with $W \leq 0.5\,\text{mm}$. The comparison in Figure 6.1 shows a slight delay in this process at the smallest structure distance $W = 0.2\,\text{mm}$. Initially, the droplet sits on the pillars for a fraction of a second before moving into the structure in several sudden steps. This indicates that wetting within the structure is not gradual but occurs

from row to row of pillars. When the channel width between the pillars exceeds 0.2 mm, the droplets no longer temporarily rest on top but immediately disappear into the structure, as illustrated in Figure 6.1b.

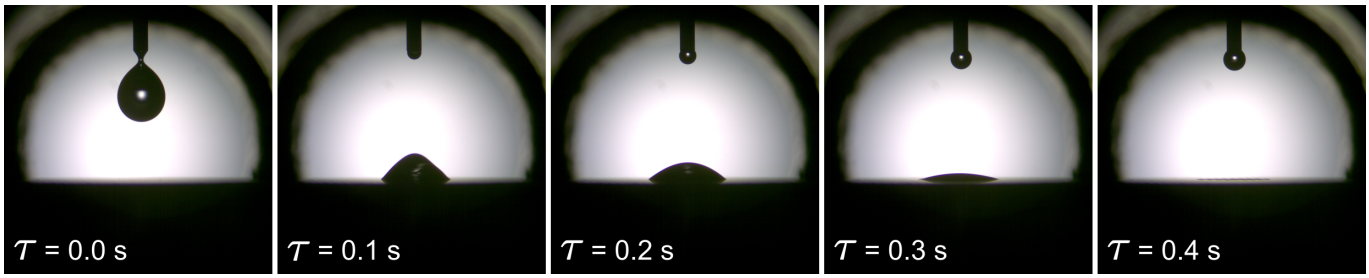

(a) Structure distance $W = 0.2\,\mathrm{mm}$

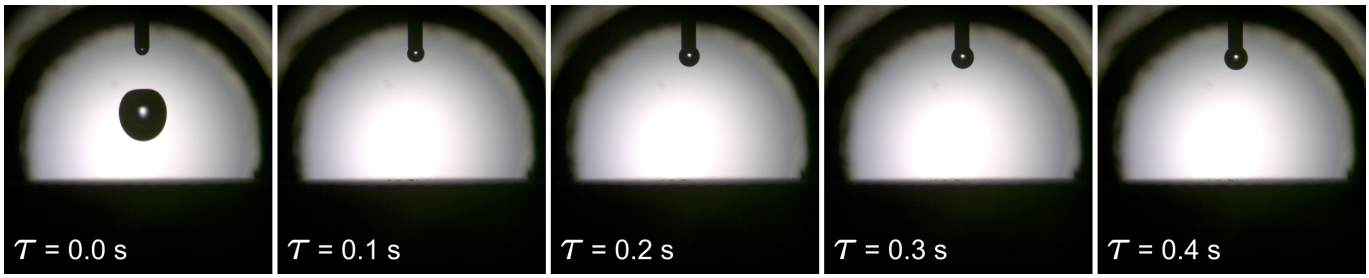

(b) Structure distance $W = 0.5\,\mathrm{mm}$

Figure 6.1.: Initial droplets on structured and hydrophilically coated surfaces being absorbed into the structure by capillary force

Non-hydrophilic surfaces with structure distances of 0.2 mm and 0.5 mm exhibit the opposite behavior. All five applied droplets accumulate on top of the pillars and remain there until the second phase of heating begins. Figure 6.2 provides an overview of this phenomenon on all uncoated and hydrophobically treated surfaces with structure distances $W \leq 0.5\,\mathrm{mm}$.

For $W = 0.2\,\mathrm{mm}$ in Figure 6.2a, it is not possible to verify whether the hydrophobic coating results in a Cassie-Baxter state, where the liquid rests on top of the pillars rather than being absorbed into the structure. The small distances inside the structure prevent a conclusive evaluation of the recordings in this respect. However, the contact angles in the right image of Figure 6.2a suggest that this is not the case, as they are not noticeably larger than those on a smooth surface with the same coating [106]. This becomes even more apparent at $W = 0.5\,\mathrm{mm}$, as shown in the right image of Figure 6.2b. For better visualization, the liquid is highlighted in red. The positioning of the pillars allows a direct view into the structure and reveals that the droplet covers the sides of the leftmost wetted pillar almost down to the bottom surface, refuting the notion of a Cassie-Baxter state.

The same image on the right in Figure 6.2b further reveals noticeable pinning of the droplet front at the pillar edges. This behavior can be observed on both uncoated and hydrophobically coated surfaces with $W \leq 0.5\,\mathrm{mm}$. Unlike on smooth surfaces, the droplets do not spread radially after impact because surface tension keeps the liquid front attached to the outermost pillar. Only when a new droplet is added does the three-phase contact line move outward abruptly, after which it remains in this new position. Figure 6.2b also shows no liquid spreading on the base surface at the bottom of the channel grooves. Similar to the stepwise

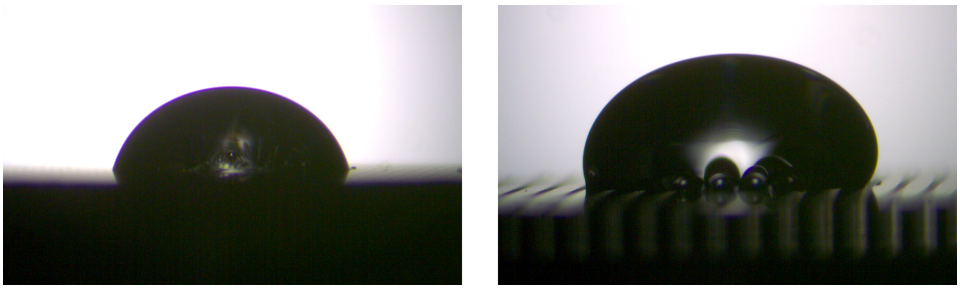

(a) $W = 0.2\,\mathrm{mm}$, left: uncoated, right: hydrophopically coated

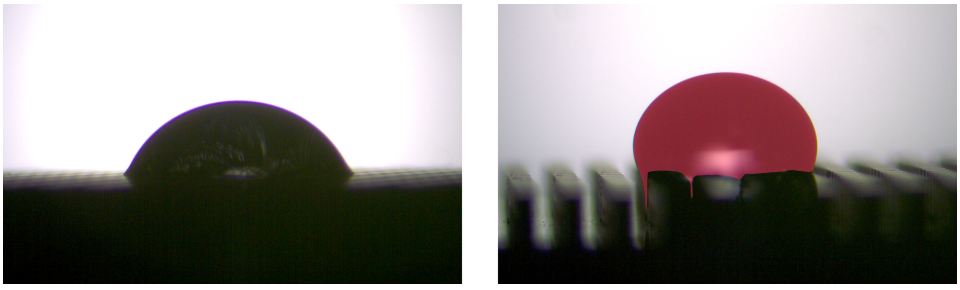

(b) $W = 0.5\,\mathrm{mm}$, left: uncoated, right: hydrophopically coated (droplet highlighted in red for better visualization)

Figure 6.2.: Non impinging droplets on structured surfaces

wicking into the hydrophilic structures, it can be concluded that the structures hinder rather than improve the wetting process.

This negative impact of the surface structure becomes even more apparent with the largest structure distances. Figure 6.3 shows the wetting by the first droplet for uncoated (a) and hydrophobically coated (b) surfaces. The largest horizontal extend of the droplet is now observed at or, in the case of the hydrophobic coating, near the base surface. Compared to smaller channel widths, where spreading is predominantly influenced by the structure, the relative influence of the coating on the wetting process now becomes more significant. This is because the surface begins to resemble a smooth surface with few, sparsely distributed pillars. However, the inhibitory effect of the pillars on droplet propagation remains evident here as well. Due to surface tension, the liquid mass adheres to each pillar, and each channel represents a new resistance to film spreading.

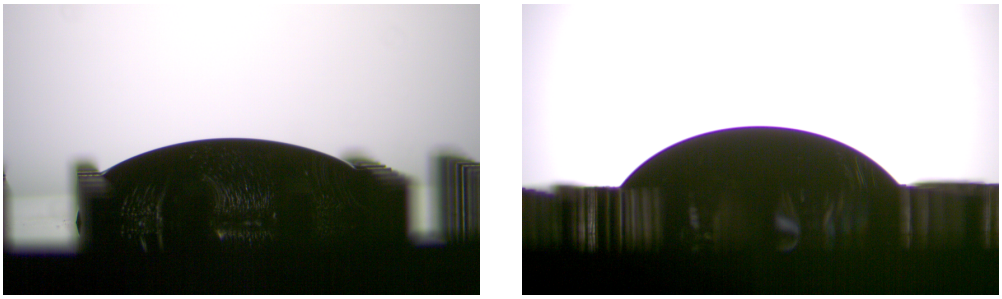

(a) Uncoated **(b)** Hydrophobically coated

Figure 6.3.: Wetting of structured surfaces with structure distance $W = 1.5\,\mathrm{mm}$

Figure 6.4 additionally illustrates that the droplet inside the structure does not primarily spread horizontally. Instead, driven by capillary force, it tends to fill the space between two already wetted pillars before moving on to the next row. This means that although the solid-liquid interface is increased compared to a smooth sample, the liquid-gas interface is now significantly reduced. This negatively affects the subsequent evaporation. Furthermore, the influence of gravity on droplet propagation is reduced due to the pillar height. As seen in Figure 6.4, the liquid assumes the height of the pillars over a wide area. Lower structures could potentially lead to a flatter and more horizontally distributed film.

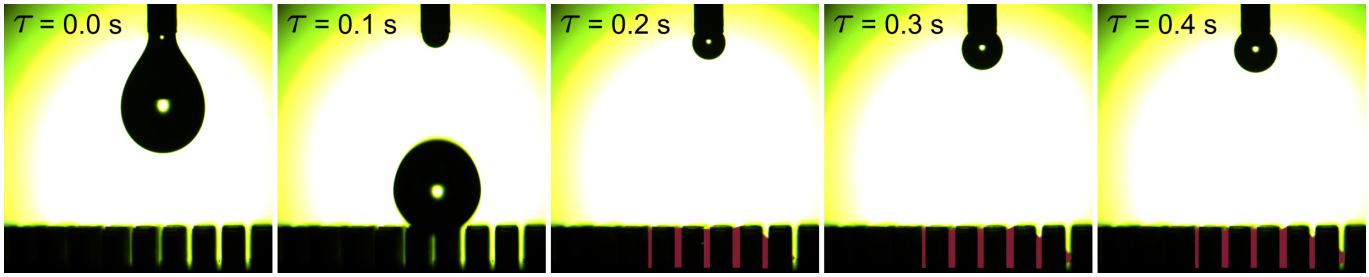

Figure 6.4.: Spreading of the liquid (marked in red) inside the structure for $W = 1.5\,\mathrm{mm}$

In summary, the investigated structure geometries do not appear to be beneficial for maximizing surface wettability. With increasing structure density, the effect of coating is suppressed. Additionally, the large pillar heights result in decreasing liquid-gas interface area, likely affecting subsequent evaporation.

Boiling on structured surfaces

After the last droplet has been applied, the surface is heated to the respective target temperature. In all cases, this causes the initial solution to boil, significantly increasing the urea concentration. As a result, liquid urea remains and begins to thermally decompose. Except for hydrophobically coated substrates, the boiling phase lasts less than 1 min.

As described earlier, wicking by the initial solution only occurs on the hydrophilic surfaces. This also affects the subsequent boiling process. As the wall temperature rises, vapor bubbles emerge from the structure, while the main bulk of the liquid remains within.

The uncoated and hydrophobic surfaces instead exhibit delayed imbibition into the structure channels during or shortly after the boiling phase. As discussed previously, most of the applied solution remains on top of the structure, causing the boiling process to begin there. As a result, the water content of the solution is significantly reduced. Once the majority of the water has evaporated, boiling subsides, and the remaining liquid is drawn into the structure once again. This indicates a significant reduction in surface tension due to the increased urea concentration, as reported by Shahidzadeh-Bonn et al. [121] and in own works [115]. Figure 6.5 shows how the boiling process subsides over time and how the resulting liquid finally disappears into the structure.

As a result of bubble formation during boiling, the initial droplet volume increases significantly regardless of the structure width. This simultaneously increases the contact area, or liquid-solid interface, compared to the initial wetting. After boiling subsides, this new area is retained, because pinning on the pillars prevents the liquid from contracting again. This behavior is observable only if boiling occurs on the structures, i.e., on

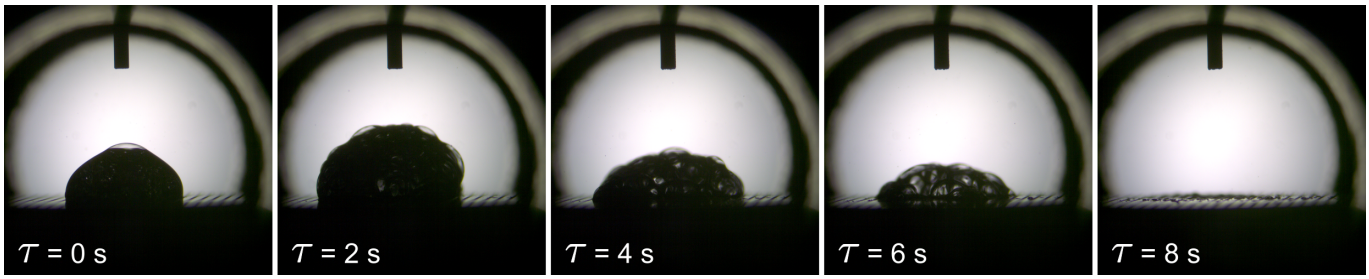

Figure 6.5.: Sequence of images showing the boiling on the pillars and the liquid eventually dissapearing

uncoated and hydrophobic samples. While the additional spreading of the liquid-solid interface is extensive on uncoated samples, it is significantly reduced in the hydrophobic case, as shown in Figure 6.6. This suggests that the hydrophobic coating exhibits a positive effect towards minimizing the deposit area beyond the initial wetting.

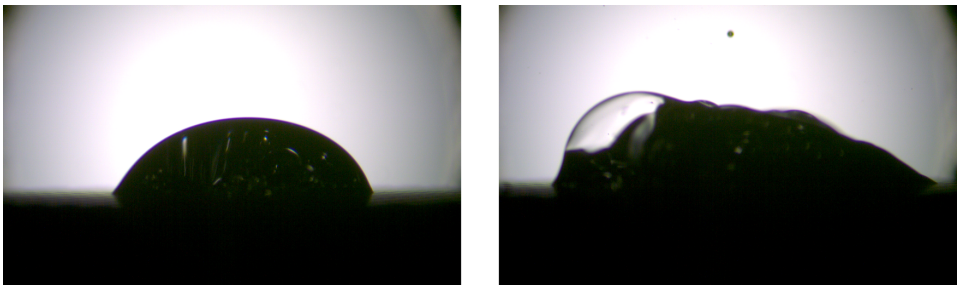

(a) Uncoated surface

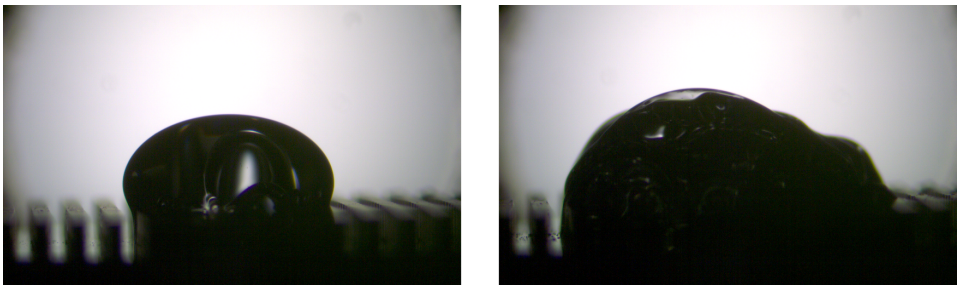

(b) Hydrophobically coated surface

Figure 6.6.: Expansion of volume and liquid-solid contact area during boiling on structured surfaces

Regardless of the structure density, the boiling process is noticeably slower on hydrophobic samples compared to non-hydrophobic surfaces, lasting up to 1.5 min. This can be attributed to the smaller liquid-solid interface and reduced heat transfer. The larger droplet height also leads to a more pronounced temperature gradient in the vertical direction, causing vapor bubbles to recondense as they rise in the liquid. Additionally, the hydrophobic surface increases the bubble break-off diameter, as the advancing contact angle at the bubble base is greater [63]. Sun et al. [140] demonstrated that bubbles on hydrophobic surfaces detach poorly and tend to become very large, leading to early critical heat flux and further reducing heat transfer. In own works with UWS [116], this behavior was also observed on hydrophobically coated rough surfaces.

At the maximum structure distance $W = 1.5\,\text{mm}$, boiling always takes place within the structure, regardless of the coating. Here the limiting influence of the pillars becomes apparent again. Figure 6.7 shows that the contact line shifts exactly one row of pillars to the right and left during the boiling process, but then halts again. As evaporation continues, the highly concentrated liquid collects at the base of the columns, as seen in the rightmost image.

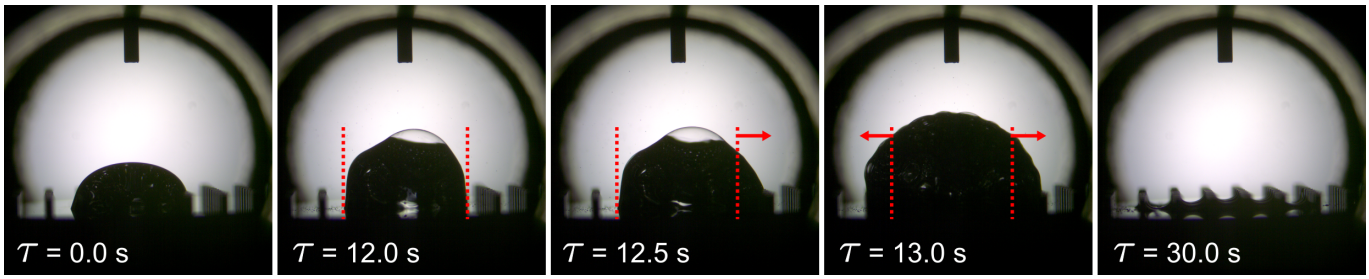

Figure 6.7.: Structure pillars restricting the volume expansion during boiling, as the liquid only moves from one row to the next

Overall, the following points can be emphasized: After the initial boiling process, the wetting behavior of the remaining liquid changes, causing it to be absorbed into the structure. The limiting influence of the pillars on liquid propagation, described in the previous section, is also noticeable during boiling. Furthermore, hydrophobic surfaces show a significantly delayed onset of boiling and a comparatively smaller expansion of the contact area during bubble formation.

6.1.2. Rough surfaces

Wetting and spreading on rough surfaces

On rough surfaces, the wetting processes are easier to observe due to the absence of obscuring structures. Once deposited on the substrate, the liquid spreads gradually and slowly to varying degrees on almost all surfaces. This is most noticeable on hydrophilically coated surfaces. The slow spreading is not inertia-driven but rather the result of capillary forces induced by surface roughness [30, 1]. This is also referred to as lateral imbibition [48].

Figure 6.8 illustrates the lateral imbibition of the first droplet on each of the three hydrophilically coated surfaces. In each case, the horizontal expansion of the initial liquid-wall contact is highlighted for comparison. This phenomenon is strongly influenced not only by the coating, but also by the surface roughness: higher Ra values lead to enhanced lateral imbibition. While the droplets at $Ra = 0.7\,\mu\text{m}$ still form a clear contact angle, at 1.6 µm the liquid begins to spread out to such an extent that the droplet exceeds the lateral boundary of the camera's field of view. In comparison, the spreading behavior increases much less when the roughness is further raised to 3.2 µm.

In contrast to all other studied surfaces, immediate evaporation of the water from the solution can be observed on the hydrophilically coated samples with roughness $Ra \geq 1.6\,\mu\text{m}$ as soon as the liquid comes into contact with the substrate. The excellent wettability causes the droplets to spread out as a very flat and wide film, while the roughness significantly increases the liquid-solid interface. Although the wall temperature is still

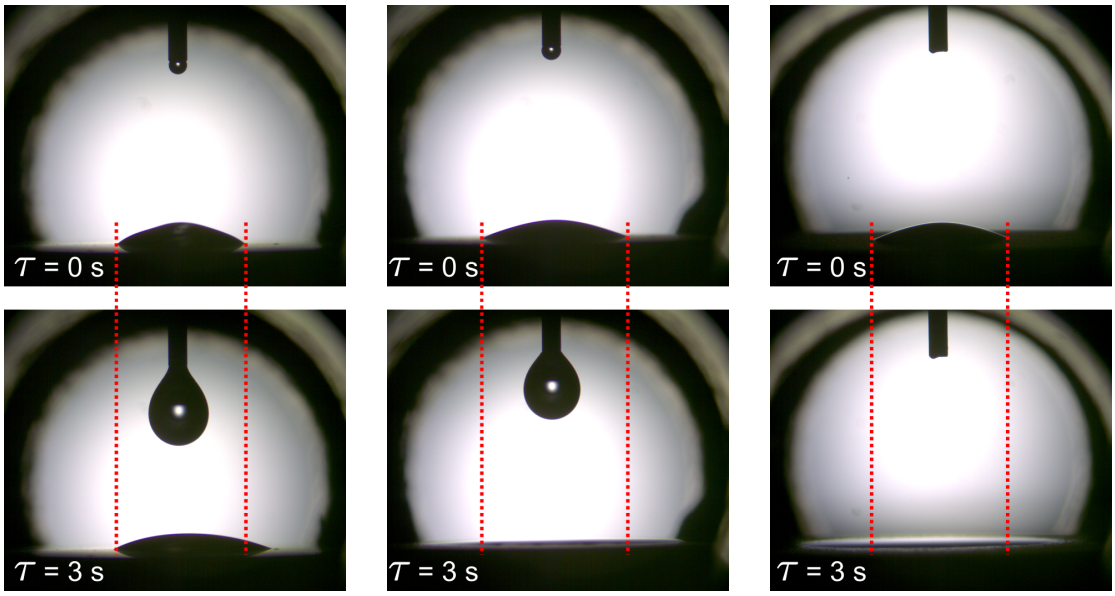

(a) $Ra = 0.7\,\mu m$ **(b)** $Ra = 1.6\,\mu m$ **(c)** $Ra = 3.2\,\mu m$

Figure 6.8.: Lateral imbibition of the first droplet on hydrophilically coated rough surfaces

controlled at 90 °C at this point, considerable evaporation occurs as a result, causing the urea concentration to rise noticeably. Once all five droplets have been applied, solid urea structures are already recognizable in the highly concentrated film (see the leftmost image in Figure 6.9). Within approximately 20 s, a solid deposit layer of crystallized urea forms, as the sequence in Figure 6.9 illustrates.

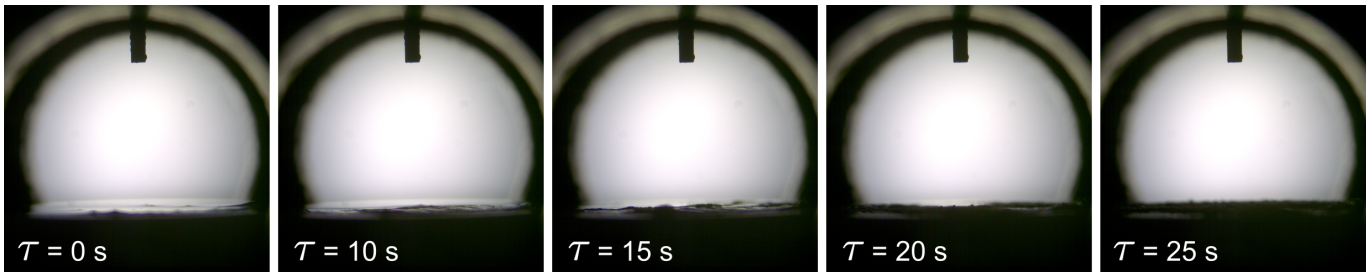

Figure 6.9.: Solid artifacts in the final film on hydrophilic surface with $Ra = 1.6\,\mu m$ and subsequent crystallization of urea

A similar but reversed wetting behavior is observed on the hydrophobically coated surfaces. While substrates with a roughness of 0.7 µm are wetted by the droplet, albeit with a large contact angle, the two rougher surfaces can no longer be wetted conventionally. Each droplet is fully repelled by the surface and bounces off the sample. As described in Section 4.4, the first droplet must be held in place manually using a thin needle. Each subsequent droplet increases the liquid volume, and the resulting liquid bulk becomes wider and flatter under the influence of gravity. Although the contact radius increases incrementally, the contact angle remains well above 90°. Eventually, the mass of the droplet is sufficient to adhere to the substrate by itself. Figure 6.10 shows the shape of the final whole droplet before the second heating phase starts. Overall, these opposing wetting trends for hydrophilic and hydrophobic surfaces with increasing roughness align closely with the fundamental theory of the Wenzel model.

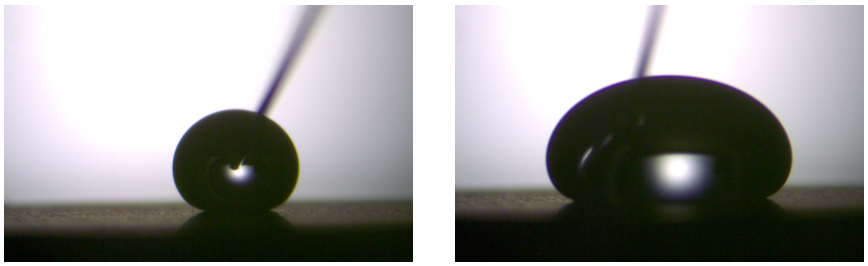

(a) First droplet, held with a needle

(b) Final accumulation of 5 droplets, held by its own weight

Figure 6.10.: Collection of UWS droplets on non-wetting surfaces with a needle

In summary, the wetting behavior differs significantly more between the lowest (0.7 µm) and the medium (1.6 µm) roughness than between 1.6 µm and 3.2 µm. This is particularly true for the coated surfaces. In the hydrophilic case, starting from 1.6 µm, significantly increased wetting and immediate evaporation are observed. On hydrophobic surfaces, medium roughness causes complete non-wetting to occur for the first time. Similarly to the structured surfaces, the wetting and spreading behavior is largely determined by the particular combination of surface characteristics and coating. The various configurations reveal a strong interaction between roughness and chemical surface treatment, as predicted by the Wenzel model. Figure 6.11 provides a comprehensive overview of the wetting from the first droplet on each of the rough surfaces.

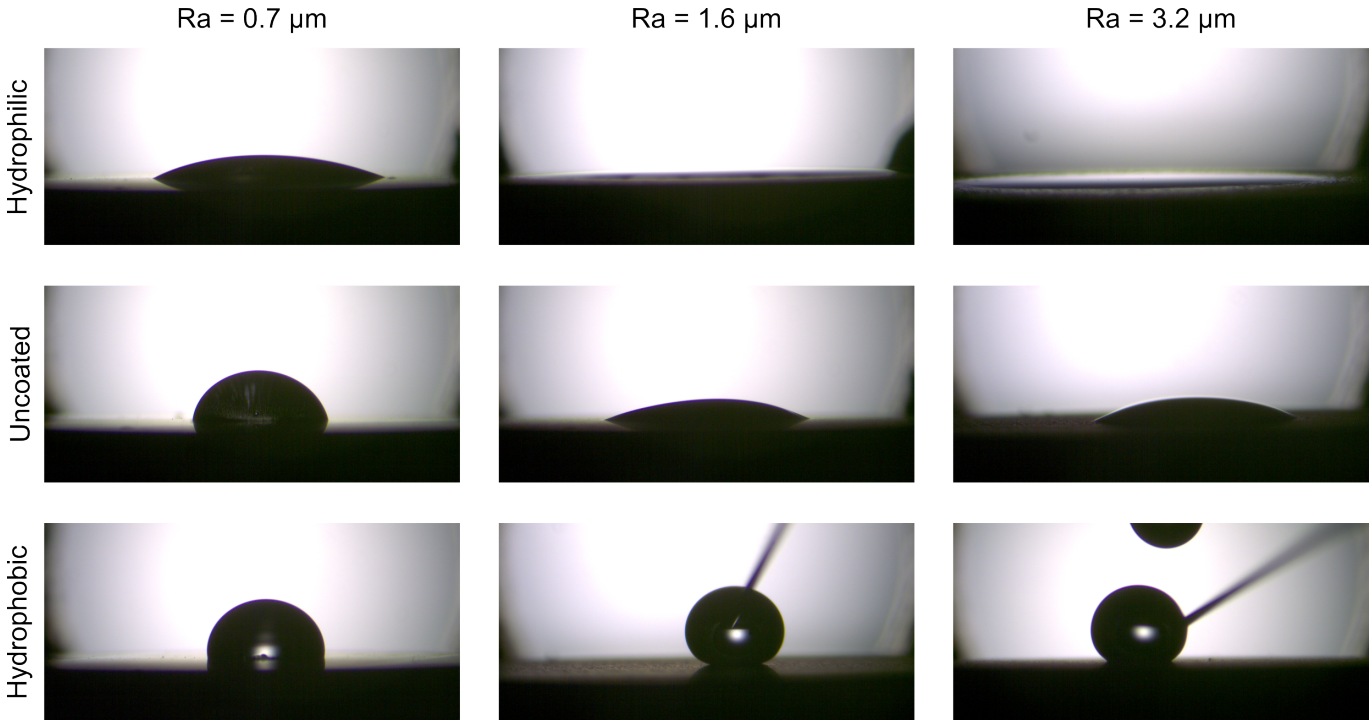

Figure 6.11.: Comparison of wetting by the first droplet on all rough surfaces

Boiling on rough surfaces

Since the droplets on rough surfaces are not obscured by pillars, the onset of deposit formation can, in some cases, be observed during evaporation. Therefore, unlike with the structured surfaces, the formation of solid residues from the evaporating film is included in the discussion below.

As observed for the structured surfaces, the boiling induced expansion of the contact surface also occurs on rough substrates. Figure 6.12a shows that this spreading is very limited on hydrophobic surfaces, even though the volume of the boiling mixture increases significantly for a short time. This again demonstrates the persistent effect of a hydrophobic coating beyond the initial wetting phase. Hydrophilic substrates also show little to no contact area spreading during boiling, as Figure 6.12b shows. This is partly due to the fact that the film is already very well spread, as described earlier. Additionally, hydrophilic surfaces exhibit predominantly quiet boiling, characterized by minimal vapor bubble formation and only slight changes in the mixture's total volume. Substrates without coating, on the other hand, exhibit significant increases in volume and contact area once bubble formation occurs during boiling. This is shown in Figure 6.12c. The extend of this expansion decreases as the surface roughness increases.

As described earlier, hydrophilic surfaces with $Ra \geq 1.6\,\mu m$ allow the water in the UWS to evaporate early during the liquid application phase. As a result, there are several instances of solid urea crystallizing out of the concentrated liquid film at $T_{wall} = 90\,°C$. In some cases, the heated surface is covered fully with solid urea before or shortly after the start of the second heating phase. Once the wall temperature reaches 135 °C, this layer melts and turns back into a film, demonstrating at least the same degree of wetting as the previous solution. This process is illustrated in Figure 6.13.

As the process continues, the solidification of the highly concentrated liquid is significantly influenced by the wall temperature. When the sample reaches 190 °C, solid structures are formed on all surfaces and continue to grow over time. However, if the wall temperature is limited to 150 °C, the deposit formation behavior becomes time-dependent. In this case, solid structures form only on surfaces heated for at least 30 min. In some cases, solidification is observed as late as 50 min. Samples with a shorter residence time are still covered with a liquid film when dismounted, which gradually solidifies as the sample cools.

A unique phenomenon is observed on hydrophobically coated surfaces with $Ra \geq 1.6\,\mu m$ (see Figure 6.14). After boiling subsides, a liquid film of primarily pure urea remains, as on all other samples, retaining its previous contact radius. However, when the wall temperature reaches approximately 150 °C, the droplet suddenly spreads across the surface, indicating a change in wettability. Additional tests, described in Section 4.2, rule out a temperature-related failure of the coating. Instead, it is likely that the chemical composition of the solution has changed in such a way that the coating is no longer effective. The extent of the subsequent film spread is again determined by the roughness. The resulting liquid wets the samples significantly more at $Ra = 3.2\,\mu m$ compared to $Ra = 1.6\,\mu m$, despite both surfaces being initially non-wetting with the original UWS.

In conclusion, the results demonstrate that highly wettable surfaces lead to early drying and crystallization of pure urea, which subsequently melts as wall temperature rises. This includes all hydrophilically coated samples with $Ra \geq 1.6\,\mu m$. With further temperature increase, solidification of the wall film occurs almost immediately once temperatures exceed 190 °C, with duration playing a secondary role. A phenomenon unique

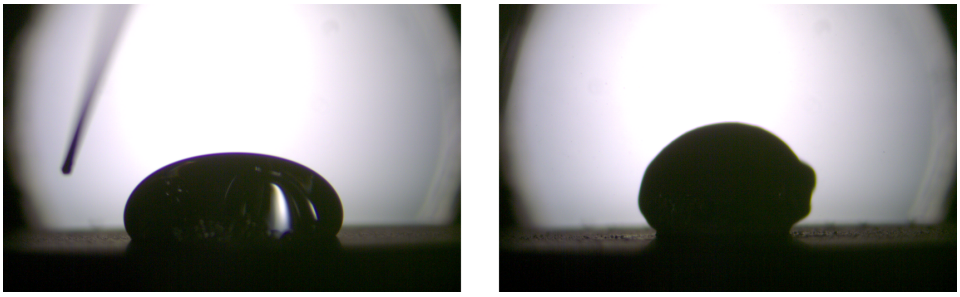

(a) Hydrophobically coated surface, left: sessile droplet after deposition, right: (late) boiling phase

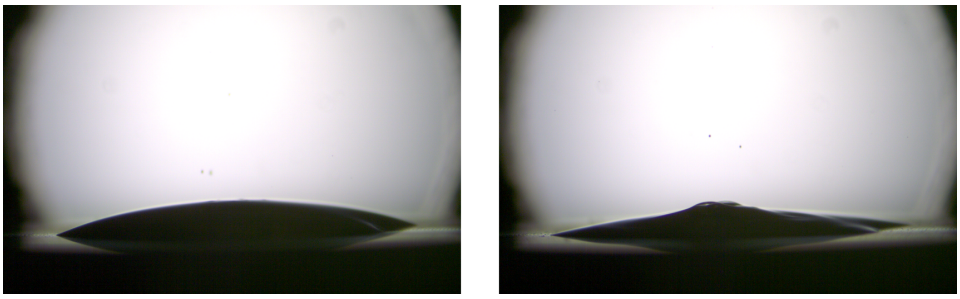

(b) Hydrophilically coated surface, left: sessile droplet after deposition, right: boiling phase exhibiting quiet boiling with only few emerging vapor bubbles

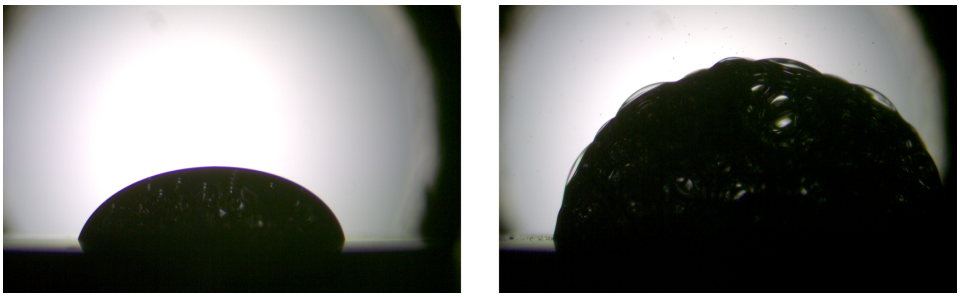

(c) Uncoated surface, left: sessile droplet after deposition, right: boiling phase with considerably increased volume and contact area

Figure 6.12.: Contact area expansion during boiling on rough surfaces

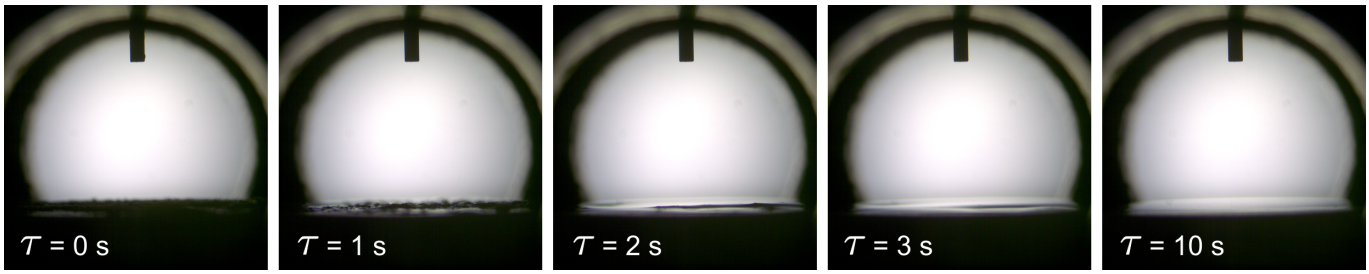

Figure 6.13.: Melting of the previously formed layer of crystallized urea once the substrate reaches $T_{\text{wall}} = 135\,^{\circ}\text{C}$

(a) Boiling droplet **(b)** Liquid urea after boiling **(c)** Spreading of the remaining liquid

Figure 6.14.: Pure urea spreading on a hydrophobic surfaces after reaching $T_{\text{wall}} = 150\,^{\circ}\text{C}$

to hydrophobically coated substrates is observed for $Ra \geq 1.6\,\mu\text{m}$: the hydrophobic surfaces maintain their low wettability during boiling but exhibit sudden lateral imbibition as the decomposition in the film progresses.

6.2. Experimental and model results

The following section presents the results and model responses for the final mass m_{dep}, area A_{dep}, and volume V_{dep} of the deposits, each in their own subsection. The factors influencing each of these these quantities are discussed separately and are sorted in descending order of effect size. The main effects are discussed first, with relevant interactions included where appropriate.

Since each of the models contains a large number of coefficients, it is not possible to display the model responses across the entire factor space in the 2D figures of this chapter. Instead, only the specific independent variable under consideration is varied between its minimum and maximum experimental values. All other independent variables are kept constant at their respective median values (see Table 3.1). For example, a plot illustrating the impact of contact angle through its model response will have the variable for roughness in the model set to $Ra = 1.6\,\mu\text{m}$, the duration set to $\Delta\tau = 30\,\text{min}$, and so forth. Additionally, all experimentally collected data points are shown in each plot to illustrate the entire result space. Data points where the settings of the independent variables correspond to those of the displayed model curves are highlighted for direct comparison.

Two points need to be emphasized in this context: First, the median value of T_{wall} , due to only having two factor levels, is 175 °C, meaning there are no experimental results for this setting. Therefore, data points for both wall temperatures are highlighted. As shown in Figure 6.18, this can lead to apparent deviations between the measurement results and the model curves, which are plotted for $T_{\text{wall}} = 175\,°\text{C}$. Plots where wall temperature is discussed as an interaction variable, such as Figure 6.16, are not affected by this, as both wall temperatures are displayed separately for both the experimental and model results.

Second, this graphical reduction of the model dimensions may, in some figures, give the false impression that the measurement data is poorly approximated by the models. It must be remembered that each model minimizes the error across all included features simultaneously, not just for the single factor shown in the 2D projection. Despite occasional deviations, the models provide an excellent overall fit for the full multidimensional space, enabling them to describe the complex system behavior as accurately as possible. This is demonstrated by the model evaluation in Section 5.3.3.

6.2.1. Deposit mass

The mass of the deposits is most significantly affected by the wall temperature T_{wall}, which aligns well with literature findings [19, 24, 113]. Figure 6.15 shows the corresponding measurement results and the model prediction within the covered temperature range. Specifically, the mean deposit mass from experimental data decreases from 14.2 mg to 6.3 mg between 150 °C and 200 °C. This means that only 45 % of the initial mass remains at the higher temperature. This reduction is higher than what was observed by Schaber et al. [113], who reported approximately 71 % mass remaining at 200 °C, and Brack [23], who found about 68 % remaining at the same temperature. These results were each obtained from thermogravimetric analyses in which the temperature was continuously increased without varying other factors. This suggests that the deposit mass from evaporating UWS can be further reduced by selecting appropriate surface characteristics for the substrate.

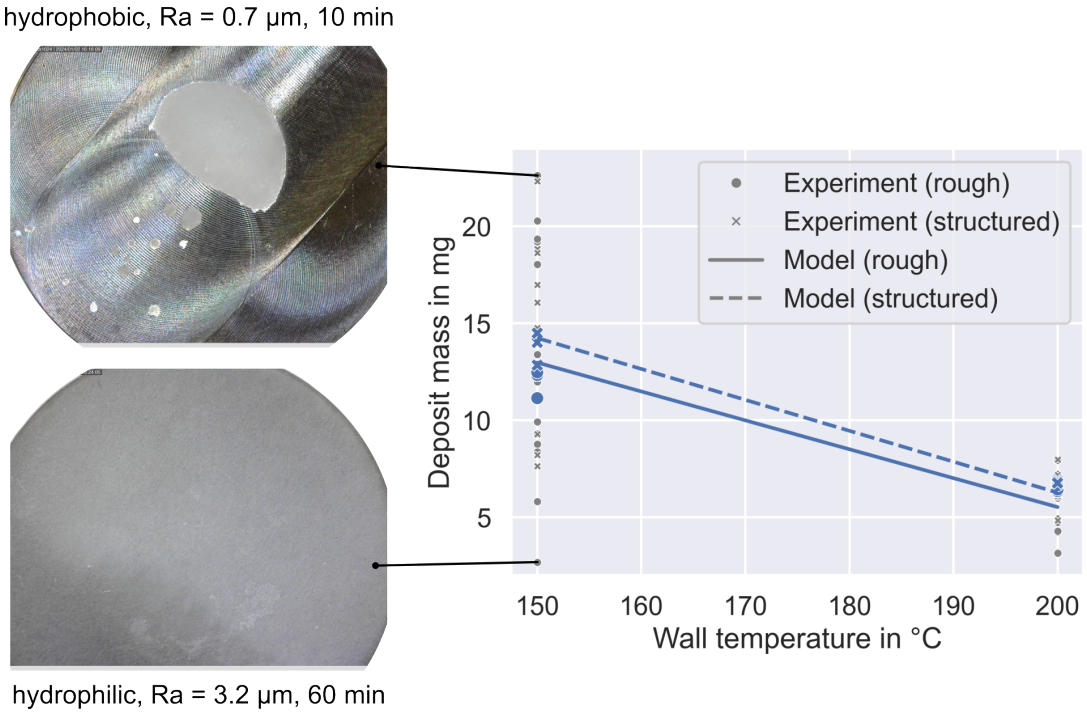

Figure 6.15.: Model response for deposit mass versus wall temperature, including images samples with the highest and lowest deposit masses. Experimental data points highlighted in blue are taken at identical settings as provided to the model: $\Delta\tau = 30\,\text{min}$, $Ra = 1.6\,\mu\text{m}$ / $R_A = 3$, $\theta_c = 77.7°$.

The variation in deposit mass at the lower temperature in Figure 6.15 is quite significant, showing a large range of measured values. At 200 °C, the results are much more uniform. Comparing the deposit images reveals that the deposit with the highest mass appears very compact, suggesting minimal spreading throughout the wetting, evaporation, and crystallization processes. This results in inhibited heat transfer and transition into the gas phase. Conversely, the lowest deposit mass is found on a hydrophilic surface with the highest studied roughness value. Here, the deposit appears as a thin, solid layer that is very spread out and has a large, indistinct transition region to the dry substrate. As detailed in Section 6.1.2, this is the result of a flat film of pure urea spreading on the heated surface. Notably, the four lowest mass deposits at 150 °C, which are close to the results at 200 °C, are all from hydrophilic surfaces.

This comparison supports the hypothesis that enhanced spreading can significantly reduce the remaining deposit mass, particularly at low temperatures. At 150 °C, the mean of the four lowest mass values is only 27 % of the highest value for the same temperature. At higher temperatures, the variance in deposit mass is much smaller, indicating comparatively less influence of the remaining other factors.

This can be confirmed by examining the interactions between wall temperature and the main effects, the first of which is shown in Figure 6.16a. This figure illustrates the impact of the duration, which is the most significant of the investigated main effects. It is evident that increasing durations lead to a considerable decrease in mass at 150 °C, while there is very little effect at 200 °C. The model response for the higher T_{wall} even suggests a minimum in the intermediate duration range. This is, however, not plausible and merely a result of the squared function undershooting after the slight decrease between 10 min and 30 min. For comparison, Figure 6.16b presents an otherwise identical model where only the squared duration term has

been removed. This version is provided only as a reference since removing this term worsens the predictive performance of the overall model and is not used further.

Figure 6.16 further shows that with increasing duration, the differences between temperatures diminish, as the continued evaporation at lower temperatures slowly converges with the nearly constant behavior at 200 °C. This suggests that the slow evaporation of urea may eventually catch up with the higher temperature decomposition. In the latter case, solid by-products such as cyanuric acid are formed, which increases overall mass and does not occur at temperatures as low as 150 °C [10, 19, 86]. This indicates a potential advantage of using low temperatures in exhaust gas treatment when long durations can be assured. These results also align with considerations from Smith et al. [130], who suggest a lower risk of deposit formation at temperatures below 160 °C due to the lack of decomposition, provided the time scale is sufficiently large. However, the rate of mass loss appears to slow down with increasing duration. Therefore, no definitive conclusion can be drawn from the current data as to whether the low-temperature mass curve will eventually catch up to or surpass the higher temperature curve for even longer durations.

Figure 6.17 illustrates how deposit mass changes with contact angle, as determined by the respective surface coating. The model responses and experimental results are again separated by wall temperature and surface type. As with the duration before, the effect of contact angle is very pronounced at the lower wall temperature but much less significant at 200 °C. Notably, while structured surfaces consistently lead to higher deposit masses in the previous figures, this difference diminishes towards higher contact angles, regardless of temperature. On rough, hydrophobically coated surfaces at 150 °C, this trend even reverses, resulting in a greater deposit mass compared to the structured samples. At 200 °C, the model even suggests a decrease in deposit mass with increasing contact angle on structured surfaces, represented by the dashed orange curve. However, the highlighted experimental data points (orange crosses) clarify that this particular trend is due to the overall model fit. In the experiments, the deposit mass does slightly increase with contact angle, as expected.

It is evident that while deposit mass starts higher on structured surfaces, it increases with contact angle at a much lower rate than it does on rough surfaces. This likely results from how spreading is affected by the respective surface type. As shown in Section 6.1.2, for rough surfaces, the liquid wets hydrophilically coated samples very well, while it exhibits low to non-wetting behavior on hydrophobic surfaces. This leads to a strong decrease in heat transfer and evaporation/decomposition rate with increasing contact angle, ultimately increasing the amount of remaining deposits. On structured surfaces, the effect of the coating is much smaller, and wetting is more influenced by the structure pillars and resulting capillary forces, as shown in Section 6.1.1 and discussed in the following section on deposit area. This means that evaporation is not decreased as much by contact angle on structured surfaces as it is on rough surfaces. Additionally, the pillars allow the structured surfaces to compensate for the decreased heat transfer and evaporation due to large droplet heights. As the pillars penetrate the liquid along its entire height, they improve the distribution of heat supply throughout the liquid bulk, thereby increasing evaporation and decomposition when contact angles are large.

Of the two surface topography features – roughness and surface area ratio – shown in Figure 6.18, deposit mass appears to be clearly dependent only on roughness. This is not surprising since increased roughness also increases the surface area of the film, thereby enhancing the evaporation and decomposition rates. In contrast, surface area ratio exhibits an only slightly declining curve, with a p-value of 0.828 for the corresponding regression coefficient. This indicates that, based on the experimental data, the distance between structures does not have a significant effect on the final mass of the formed deposits.

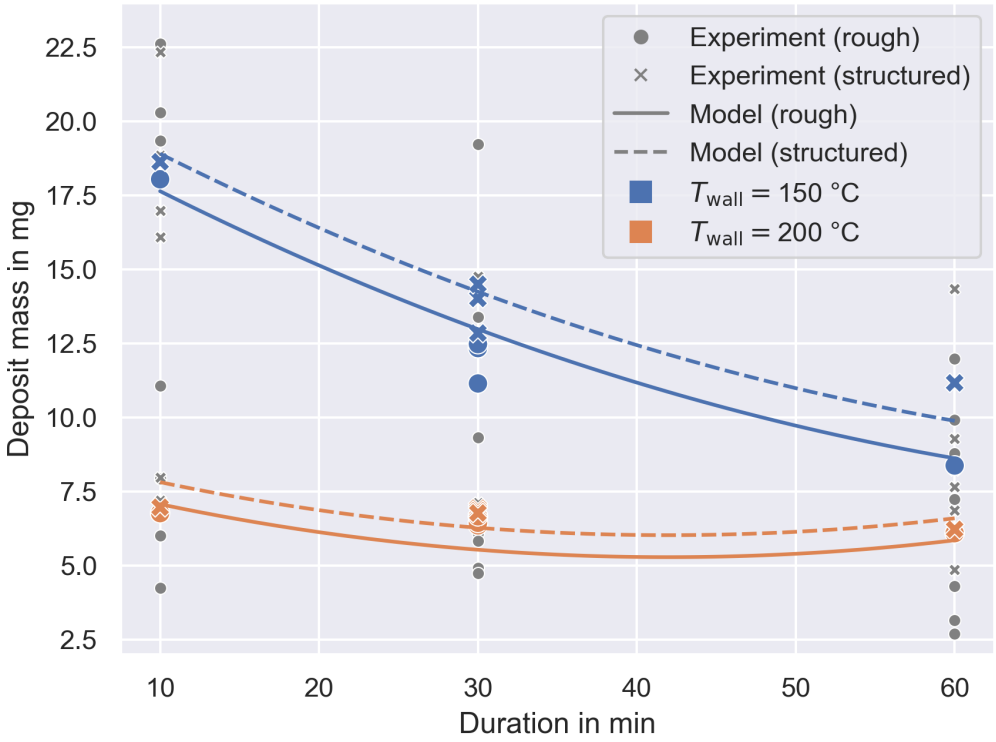

(a) Original model

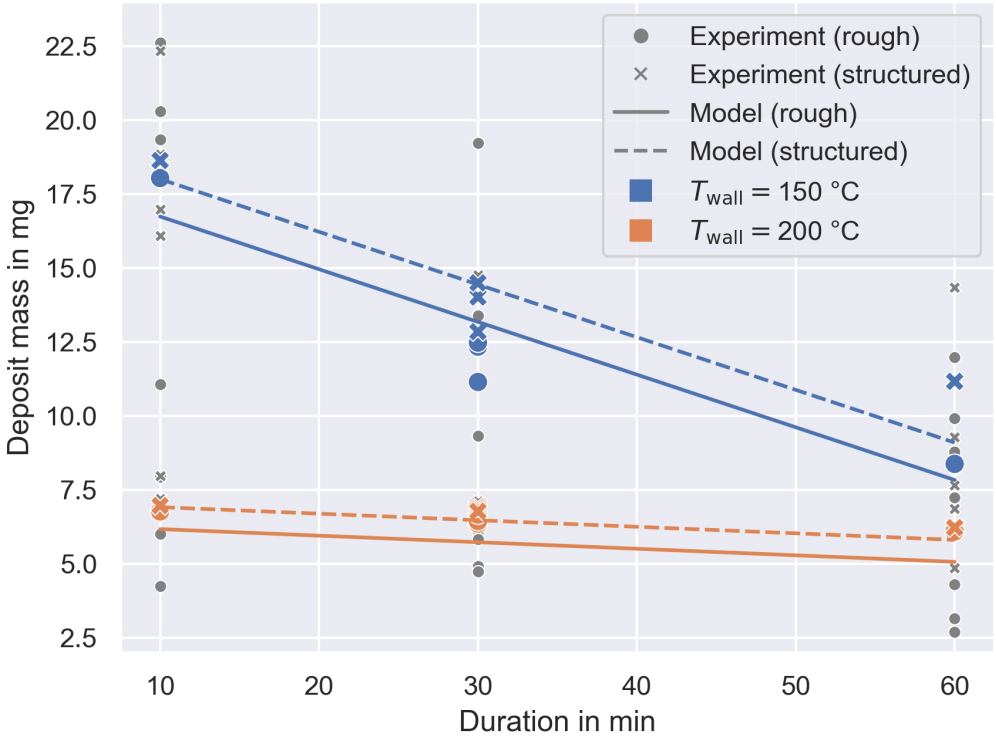

(b) Without squared duration feature, only for comparison

Figure 6.16.: Interaction of duration and wall temperature for predicting deposit mass

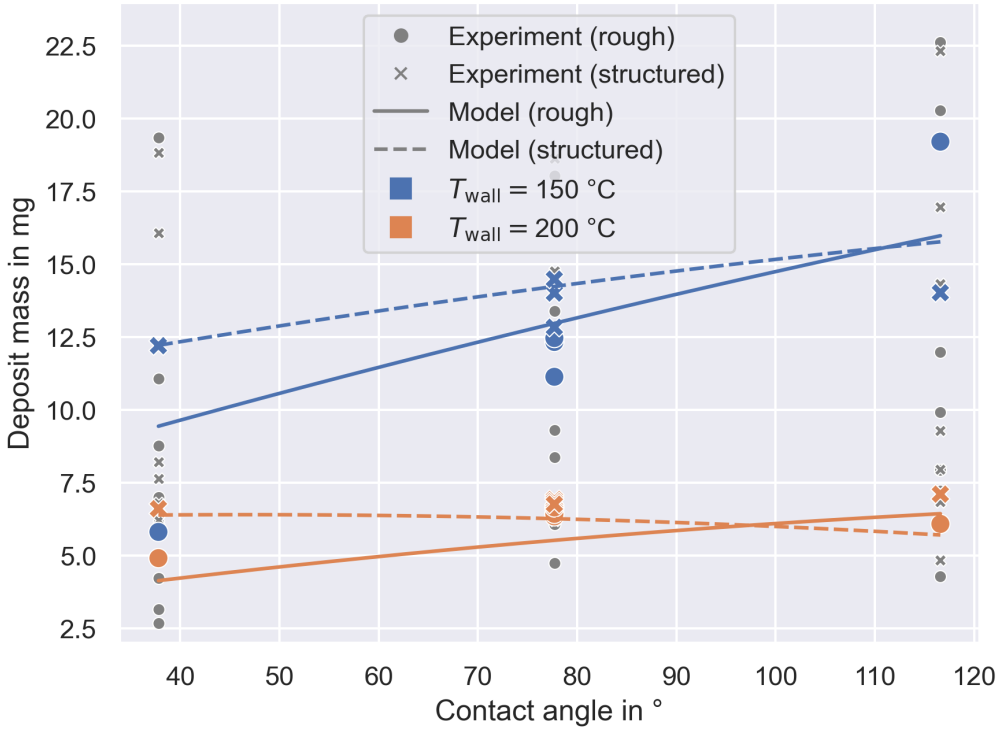

Figure 6.17.: Deposit mass depending on contact angle, separated by wall temperature and surface type

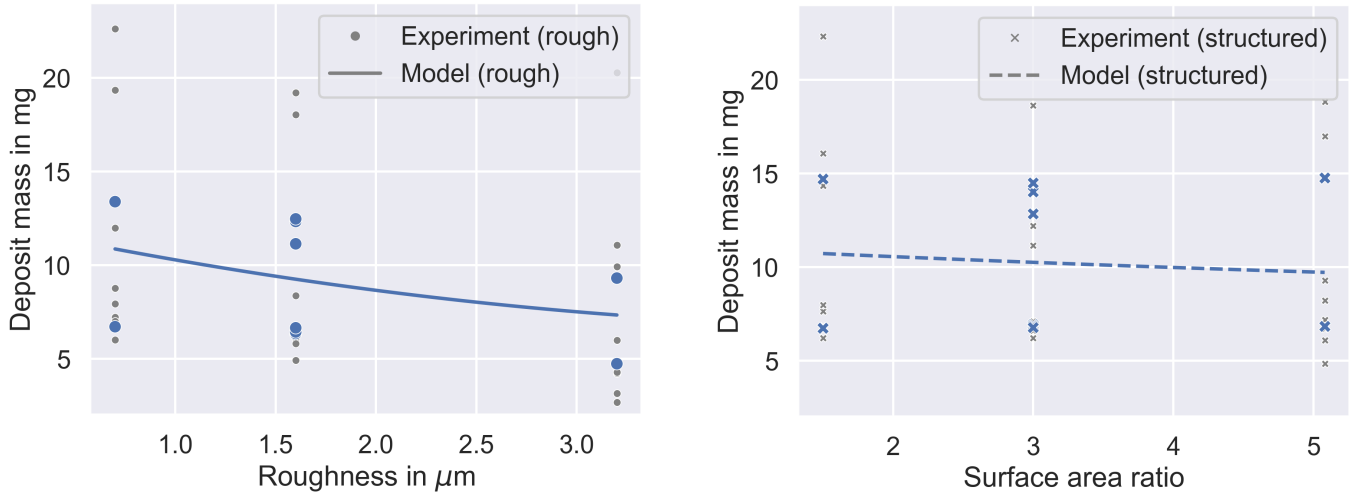

(a) Roughness as independent variable

(b) Surface area ratio as independent variable

Figure 6.18.: Model response for deposit mass depending on surface topography features. Experimental data is highlighted for both wall temperatures, while the model curves are based on $T_{\text{wall}} = 175\,^{\circ}\text{C}$. As a result, the model curves interpolate between the highlighted data points.

This lack of an effect cannot simply be attributed to the structure distance not affecting the spreading of the wall film, as results such as those in Figure 6.22 demonstrate that the final deposit area does depend on the structure distance. Additionally, newly formed contact lines of the film due to the pillars penetrating the liquid-gas interface are expected to enhance heat transfer as shown by Sodtke and Stephan [131]. The amount of these additional contact lines increases as the structure distance decreases. However, it is also very likely that a dense structure of high pillars, as seen in this case, inhibits the diffusion of evaporated urea or decomposition products such as ammonia into the surrounding atmosphere. In other words, the partial gas pressure of the gaseous products might locally increase, especially in the tighter channels of structures with a higher surface area ratio, thereby decreasing evaporation and thermal decomposition. This effect, being inversely proportional to the surface area ratio, would then offset the increased spreading and heat transfer that results from smaller structure distances.

The final relevant interaction for deposit mass is illustrated by separating the effects of roughness and surface area ratio from Figure 6.18 by the contact angles. As Figure 6.19a shows, there is little interaction on rough surfaces, with surfaces of each coating exhibiting similar behavior in terms of deposit mass versus roughness. This observation is supported by the results from Section 6.1.2, which show that on both hydrophilic and uncoated surfaces, the initial droplet spreading increases with roughness. Hydrophobic surfaces with $Ra \geq 1.6\,\mu m$, on the other hand, were shown to always be non-wetting. Initially, this might contradict the consistently negative trend of the green curve, as one would expect a more horizontal progression starting from 1.6 µm due to the seemingly identical wetting behavior from this roughness onward. However, as discussed in Section 6.1.2, the droplet exhibits a second spreading phase when heated to 150 °C, the extent of which is again determined by the roughness value.

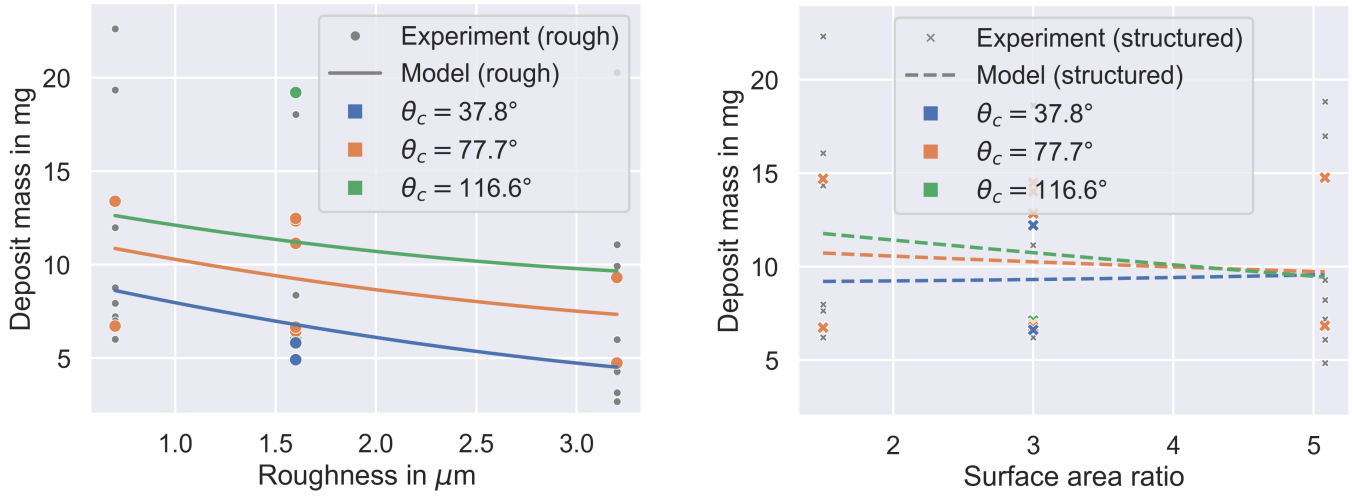

(a) Roughness as independent variable

(b) Surface area ratio as independent variable

Figure 6.19.: Model response for deposit mass depending on surface topography features for different contact angles. Due to the design of experiments (see Chapter 3), experimental data is only available on hydrophobic and hydrophilic samples for $Ra = 1.6\,\mu m$ / $R_A = 3$.

Structured surfaces, as shown in Figure 6.19b, display a larger interaction between contact angle and the surface morphology concerning deposit mass. While for low contact angles the effect of surface area ratio appears minimal, hydrophobic surfaces benefit from higher density structures. This is likely because the additional solid-liquid interface and the supply of heat to the higher portions of the film through many high

pillars are advantageous at larger contact angles. Furthermore, it is apparent that the advantage of the coating, while consistent on rough surfaces, disappears at the highest surface area ratio for structured surfaces. Therefore, coatings on densely structured surfaces do not provide any benefit in terms of deposit mass.

Comparing both images in Figure 6.19 reveals that even hydrophobically coated rough surfaces, which result in the highest deposit masses among rough samples, can lead to similar mass values as structured surfaces, regardless of the coating on the latter.

6.2.2. Deposit area

The contact angle, which reflects the effect of surface coating, has the strongest influence on deposit area, as shown in Figure 6.20. The decline in deposit area is most pronounced from low to intermediate contact angles and subsequently slows down. For structured surfaces, the deposit area remains almost constant starting from 90°, while on rough surfaces, the coating continues to be effective across the entire studied range. This indicates that the effect of hydrophobic coatings on the final deposit area is not fully negated by the late lateral imbibition of the highly concentrated liquid upon reaching 150 °C, as discussed in Section 6.1.2.

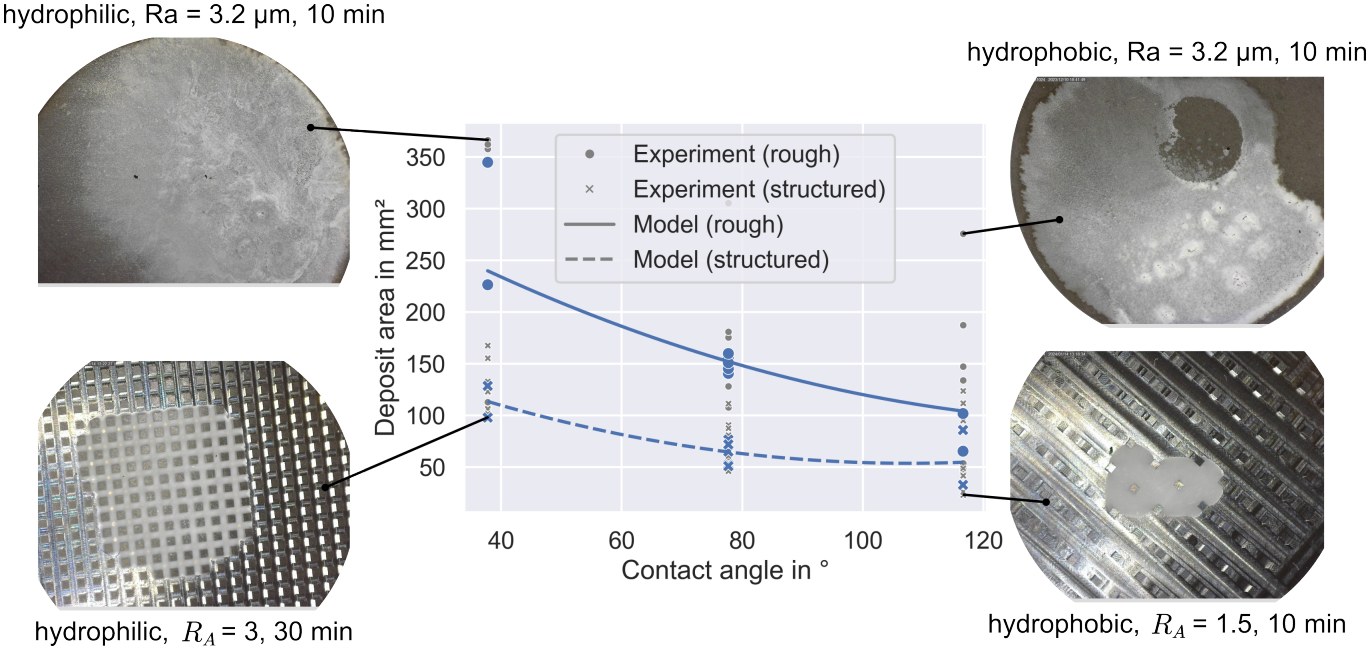

Figure 6.20.: Model response for deposit area versus contact angle with added photographs of final deposit shape for hydrophilic and hydrophobic surfaces

Regarding the deposit area, there is a significant difference between structured and rough surfaces for all experiments, most prominently on hydrophilic samples. The six highest area deposits are measured on rough surfaces, while four of the six lowest area deposits are found on structured surfaces. The range of deposit area values is substantial, with the largest area being almost three times that of the smallest for each coating, even when duration and temperature are kept constant. The accompanying photographs of the deposits in Figure 6.20 illustrate the considerable differences in deposit area and the clear distinction between rough and structured surfaces. As the contact angle increases, the difference between the surface types diminishes due to

the overall stronger impact of the coating on rough surfaces, but it remains significantly large. This confirms the results from Section 6.1.1, indicating a strong inhibiting effect of the structures on liquid spreading, and emphasizes that this effect persists in the final deposits.

Figure 6.21 provides a more detailed look at the interaction between wall temperature and contact angle concerning deposit area. As observed previously, the trends of decreasing area with increasing contact angles and generally lower areas on structured surfaces persist. There is almost no difference in the final area between the two temperatures when the surface is coated hydrophilically, independent of the surface type. In contrast, as the contact angle increases, the curves for the two temperatures begin to diverge significantly regardless of surface type. At lower temperatures, the decrease in area with increasing contact angles is more pronounced, while the decrease diminishes faster at higher temperatures, particularly on structured surfaces. This can be attributed to the earlier onset of the second spreading phase of the highly concentrated liquid when the samples are heated to 200 °C. In these cases, the heating power, and therefore the heating rate, is increased, leaving less time for the urea to evaporate on the hydrophobic substrates before the wettability abruptly changes and the liquid spreads out. Nevertheless, on rough surfaces, higher contact angles consistently result in smaller deposit areas, even at higher temperatures. This demonstrates the sustained influence of surface wettability on the final distribution and area of the deposits.

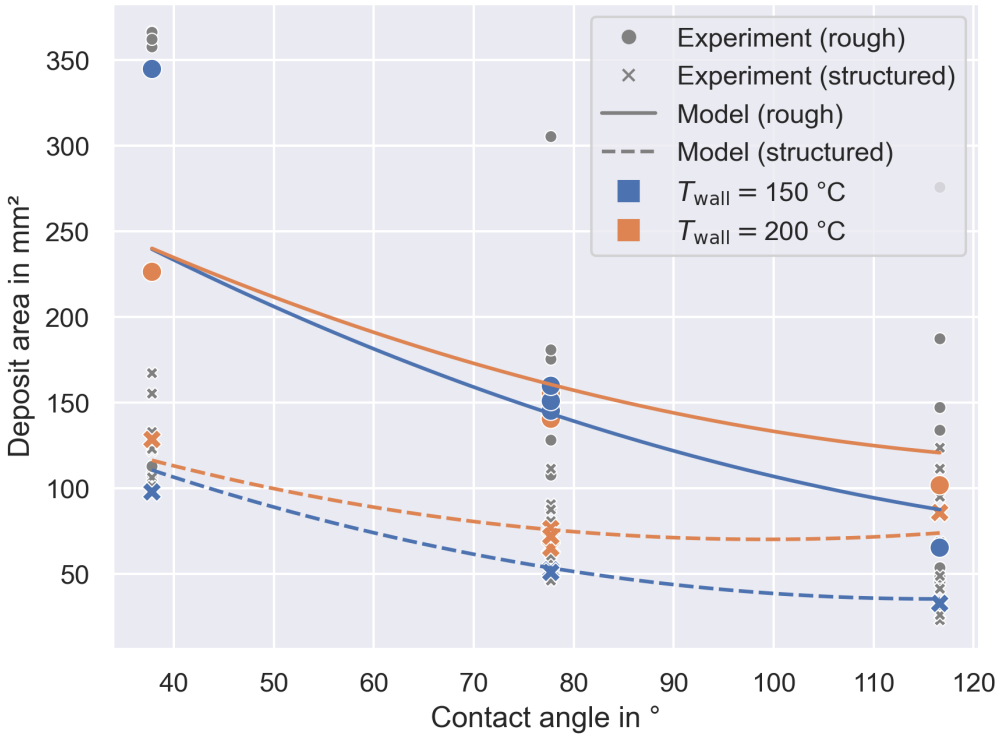

Figure 6.21.: Interaction of contact angle and wall temperature for predicting deposit area

The second most important main effect on the final deposit area is the respective surface topography, with roughness having a much larger impact than surface area ratio, as seen in Figure 6.22. The plots are further separated by the previously discussed contact angle, illustrating that while the area increase with roughness is lower for hydrophobic surfaces, it still follows the same trend as on wetting surfaces. This observation contradicts the Wenzel model and findings from the literature, which state that roughness generally enhances wetting behavior [28, 75, 106, 124, 153]. Specifically, hydrophobic surfaces are expected to become more

hydrophobic with higher roughness, which contradicts the green curve in Figure 6.22a. However, with the sudden transition of hydrophobically coated surfaces to good wettability at $T_{\text{wall}} \approx 150\,°\text{C}$, the contact angle θ_e in Equation (2.3) is actually smaller than 90° for this specific case. Together with the previously presented impact of roughness on this late lateral imbibition, the consistently enhancing effect of roughness on the deposit area is plausible.

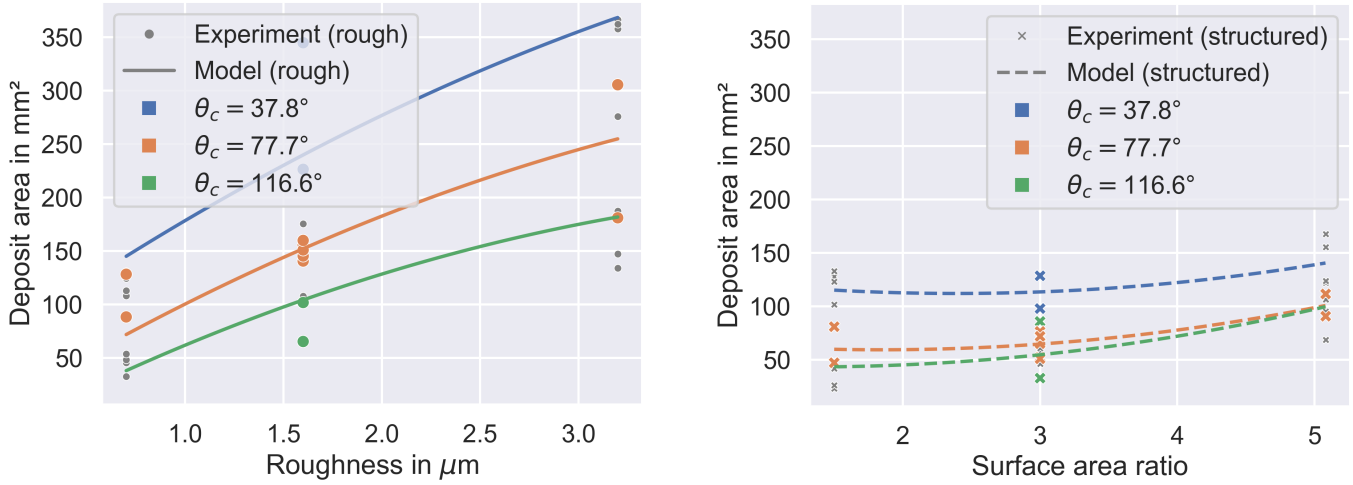

(a) Roughness as independent variable

(b) Surface area ratio as independent variable

Figure 6.22.: Model response for deposit area depending on surface topography features for different contact angles

In comparison, the effect of surface area ratio, shown in Figure 6.22b, is much lower. It is evident that uncoated and hydrophobic samples exhibit no difference at the highest surface area ratio, while the hydrophilic coating consistently results in larger deposit areas. Moreover, only the highest surface area ratio, representing the densest structures, seems to affect the deposit area at all, as indicated by the overall distribution of the measurement data. Likely, only with such small channels does the capillary force act to increase the spreading of the solution.

The interaction between wall temperature and topography features, shown in Figure 6.23, resembles the effect of temperature illustrated in Figure 6.21. Once again, higher temperatures result in larger deposit areas by amplifying the impact of increased roughness and surface area ratio on the liquid spreading. This enhancement results from an earlier and more pronounced switch in wetting behavior on hydrophobic surfaces at higher wall temperatures, as well as a generally improved wetting behavior at elevated temperatures [5, 9]. This temperature effect is further intensified when roughness and surface area ratio are high. Thus, higher wall temperatures, combined with increased roughness and surface area ratio, contribute to a more significant spread of the liquid and a larger deposit area.

By itself, the effect of wall temperature is not statistically significant for the final deposit area, as shown in Figure 6.24a. The same is true for the impact of duration, as Figure 6.24b shows. This appears reasonable for both of these variables because, once the initial spreading – whether influenced by surface topography or coating or both – is complete, any subsequent changes in the extent of the liquid film due to either wall temperature or duration will leave behind deposits that contribute to the final area. In other words, although a higher wall temperature or longer heating duration will increase evaporation and reduce the liquid film over time, deposits will remain on any previously wetted surface.

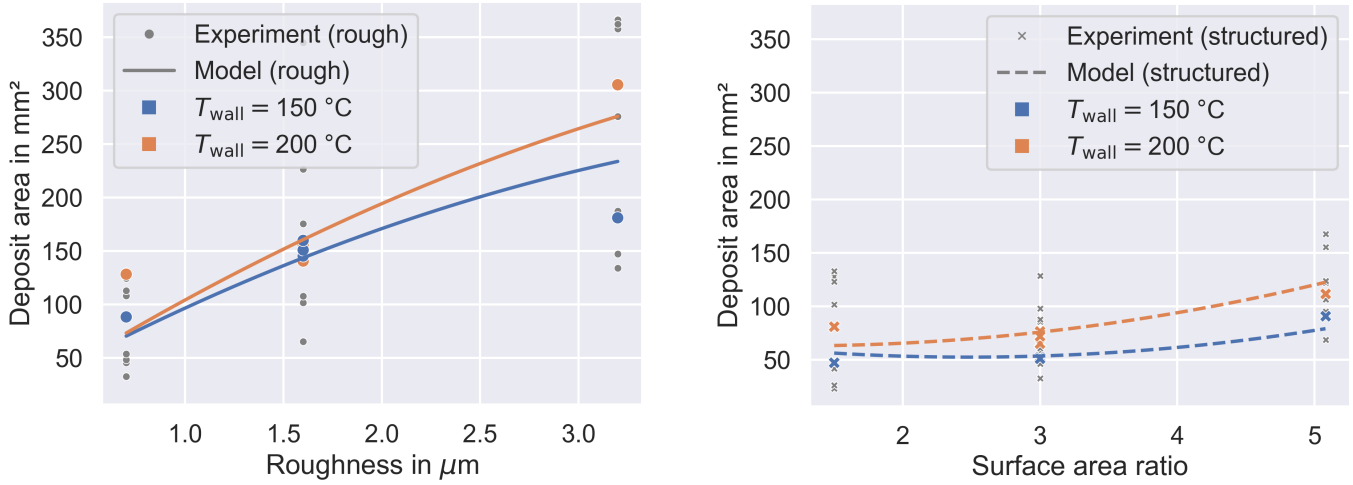

(a) Roughness as independent variable

(b) Surface area ratio as independent variable

Figure 6.23.: Model response for deposit area depending on surface topography features for different wall temperatures

However, as the previous results illustrate, wall temperature plays an important role in the initial wetting via its interactions with the other main influences. This significance is not observed for the duration, as seen in Figure 6.25, where there is only minimal change in deposit area for different durations.

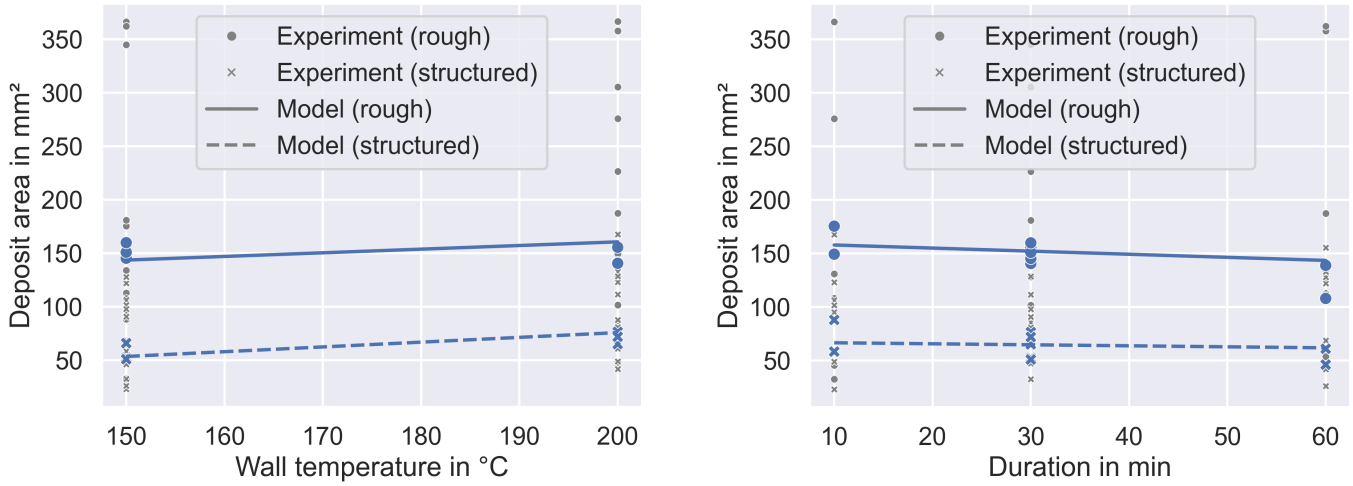

(a) Wall temperature as independent variable

(b) Duration as independent variable

Figure 6.24.: Model response for deposit area depending on wall temperature and duration

The discussion on deposit area is concluded by examining the relationship between deposit area and deposit mass. Figure 6.26 displays all measurement results, with deposit area on the x-axis and mass on the y-axis. The expected behavior is a negative trend, as better spreading of the liquid would lead to a larger area and, due to enhanced evaporation, a lower deposit mass.

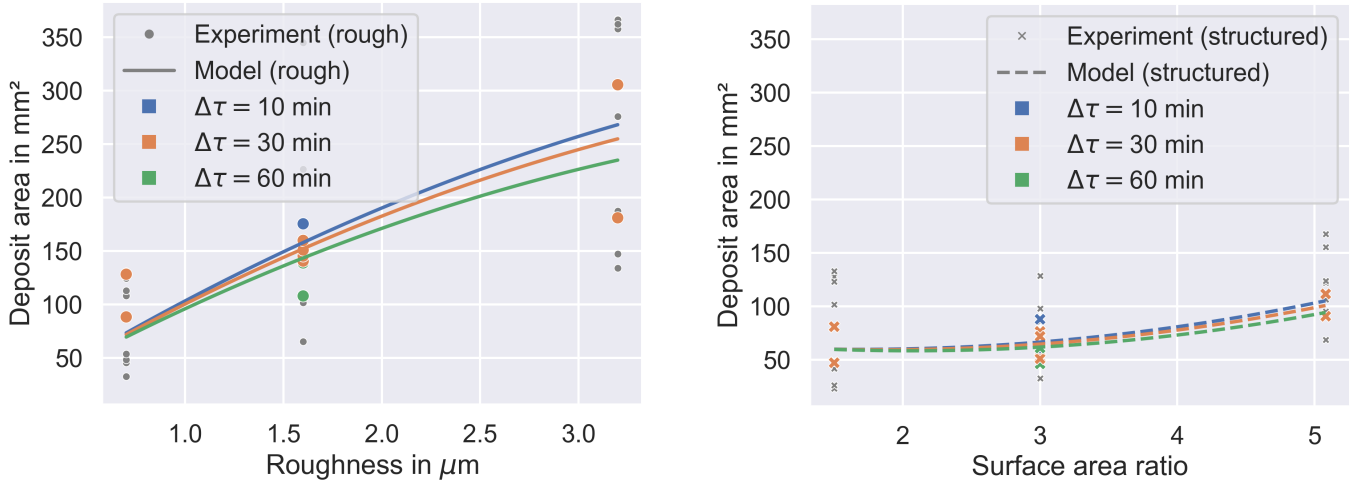

(a) Roughness as independent variable

(b) Surface area ratio as independent variable

Figure 6.25.: Model response for deposit area depending on surface topography features for different durations

The results are differentiated by wall temperature, surface type, and duration. The reason for separating by duration is evident in Figure 6.26a, which combines results from all durations. At 200 °C, the postulated trend is clearly visible: the mass decreases slowly from about 7.5 mg to 4 mg while the deposit area increases more than sevenfold. However, the results for 150 °C are much more scattered, preventing a clear conclusion. According to Figure 6.16, duration is a very strong predictor for deposit mass at this temperature. Therefore, Figure 6.26b–d separate the results by the respective duration, making the clear correlation between deposit area and deposit mass apparent again, also at 150 °C. Here, the relationship between area and mass is more pronounced due to the smaller superimposed temperature influence.

This final result demonstrates a conflict of objectives in controlling the formation of deposits. When selecting suitable design parameters, a trade-off must be made between minimizing the surface area and minimizing the mass of the deposits.

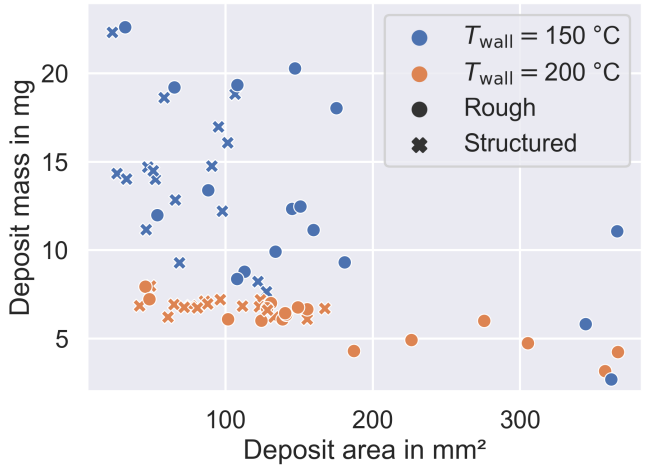

(a) All durations

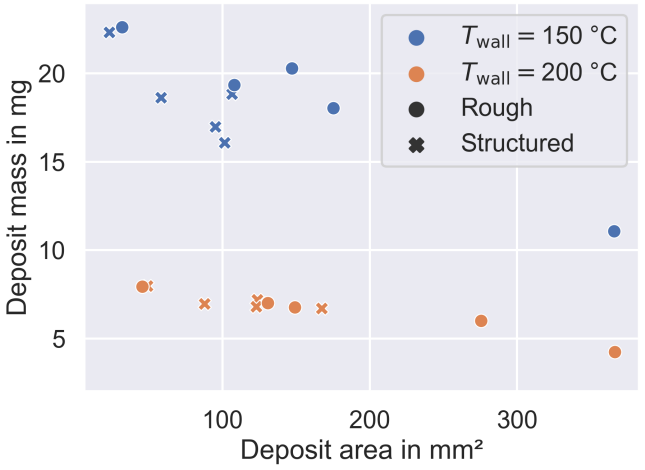

(b) Duration: 10 min

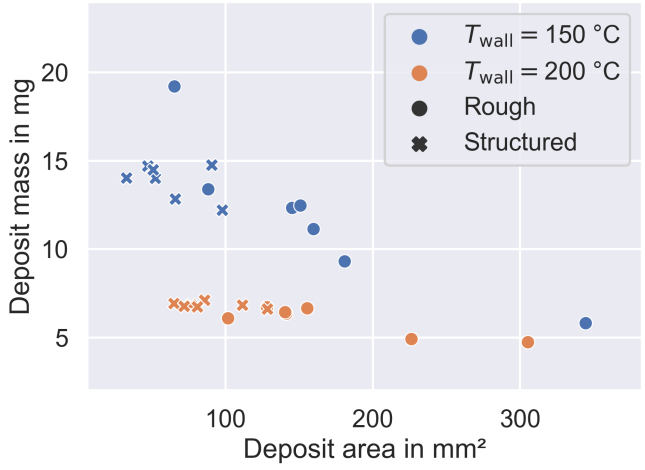

(c) Duration: 30 min

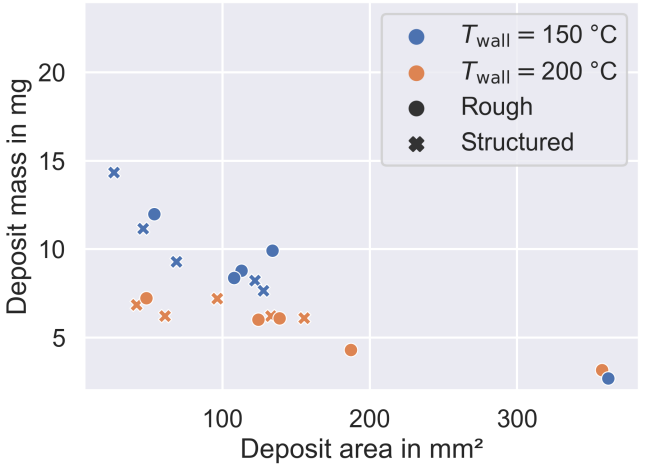

(d) Duration: 60 min

Figure 6.26.: Experimental results for the deposit mass against the final deposit area, subdivided according to residence time

6.2.3. Deposit volume

As mentioned in Section 5.3.3, modeling of the deposit volume is affected by a suspected measurement error in case of the smallest structure distance, i.e., highest surface area ratio. Therefore, the following results are based on the subset model for deposit volume.

Figure 6.27a illustrates the effect of duration on deposit volume, identifying it as the largest main impact factor aside from T_{wall}. As expected, the deposit volume decreases over time, aligning with similar results for deposit mass. Given that deposit area is not affected by duration, as shown in Figure 6.24b, the volume decrease must primarily occur through a reduction in deposit height.

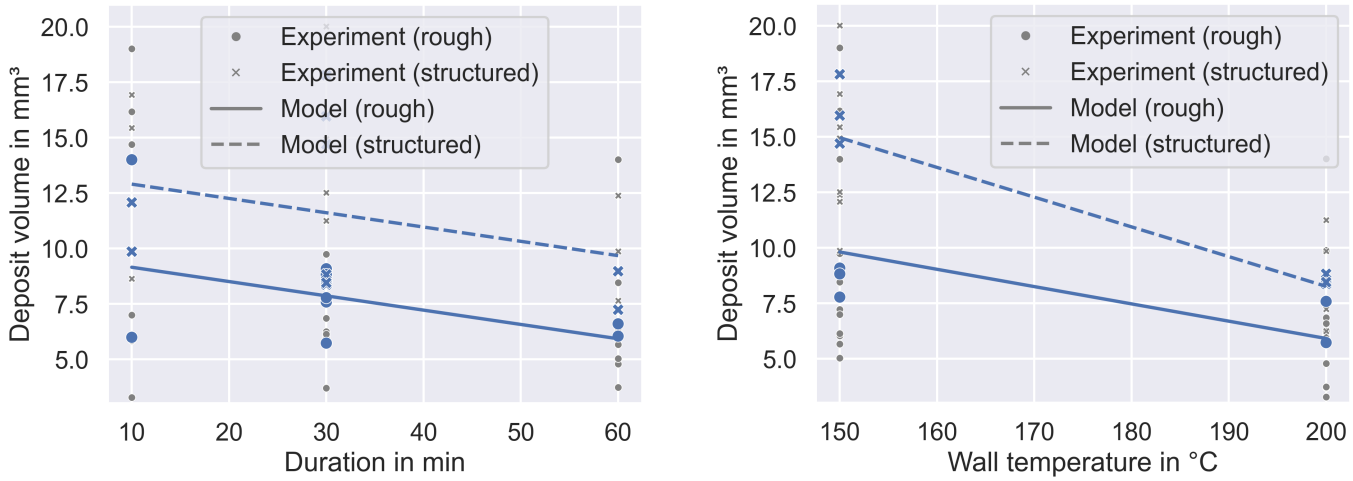

(a) Duration as independent variable

(b) Wall temperature as independent variable

Figure 6.27.: Model response for deposit volume depending on duration and wall temperature

The reduction in volume with increasing duration is linear and shows no differences in the slope between the two structure types. However, the same does not hold for the impact of wall temperature, as shown in Figure 6.27b. Although all surfaces result in smaller deposit volumes at higher temperatures, this effect is more pronounced on structured samples. Similar to the deposit mass, results from 200 °C are less varied than those at 150 °C, but the extent of the reduction is smaller here. Overall, rough surfaces end up with lower volume deposits, which is consistent with the results for deposit mass.

Figure 6.28 separates the results of volume versus duration by wall temperature. While both individual effects on deposit volume were discussed above, this figure reveals a more complex interaction behavior. Duration strongly affects deposits formed at 150 °C, while there is no significant effect at the higher wall temperature. This behavior strongly resembles how deposit mass is influenced by duration, as discussed in Section 6.2.1.

The results illustrate how the formation of solid reaction products such as biuret, cyanuric acid, and ammelide by thermal decomposition can resist further decomposition over time, making the temperature range around 200 °C critical for operation. Even higher operating temperatures are necessary to further reduce deposits [19, 24]. In contrast, lower temperatures up to 150 °C allow formed deposits to decompose into the gas phase when given sufficient time. A notable difference between surface types is retained over the entire duration, though it is overall smaller at the higher temperature.

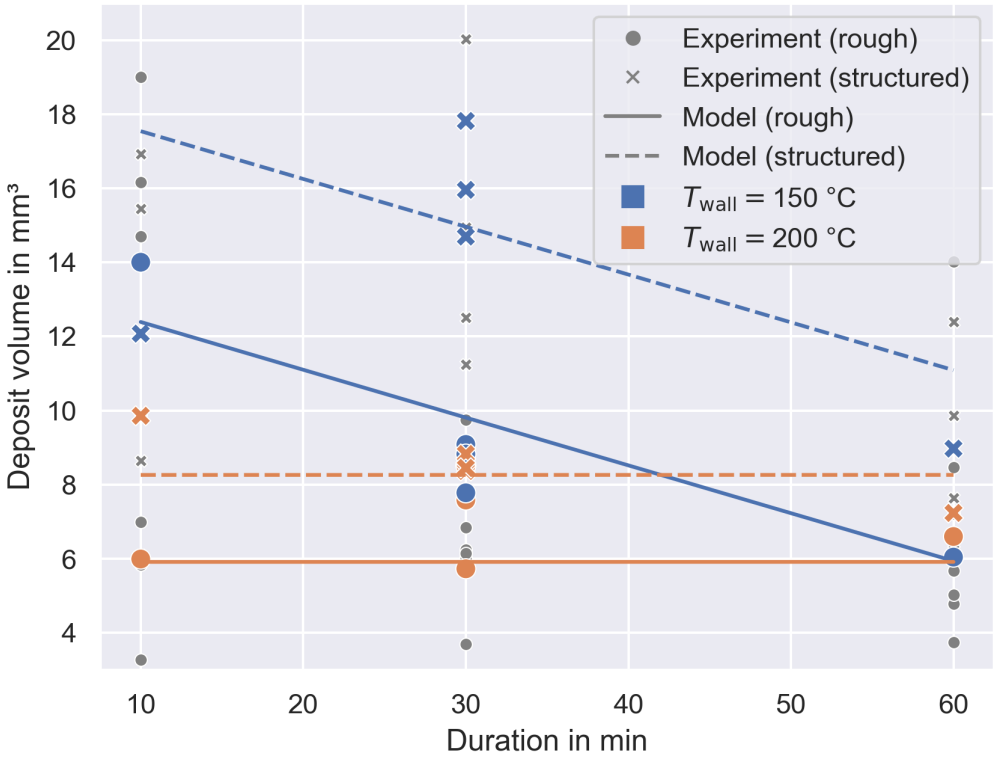

Figure 6.28.: Interaction of duration and wall temperature for predicting deposit volume

Deposit volume decreases linearly with roughness, as Figure 6.29a shows, again exhibiting similar behavior to deposit mass. Given the significant increase in deposit area with roughness, this indicates that final deposits tend to become very flat at higher roughness values. A comparison of uncoated substrates of the same duration and temperature for different roughnesses, shown in Figure 6.30, makes it apparent that with increasing Ra, more of the underlying surface becomes visible through the increasingly sparse deposit. There are also more areas with locally increased deposit accumulation, while wide regions display only a very thin deposit layer.

This observation suggests that over multiple wetting events, the roughness cavities could fill with a thin deposit layer, potentially negating the effect of roughness altogether. Although multiple wetting events were not investigated here, other works by the author [115] indicate that the porous structure of previous deposits will act similarly to surface roughness in affecting liquid spreading, effectively replacing the roughness effect if necessary. Further research would be valuable to explore this phenomenon and contextualize the current findings for longer operating times with multiple injections. In contrast, surface area ratio, shown in Figure 6.29b, has little impact on the final deposit volume, showing only a small increase with larger surface area ratios.

Figure 6.31 shows that, similar to deposit mass, the more hydrophobic a rough surface becomes, the greater the remaining deposit volume due to inhibited evaporation and decomposition. Additionally, hydrophobic surfaces promote rapid solidification at the liquid-gas interface due to better distribution of urea along the liquid surface. This rapid formation of an outer solid layer entraps any remaining liquid inside – a phenomenon not observed on non-hydrophobic surfaces. This has been demonstrated by Schmid et al. [114] and corroborated by own studies [115]. Figure 6.32a shows such a rapidly solidifying droplet interface. Although the entrapped liquid

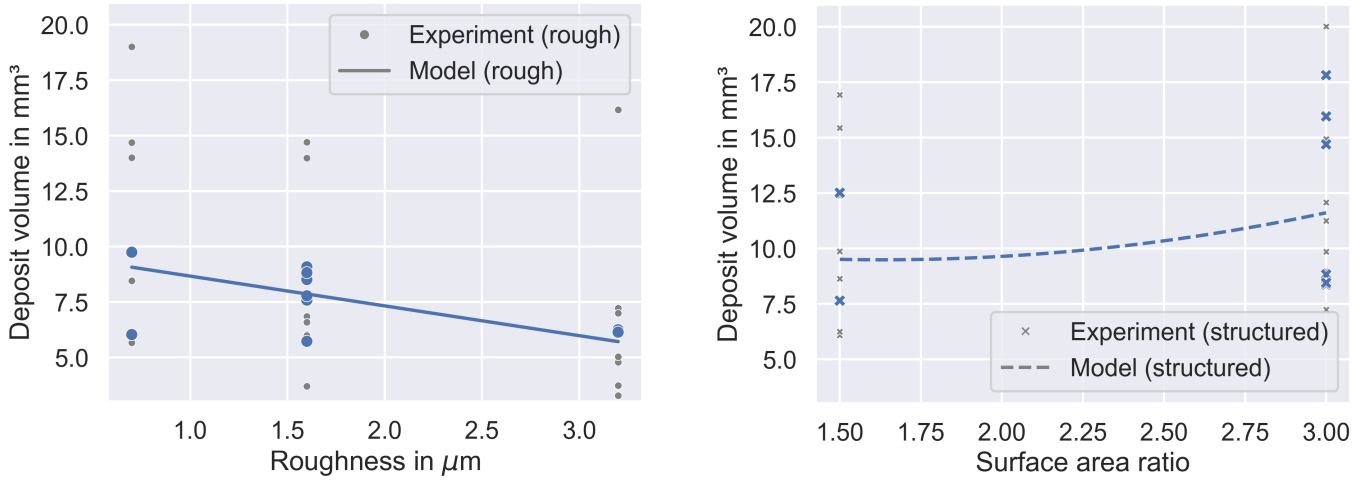

(a) Roughness as independent variable

(b) Surface area ratio as independent variable

Figure 6.29.: Model response for deposit volume depending on surface topography features

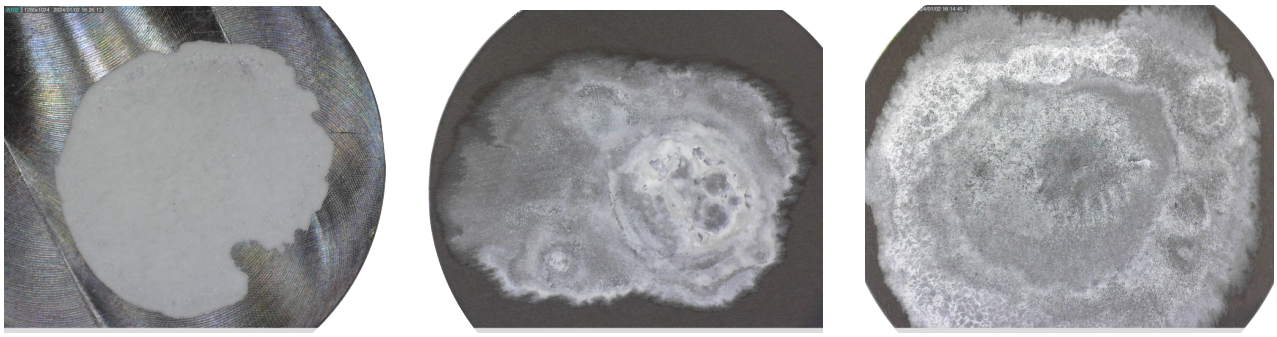

(a) $Ra = 0.7\,\mu\text{m}$

(b) $Ra = 1.6\,\mu\text{m}$

(c) $Ra = 3.2\,\mu\text{m}$

Figure 6.30.: Final deposits on uncoated surfaces of different roughnesses

eventually solidifies or decomposes and diffuses through the outer layer, the resulting porous crystal structure leads to large deposit volumes. In contrast, spread-out droplets on well-wettable surfaces solidify much slower, often with crystal growth initially confined to the three-phase contact line due to local supersaturation from capillary flow [7]. Figure 6.32b shows this slow crystallization sequence.

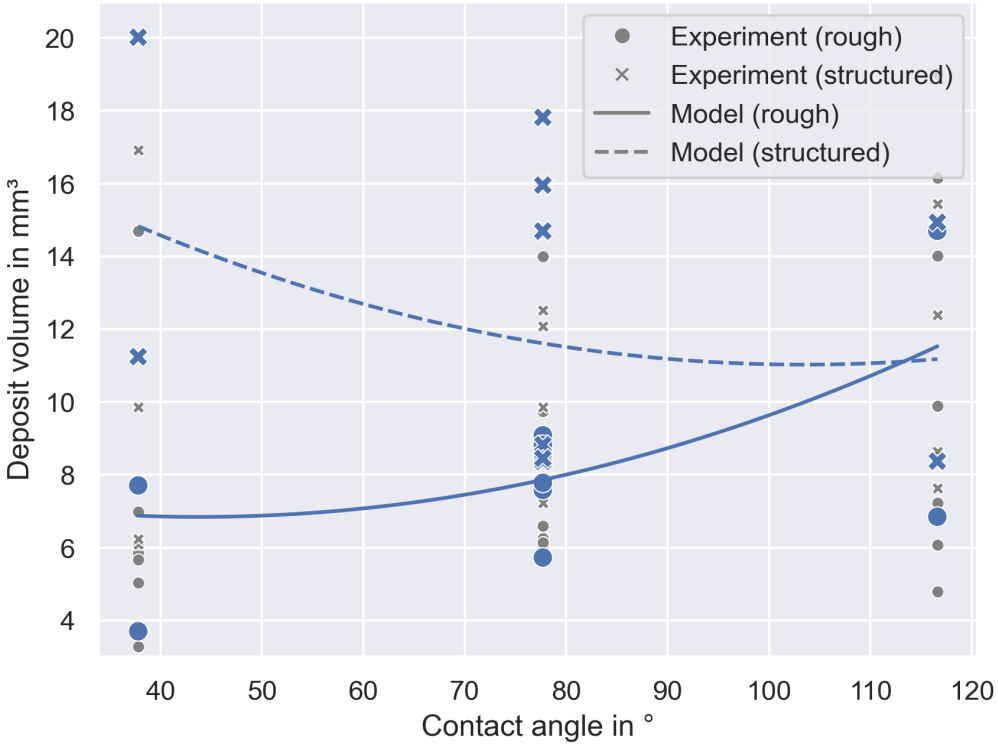

Figure 6.31.: Model response for deposit volume versus contact angle

Figure 6.33c illustrates a rapidly solidified droplet on a hydrophobically coated surface. The deposit retained the interface of the previous liquid, thereby enhancing the final outer deposit volume. This contrasts with the more spread-out and thin deposits from uncoated and hydrophilic surfaces in Figure 6.33a–b, which do not allow for hollow interiors.

On structured surfaces, hydrophilic coatings result in larger volumes, as Figure 6.31 shows, while uncoated and hydrophobic samples exhibit nearly equal volumes. This is because only hydrophilic surfaces allow immediate wicking into the structure, where subsequent boiling wets the pillar sides extensively along the entire height. Deposits then form on all previously wetted surfaces, with the pillars acting as a framework. This causes deposit growth at much higher positions than it would be possible on rough surfaces. Because the confocal microscope captures only the highest point at each pixel, these elevated deposits, possibly with large hollow volumes beneath, result in the large measured volumes at low contact angles in Figure 6.31.

This explains why the effect of contact angle on structured surfaces is only apparent with the two smaller structure distances, i.e., the highest surface area ratios, as shown in Figure 6.34 for the model including all measurement data. Only for the two highest surface area ratios is there a clear separation between hydrophilic surfaces and those with hydrophobic or no coating. With the widest distance, i.e., the smallest R_A, the structure cannot act as the aforementioned framework. The resulting deposits on hydrophilic surfaces with

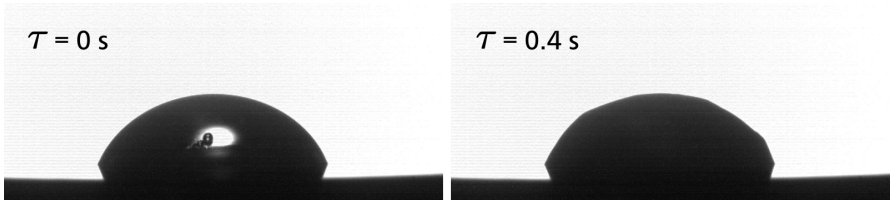

(a) Rapid solidification on hydrophobic surface

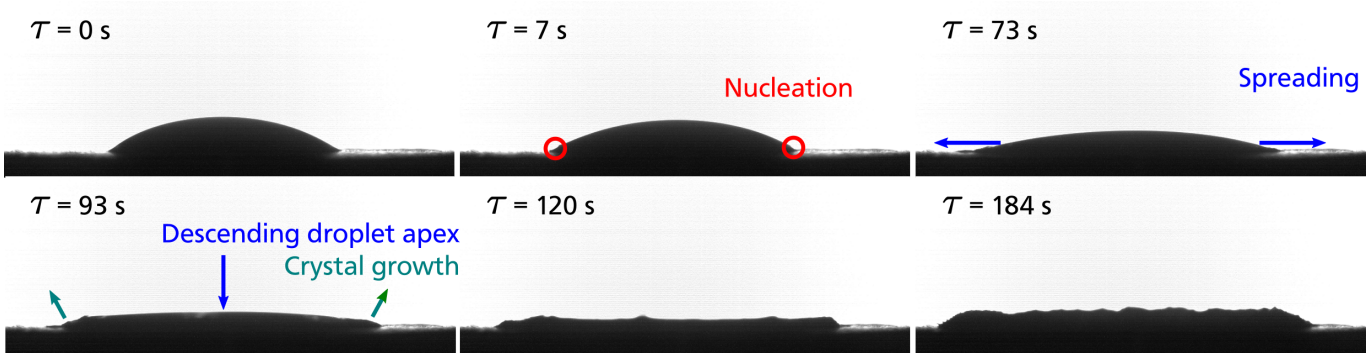

(b) Very slow crystallization on rough, well wettable surface

Figure 6.32.: Comparison of the solidification process of highly concentrated UWS on substrates of different wettability, taken from [115]

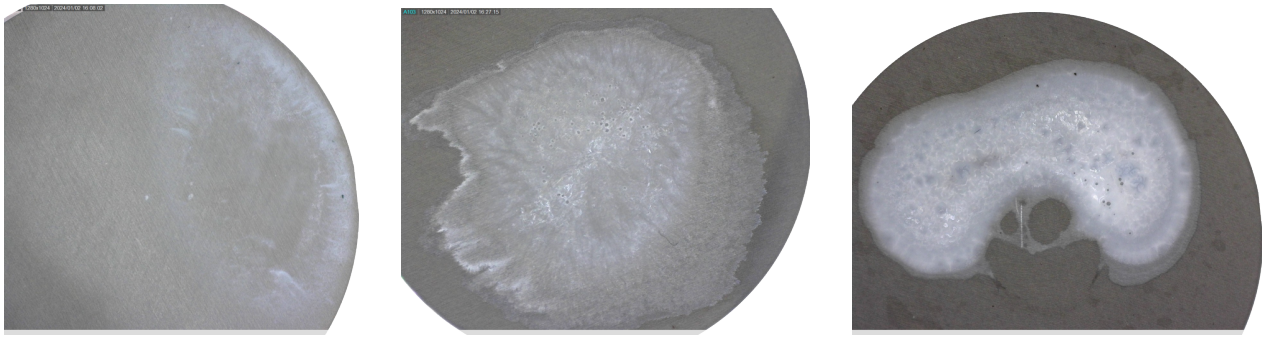

(a) Hydrophilic coating **(b)** No coating **(c)** Hydrophobic coating

Figure 6.33.: Comparison of final deposits on rough surfaces depending on the surface coating

intermediate and high surface area ratios are much less dense but have a higher overall volume. This is evident in the photographs in Figure 6.34, which show much more porous deposits on the hydrophilic sample. In comparison, boiling on uncoated and hydrophobic structures mainly occurs on top of the pillars, leading to less wetting of additional pillar surfaces by the expanding liquid. Consequently, there are fewer areas, especially in the upward direction, from which deposits will later grow.

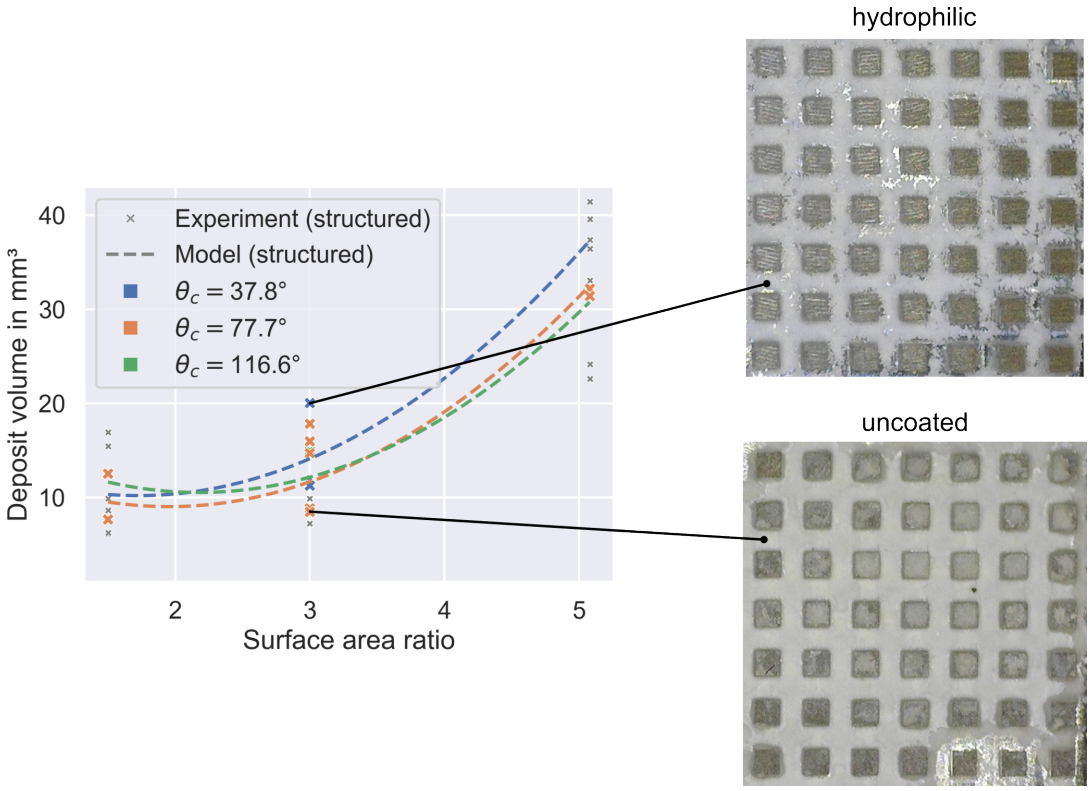

Figure 6.34.: Full model response to deposit volume for varying surface area ratios and photographs of selected deposits

Figure 6.35 presents experimental data illustrating the relationship between final deposit mass and respective deposit volume. Unlike the clear relationship observed between deposit mass and area in Figure 6.26, the relationship between deposit mass and volume is more ambiguous, characterized by larger scatter, particularly for volumes $\geq 10\,\mathrm{mm}^3$. This variability is less pronounced at $T_{\mathrm{wall}} = 200\,°\mathrm{C}$ and more evident at the lower temperature.

At 200 °C, deposit mass appears to plateau around 7.5 mm^3 for all durations, indicating that additional deposit volume does not necessarily correspond to increased deposit mass. This phenomenon may be attributed to the increasing porosity of the resulting deposits, as discussed previously. A similar trend is observed at 150 °C, particularly for structured surfaces, where deposit mass decreases continuously with increasing volume, as depicted in Figure 6.35c.

When optimizing system and operating parameters to minimize deposits, both deposit mass and volume on rough surfaces benefit from similar settings. This suggests that selecting surface characteristics to minimize mass will also minimize the volume of final deposits. However, for structured deposits, minimal mass

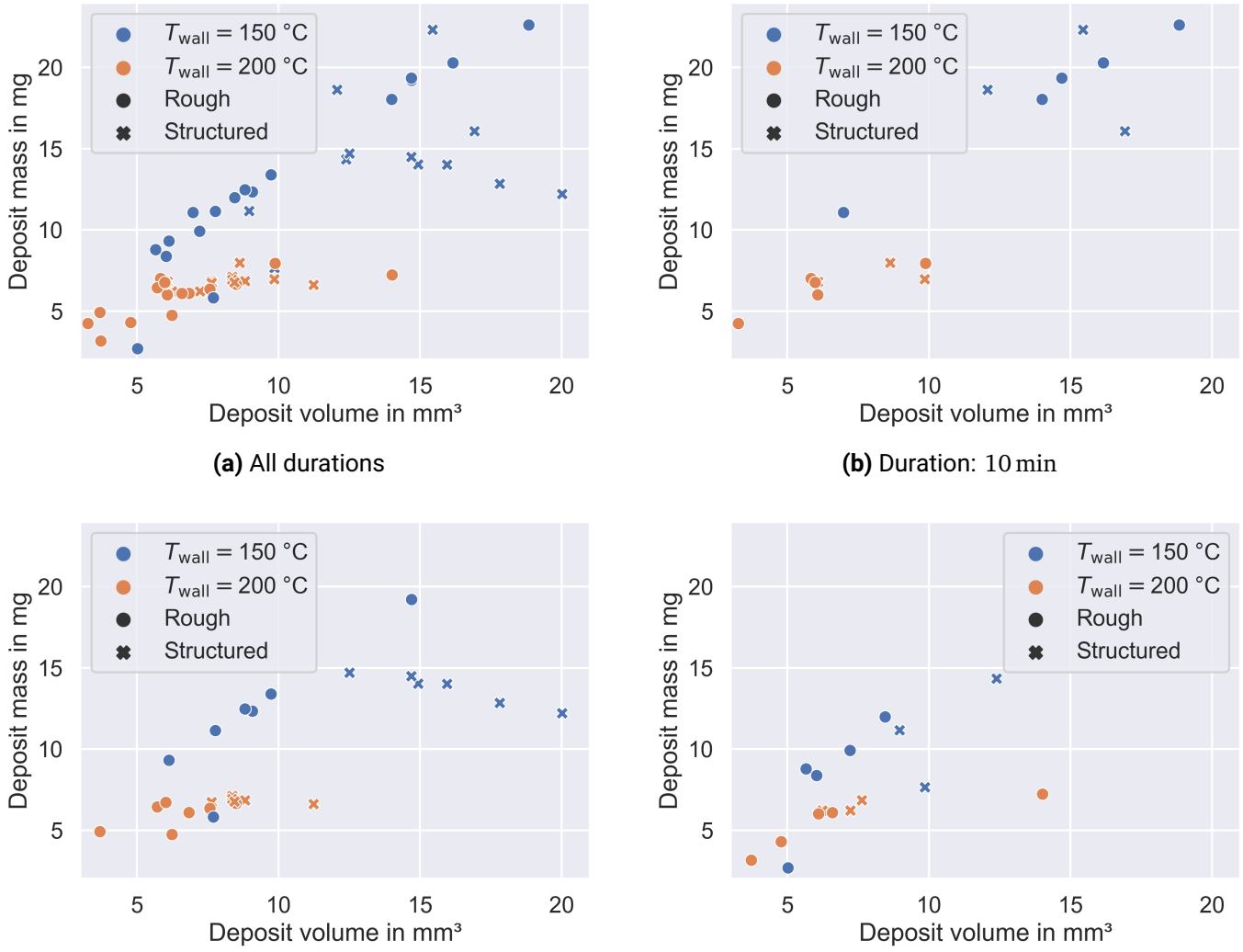

(a) All durations

(b) Duration: 10 min

(c) Duration: 30 min

(d) Duration: 60 min

Figure 6.35.: Experimental results for the deposit mass against the final deposit volume, subdivided according to residence time

is observed alongside maximum volumes, especially at lower wall temperatures, highlighting conflicting optimization objectives in such cases.

6.2.4. Summary

The experimental and model results can be summarized as follows:

1. **Deposit mass:** The mass of deposits from evaporating UWS wall films is significantly influenced by wall temperature and duration. Unfortunately, these factors are challenging to control in a practical application. Rough surfaces generally exhibit lower deposit mass compared to structured surfaces, particularly benefiting from hydrophilic coatings. Notably, even highly rough, hydrophobically coated surfaces can yield similar deposit mass as structured surfaces while at the same time minimizing deposit area.

2. **Deposit area:** Structured surfaces consistently result in smaller deposit areas due to the inhibition of liquid spreading by structure pillars, whereby uncoated and hydrophobic surfaces perform similarly well in this regard. Care should be taken with very small structure distances due to enhanced spreading facilitated by capillary forces. On rough surfaces, the contact angle exhibits a more pronounced effect on the deposit area, with better wetting leading to larger areas. This effect is enhanced with increasing roughness values.

3. **Deposit volume:** On rough surfaces, deposit volume follows trends similar to deposit mass, consistently being smaller than on structured surfaces. Conversely, on structured surfaces, volume is highest with hydrophilic coatings and increases with smaller structure distances. This behavior is attributed to unique phenomena on structured surfaces such as boiling within structures or deposits growing from upper parts of the pillars and being supported by the structure, especially with smaller distances.

6.3. Optimization

The above presented development of predictive models for deposit severity, characterized by mass, area, and volume, enables the comparison of various surface characteristics to identify optimal configurations for the desired use case. Such models are invaluable as they reduce the need for costly prototype building and testing, potentially avoiding suboptimal outcomes. This is particularly crucial given the complex interactions, such as coatings on structured surfaces, which can yield unexpected results.

However, the sometimes significant influence of operating conditions, such as wall temperature, and the wide variety of resulting deposits emphasize that consistent control of the outcome remains a challenge. Moreover, minimizing deposits often involves trade-offs between metrics such as volume and mass. Therefore, while modeling deposit behavior and optimization based on these models are powerful tools, expert domain knowledge and precise goal-setting remain essential. Factors like available technologies and cost considerations must also be weighed in prioritizing target outcomes.

The following section will detail the development of an optimization tool, utilizing the presented data and models, to facilitate informed decision-making in deposit mitigation strategies.

6.3.1. Multi-objective optimization

The introduced problem of optimizing deposit characteristics involves three objective functions: deposit mass, area, and volume, each represented by their respective linear regression model in Section 6.2.1, Section 6.2.2 and Section 6.2.3. This constitutes a multi-objective problem, more generally formulated as:

$$\min_{\vec{x}\in\mathbf{X}} f(\vec{x}) = (f_1(\vec{x}), f_2(\vec{x}), \ldots, f_k(\vec{x})). \tag{6.1}$$

As a result of its multi-objective nature, there is typically no single optimal solution. Instead, one can only determine what are known as Pareto-optimal solutions, which means that for any solution of the multi-objective function $f(\vec{x}^*)$ there is no other solution with $f(\vec{x}) \leq f(\vec{x}^*)$ [104]. Mathematically, these Pareto-optimal solutions, also known as non-dominated solutions, are equivalently optimal in the absence of additional information. In other words, none of the individual functions that compose $f(\vec{x})$ (i. e. the regression functions) can be minimized further without one or more of the other functions increasing.

One approach to multi-objective optimization, employed here, is through a weighted sum of the individual, normalized objective functions. This allows for the formulation of a single-objective optimization problem. By adjusting the weights, different Pareto-optimal solutions can be determined, enabling decision-makers to prioritize deposit characteristics based on their specific goals and constraints. This method provides flexibility in comparing and selecting from the Pareto-optimal solutions. [41, 104]

6.3.2. Working principle

The individual functions in the multi-objective optimization problem are defined by three regression models with their respective fitted parameter values, as outlined in Section 5.3. Each model's response is normalized to a value between 0 and 1 using min-max normalization to ensure equal consideration of the respective deposit characteristic. This normalization is crucial to prevent the optimization process from favoring variables with larger numerical values, such as deposit area, which could overshadow the importance of deposit mass due to their opposite responses to the independent variables. Using the experimental data, where y_{min} and y_{max} represent the respective minimum and maximum values for each dependent variable $y \in \{m_{\text{dep}}, A_{\text{dep}}, V_{\text{dep}}\}$, the normalizing function can be defined as:

$$y_{\text{scl}} = \frac{(y - y_{\text{min}})}{(y_{\text{max}} - y_{\text{min}})} \cdot (1 - 0) + 0. \tag{6.2}$$

The addition of 1 and 0 is not strictly necessary but is included for completeness. These can be adjusted if scaling to another range than $[0, 1]$ is needed. Next, weights w_i are assigned to each dependent variable to possibly prioritize specific deposit characteristics. The weighted model functions are then combined into the final target function:

$$f(\vec{x}) = \begin{pmatrix} w_{\text{m}} & w_{\text{A}} & w_{\text{V}} \end{pmatrix} \begin{pmatrix} \hat{m}_{\text{scl}}(\vec{x}) \\ \hat{A}_{\text{scl}}(\vec{x}) \\ \hat{V}_{\text{scl}}(\vec{x}) \end{pmatrix}. \tag{6.3}$$

Here, $\hat{m}_{\text{scl}}$, $\hat{A}_{\text{scl}}$ and $\hat{V}_{\text{scl}}$ denote the scaled predictions from the respective models for deposit mass m_{dep}, deposit area A_{dep}, and deposit volume V_{dep}. All weights are initialized to 1. The resulting function $f(\vec{x})$ can then be optimized with respect to $\vec{x}$.

To initiate optimization, a starting point $\vec{x}_0$ is defined where each independent variable is set to its minimum value, as indicated in Table 3.1. This starting point can be adjusted manually, similar to the weights. Additionally, the surface area ratio R_A is set to an initial value of 0 to constrain optimization to one surface type. If the ratio is instead set to a non-zero value, then roughness Ra must be set to 0, as mixing surface types was not investigated in the study (see Section 3.3).

The bounds for the optimization are set to the extreme values of each independent variable, derived from their minimum and maximum experimental settings in Table 3.1. This ensures that the optimizer remains within the experimentally validated range. The respective morphology feature not under investigation is constrained to 0, preventing its variation by the optimizer.

The target function is then optimized to find its minimum within the bounds of the independent variables, beginning at the defined starting point. The optimization process employs the differential evolution method, developed by Storn and Price [137]. This stochastic approach is favored for its ability to find the global optimum of the target function without relying on gradient-based methods. Unlike methods such as the *Broyden–Fletcher–Goldfarb–Shanno* (BFGS) algorithm [100, pp. 136], which require the function's first derivative and converge to local minima, differential evolution seeks to achieve the best possible solution within the specified bounds.

Due to its stochastic nature, differential evolution requires a substantial number of function evaluations, resulting in a slower optimization process. Typically, it takes approximately 20 s to determine the optimal variable settings. This is much slower than using local methods like BFGS, which can find an optimum within 1 s. Given the potential variability in results from local optimization methods due to local minima and the still acceptable time frame for global optimization, differential evolution is chosen as the default method for optimizing the target function in this study.

6.3.3. Demonstrator for deposit optimization

To make the determination of an optimal set of independent variables accessible, a dedicated application was developed using the Python programming language. This application features an interface that allows users to input custom weights, set the bounds for the independent variables and define a custom starting point. This prototype is meant to demonstrate the potential of utilizing the experimental and modeling results in practical engineering contexts, making the scientific work accessible for implementation. It is not intended to resemble a final product. Note that calculated numerical values and optimization results obtained from this application are subject to errors due to measurement inaccuracies and model residuals. With the current database, any results should be used only as estimates for comparing different designs or choosing between various possible approaches. However, the Python code written to train the models and provide the optimizer application is specifically designed to allow for extendability by additional measurement data to further improve the applications potential practicality.

The user interface of the application is depicted in Figure 6.36. Upon launching the application, it loads the trained models and presets the starting points, weights, and ranges for the variables as described. Users can modify any of the input values within the experimental ranges, as shown in the highlighted section (1) of Figure 6.37. By clicking the “Calculate” button, the program computes and returns the predicted deposit values from the three individual models for the specified independent variables. These results are displayed on the right side of the interface (2). Note that the input for the structured surface morphology is given by the structure distance instead of the surface area ratio. Equivalently, the optimal surface area ratio is transformed to its corresponding structure distance. In both cases, this serves to simplify the visualization of the variable.

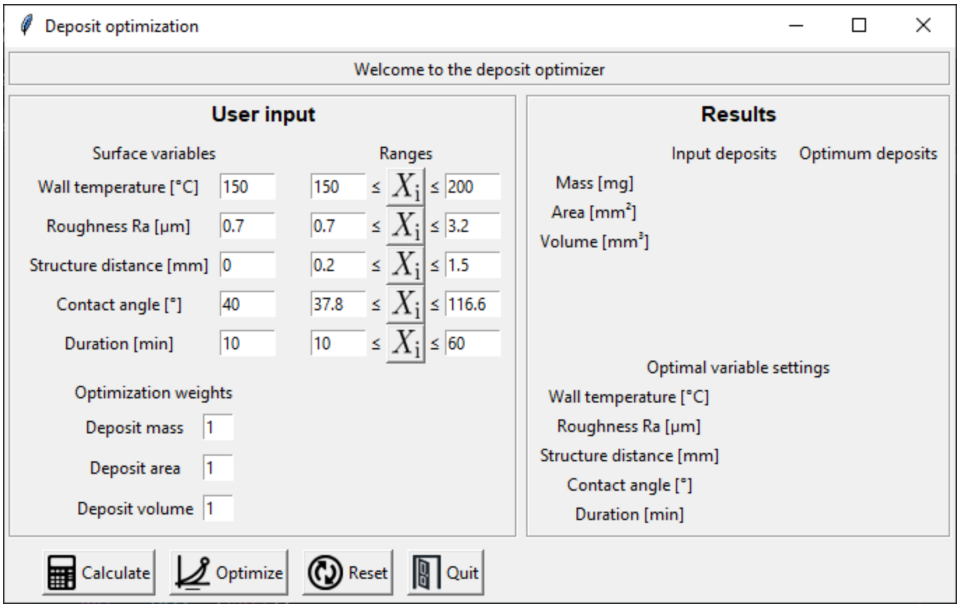

Figure 6.36.: User interface of the optimizer application after starting the program

To find the optimal variables for minimizing deposit severity, users have several options. By clicking the X_i button, certain variables can be locked, preventing them from being altered during the optimization process. This is indicated by the button symbol changing to a lock ((1) in Figure 6.38). This feature is useful when some surface characteristics cannot be changed, for example due to overall system design constraints or cost considerations. Additionally, the predefined range for variable variation can be manually adjusted (2), provided that the new range remains within the experimental boundaries. Finally, the weights can be adjusted arbitrarily (3) to prioritize individual characteristics of the deposits, allowing for a more tailored optimization process.

Clicking the “Optimize” button starts the optimization algorithm, which uses the model responses to determine optimal settings for the independent variables (4). The application then calculates the respective deposit values and displays the percentage improvement over the results obtained from the initial input values (5). To illustrate the application’s usage, five exemplary scenarios are considered:

Scenario 1 “Overall, rough”: This scenario identifies the overall optimal solution across the entire range of variables for rough surfaces with equal weights.

Scenario 2 “Overall, structured”: Similar to the first scenario, this one identifies the overall optimal solution but for structured surfaces.

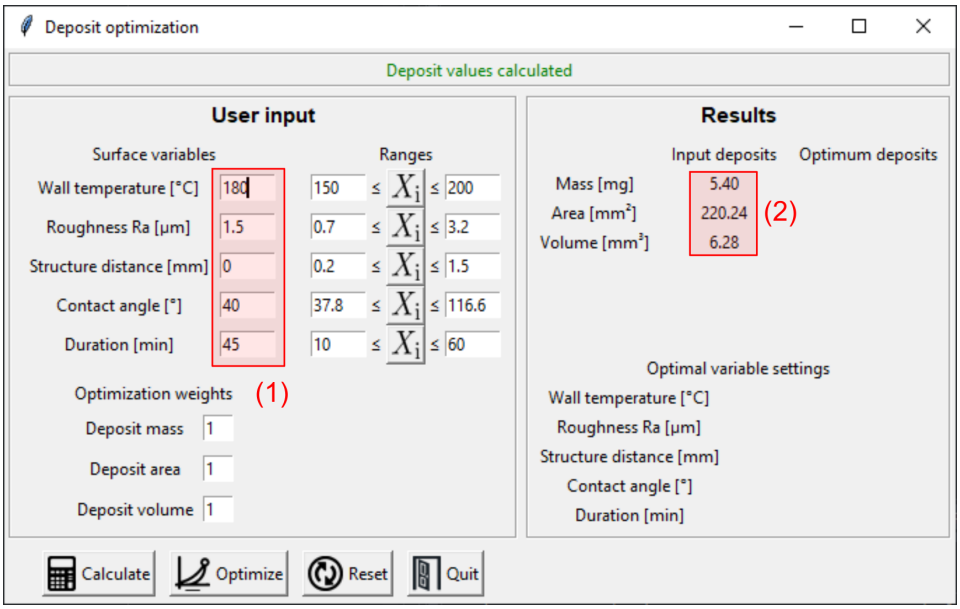

Figure 6.37.: Custom inputs can be given for the independent variables (1) and the deposit characteristics will be calculated based on these inputs (2)

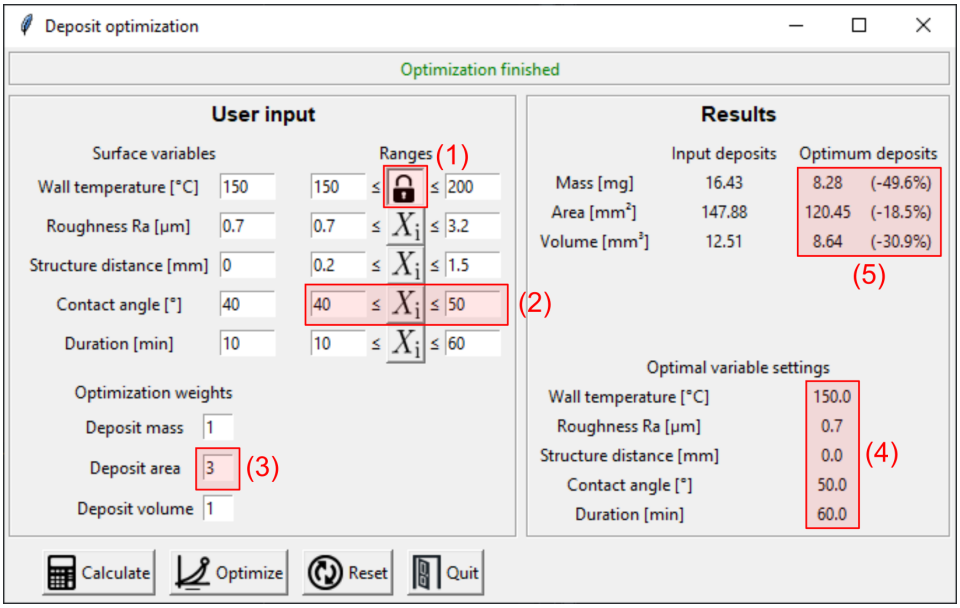

Figure 6.38.: By locking variables from being varied (1), defining ranges (2) and providing different weights (3), the optimal conditions can be determined (4) together with the resulting deposits (5)

Scenario 3 "Critical conditions, rough": This scenario determines the optimal solution for conditions of 150 °C and a duration of 10 min, representing critical conditions for deposit formation with low wall temperatures and short durations due to multiple injections. Here, the deposit mass is given double weight to emphasize the goal of reducing the overall mass.

Scenario 4 "Critical conditions, structured": Similar to Scenario 3, this scenario focuses on structured surfaces under critical conditions.

Scenario 5 "Area focus": In this scenario, the deposit area is prioritized by setting its weight to 5. This approach might be advantageous in applications where it is possible to include removable parts in sections highly prone to deposit formation, such as mixer elements or the wall opposite the injector. These sections could be disassembled and cleaned regularly, so reducing the overall area of deposits can help minimize the geometry of these parts.

The results of the optimization for each scenario are summarized in Table 6.1. For the overall optimization, the outcomes for structured (Scenario 1) and rough surfaces (Scenario 2) are very similar. As expected from the results presented in Section 6.2, the optimal conditions for both scenarios feature the highest wall temperature and long residence times. In contrast, the optimal roughness is found at the lowest possible value, likely due to its significant impact on reducing the final deposit area, although this is accompanied by a slightly increased deposit mass. The optimal structure distance, however, is relatively large at $W = 0.9\,\text{mm}$, corresponding to a surface area ratio of $R_A = 2$. Figure 6.22b and Figure 6.29b show that up to this value, no significant increase in deposit area or volume occurs, while the deposit mass is slightly reduced compared to the largest structure spacing (i.e., the smallest R_A).

	Scenario 1	**Scenario 2**	**Scenario 3**	**Scenario 4**	**Scenario 5**
$\hat{m}_{\text{dep}}$ [mg]	6.8	6.4	11.3	17.5	11.6
$\hat{A}_{\text{dep}}$ [mm^2]	63.4	57.0	368.7	97.8	30.9
$\hat{V}_{\text{dep}}$ [mm^3]	6.3	5.9	7.4	14.32	7.1
T_{wall} [°C]	200	200	150	150	150
Ra [µm]	0.7	0.0	3.2	0.0	0.0
W [mm]	0.0	0.9	0.0	0.9	0.7
θ_{c} [°]	86.0	98.1	37.8	46.9	110.6
$\Delta\tau$ [min]	45.9	51.9	10.0	10.0	60.0

Table 6.1.: Optimization results for five possible scenarios of reducing deposit severity

The optimal contact angles for both surface types are approximately 90°, with the slightly lower value on rough surfaces and the higher value on structured surfaces reflecting the opposing behavior of the two surface types, as seen in Figure 6.31. This mid-range result also highlights the competing effects of coating on deposit mass (which increases with higher contact angles) and deposit area (which decreases with higher contact angles).

Interestingly, the optimal structured surface (Scenario 2) results in a slightly lower deposit mass than the rough surface, seemingly contradicting the findings of Section 6.2.1. However, this results from the fact that, without any restrictions, the optimization algorithm exploits the remaining model deviations, identifying an optimum that deviates from the general trend of higher deposit masses on structured surfaces.

When rough and structured surfaces are compared under fixed conditions, as in Scenarios 3 and 4, the previous discussions based on the model curves are confirmed. The rough surface with the highest *Ra* and the lowest possible contact angle results in considerably less deposit mass and volume, although this comes at the cost of a much larger spread of the deposits. Due to its overall small influence on deposit mass, the surface area ratio remains unchanged compared to Scenario 2. Comparing Scenarios 3 and 4 with the first two scenarios emphasizes the impact of the predefined critical conditions, leading to significantly greater deposit mass, area, and volume.

Finally, in Scenario 5, structured surfaces achieve the smallest possible deposit area, potentially giving them an advantage over rough surfaces in certain applications. However, this outcome is highly dependent on the residence time, which is optimized to 60 min. When the duration is fixed at 10 min, the rough surface results in the smallest deposit area, though this outcome is not included in the table.

In conclusion, these findings emphasize the importance of carefully considering specific goals and constraints when selecting surface characteristics for practical engineering applications.

CHAPTER 7

Summary, Conclusion and Outlook

The findings of this work contribute to improving the necessary exhaust gas treatment for combustion processes, thereby further reducing pollutant emissions. Specifically, the study aims to prevent undesirable deposit formation from injected urea-water solution during selective catalytic reduction for the reduction of NO_x emissions. The investigation focuses on the surface characteristics of the system walls, where liquid films form and evaporate, leading to solid residue formation. The objective was to identify the wall surface characteristics whose optimization offers the greatest potential for reducing deposit formation. Additionally, modeling the effects of influencing factors and their complex interactions was intended to enable the determination of optimal wall characteristics depending on the specific requirements.

The conducted experiments were based on a suitable experimental design, enabling the collection of a sufficient dataset for model development with a feasible number of trials. The studied factors include the wall temperature, the heating duration of the liquid, the surface wettability due to chemical treatment, and the surface morphology. Specifically, two different surface types were investigated: rough surfaces with various mean roughness values (Ra) and surfaces with milled sub-millimeter structures with varying structure spacings. To capture nonlinear effects, three settings were chosen for each of these variables, except for the wall temperature, with only two different values. These settings were strategically combined to determine all possible interactions between the individual factors. By employing an adjusted experimental plan following the central-composite design, the necessary number of trials was reduced from 108 to 68, without compromising the ability to analyze the results.

The selected target variables for the investigations were the mass of the formed deposits, the deposit volume, and the wall area covered by deposits. These variables cover a wide range of potential challenges posed by deposit formation and allow for a focused analysis of the collected data depending on the application and objectives. The experiments were conducted as generic experiments in a test cell, which allowed precise control of all relevant boundary conditions. The system walls on which the deposits form in a practical application were represented by specially prepared samples made from the aluminum-magnesium alloy AlMg4.5Mn0.7. The test fluid, a urea-water solution with 32 wt% urea, was applied dropwise onto the heated samples using a needle and a syringe pump. After the specified heating duration at the respective wall temperature, the samples were removed and characterized using an analytical balance and 3D confocal microscopy. This procedure ensures that the deposit characteristics are determined with high precision, while excluding any unwanted effects of confounding variables.

The experimentally collected dataset served as the foundation for developing three models using multivariate linear regression. Each model aims to predict one of the chosen deposit properties based on the values of the investigated wall surface characteristics. Additionally, these models provide the capability to quantify the complex effects of interacting influences, thereby contributing to a better understanding of the deposit formation process. To refine this analysis, various preprocessing approaches were compared, and a knowledge-based feature selection was conducted. The resulting models demonstrate excellent agreement with the data, reflected in high R^2 values. The prediction accuracy for unknown data is also very good, especially considering the relatively small dataset. The practical applicability of the study's results was ultimately demonstrated through a prototype application. This application determines optimal configurations for the system walls based on user inputs to minimize potential deposits, while also allowing for manual adjustments of target specifications or constraints.

The analysis of the model results indicates that both the deposit mass and volume are most significantly influenced by the wall temperature, aligning with numerous insights from the literature [17]. In contrast, wall temperature is irrelevant when it comes to minimizing the wall area covered by deposits, and the same applies to the heating duration. Furthermore, heating duration becomes insignificant for both mass and volume when wall temperatures are increased to 200 °C.

The morphological characteristics of the surfaces significantly affect film spreading, both during initial wetting and the boiling phase. As predicted by the Wenzel model, these effects can be strongly amplified by a chemical coating, enhancing both wetting and non-wetting behavior. On structured surfaces, the interactions are less straightforward due to the additional influence of capillary forces. When the width of the milled channels is increased, the spreading film increasingly pins at the pillars, reducing the overall impact of coatings on the wetting.

More generally, maximizing the spreading of the wall film through appropriate combination of roughness and coating is most effective for minimizing deposit mass and volume. In comparison, structured surfaces consistently exhibit limited film spread, resulting in higher values for deposit mass and volume but less wall area covered by the deposits. These results also highlight that different deposit characteristics, such as the mass and the covered area, can behave oppositely, complicating deposit mitigation efforts. Therefore, approaches such as the demonstrated optimization are particularly promising to further improve existing processes and designs.

Phenomenological observations of wetting, evaporation, and deposit formation during the experiments reveal additional potentials. Ideally, process walls should be designed to be poorly wetting to minimize wall film formation and the associated deposit formation from the beginning. This approach primarily aims to induce the Leidenfrost effect at the lowest possible temperatures [117]. The present study demonstrates that hydrophobically coated samples with high roughness values initially exhibit poor wetting, but result in delayed spreading of a deposited film upon reaching approximately 150 °C. This can be attributed to the altered chemical composition of the liquid due to thermal decomposition, which reduces the effectiveness of the coating. By strategically combining chemical surface treatment and surface morphology, the initial liquid-wall interaction could be shifted towards non-wetting regimes, while maximizing film spreading if wetting does occur. Ultimately, this can minimize the mass of unavoidable deposits.

Another interesting phenomenon is the difference between structures that allow or do not allow wicking of the applied liquid, which alters the boiling behavior. Additionally, surface structures can enhance evaporation and thermal decomposition through better heat flux distribution. Due to the large number of relevant variables, only

one structure type with varying pillar spacings was investigated here. However, numerous other geometries are conceivable and provide opportunities for future research.

Reflecting on the scientific questions formulated in Section 2.3, this study has demonstrated that the employed methodology is highly effective for investigating a comprehensive range of influences on deposit formation by urea-water solution, quantifying the effects, and making the results accessible for practical application. The core findings presented above provide answers to the question of how deposit formation can be prevented or minimized through suitable wall characteristics.

As with any scientific work, trade-offs were necessary regarding the number of included variables and their extend. Therefore, the employed method and the written code have been designed to allow for the expansion of the dataset to include additional variables, both independent and dependent (i.e., deposit characteristics). This expansion can further improve the accuracy of the models and broaden the range of influences covered, including, for example, higher temperatures, different wall materials, or other coatings.

Repeated wetting of the same surface with intermittent deposit formation can also be considered highly relevant in practice and would provide insights into the persistence of the observed effects. Employing other modeling approaches from the field of machine learning, such as tree-based models, could further enhance the interpretability of the results, especially as the number of considered variables increases. On the other hand, neural networks might offer even more accurate predictions and better capture the underlying principles, albeit at the expense of interpretability.

The experiments themselves could be expanded to include even more precise control of the surrounding atmosphere, allowing targeted investigations of various pressures, humidity levels, or the influence of shearing gas flows. Using a spray injector could enable the transition to studying sprays or large-area wall films, bringing the findings closer to real-world applications. However, maintaining control of boundary conditions and precision in measurements must always remain the focus to ensure model accuracy.

Ultimately, a comparison of the generic study with investigations that are very close to the practical application, such as those conducted at hot gas test benches, is necessary. This however, requires previously established comparison criteria. One example for this could be power spectral density analysis of the morphology of deposits, which, as shown in another publication [115], shows good potential for comparing urea deposits from different experimental setups.

Bibliography

[1] M. Apel-Paz and A. Marmur. “Spreading of liquids on rough surfaces”. In: *Colloids and Surfaces A: Physicochemical and Engineering Aspects* 146.1-3 (1999), pp. 273–279. ISSN: 0927-7757. DOI: 10.1016/S0927-7757(98)00778-X.

[2] C. Ates, M. Börnhorst, R. Koch, M. Eck, O. Deutschmann, and H.-J. Bauer. “Morphological characterization of urea derived deposits in SCR systems”. In: *Chemical Engineering Journal* 409 (2021), pp. 1–13. ISSN: 13858947. DOI: 10.1016/j.cej.2020.128230.

[3] C. Bai and A. D. Gosman. “Development of Methodology for Spray Impingement Simulation”. In: *International Congress & Exposition*. SAE International, 1995. DOI: 10.4271/950283.

[4] S. Z. Bai, S. G. Lang, K. P. Yuan, Y. Liu, and G. X. Li. “Experimental Study of Urea Depositions in Urea-SCR System”. In: *Advanced Materials Research* 937 (2014), pp. 74–79. DOI: 10.4028/www.scientific.net/AMR.937.74.

[5] S. Becker, H. M. Urbassek, M. Horsch, and H. Hasse. “Contact angle of sessile drops in Lennard-Jones systems”. In: *Langmuir* 30.45 (2014), pp. 13606–13614. ISSN: 0743-7463. DOI: 10.1021/la503974z.

[6] A. Bender, P. Hanichen, P. Stephan, and T. Gambaryan-Roisman. “MODELING CRYSTALLIZATION AND HEAT TRANSFER IN AN EVAPORATING UREA-WATER DROP”. In: pp. 6679–6686. DOI: 10.1615/IHTC16.mpf.022242.

[7] A. Bender, P. Stephan, and T. Gambaryan-Roisman. “A fully coupled numerical model for deposit formation from evaporating urea-water drops”. In: *International Journal of Heat and Mass Transfer* 159 (2020). ISSN: 00179310. DOI: 10.1016/j.ijheatmasstransfer.2020.120069.

[8] J. D. Bernardin and I. Mudawar. “The Leidenfrost Point: Experimental Study and Assessment of Existing Models”. In: *Journal of Heat Transfer* 121.4 (1999), pp. 894–903. ISSN: 0022-1481. DOI: 10.1115/1.2826080.

[9] J. D. Bernardin, I. Mudawar, C. B. Walsh, and E. I. Franses. “Contact angle temperature dependence for water droplets on practical aluminum surfaces”. In: *International Journal of Heat and Mass Transfer* 40.5 (1997), pp. 1017–1033. ISSN: 00179310. DOI: 10.1016/0017-9310(96)00184-6.

[10] A. M. Bernhard, D. Peitz, M. Elsener, A. Wokaun, and O. Kröcher. “Hydrolysis and thermolysis of urea and its decomposition byproducts biuret, cyanuric acid and melamine over anatase TiO2”. In: *Applied Catalysis B: Environmental* 115-116 (2012), pp. 129–137. ISSN: 09263373. DOI: 10.1016/j.apcatb.2011.12.013.

[11] BIPM, IEC, IFCC, ILAC, ISO, IUPAC, IUPAP, and OIML. *Evaluation of measurement data — Guide to the expression of uncertainty in measurement*. Joint Committee for Guides in Metrology, JCGM, 2008. DOI: 10.59161/JCGM100-2008E.

[12] K. S. Birdi and D. T. Vu. “Wettability and the evaporation rates of fluids from solid surfaces”. In: *Journal of Adhesion Science and Technology* 7.6 (1993), pp. 485–493. ISSN: 0169-4243. DOI: 10.1163/156856193X00808.

[13] F. Birkhold. “Selektive katalytische Reduktion von Stickoxiden in Kraftfahrzeugen: Untersuchung der Einspritzung von Harnstoffwasserlösung”. Dissertation. Karlsruhe: Karlsruhe Institute of Technology, 2007.

[14] F. Birkhold, U. Meingast, P. Wassermann, and O. Deutschmann. “Modeling and simulation of the injection of urea-water-solution for automotive SCR DeNOx-systems”. In: *Applied Catalysis B: Environmental* 70.1-4 (2007), pp. 119–127. ISSN: 09263373. DOI: 10.1016/j.apcatb.2005.12.035.

[15] G. Blasek and G. Bräuer. *Vakuum - Plasma - Technologien: Beschichtung und Modifizierung von Oberflächen*. Bad Saulgau: Leuze, 2010. ISBN: 9783874802574.

[16] M. Boernhorst, X. Cai, M. Woerner, and O. Deutschmann. “Maximum Spreading of Urea Water Solution during Drop Impingement”. In: *CHEMICAL ENGINEERING & TECHNOLOGY* 42.11 (2019), pp. 2419–2427. ISSN: 1521-4125. DOI: 10.1002/ceat.201800755.

[17] M. Börnhorst and O. Deutschmann. “Advances and challenges of ammonia delivery by urea-water sprays in SCR systems”. In: *Progress in Energy and Combustion Science* 87 (2021), p. 100949. ISSN: 03601285. DOI: 10.1016/j.pecs.2021.100949.

[18] M. Börnhorst and O. Deutschmann. “Single droplet impingement of urea water solution on a heated substrate”. In: *International Journal of Heat and Fluid Flow* 69 (2018), pp. 55–61. ISSN: 0142727X. DOI: 10.1016/j.ijheatfluidflow.2017.10.007.

[19] M. Börnhorst, S. Langheck, H. Weickenmeier, C. Dem, R. Suntz, and O. Deutschmann. “Characterization of solid deposits from urea water solution injected into a hot gas test rig”. In: *Chemical Engineering Journal* 377 (2019), p. 119855. ISSN: 13858947. DOI: 10.1016/j.cej.2018.09.016.

[20] M. Börnhorst. “Urea-water sprays in NOx emission control systems: Interaction with solid walls and deposit formation”. Dissertation. Karlsruhe: Karlsruhe Institute of Technology, 2019.

[21] C. Bourges-Monnier and M. E. R. Shanahan. “Influence of Evaporation on Contact Angle”. In: *Langmuir* 11.7 (1995), pp. 2820–2829. ISSN: 0743-7463. DOI: 10.1021/la00007a076.

[22] B. Bozorgmehr and B. T. Murray. “Numerical Simulation of Evaporation of Ethanol-Water Mixture Droplets on Isothermal and Heated Substrates”. In: *ACS omega* 6.19 (2021), pp. 12577–12590. DOI: 10.1021/acsomega.1c00545.

[23] W. Brack. “Untersuchung der Ablagerungsbildung durch Harnstofffolgeprodukte im Abgasstrang”. Dissertation. Karlsruhe: Karlsruhe Institute of Technology, 2016.

[24] W. Brack, B. Heine, F. Birkhold, M. Kruse, and O. Deutschmann. “Formation of Urea-Based Deposits in an Exhaust System: Numerical Predictions and Experimental Observations on a Hot Gas Test Bench”. In: *Emission Control Science and Technology* 2.3 (2016), pp. 115–123. ISSN: 2199-3629. DOI: 10.1007/s40825-016-0042-2.

[25] S. Brandt. *Datenanalyse für Naturwissenschaftler und Ingenieure: Mit statistischen Methoden und Java-Programmen*. 5. Aufl. Lehrbuch. Berlin and Heidelberg: Springer Spektrum, 2013. ISBN: 978-3-642-37664-1. DOI: 10.1007/978-3-642-37664-1.

[26] M. A. Bruning, L. Loeffen, and A. Marin. “Particle monolayer assembly in evaporating salty colloidal droplets”. In: *Physical Review Fluids* 5.8 (2020). DOI: 10.1103/PhysRevFluids.5.083603.

[27] U. Budziankou, M. Börnhorst, C. Kuntz, O. Deutschmann, and T. Lauer. “Deposit Formation from Urea Injection: a Comprehensive Modeling Approach”. In: *Emission Control Science and Technology* 6.2 (2020), pp. 211–227. ISSN: 2199-3629. DOI: 10.1007/s40825-020-00159-x.

[28] H. J. Busscher, A. van Pelt, P. de Boer, H. P. de Jong, and J. Arends. “The effect of surface roughening of polymers on measured contact angles of liquids”. In: *Colloids and Surfaces* 9.4 (1984), pp. 319–331. ISSN: 01666622. DOI: 10.1016/0166-6622(84)80175-4.

[29] A. B. D. Cassie and S. Baxter. “Wettability of porous surfaces”. In: *Transactions of the Faraday Society* 40 (1944), p. 546. ISSN: 0014-7672. DOI: 10.1039/tf9444000546.

[30] A. M. Cazabat and M. A. C. Stuart. “Dynamics of wetting: effects of surface roughness”. In: *The Journal of Physical Chemistry* 90.22 (1986), pp. 5845–5849. ISSN: 0022-3654. DOI: 10.1021/j100280a075.

[31] S. Chandra, M. Di Marzo, Y. M. Qiao, and P. Tartarini. “Effect of liquid-solid contact angle on droplet evaporation”. In: *Fire Safety Journal* 27.2 (1996), pp. 141–158. ISSN: 03797112. DOI: 10.1016/S0379-7112(96)00040-9.

[32] C. Chatfield. “Model Uncertainty, Data Mining and Statistical Inference”. In: *Journal of the Royal Statistical Society. Series A (Statistics in Society)* 158.3 (1995), p. 419. ISSN: 09641998. DOI: 10.2307/2983440.

[33] E. F. Crafton and W. Z. Black. “Heat transfer and evaporation rates of small liquid droplets on heated horizontal surfaces”. In: *International Journal of Heat and Mass Transfer* 47.6-7 (2004), pp. 1187–1200. ISSN: 00179310. DOI: 10.1016/j.ijheatmasstransfer.2003.09.006.

[34] Q. Cui, S. Chandra, and S. McCahan. “The Effect of Dissolving Gases or Solids in Water Droplets Boiling on a Hot Surface”. In: *Journal of Heat Transfer* 123.4 (2001), pp. 719–728. ISSN: 0022-1481. DOI: 10.1115/1.1376394.

[35] S. David, K. Sefiane, and L. Tadrist. “Experimental investigation of the effect of thermal properties of the substrate in the wetting and evaporation of sessile drops”. In: *Colloids and Surfaces A: Physicochemical and Engineering Aspects* 298.1-2 (2007), pp. 108–114. ISSN: 0927-7757. DOI: 10.1016/j.colsurfa.2006.12.018.

[36] Deegan, Bakajin, Dupont, Huber, Nagel, and Witten. “Contact line deposits in an evaporating drop”. In: *Physical review. E, Statistical physics, plasmas, fluids, and related interdisciplinary topics* 62.1 Pt B (2000), pp. 756–765. ISSN: 1063-651X. DOI: 10.1103/physreve.62.756.

[37] R. D. Deegan, O. Bakajin, T. F. Dupont, G. Huber, S. R. Nagel, and T. A. Witten. “Capillary flow as the cause of ring stains from dried liquid drops”. In: *Nature* 389.6653 (1997), pp. 827–829. ISSN: 0028-0836. DOI: 10.1038/39827.

[38] Deutsche Institut für Normung e.V. *DIN EN 60584-1:2014-07, Thermoelemente - Teil 1: Thermospannungen und Grenzabweichungen (IEC 60584-1:2013); Deutsche Fassung EN 60584-1:2013*. Berlin, 2014. DOI: 10.31030/2153253.

[39] Deutsche Institut für Normung e.V. *DIN EN ISO 1302:2002-06, Geometrische Produktspezifikation (GPS) - Angabe der Oberflächenbeschaffenheit in der technischen Produktdokumentation (ISO 1302:2002); Deutsche Fassung EN ISO 1302:2002*. Berlin, 2002. DOI: 10.31030/9227726.

[40] S. Eakle, S. Kroll, A. Yau, J. Gomez, and C. Henry. “Investigation of Urea Derived Deposits Composition in SCR Systems and Their Potential Effect on Overall PM Emissions”. In: *SAE Technical Paper Series*. SAE Technical Paper Series. SAE International400 Commonwealth Drive, Warrendale, PA, United States, 2016. DOI: 10.4271/2016-01-0989.

[41] M. Ehrgott. *Multicriteria Optimization*. Second edition. SpringerLink Bücher. Berlin, Heidelberg: Springer Berlin · Heidelberg, 2005. ISBN: 978-3-540-27659-3. DOI: 10.1007/3-540-27659-9.

[42] Energy Institute. *Statistical Review of World Energy 2024*. London, 2024.

[43] G. M. Faeth. “CURRENT STATUS OF DROPLET AND LIQUID COMBUSTION”. In: *Energy and Combustion Science*. Elsevier, 1979, pp. 149–182. ISBN: 9780080247809. DOI: 10.1016/B978-0-08-024780-9.50013-7.

[44] L. Fahrmeir, C. Heumann, R. Künstler, I. Pigeot, and G. Tutz. *Statistik*. Berlin, Heidelberg: Springer Berlin Heidelberg, 2023. ISBN: 978-3-662-67525-0. DOI: 10.1007/978-3-662-67526-7.

[45] L. Fahrmeir, T. Kneib, and S. Lang. *Regression: Modelle, Methoden und Anwendungen*. 2. Aufl. Statistik und ihre Anwendungen. Heidelberg and Berlin: Springer, 2009. ISBN: 978-3-642-01837-4.

[46] P. L. Flom. “Stopping stepwise: Why stepwise and similar selection methods are bad, and what you should use”. In: *Conference Proceedings*. Ed. by North East SAS Users Group. 2007, pp. 1–7.

[47] I. Frost. *Einfache Lineare Regression: Die Grundlage Für Komplexe Regressionsmodelle Verstehen*. Essentials Ser. Wiesbaden: Springer Fachmedien Wiesbaden GmbH, 2018. ISBN: 978-3-658-19732-2.

[48] T. Gambaryan-Roisman. “Liquids on porous layers: wetting, imbibition and transport processes”. In: *Current Opinion in Colloid & Interface Science* 19.4 (2014), pp. 320–335. ISSN: 13590294. DOI: 10.1016/j.cocis.2014.09.001.

[49] T. Geddert, S. Kipp, W. Augustin, and S. Scholl. “INFLUENCE OF DIFFERENT SURFACE MATERIALS ON NUCLEATION AND CRYSTAL GROWTH IN HEAT EXCHANGERS”. In: *Proceedings of 7th International Conference on Heat Exchanger Fouling and Cleaning - Challenges and Opportunities*. 2007.

[50] P. G. de Gennes. “Wetting: statics and dynamics”. In: *Reviews of Modern Physics* 57.3 (1985), pp. 827–863. ISSN: 0034-6861. DOI: 10.1103/RevModPhys.57.827.

[51] A. Gholijani, T. Gambaryan-Roisman, and P. Stephan. “Experimental investigation of hydrodynamics and heat transport during horizontal coalescence of two drops impinging a hot wall”. In: *Experimental Thermal and Fluid Science* 131 (2022), p. 110520. ISSN: 08941777. DOI: 10.1016/j.expthermflusci.2021.110520.

[52] J. W. Gibbs. “On the equilibrium of heterogeneous substances”. In: *American Journal of Science and Arts* s3-16 (1878), pp. 441–458.

[53] K. Gleason, H. Voota, and S. A. Putnam. “Steady-state droplet evaporation: Contact angle influence on the evaporation efficiency”. In: *International Journal of Heat and Mass Transfer* 101 (2016), pp. 418–426. ISSN: 00179310. DOI: 10.1016/j.ijheatmasstransfer.2016.04.075.

[54] W. R. Good. “A comparison of contact angle interpretations”. In: *Journal of colloid and interface science* 44.1 (1973), pp. 63–71. DOI: 10.1016/0021-9797(73)90192-6.

[55] P. Grosfils and J. F. Lutsko. “Impact of Surface Roughness on Crystal Nucleation”. In: *Crystals* 11.1 (2021), p. 4. DOI: 10.3390/cryst11010004.

[56] S. Grout, J.-B. Blaisot, K. Pajot, and G. Osbat. “Experimental investigation on the injection of an urea–water solution in hot air stream for the SCR application: Evaporation and spray/wall interaction”. In: *Fuel* 106 (2013), pp. 166–177. ISSN: 00162361. DOI: 10.1016/j.fuel.2012.09.022.

[57] J. Hardin and J. Kloke. “Statistical Analyses”. In: *Current Protocols Essential Laboratory Techniques* 14.1 (2017). ISSN: 1948-3430. DOI: 10.1002/cpet.10.

[58] F. E. Harrell. *Regression modeling strategies: With applications to linear models, logistic and ordinal regression, and survival analysis*. Second edition. Springer series in statistics. Cham, Heidelberg, and New York: Springer, 2015. ISBN: 978-3-319-19425-7.

[59] T. Hastie, R. Tibshirani, and J. H. Friedman. *The elements of statistical learning: Data mining, inference, and prediction*. 2. ed., corr. at 4. print. Springer series in statistics. New York, NY: Springer, 2009. ISBN: 978-0-387-84858-7.

[60] G. He, V. Bhamidi, R. B. H. Tan, P. J. A. Kenis, and C. F. Zukoski. “Determination of Critical Supersaturation from Microdroplet Evaporation Experiments”. In: *Crystal Growth & Design* 6.5 (2006), pp. 1175–1180. ISSN: 1528-7483. DOI: 10.1021/cg050681f.

[61] M. Heinz, P. Stephan, and T. Gambaryan-Roisman. “Influence of nanofiber coating thickness and drop volume on spreading, imbibition, and evaporation”. In: *Colloids and Surfaces A: Physicochemical and Engineering Aspects* (2021), p. 127450. ISSN: 0927-7757. DOI: 10.1016/j.colsurfa.2021.127450.

[62] A. von der Heyden. “Charakterisierung von Flüssigkeitsfilmen mittels Laserabsorptionsspektroskopie in der Abgasnachbehandlung”. Dissertation. Darmstadt: Technische Universität Darmstadt, 2023. DOI: 10.26083/TUPRINTS-00024072.

[63] C.-C. Hsu, T.-W. Su, C.-H. Wu, L.-S. Kuo, and P.-H. Chen. “Influence of surface temperature and wettability on droplet evaporation”. In: *Applied Physics Letters* 106.14 (2015), p. 141602. ISSN: 0003-6951. DOI: 10.1063/1.4917291.

[64] H. Hu and R. G. Larson. “Evaporation of a Sessile Droplet on a Substrate”. In: *The Journal of Physical Chemistry B* 106.6 (2002), pp. 1334–1344. ISSN: 1520-6106. DOI: 10.1021/jp0118322.

[65] H. Hu and R. G. Larson. “Marangoni effect reverses coffee-ring depositions”. In: *The Journal of Physical Chemistry B* 110.14 (2006), pp. 7090–7094. ISSN: 1520-6106. DOI: 10.1021/jp0609232.

[66] M. Iwasaki and H. Shinjoh. “A comparative study of “standard”, “fast” and “NO2” SCR reactions over Fe/zeolite catalyst”. In: *Applied Catalysis A: General* 390.1-2 (2010), pp. 71–77. ISSN: 0926860X. DOI: 10.1016/j.apcata.2010.09.034.

[67] G. James, D. Witten, T. Hastie, and R. Tibshirani. *An introduction to statistical learning: With applications in R*. Second edition. Springer texts in statistics. New York: Springer, 2021. ISBN: 9781071614181.

[68] R. E. Johnson and R. H. Dettre. “Contact Angle Hysteresis”. In: *Contact angle, wettability and adhesion*. Ed. by F. M. Fowkes. Vol. 43. Advances in chemistry series. Washington, District of Columbia: American Chemical Society, 1964, pp. 112–135. ISBN: 9780841200449. DOI: 10.1021/ba-1964-0043.ch007.

[69] D. Kaya, V. A. Belyi, and M. Muthukumar. “Pattern formation in drying droplets of polyelectrolyte and salt”. In: *The Journal of chemical physics* 133.11 (2010), p. 114905. DOI: 10.1063/1.3493687.

[70] R. Killick, P. Fearnhead, and I. A. Eckley. “Optimal Detection of Changepoints With a Linear Computational Cost”. In: *Journal of the American Statistical Association* 107.500 (2012), pp. 1590–1598. ISSN: 0162-1459. DOI: 10.1080/01621459.2012.737745.

[71] S. H. A. Kim, J. Y. Kang, H. S. Ahn, H. J. Jo, and M. H. Kim. “STUDY OF LEIDENFROST MECHANISM IN DROPLET IMPACTING ON HYDROPHILIC AND HYDROPHOBIC SURFACES”. In: *International Journal of Air-Conditioning and Refrigeration* 21.04 (2013), p. 1350028. ISSN: 2010-1325. DOI: 10.1142/S2010132513500284.

[72] W. Kleppmann. *Versuchsplanung: Produkte und Prozesse optimieren*. 10., überarbeitete Auflage. Hanser eLibrary. München: Hanser, 2020. ISBN: 9783446463974. DOI: 10.3139/9783446463974?locatt=mode:legacy.

[73] R. Kohavi. “A Study of Cross-Validation and Bootstrap for Accuracy Estimation and Model Selection”. In: *Proceedings of the 14th International Joint Conference on Artificial Intelligence*. Ed. by Morgan Kaufmann Publishers Inc. 1995, pp. 1137–1143.

[74] S. Kontin, A. Höfler, R. Koch, and H.-J. Bauer. “Heat and Mass Transfer accompanied by Crystallisation of single Particles containing Urea-water-solution”. In: *23rd Annual Conference on Liquid Atomization and Spray Systems*. 2010.

[75] K. J. Kubiak, M. Wilson, T. G. Mathia, and P. Carval. “Wettability versus roughness of engineering surfaces”. In: *Wear* 271.3-4 (2011), pp. 523–528. ISSN: 00431648. DOI: 10.1016/j.wear.2010.03.029.

[76] U. Kuckartz. *Statistik: Eine verständliche Einführung*. 2., überarb. Aufl. 2013. SpringerLink Bücher. Wiesbaden: VS Verlag für Sozialwissenschaften, 2013. ISBN: 9783531198903. DOI: 10.1007/978-3-531-19890-3.

[77] C. Kuhn, D. Schweigert, C. Kuntz, and M. Börnhorst. “Single droplet impingement of urea water solution on heated porous surfaces”. In: *International Journal of Heat and Mass Transfer* 181 (2021), p. 121836. ISSN: 00179310. DOI: 10.1016/j.ijheatmasstransfer.2021.121836.

[78] D. Kuhnke. “Spray/wall-interaction modelling by dimensionless data analysis”. Dissertation. Darmstadt: Technische Universität Darmstadt, 2004.

[79] A. P. Kulkarni, T. Megaritis, and L. C. Ganippa. “Impact dynamics and morphology of urea-water-solution droplets impinging on a hot plate under urea-SCR relevant conditions: Influence of surface tension”. In: *Fuel* 298 (2021), p. 120671. ISSN: 00162361. DOI: 10.1016/j.fuel.2021.120671.

[80] A. P. Kulkarni, T. Megaritis, and L. C. Ganippa. “Insights on the morphology of air-assisted breakup of urea-water-solution sprays for varying surface tension”. In: *INTERNATIONAL JOURNAL OF MULTIPHASE FLOW* 133 (2020). ISSN: 1879-3533. DOI: 10.1016/j.ijmultiphaseflow.2020.103448.

[81] T. Lauer. “Preparation of Ammonia from Liquid AdBlue - Modeling Approaches and Future Challenges”. In: *Chemie Ingenieur Technik* 90.6 (2018), pp. 783–794. ISSN: 0009286X. DOI: 10.1002/cite.201700107.

[82] M. Lavielle. “Using penalized contrasts for the change-point problem”. In: *Signal Processing* 85.8 (2005), pp. 1501–1510. ISSN: 0165-1684. DOI: 10.1016/j.sigpro.2005.01.012.

[83] L. Leger and J. F. Joanny. “Liquid spreading”. In: *Reports on Progress in Physics* 55.4 (1992), pp. 431–486. ISSN: 0034-4885. DOI: 10.1088/0034-4885/55/4/001.

[84] Y. Li, Q. Yang, M. Li, and Y. Song. “Rate-dependent interface capture beyond the coffee-ring effect”. In: *Scientific reports* 6 (2016), p. 24628. DOI: 10.1038/srep24628.

[85] Y. Liao, P. Dimopoulos Eggenschwiler, D. Rentsch, F. Curto, and K. Boulouchos. “Characterization of the urea-water spray impingement in diesel selective catalytic reduction systems”. In: *Applied Energy* 205 (2017), pp. 964–975. ISSN: 03062619. DOI: 10.1016/j.apenergy.2017.08.088.

[86] A. Lundström, B. Andersson, and L. Olsson. “Urea thermolysis studied under flow reactor conditions using DSC and FT-IR”. In: *Chemical Engineering Journal* 150.2-3 (2009), pp. 544–550. ISSN: 13858947. DOI: 10.1016/j.cej.2009.03.044.

[87] P. Mishra, C. M. Pandey, U. Singh, A. Keshri, and M. Sabaretnam. “Selection of appropriate statistical methods for data analysis”. In: *Annals of cardiac anaesthesia* 22.3 (2019), pp. 297–301. DOI: 10.4103/aca.ACA{\textunderscore}248{\textunderscore}18.

[88] S. Y. Misyura and V. S. Morozov. “Influence of the wall on the droplet evaporation”. In: *MATEC Web of Conferences* 23 (2015), p. 01030. DOI: 10.1051/matecconf/20152301030.

[89] S. Y. Misyura, P. A. Strizhak, R. S. Volkov, and V. S. Morozov. “The influence of the wall microtexture on functional properties and heat transfer”. In: *Journal of Molecular Liquids* 294 (2019), p. 111670. ISSN: 01677322. DOI: 10.1016/j.molliq.2019.111670.

[90] J. H. Moon, M. Cho, and S. H. Lee. “Dynamic wetting and heat transfer characteristics of a liquid droplet impinging on heated textured surfaces”. In: *International Journal of Heat and Mass Transfer* 97 (2016), pp. 308–317. ISSN: 00179310. DOI: 10.1016/j.ijheatmasstransfer.2016.02.041.

[91] S. Morin, J. Savarino, M. M. Frey, N. Yan, S. Bekki, J. W. Bottenheim, and J. M. F. Martins. “Tracing the origin and fate of NOx in the Arctic atmosphere using stable isotopes in nitrate”. In: *Science (New York, N.Y.)* 322.5902 (2008), pp. 730–732. DOI: 10.1126/science.1161910.

[92] A. Moriyama, K. Araki, and T. Okouchi. “HEAT-TRANSFER FROM HOT METAL-SURFACE TO AN IMPINGING WATER DROPLET IN TRANSITIONAL BOILING REGIME”. In: *TRANSACTIONS OF THE IRON AND STEEL INSTITUTE OF JAPAN* 25.3 (1985), pp. 198–203.

[93] C. Mundo, M. Sommerfeld, and C. Tropea. “Droplet-wall collisions: Experimental studies of the deformation and breakup process”. In: *INTERNATIONAL JOURNAL OF MULTIPHASE FLOW* 21.2 (1995), pp. 151–173. ISSN: 1879-3533. DOI: 10.1016/0301-9322(94)00069-V.

[94] S. N. A. Musa, M. Saito, T. Furuhata, and M. Arai. “EVAPORATION CHARACTERISTICS OF A SINGLE AQUEOUS UREA SOLUTION DROPLET”. In: *10th International Conference on Liquid Atomization and Spray Systems*. 2006.

[95] V. Nakoryakov, S. Misyura, and S. Elistratov. “Nonisothermal desorption of droplets of complex compositions”. In: *Thermal Science* 16.4 (2012), pp. 997–1004. ISSN: 0354-9836. DOI: 10.2298/TSCI120428116N.

[96] C. Neinhuis. “Characterization and Distribution of Water-repellent, Self-cleaning Plant Surfaces”. In: *Annals of Botany* 79.6 (1997), pp. 667–677. ISSN: 03057364. DOI: 10.1006/anbo.1997.0400.

[97] A. Nicolle, S. Cagnina, and T. de Bruin. “First-principle based modeling of urea decomposition kinetics in aqueous solutions”. In: *Chemical Physics Letters* 664 (2016), pp. 149–153. ISSN: 00092614. DOI: 10.1016/j.cplett.2016.10.032.

[98] M. A. Nilsson, R. J. Daniello, and J. P. Rothstein. “A novel and inexpensive technique for creating superhydrophobic surfaces using Teflon and sandpaper”. In: *Journal of Physics D: Applied Physics* 43.4 (2010), p. 045301. ISSN: 0022-3727. DOI: 10.1088/0022-3727/43/4/045301.

[99] K. Nishad, A. Sadiki, and J. Janicka. “Numerical Investigation of AdBlue Droplet Evaporation and Thermal Decomposition in the Context of NOx-SCR Using a Multi-Component Evaporation Model”. In: *Energies* 11.1 (2018), p. 222. DOI: 10.3390/en11010222.

[100] J. Nocedal and S. J. Wright. *Numerical optimization*. Second edition. Springer series in operation research and financial engineering. New York, NY: Springer, 2006. ISBN: 978-0-387-30303-1. DOI: 10.1007/978-0-387-40065-5.

[101] J. Oliver, C. Huh, and S. Mason. “Resistance to spreading of liquids by sharp edges”. In: *Journal of colloid and interface science* 59.3 (1977), pp. 568–581. DOI: 10.1016/0021-9797(77)90052-2.

[102] OpenAI. *ChatGPT: Large language model*. 2024.

[103] R. Picknett and R. Bexon. “The evaporation of sessile or pendant drops in still air”. In: *Journal of colloid and interface science* 61.2 (1977), pp. 336–350. DOI: 10.1016/0021-9797(77)90396-4.

[104] M. Pieper. *Mathematische Optimierung: Eine Einführung in die kontinuierliche Optimierung mit Beispielen*. essentials. Wiesbaden and Heidelberg: Springer Fachmedien Wiesbaden GmbH, 2017. ISBN: 978-3-658-16975-6. DOI: 10.1007/978-3-658-16975-6.

[105] S. S. Prabhu, N. S. Nayak, N. Kapilan, and Vijaykumar Hindasageri. “An experimental and numerical study on effects of exhaust gas temperature and flow rate on deposit formation in Urea-Selective Catalytic Reduction (SCR) system of modern automobiles”. In: *Applied Thermal Engineering* 111 (2017), pp. 1211–1231. ISSN: 1359-4311. DOI: 10.1016/j.applthermaleng.2016.09.134.

[106] D. Quéré. “Wetting and Roughness”. In: *Annual Review of Materials Research* 38.1 (2008), pp. 71–99. ISSN: 1545-4118. DOI: 10.1146/annurev.matsci.38.060407.132434.

[107] M. Quissek, T. Lauer, O. García-Afonso, and S. Fowles. “Identification of Film Breakup for a Liquid Urea-Water-Solution and Application to CFD”. In: *WCX SAE World Congress Experience*. SAE International, 2019. DOI: 10.4271/2019-01-0983.

[108] R. Rioboo, C. Tropea, and M. Marengo. “OUTCOMES FROM A DROP IMPACT ON SOLID SURFACES”. In: *Atomization and Sprays* 11.2 (2001), p. 12. ISSN: 1044-5110. DOI: 10.1615/AtomizSpr.v11.i2.40.

[109] A. K. Rizvi, K. J. Roberts, and T. Izumi. “The Influence of Supersaturation and the Presence of Biuret on the Nucleation, Growth and Morphology of Urea Crystallised from Ethanolic Solutions”. In: *Israel Journal of Chemistry* 61.11-12 (2021), pp. 727–742. ISSN: 0021-2148. DOI: 10.1002/ijch.202100089.

[110] I. V. Roisman, J. Breitenbach, and C. Tropea. “Thermal atomisation of a liquid drop after impact onto a hot substrate”. In: *Journal of Fluid Mechanics* 842 (2018), pp. 87–101. ISSN: 0022-1120. DOI: 10.1017/jfm.2018.123.

[111] D. T. Ryddner and M. F. Trujillo. “Modeling Urea-Water Solution Droplet Evaporation”. In: *Emission Control Science and Technology* 1.1 (2015), pp. 80–97. ISSN: 2199-3629. DOI: 10.1007/s40825-014-0006-3.

[112] R. Savino, D. Paterna, and N. Favaloro. “Buoyancy and Marangoni Effects in an Evaporating Drop”. In: *Journal of Thermophysics and Heat Transfer* 16.4 (2002), pp. 562–574. ISSN: 0887-8722. DOI: 10.2514/2.6716.

[113] P. M. Schaber, J. Colson, S. Higgins, D. Thielen, B. Anspach, and J. Brauer. “Thermal decomposition (pyrolysis) of urea in an open reaction vessel”. In: *Thermochimica Acta* 424.1-2 (2004), pp. 131–142. ISSN: 00406031. DOI: 10.1016/j.tca.2004.05.018.

[114] J. Schmid, I. Zarikos, A. Terzis, N. Roth, and B. Weigand. “Crystallization of urea from an evaporative aqueous solution sessile droplet at sub-boiling temperatures and surfaces with different wettability”. In: *Experimental Thermal and Fluid Science* 91 (2018), pp. 80–88. ISSN: 08941777. DOI: 10.1016/j.expthermflusci.2017.10.008.

[115] O. Schumacher, C. Ates, M. Börnhorst, R. Koch, and P. Stephan. “Deposit formation from evaporating urea-water droplets on substrates of different wettability”. In: *Journal of colloid and interface science* 634 (2023), pp. 1–13. DOI: 10.1016/j.jcis.2022.12.021.

[116] O. Schumacher, M. Mildenberger, T. Gambaryan-Roisman, and P. Stephan. “Wetting and evaporation of pinned urea–water-droplets on substrates of different wettability”. In: *International Journal of Heat and Fluid Flow* 92 (2021), p. 108886. ISSN: 0142727X. DOI: 10.1016/j.ijheatfluidflow.2021.108886.

[117] D. Schweigert. “Wandwärmeübergang bei der Injektion von Harnstoffwassersprays: Einfluss von Material- und Oberflächeneigenschaften”. Dissertation. Karlsruhe: Karlsruhe Institute of Technology, 2020.

[118] D. Schweigert, B. Damson, H. Lüders, P. Stephan, and O. Deutschmann. “The effect of wetting characteristics, thermophysical properties, and roughness on spray-wall heat transfer in selective catalytic reduction systems”. In: *International Journal of Heat and Mass Transfer* 152 (2020), p. 119554. ISSN: 00179310. DOI: 10.1016/j.ijheatmasstransfer.2020.119554.

[119] C. Semprebon, P. Forsberg, C. Priest, and M. Brinkmann. “Pinning and wicking in regular pillar arrays”. In: *Soft matter* 10.31 (2014), pp. 5739–5748. DOI: 10.1039/c4sm00684d.

[120] G. M. H. Shahariar and O. T. Lim. “A Study on Urea-Water Solution Spray-Wall Impingement Process and Solid Deposit Formation in Urea-SCR de-NOx System”. In: *Energies* 12.1 (2019), p. 125. DOI: 10.3390/en12010125.

[121] N. Shahidzadeh-Bonn, S. Rafaï, D. Bonn, and G. Wegdam. “Salt crystallization during evaporation: impact of interfacial properties”. In: *Langmuir* 24.16 (2008), pp. 8599–8605. ISSN: 0743-7463. DOI: 10.1021/la8005629.

[122] M. Shanahan and C. Bourgès. “Effects of evaporation on contact angles on polymer surfaces”. In: *International Journal of Adhesion and Adhesives* 14.3 (1994), pp. 201–205. ISSN: 01437496. DOI: 10.1016/0143-7496(94)90031-0.

[123] S. S. Shapiro and M. B. Wilk. “An analysis of variance test for normality (complete samples)”. In: *Biometrika* 52.3-4 (1965), pp. 591–611. ISSN: 0006-3444. DOI: 10.1093/biomet/52.3-4.591.

[124] S. Shibuichi, T. Onda, N. Satoh, and K. Tsujii. “Super Water-Repellent Surfaces Resulting from Fractal Structure”. In: *The Journal of Physical Chemistry* 100.50 (1996), pp. 19512–19517. ISSN: 0022-3654. DOI: 10.1021/jp9616728.

[125] D. H. Shin, S. H. Lee, J.-Y. Jung, and J. Y. Yoo. “Evaporating characteristics of sessile droplet on hydrophobic and hydrophilic surfaces”. In: *Microelectronic Engineering* 86.4-6 (2009), pp. 1350–1353. ISSN: 0167-9317. DOI: 10.1016/j.mee.2009.01.026.

[126] T. Shudo, K. Omori, and O. Hiyama. “NO reduction and NO2 emission characteristics in rich-lean combustion of hydrogen”. In: *International Journal of Hydrogen Energy* 33.17 (2008), pp. 4689–4693. ISSN: 03603199. DOI: 10.1016/j.ijhydene.2008.05.034.

[127] K. Siebertz, D. van Bebber, and T. Hochkirchen. *Statistische Versuchsplanung: Design of Experiments (DoE)*. 2. Aufl. 2017. VDI-Buch. Berlin, Heidelberg: Springer Berlin Heidelberg, 2017. ISBN: 9783662557433.

[128] D. Sivakumar, K. Katagiri, T. Sato, and H. Nishiyama. “Spreading behavior of an impacting drop on a structured rough surface”. In: *Physics of Fluids* 17.10 (2005), p. 100608. ISSN: 10706631. DOI: 10.1063/1.2033627.

[129] H. Smith, T. Lauer, M. Mayer, and S. Pierson. “Optical and Numerical Investigations on the Mechanisms of Deposit Formation in SCR Systems”. In: *SAE International Journal of Fuels and Lubricants* 7.2 (2014), pp. 525–542. ISSN: 1946-3960. DOI: 10.4271/2014-01-1563.

[130] H. Smith, T. Lauer, V. Schimik, and K. Gabel. “Evaluation and Prediction of Deposit Severity in SCR Systems”. In: *SAE International Journal of Engines* 9.3 (2016), pp. 1735–1750. ISSN: 1946-3944. DOI: 10.4271/2016-01-0970.

[131] C. Sodtke and P. Stephan. “Spray cooling on micro structured surfaces”. In: *International Journal of Heat and Mass Transfer* 50.19-20 (2007), pp. 4089–4097. ISSN: 00179310. DOI: 10.1016/j.ijheatmasstransfer.2006.12.037.

[132] V. Soulié, S. Karpitschka, F. Lequien, P. Prené, T. Zemb, H. Moehwald, and H. Riegler. “The evaporation behavior of sessile droplets from aqueous saline solutions”. In: *Physical chemistry chemical physics : PCCP* 17.34 (2015), pp. 22296–22303. DOI: 10.1039/c5cp02444g.

[133] D. M. Spori, T. Drobek, S. Zürcher, M. Ochsner, C. Sprecher, A. Mühlebach, and N. D. Spencer. “Beyond the lotus effect: roughness influences on wetting over a wide surface-energy range”. In: *Langmuir* 24.10 (2008), pp. 5411–5417. ISSN: 0743-7463. DOI: 10.1021/la800215r.

[134] H. J. J. Staat, T. Tran, B. Geerdink, G. Riboux, C. Sun, J. M. Gordillo, and D. Lohse. “Phase diagram for droplet impact on superheated surfaces”. In: *Journal of Fluid Mechanics* 779 (2015). ISSN: 0022-1120. DOI: 10.1017/jfm.2015.465.

[135] M. Stein, V. Bykov, A. Bertótiné Abai, C. Janzer, U. Maas, O. Deutschmann, and M. Olzmann. “A reduced model for the evaporation and decomposition of urea–water solution droplets”. In: *International Journal of Heat and Fluid Flow* 70 (2018), pp. 216–225. ISSN: 0142727X. DOI: 10.1016/j.ijheatfluidflow.2018.02.005.

[136] T. Still, P. J. Yunker, and A. G. Yodh. “Surfactant-induced Marangoni eddies alter the coffee-rings of evaporating colloidal drops”. In: *Langmuir* 28.11 (2012), pp. 4984–4988. ISSN: 0743-7463. DOI: 10.1021/la204928m.

[137] R. Storn and K. Price. “Differential Evolution – A Simple and Efficient Heuristic for global Optimization over Continuous Spaces”. In: *Journal of Global Optimization* 11.4 (1997), pp. 341–359. ISSN: 09255001. DOI: 10.1023/A:1008202821328.

[138] K. Stroh and C. Marb. *Bodennahes Ozon und Sommersmog*. 2020.

[139] V. O. Strots, S. Santhanam, B. J. Adelman, G. A. Griffin, and E. M. Derybowski. “Deposit Formation in Urea-SCR Systems”. In: *SAE International Journal of Fuels and Lubricants* 2.2 (2009), pp. 283–289. ISSN: 1946-3960. DOI: 10.4271/2009-01-2780.

[140] Z. Sun, X. Chen, and H. Qiu. “Bubble Dynamics and Heat Transfer During Pool Boiling on Wettability Patterned Surfaces”. In: *Heat Transfer Engineering* 39.7-8 (2018), pp. 663–671. ISSN: 1521-0537. DOI: 10.1080/01457632.2017.1325676.

[141] S. Suzuki and K. Abe. “Topological structural analysis of digitized binary images by border following”. In: *Computer Vision, Graphics, and Image Processing* 30.1 (1985), pp. 32–46. ISSN: 0734189X. DOI: 10.1016/0734-189X(85)90016-7.

[142] P. Takhistov and H.-C. Chang. “Complex Stain Morphologies”. In: *Industrial & Engineering Chemistry Research* 41.25 (2002), pp. 6256–6269. ISSN: 1520-5045. DOI: 10.1021/ie010788.

[143] R. Tekidou, G. Duursma, C. Mackenzie-Dover, V. Kubyshkina, J. Terry, and K. Sefiane. “Wetting phenomena observed in evaporating droplets on structured surfaces”. In: *Heat Transfer Engineering* 41.19-20 (2019), pp. 1645–1653. ISSN: 1521-0537. DOI: 10.1080/01457632.2019.1640450.

[144] P. Tsai, R. G. H. Lammertink, M. Wessling, and D. Lohse. “Evaporation-triggered wetting transition for water droplets upon hydrophobic microstructures”. In: *Physical review letters* 104.11 (2010), p. 116102. DOI: 10.1103/PhysRevLett.104.116102.

[145] Umweltbundesamt. *Emissionen ausgewählter Luftschadstoffe nach Quellkategorien*. 2024.

[146] V. Vaikuntanathan and D. Sivakumar. “Transition from Cassie to impaled state during drop impact on groove-textured solid surfaces”. In: *Soft matter* 10.17 (2014), pp. 2991–3002. DOI: 10.1039/c4sm00050a.

[147] M. T. van Os. “Surface modification by plasma polymerization: Film deposition, tailoring of surface properties and biocompatibility”. Dissertation. Enschede: University of Twente, 2000.

[148] J. Wang, Y. Wu, Y. Cao, G. Li, and Y. Liao. “Influence of surface roughness on contact angle hysteresis and spreading work”. In: *Colloid and Polymer Science* 298.8 (2020), pp. 1107–1112. ISSN: 0303-402X. DOI: 10.1007/s00396-020-04680-x.

[149] T. J. Wang, S. W. Baek, S. Y. Lee, D. H. Kang, and G. K. Yeo. “Experimental investigation on evaporation of urea-water-solution droplet for SCR applications”. In: *AIChE Journal* 55.12 (2009), pp. 3267–3276. ISSN: 00011541. DOI: 10.1002/aic.11939.

[150] D. E. R. Warburton, S. S. D. Bredin, E. M. Shellington, C. Cole, A. de Faye, J. Harris, D. D. Kim, and A. Abelsohn. “A Systematic Review of the Short-Term Health Effects of Air Pollution in Persons Living with Coronary Heart Disease”. In: *Journal of clinical medicine* 8.2 (2019). ISSN: 2077-0383. DOI: 10.3390/jcm8020274.

[151] C. L. Weeks, D. R. Ibeling, S. Han, L. Ludwig, and P. Ayyappan. “Analytical Investigation of Urea Deposits in SCR System”. In: *SAE International Journal of Engines* 8.3 (2015), pp. 1219–1239. ISSN: 1946-3944. DOI: 10.4271/2015-01-1037.

[152] L. Wei, Z. Youtong, and M. Asif. “Investigation on UWS evaporation for vehicle SCR applications”. In: *AIChE Journal* 62.3 (2016), pp. 880–890. ISSN: 00011541. DOI: 10.1002/aic.15078.

[153] R. N. Wenzel. “RESISTANCE OF SOLID SURFACES TO WETTING BY WATER”. In: *Industrial & Engineering Chemistry* 28.8 (1936), pp. 988–994. ISSN: 0019-7866. DOI: 10.1021/ie50320a024.

[154] H. White. “A Heteroskedasticity-Consistent Covariance Matrix Estimator and a Direct Test for Heteroskedasticity”. In: *Econometrica* 48.4 (1980), p. 817. ISSN: 00129682. DOI: 10.2307/1912934.

[155] G. Wolansky and A. Marmur. “Apparent contact angles on rough surfaces: the Wenzel equation revisited”. In: *Colloids and Surfaces A: Physicochemical and Engineering Aspects* 156.1-3 (1999), pp. 381–388. ISSN: 0927-7757. DOI: 10.1016/S0927-7757(99)00098-9.

[156] World Health Organization WHO. *Health Aspects of Air Pollution with Particulate Matter, Ozone and Nitrogen Dioxide*. Bonn, 2003.

[157] M. L. Wright and A. C. Lewis. “Emissions of NO x from blending of hydrogen and natural gas in space heating boilers”. In: *Elementa: Science of the Anthropocene* 10.1 (2022). DOI: 10.1525/elementa.2021.00114.

[158] Z. Yan and Y. Li. “A Comprehensive Study of Dynamic and Heat Transfer Characteristics of Droplet Impact on Micro-Scale Rectangular Grooved Surface”. In: *Energies* 11.6 (2018), p. 1390. DOI: 10.3390/en11061390.

[159] L. Zhang, B. Wang, J. Tang, Y. Liu, Q. Hua, and L. Liu. “Determination of the Metastable Zone and Induction Period of Urea Phosphate Solution”. In: *International Journal of Chemical Reactor Engineering* 17.8 (2019). DOI: 10.1515/ijcre-2018-0174.

CHAPTER A

Appendix

A.1. Model results

Deposit mass

	Coefficient	Standard error	t	p	[0.025	0.975]
const	0.0099	0.000	61.462	0.000	0.010	0.010
$\Delta\tau$	-0.0149	0.001	-10.130	0.000	-0.018	-0.012
θ_c	0.0078	0.002	4.597	0.000	0.004	0.011
Ra	-0.0059	0.002	-2.537	0.014	-0.011	-0.001
R_A	-0.0006	0.003	-0.218	0.828	-0.006	0.005
T_{wall}	-0.0045	0.001	-7.362	0.000	-0.006	-0.003
surface type	-0.0006	0.001	-0.604	0.549	-0.002	0.001
$\Delta\tau^2$	0.0025	0.001	2.583	0.013	0.001	0.004
$\Delta\tau \times T_{\text{wall}}$	0.0110	0.001	9.383	0.000	0.009	0.013
θ_c^2	-0.0007	0.001	-0.545	0.588	-0.003	0.002
$\theta_c \times Ra$	0.0006	0.001	1.045	0.301	-0.001	0.002
$\theta_c \times R_A$	-0.0016	0.001	-2.769	0.008	-0.003	-0.000
$\theta_c \times T_{\text{wall}}$	-0.0061	0.001	-5.058	0.000	-0.009	-0.004
Ra^2	0.0008	0.001	0.657	0.514	-0.002	0.003
$Ra \times T_{\text{wall}}$	0.0028	0.002	1.782	0.081	-0.000	0.006
R_A^2	0.0001	0.001	0.092	0.927	-0.003	0.003
$R_A \times T_{\text{wall}}$	0.0013	0.002	0.816	0.418	-0.002	0.004

Table A.1.: Coefficients with corresponding t and p values of a two-tailed t-test and the 95 % confidence interval for the deposit mass model

Deposit area

	Coefficient	Standard error	t	p	[0.025	0.975]
const	127.1206	3.201	39.716	0.000	120.695	133.546
$\Delta\tau$	1.6646	6.681	0.249	0.804	-11.748	15.077
θ_c	-133.7038	32.644	-4.096	0.000	-199.240	-68.168
Ra	108.4374	46.050	2.355	0.022	15.988	200.886
R_A	-105.5286	52.018	-2.029	0.048	-209.960	-1.098
T_{wall}	-20.2283	10.979	-1.842	0.071	-42.270	1.814
surface type	37.1932	18.600	2.000	0.051	-0.148	74.534
$\Delta\tau \times Ra$	-11.3243	8.364	-1.354	0.182	-28.115	5.466
$\Delta\tau \times R_A$	-4.7603	8.539	-0.557	0.580	-21.903	12.382
θ_c^2	57.9239	23.087	2.509	0.015	11.575	104.273
$\theta_c \times Ra$	-40.2426	10.953	-3.674	0.001	-62.231	-18.254
$\theta_c \times R_A$	17.8625	11.216	1.593	0.117	-4.655	40.380
$\theta_c \times T_{\text{wall}}$	47.2806	24.072	1.964	0.055	-1.046	95.607
Ra^2	-35.0966	24.761	-1.417	0.162	-84.806	14.612
$Ra \times T_{\text{wall}}$	63.5324	30.948	2.053	0.045	1.402	125.663
R_A^2	35.1599	28.729	1.224	0.227	-22.517	92.837
$R_A \times T_{\text{wall}}$	67.2596	30.976	2.171	0.035	5.072	129.447

Table A.2.: Coefficients with corresponding t and p values of a two-tailed t-test and the 95 % confidence interval for the deposit area model

Deposit volume

	Coefficient	Standard error	t	p	[0.025	0.975]
const	12.9368	0.316	40.945	0.000	12.303	13.570
$\Delta\tau$	-6.0724	2.355	-2.579	0.013	-10.795	-1.350
θ_c	-1.9152	2.170	-0.883	0.381	-6.267	2.437
Ra	-7.0696	3.050	-2.318	0.024	-13.188	-0.951
R_A	-20.5794	5.039	-4.084	0.000	-30.687	-10.472
T_{wall}	-4.8237	0.896	-5.385	0.000	-6.621	-3.027
surface type	4.1150	1.632	2.522	0.015	0.842	7.388
$\Delta\tau \times \theta_c$	-1.5365	0.902	-1.704	0.094	-3.345	0.272
$\Delta\tau \times R_A$	-1.3990	0.658	-2.127	0.038	-2.718	-0.080
$\Delta\tau \times T_{\text{wall}}$	6.4147	2.298	2.791	0.007	1.805	11.024
θ_c^2	4.4508	2.105	2.115	0.039	0.229	8.672
$\theta_c \times R_A$	-4.5331	0.865	-5.241	0.000	-6.268	-2.798
$Ra \times T_{\text{wall}}$	5.6322	3.055	1.844	0.071	-0.496	11.760
R_A^2	21.4214	2.804	7.640	0.000	15.798	27.045
$R_A \times T_{\text{wall}}$	8.2689	3.058	2.704	0.009	2.136	14.402

Table A.3.: Coefficients with corresponding t and p values of a two-tailed t-test and the 95 % confidence interval for the deposit volume model

Deposit volume subset

	Coefficient	Standard error	t	p	[0.025	0.975]
const	9.4565	0.242	39.013	0.000	8.969	9.944
$\Delta\tau$	-9.6699	1.715	-5.639	0.000	-13.121	-6.218
θ_c	-1.9558	1.604	-1.219	0.229	-5.184	1.273
Ra	-0.9751	0.858	-1.137	0.262	-2.702	0.752
R_A	3.2454	0.738	4.397	0.000	1.760	4.731
T_{wall}	-3.8834	0.528	-7.359	0.000	-4.946	-2.821
surface type	1.2289	0.717	1.713	0.093	-0.215	2.673
$\Delta\tau \times T_{\text{wall}}$	8.8048	1.766	4.985	0.000	5.249	12.360
θ_c^2	4.0392	1.534	2.633	0.011	0.951	7.127
$\theta_c \times Ra$	-0.6667	0.885	-0.754	0.455	-2.448	1.114
$\theta_c \times R_A$	-4.0516	1.082	-3.744	0.001	-6.230	-1.873
R_A^2	4.2205	0.906	4.657	0.000	2.396	6.045
$R_A \times T_{\text{wall}}$	-4.1971	1.725	-2.433	0.019	-7.669	-0.725

Table A.4.: Coefficients with corresponding t and p values of a two-tailed t-test and the 95 % confidence interval for the deposit volume subset model

A.2. Model evaluation

Deposit area

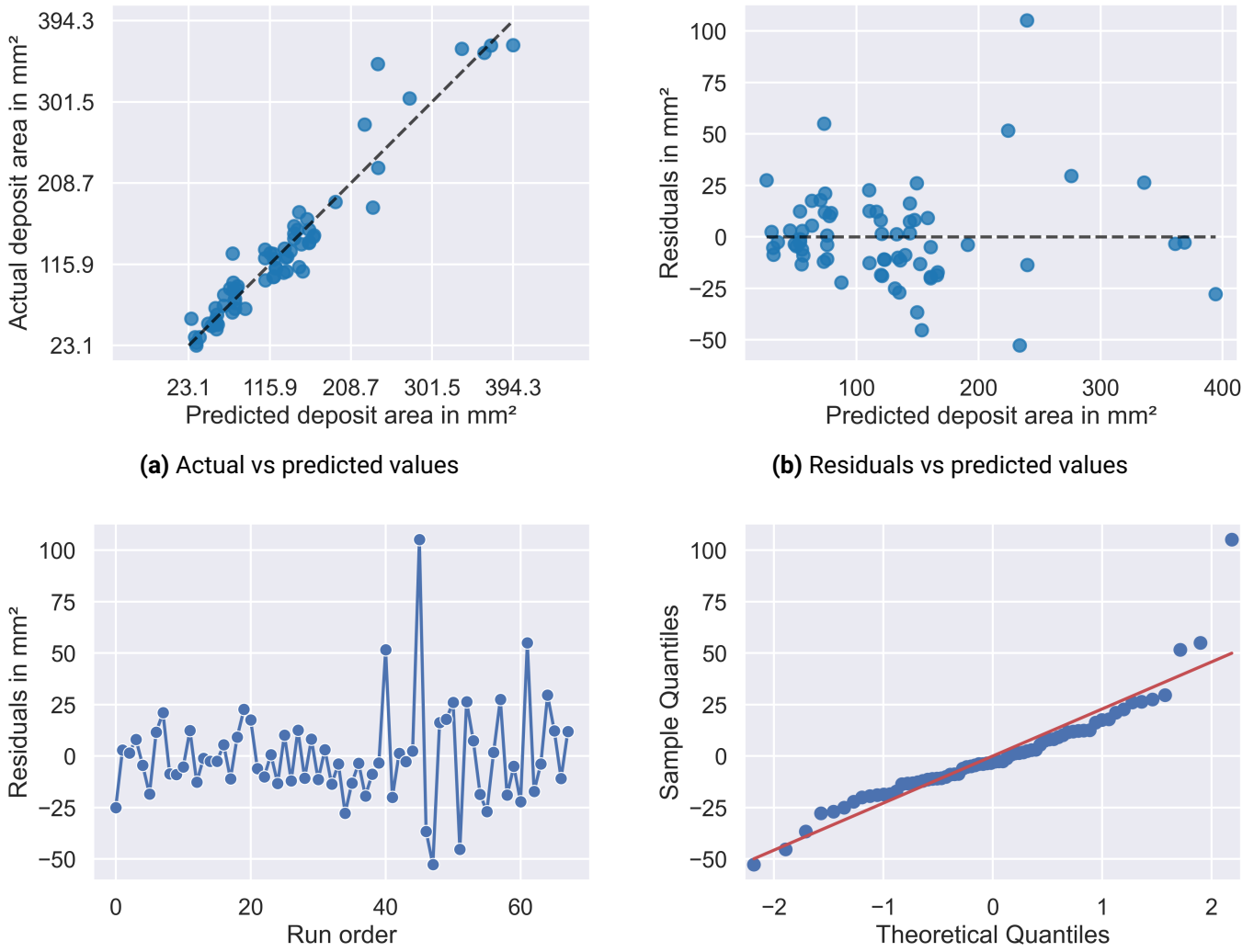

(a) Actual vs predicted values

(b) Residuals vs predicted values

(c) Residuals vs run order of the respective experiments

(d) Q-Q-plot illustrating how the distribution of measured values compares to a normal distribution

Figure A.1.: Model evaluation plots of the regression model for deposit area

Deposit volume

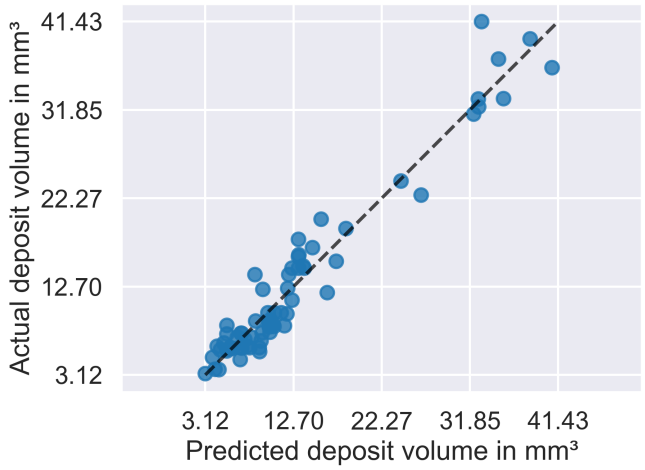

(a) Actual vs predicted values

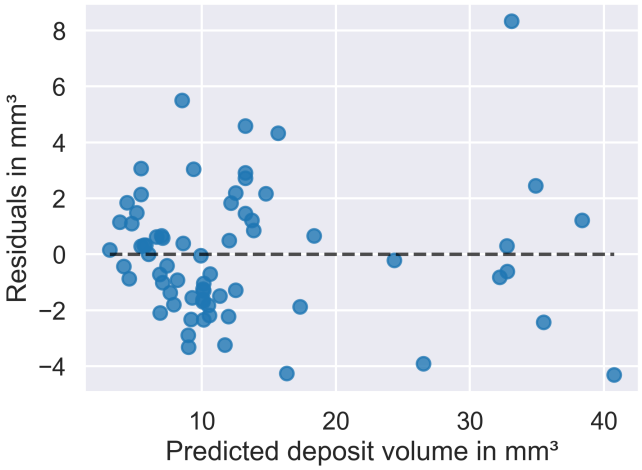

(b) Residuals vs predicted values

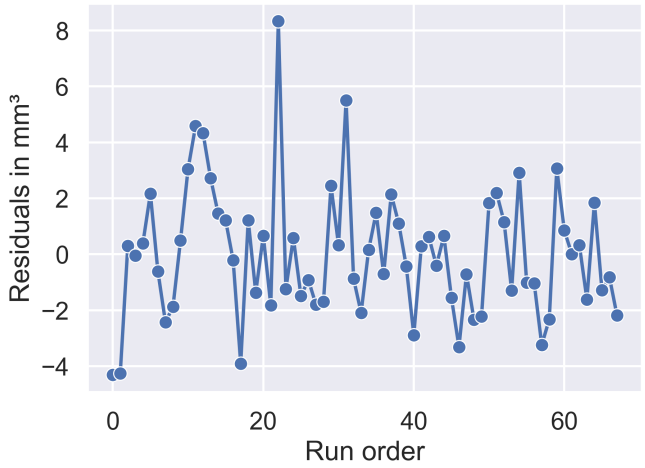

(c) Residuals vs run order of the respective experiments

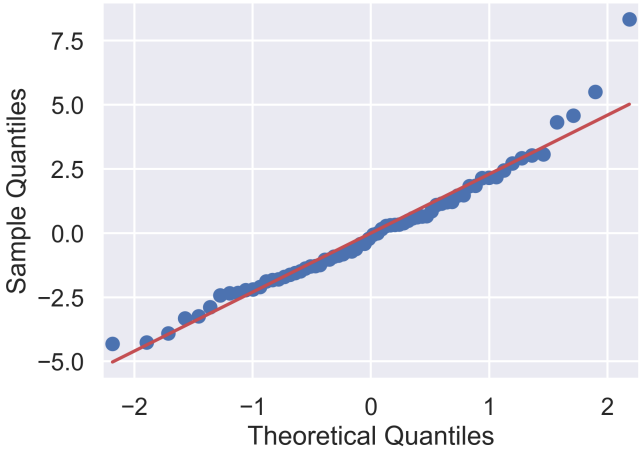

(d) Q-Q-plot illustrating how the distribution of measured values compares to a normal distribution

Figure A.2.: Model evaluation plots of the regression model for deposit volume

Deposit volume subset

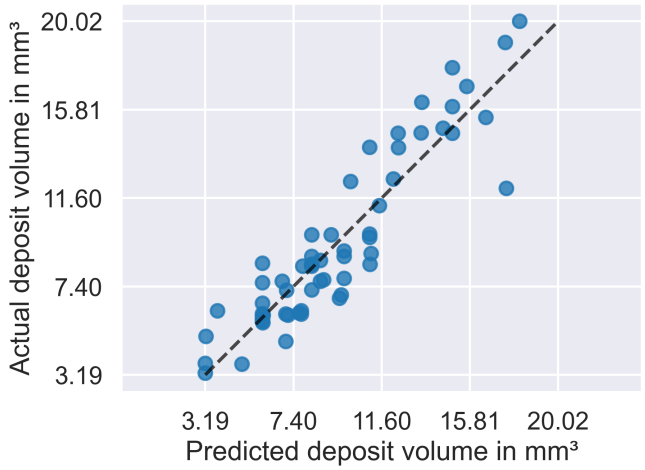

(a) Actual vs predicted values

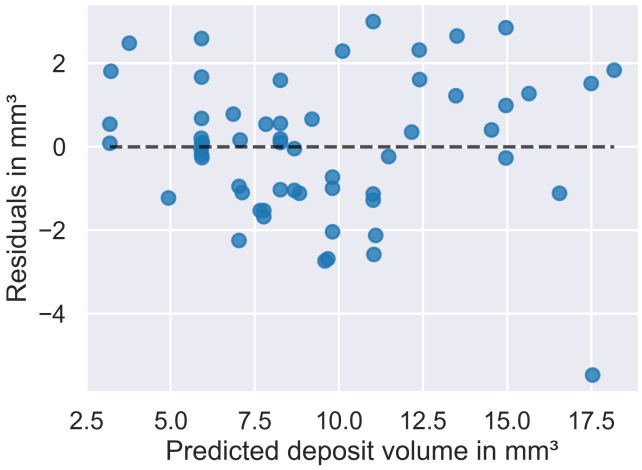

(b) Residuals vs predicted values

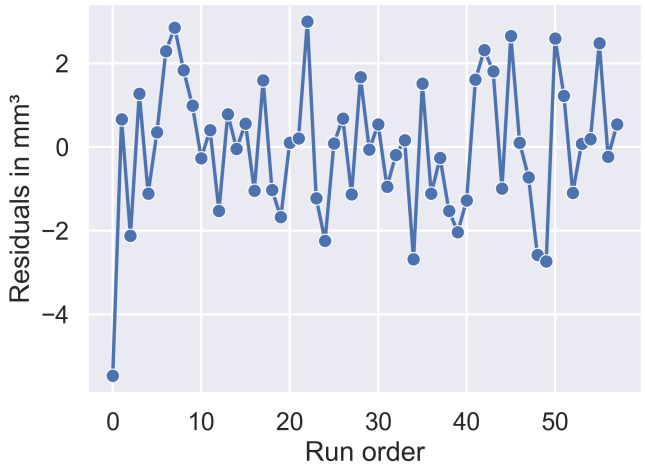

(c) Residuals vs run order of the respective experiments

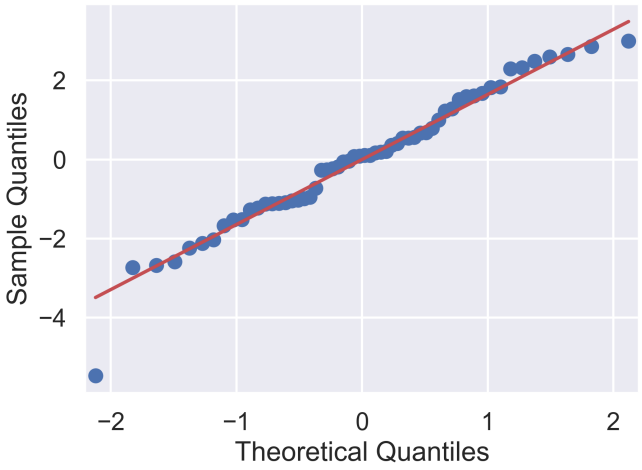

(d) Q-Q-plot illustrating how the distribution of measured values compares to a normal distribution

Figure A.3.: Model evaluation plots of the regression model for deposit volume built by using a subset of the data

Publications

Peer reviewed articles

O. Schumacher, M. Mildenberger, T. Gambaryan-Roisman, and P. Stephan. “Wetting and evaporation of pinned urea–water-droplets on substrates of different wettability”. In: *International Journal of Heat and Fluid Flow 92*, 2021.

M. Maliha, J. Ickinger, H. Kubach, **O. Schumacher**, T. Koch, and P. Stephan. “Influence of DMC percentage in fuel on deposit formation and emission behaviour”. In: *International Journal of Heat and Fluid Flow 95*, 2022.

M. Mildenberger, **O. Schumacher**, M. Stein, P. Stephan, and T. Gambaryan-Roisman. “Numerical simulation of the evaporation process of pinned urea-water droplets in cavities”. In: *International Journal of Heat and Fluid Flow 95*, 2022.

O. Schumacher, C. Ates, M. Börnhorst, R. Koch, and P. Stephan. “Deposit formation from evaporating urea-water droplets on substrates of different wettability”. In: *Journal of Colloid and Interface Science 634*, 2023.

O. Schumacher, A. Sielaff, and P. Stephan. “EVAPORATION AND RESIUDE FORMATION OF DIMETHYL CARBONATE DROPLETS ON HOT WALLS”. In: *Proceedings of the 17th International Heat Transfer Conference*, 2023.

Conference contributions (not reviewed or abstracts only)

O. Schumacher, T. Gambaryan-Roisman, and P. Stephan. “Einfluss der Benetzbarkeit von Oberflächen auf die Verdampfung und Ablagerungsbildung von AdBlue-Einzeltropfen”. In: *Jahrestreffen der ProcessNet-Fachgruppen Fluidverfahrenstechnik und Wärme- und Stoffübertragung*, virtual conference, 2021.

O. Schumacher, T. Gambaryan-Roisman, and P. Stephan. “Deposit formation of AdBlue on surfaces of different wettability”. In: *The International Combustion Institute Summer School*, virtual conference, 2021.

M. Mildenberger, **O. Schumacher**, P. Stephan, and T. Gambaryan-Roisman. "Numerical Simulation of Evaporation of Pinned Urea-Water Droplets in Restricted Domain". In: *5th International Conference on Droplets*, virtual conference, 2021.

O. Schumacher, A. Sielaff, T. Gambaryan-Roisman, and P. Stephan. "Deposit formation of multicomponent fluids in evaporating droplets". In: *Annual Meeting on Reaction Engineering and ProcessNet Subject Division Heat and Mass Transfer*, Würzburg, Germany, March 21-23, 2021.

O. Schumacher, A. Sielaff, and P. Stephan. "Evaporation and deposit formation of hydrocarbon fluids on hot walls". In: *3rd International Workshop on Near-Wall Reactive Flows*, Darmstadt, Germany, November 3-4, 2022.

O. Schumacher, T. Hintz, and P. Stephan. "Analyse & Modellierung der Effekte von Wandeigenschaften auf die Ablagerungsbildung verdampfender Harnstoff-Wasser-Lösung". In: *Jahrestreffen der DECHEMA/VDI-Fachgruppen Wärme- und Stoffübertragung und Trocknungstechnik*, Magdeburg, Germany, March 11-13, 2024.